Double-Resonance Studies on Compact, High-performance Rubidium Cell Frequency Standards

Thejesh N. Bandi

2013

UNIVERSITÉ DE
NEUCHÂTEL

This thesis presents experimental studies on continuous-wave (CW) laser-microwave double-resonance (DR) spectroscopy and metrology in rubidium (^{87}Rb) vapor cells in view of new high-performance, compact Rb-cell atomic clocks. Two different approaches were studied in this work; the wall-coated cell approach and the enlarged cell buffer gas cell approach. New magnetron-type cavity microwave resonator (MWR) that can hold the vapor cells as large as 25 mm diameter was developed and studied. Detailed analyses on the short- medium- and long-term clock stabilities are measured and presented for both the approaches.

Laboratoire Temps-Fréquence, UniNE

Thèse présentée à la faculté des sciences, université de Neuchâtel
pour l'obtention du grade de docteur ès sciences.

DOUBLE-RESONANCE STUDIES ON COMPACT, HIGH-PERFORMANCE RUBIDIUM CELL FREQUENCY STANDARDS

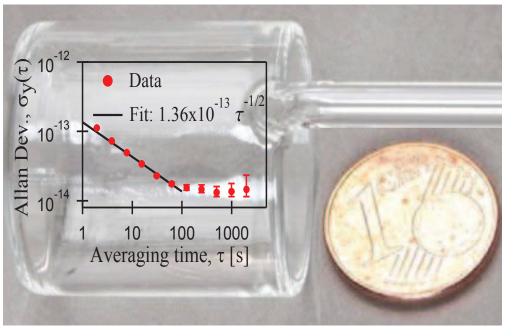

Presented by:
Thejesh N. Bandi

M.Sc., by research, Quantum optics
Cork Institute of Technology (CIT), Ireland.

Acceptée sur proposition du jury:

Prof. Gaetano Mileti, Directeur de thése, Université de Neuchâtel
Dr. Christoph Affolderbach, Rapporteur, Université de Neuchâtel
Dr. Filippo Levi, Rapporteur, INRIM, Italy
Prof. Phillip Treutlein, Rapporteur, Universität Basel
Prof. Anja Skrivervik, Examinateur, EPFL, Lausanne

Soutenue le 19 Avril 2013

Laboratoire Temps-Fréquence (LTF)

UNIVERSITÉ DE
NEUCHÂTEL

Faculté des sciences
Secrétariat-décanat de Faculté
Rue Emile-Argand 11
2000 Neuchâtel - Suisse
Tél: + 41 (0)32 718 2100
E-mail: secretariat.sciences@unine.ch

IMPRIMATUR POUR THESE DE DOCTORAT

**La Faculté des sciences de l'Université de Neuchâtel
autorise l'impression de la présente thèse soutenue par**

Monsieur Thejesh BANDI NAGABHUSHAN

Titre:

“Double-Resonance Studies on Compact High-performance Rubidium Cell Frequency Standards”

sur le rapport des membres du jury:

- Prof. ass. Gaetano Mileti, Université de Neuchâtel, directeur de thèse
- Dr Filippo Levi, INRIM, Torino, Italie
- Prof. Philip Treutlein, Université de Bâle
- Dr. Christoph Affolderbach, Université de Neuchâtel
- Prof. Anja Skrivervik, LEMA, EPF Lausanne

Neuchâtel, le 16 mai 2013

Le Doyen, Prof. P. Kropf

Abstract

This thesis presents experimental studies on continuous-wave (CW) laser-microwave double-resonance (DR) spectroscopy and metrology in rubidium (^{87}Rb) vapor cells in view of new high-performance, compact Rb-cell atomic clocks. The Rb vapor cell is confined inside a magnetron-type cavity microwave resonator (MWR). The CW DR spectroscopy involves two resonant electromagnetic fields that are operated simultaneously to interrogate the atoms - the *optical field* to polarize the atoms by optical pumping, and the *microwave field* to drive the ground-state hyperfine clock transition that serves as an atomic frequency reference. Details on characterization of compact laser heads and microwave synthesizers used in this work are presented. The vapor cell standards are useful in our everyday lives for applications ranging from telecommunications, navigation, metrology etc.

In view of improving the performances of the Rb cell standards, two different clock approaches were studied in detail:

The first one is on use of vapor cells (1.4 cm^3) whose inner walls are coated with anti-relaxation material. A first ever wall-coated cell clock was demonstrated with a good short-term frequency stability. The medium- to long-term stability was found to be limited by the temperature coefficient (TC) of the coating material itself. This work gave the insight to important features to be considered in future anti-relaxation coating materials for atomic standards.

The second novel approach involves using a bigger cell (12 cm^3) within a newly developed, improved MWR towards a high-performance atomic standard. Adopting a larger cell gives a higher atomic Q-factor signal that improves the short-term clock stability. In this approach, the cell was filled with ^{87}Rb and buffer gases. With this clock, we demonstrate the state-of-the-art short-term stability of $< 1.4\times10^{-13}\ \tau^{-1/2}$. Metrological quantitative measurements on parameters influencing the medium- to long-term stability were studied in view of next generation satellite navigation systems that demand a stability level of $<1\times10^{-14}$ at 10^4 s (equivalent to <1 ns/day). The potential of short-term stability and understanding of the limiting factors on medium- to long-term time scales demonstrated in this study pave the way for future work towards the commercialization of high-performace Rb atomic clocks for a variety of applications.

Keywords: Rb standard; Double-Resonance (DR); Spectroscopy; Vapor cells; Magnetron-type cavity; Frequency stability; Wall-coating; Metrology.

Acknowledgements

> *I can no other answer make, but, thanks, and thanks.*
> *-William Shakespeare*

First and foremost, I would like to thank my supervisor Prof. Gaetano Mileti for giving me an opportunity to be part of the LTF team. His guidance and support since last five years has been encouraging and motivating me to do better research in the field of atomic clocks. He not only provided the opportunity to work in lab, but also involved me directly in project meetings and presentations. This helped me to learn how to manage a project; which is an integral part of any research activity. I must say, as for as I know, there is a lot of management skills that one can learn from Gaetano, which comes naturally to him. I equally would like to thank Dr. Christoph Affolderbach in every respect. He was always there to lend a helping hand whenever needed. Be it in the lab or to understand a physics problem. Christoph helped me also to improve my technical writing skills, of course, always towards perfection. I take this opportunity to thank all the jury members for a thorough reading of this manuscript and suggestions.

Working in LTF with fantastic views of Neuchâtel lake and the alps is only valuable when having helpful and friendly-natured colleagues. I like to thank Danijela Miletic for her help, friendliness whenever needed; Matthieu Pellaton for interesting and intriguing discussions; Florian Gruet for helping with French when needed and exchanges on laser heads characterization; Dr. Renaud Matthey for help and support; Dr. Gianni Di Domenico for the discussions on mathematica. I also would like to thank my other past and present colleagues Joab Di Francesco; Dr. Daniel Hofstetter, Prof. Thomas Südmeyer, Dr. Stéphane Schilt; Lionel Tombez; Prof. Pierre Thomann; Nikola Bukalovic; Dr. Laurent Devanoges; and Dr. Vladimir Dolgovskiy for helping me integrate better in the LTF team. Teaching in TPDs is fun with the companies like Dr. Clément Didiot, Alexander and Dr. Gunnar Garnier. The inital work I did in developing a new enlarged magnetron cavity was helped by Dr. Hartmut Schweda. His expertise and experience on magnetron cavities helped me to understand better about these devices. I take this opportunity to thank him for his help and support.

Behind the building of an atomic clock there is a lot of technical expertise that is required. I like to thank Patrick Scherler for the CAD designs, the support on cavities, and building PP assemblies. His way of working to ensure not only the job is done, but it is done to his satisfaction always brings out the best from him. Though my French is very basic, Patrick always helped to keep our conversations going smooth. The same is true with Daniel Varidel, who always is enthusiastic in learning a new vocabulary in English when we talk. Daniel's support in the electronics circuits and backing-up the precious and pain stakenly acquired research data is very helpful. His experience with computers and electronics is invaluable. I also like to thank Marc Durrenberger for building precise laser control and resonator control electronics systems; they do a great job in lab. I would like to thank Dominique Schenker for his technical support. I also thank the machine shop crew André Cornu and Isidro Fernandez along with Christian Heche.

I like to convey my heartiest thanks to the LTF secretariat Muriel Vallery . She was there whenever I was in need of managing any admin. duty. Her support and gentleness makes things easier, which is otherwise not so interesting admin. procedures.

I would like to also thank our external collaborators. Firstly, the team of LEMA, EPFL: Prof. Anja K. Skrivervik for her constant support; Dr. Francesco Merli for the simulations on 14 mm cavity and Camillo Stefanucci for the simulations on 25 mm cavity, which helped us to modify and tune our cavity to get the uniform mode. Our collaborators from INRIM, Italy: Dr. Fillipo Levi, for giving me the opportunity to work in his team; Dr. Aldo Godone, whom I worked with and learnt cavity tuning techniques; Dr. Claudio Calosso, for building an excellent low-phase noise LO for our high-performance clock, it's installation in LTF for our setup and the phase noise measurements; Dr. Salvatore Micalizio for the discussions.

The ESA collaborated project with INRIM also had industrial partners (Spectratime SA, Neuchâtel and Selex Galielo, Milan) that I like to thank. In particular, I like to thank Fabien Droz; Pascal Rochat; Dr. Giovanni Busca for analyzing and validating our work. I also take this opportunity to thank the ESA technical officer, Dr. Pierre Waller for helping me learn how to write the technical notes. I thank ESA, Swiss Space Office (SSO), and UniNE for the financial support during my PhD.

All this work wouldn't have been a possibility without the support, love, affection and understanding I have received from my wife Bindhu Nisha, and my parents–Appaji (Nagabhushan), Amma (Girija). I also like to thank the other members of my family: especially my beloved uncle Sadananda, who constantly supported me through thick and thin all these years; Tressy aunty; my Ajjis; and my mother-in-law Vanajakshi for their love and support. I thank Bindhu for carefully going through the draft manuscript of this thesis to find the typos.

I would like to extend my thanks to all my friends who encouraged and supported me throughout my PhD time. A special thanks to Pradyumna (Pradyu), EPFL who got me the journal articles whenever needed, this was of great help as we did not have access to journal papers in our University. I take this opportunity also to thank my mentor Dr. Brian Shortt for his encouragement and support to my research career, Dr. Liam McDonnell for his good will and support, and Prof. James Camparo for the invaluable tips on how to give a talk. Finally, I thank Dr. Hartmut Schweda, Prof. Pierre Thomann and Dr. Valentin Mitev for Friday (occasional) beer time discussions.

To my wife Bindhu Nisha
and
my parents

Contents

List of Figures

List of Tables

List of Publications and Presentations

Parts of this thesis are published in the following journal papers, conference proceedings/talks and technical project reports:

I. Refereed journal papers

1. T. Bandi, C. Affolderbach, and G. Mileti, *Laser-pumped wall-coated cell rubidium frequency standard*, Journal of Applied Physics, **111**, 124906 (2012).
2. C. Stefanucci, T. Bandi, F. Merli, M. Pellaton, C. Affolderbach, G. Mileti, and A. K. Skrivervik, *Compact microwave resonator for high-performance rubidium frequency standards*, Review of Scientific Instruments, **83**, 104706 (2012).
3. D. Miletic, T. Bandi, C. Affolderbach, and G. Mileti, *AC Stark-shift in double resonance and coherent population trapping in a wall-coated cell for compact Rb atomic clocks*, Physica Scripta, **T149**, 014012 (2012).
4. T. Bandi, C. Affolderbach, C. E. Calosso, and G. Mileti, *High-performance laser-pumped rubidium frequency standard for satellite navigation*, Electronics Letters, **47** (12), pp. 698-699 (2011).

II. Papers in conference proceedings

5. T. Bandi, C. Affolderbach, C. Stefanucci, F. Merli, A. K. Skrivervik, and G. Mileti, *Medium- to long-term frequency stability of high-performance cw double-resonance Rb standard*, submitted to: 2013 Joint UFFC, EFTF and PFM symposium, 21-25 July 2013, Prague, Czech Republic.
6. T. Bandi, M. Pellaton, D. Miletic, C. Affolderbach, F. Gruet, R. Matthey, C. Stefanucci, M. Violetti, F. Merli, J.-F. Zürcher, A. K. Skrivervik, and G. Mileti, *Double-resonance in alkali vapor cells for high performance and miniature atomic clocks*, In: Proceedings of the 2012 IEEE International Frequency

Control Symposium, Baltimore, MD, USA (2012), pp. 686-691. **Invited oral presentation by:** G. Mileti.

7. T. Bandi, C. Affolderbach, C. Calosso, C. Stefanucci, F. Merli, A. K. Skrivervik, and G. Mileti, *Laser-pumped high-performance compact gas-cell Rb standard with* $< 3\times 10^{-13}\ \tau^{-1/2}$ *stability*, In: Proceedings of the 26^{th} European Frequency and Time Forum (EFTF), Gothenburg, Sweden (2012), pp. 494-496. **Oral presentation by:** C. Affolderbach.

8. T. Bandi, F. Gruet, C. Affolderbach, G. Mileti, and C. E. Calosso, *Investigations on improved Rb cell standards*, In: Proceedings of the Joint Meeting of the European Frequency and Time Forum (EFTF) and the IEEE International Frequency Control Symposium (FCS), San Francisco (2011), pp. 236-238. **Poster presentation by:** G. Mileti.

9. C. Affolderbach, T. Bandi, R. Matthey, F. Gruet, M. Pellaton, and G. Mileti *Compact, high- stability Rb atomic clocks for space*, In: Proceedings of the 3rd International Colloquium -Scientific and Fundamental Aspects of the Galileo Programme, Copenhagen, Denmark, **2**, (1400), ESA special publication (2011), WPP-326. **Oral presentation by:** C. Affolderbach.

10. D. Miletic, T. Bandi, C. Affolderbach, and G. Mileti, *Light shift of double resonance and coherent population trapping in wall-coated cells for compact Rb clocks*, In: Proceedings of the Joint Meeting of the European Frequency and Time Forum (EFTF) and the IEEE International Frequency Control Symposium (FCS), San Francisco (2011), pp. 203-205. **Poster presentation by:** D. Miletic.

11. T. Bandi, C. Affolderbach, C. Calosso, and G. Mileti, *Studies on an improved compact physics package for Rb cell standards*, In: Proceedings of the 42nd annual Precise Time and Time Interval (PTTI) systems and applications meeting, Reston, Virginia (2010), pp. 329-342. **Oral and poster presentations by:** T. Bandi.

12. S. Micalizio, A. Godone, F. Levi, M. Pellaton, T. Bandi, C. Affolderbach, C. E. Calosso, F. Gruet, and G. Mileti, *Pulsed Optically Pumped Rb clock with optical detection: first results*, In: Proceedings of the 24th European Frequency and Time Forum, Noordwijk, the Netherlands (2010). **Poster presentation by:** S. Micalizio.

13. T. Bandi, C. Affolderbach, and G. Mileti, *Study of Rb 0-0 hyperfine double resonance transition in a wall-coated cell*, In: proceedings of the European Time and Frequency Forum (EFTF), ESA-ESTEC, Noordwijk, the Netherlands (2010), pp. 117-124. **Poster presentation by:** T. Bandi.

14. C. Affolderbach, R. Matthey, F. Gruet, T. Bandi and G. Mileti, *Realisation of a compact laser-pumped Rubidium frequency standard with < 1E-12 stability at 1 second*, In: Proceedings of the 24th European Frequency and Time Forum, Noordwijk, the Netherlands (2010). **Oral presentation by:** C. Affolderbach.

III. Technical project reports

15. T. Bandi, F. Gruet, and G. Mileti, *Study of the short- and long-term stabilities of the LTF Subsidiary Unit*, Tech. ESA. rep. LTF-01486-REP- 001, Laboratoire Temps-Fréquence, April 2011.

16. T. Bandi, D. Miletic, F. Gruet, M. Pellaton, C. Affolderbach, P. Scherler, M. Durrenberger, and G. Mileti, *Final report: Next Generation Compact Aomic clocks*, Tech. ESA. rep. LTF-01603-FR-0001, Laboratoire Temps-Fréquence, September 2011.

17. T. Bandi, P. Scherler, C. Affolderbach, and G. Mileti, *Auxiliary unit physiscs package subsystems design and breadboarding*, Tech. ESA. rep. LTF-01427-TN-0003A1, Laboratoire Temps-Fréquence, September 2010.

18. T. Bandi, P. Scherler, C. Affolderbach, M. Pellaton, and G. Mileti, *Subisiary unit physics package subsystems design and breadboarding*, Tech. ESA. rep. LTF-01427- TN-0003A2, Laboratoire Temps-Fréquence, September 2010.

19. G. Mileti, F. Gruet, C. Affolderbach, P. Scherler, and T. Bandi, *WP2200 - LTF contributions to the preliminary design*, Tech. ESA. rep. LTF-01427-TN-0002, Laboratoire Temps-Fréquence, June 2009.

20. T. Bandi, F. Gruet, P. Scherler, C. Affolderbach, E. Breschi, and G. Mileti, *WP1200 - LTF support to review and clock definition*, Tech. ESA. rep. LTF-01427-TN-0001, Laboratoire Temps-Fréquence, December 2008.

21. T. Bandi, *Microwave Cavities: INRIM cavity tuning for ESA-POP project*, Internal report, TNB-LTF-03, INRIM, July 2009.

Glossary of Acronyms

AM	Amplitude Modulation
AOM	Acousto Optical Modulator
BG	Buffer Gases
CPT	Coherent Population Trapping
CW	Continuous Wave
DFB	Distributed Feed-Back diode laser
DR	Double Resonance
EM	Electromagnetic
EP	Electronics Package
EPFL	École Polytechnique Fédérale de Lausanne
ESA	European Space Agency
ESTEC	European Space Research and Technology Centre
FM	Frequency Modulation
INRIM	Istituto Nazionale di Ricerca Metrologica (Torino), formerly called IEN until end 2005
LEMA	Laboratory of Electromagnetics and Acoustics
LO	Local Oscillator
LTF-UniNE	Laboratoire Temps-Fréquence - Université de Neuchâtel
ON	Observatoire de Neuchâtel
PM	Phase Modulation
POP	Pulsed Optical Pumping
PP	Physics Package
Rb	Rubidium
RCE	Resonator Control Electronics
RIN	Relative Intensity Noise
S/N	Signal to Noise
SNSF	Swiss National Science Foundation
SpT	Spectratime SA (formerly Temex Neuchâtel Time)
TC	Temperature Coefficient
FWHM	Full-Width Half Maximum
H-Q	High-Q

Introduction

> *Time = Life, Therefore, waste your time and waste your life, or master your time and master your life.*
> *-Alan Lakein*

Mastering the time means to be able to measure and maintain it efficiently. Precise measurement of time and frequency synchronization is useful for mankind in everyday life [1, 2]. For instance, in maintaining the Coordinated Universal Time (UTC) that is based on International Atomic Time (TAI) [3], accurate positioning and navigation systems [4–7] (Global Positioning System (GPS), Galileo, Glonass etc.), high-speed data transfer and synchronization in telecommunications [6]. They are also used in synchronizing time for banking and stock transactions, military applications, regulation of power grids to avoid power losses [8], in radio and television broadcasting, geophysics, metrology and other scientific endeavors such as deep space navigation and studies (e.g. Cassini Huygens) [5, 9]. Other scientific applications are the search for variation in fine-structure constant [10], test of Einstein's special theory of relativity [11], and including one of the recent experiment on the precise measurement of the speed of neutrinos [12].

The development of atomic clocks started six decades ago. The idea to build a clock using an atomic beam magnetic resonance was proposed by Isidor Rabi in 1945 [13]. Based on Rabi's technique [14], NIST (formerly known as National Bureau of Standards (NBS)) built the first atomic clock using ammonia molecules in 1949. Following to that, Essen and Parry at National Physical Laboratory (NPL) built the first thermal cesium beam clock in 1955 [15]. These developments vindicated the International System of Units (SI) in 1967 to define the SI second as 9,192,631,770 periods of vibration of the ground state hyperfine transition in an unperturbed cesium-133 atom [16], and later in 1997 it was affirmed that this definition refers to a cesium atom at rest at a temperature of 0 K.

Various types of clocks were developed since then including, the cesium thermal beam clocks [17, 18], active and passive hydrogen masers [7, 19, 20], lamp-pumped rubidium cell standards [4,21,22], cesium cold atomic fountain clocks [18], optical-lattice clocks [23], ion-trap clocks [24–27] and chip-based cold atom clocks [28–30]. However, for the applications that demand to address the issues of performance, portability, reliability, cost, weight and power consumption, the rubidium cell standards are advantageous over other kinds of clocks [31]. Presently, the industrial lamp-pumped Rb clocks are used in telecom and navigation systems. However, the constant demand for improved next generation applications requires pushing the limits on the performances of the portable clocks. With this motivation, we focus our work on improving the rubidium standards towards high-performances by adopting the laser-pumping techniques in view of next generation space and telecommunication applications.

The basics of Double-Resonance (DR) spectroscopy and clock are explained in [4, 22, 32, 33]. As the name indicates, the DR scheme has two resonances; one in the optical domain and the other in the microwave domain. The first order magnetic insensitive transition exists in the groundstate hyperfine manifold matching with the microwave wavelength, known as the clock transition that is generally used for the clock operation. At the heart of a conventional rubidium atomic frequency standard, atomic rubidium in vapor phase and buffer gases are contained in a glass enclosure, called *vapor cells*. Buffer gases help to prevent the polarized Rb atoms from colliding on to the cell walls and reduce the mean free path of a Rb atom to less than the microwave photon's wavelength of few centimeters, thereby giving rise to narrow resonance lines, this is known as Dicke narrowing [34]. Alternative to using buffer-gases in order to preserve the polarization by avoiding collisions of atoms with the glass walls, an evacuated glass cell whose inner walls are coated with an anti-relaxation material and filled with Rb vapor could be adopted as a new heart [35–37] for the clocks. The first studies on collisions between alkali atoms and coatings, such as paraffins $(CH_2)_n$ or silanes (e.g., dimethyldichlorosilane) were done by Bouchiat and Brossel during the 1960s [38] by adopting the Franzen's method of relaxation in the dark [39]. They found that in a 6 cm diameter spherical cell, it takes about 10^4 atom-wall collisions before an atom loses its state of polarization. Recent work of Balabas and colleagues shows that it is possible for the atomic polarization lifetimes to exceed one minute, with atoms undergoing up to 10^6 collisions with an alkene-based coating [40]. Although the idea to use wall-coated cells in an atomic frequency standard was suggested by Robinson [35] in the late 1950's, it was not realized due to the limitations in operating temperatures of such cells (incompatible with the use of lamps for optical pumping) and other technological difficulties, such as control of the coating quality. Part of these drawbacks is overcome with laser optical pumping, however a reliable commercial product is yet to be realized. Recently, the interest in wall-coated cells for high-precision spectroscopy and metrology is growing again, because coated cells represent good candidates to realize high-performance or micro-fabricated devices, such as miniaturized atomic clocks and/or atomic magnetometers [41, 42]. Basic studies on the application of wall-coated cells for Rb frequency standards are reported in [43–47].

The short-term frequency stability of a clock (in terms of Allan deviation) is inversely proportional to the atomic Q-factor and signal-to-noise (S/N) ratio [31]. This implies that a narrow linewidth of the atomic signal increases the Q-factor and hence improves the short-term clock stability. The conventional rubidium frequency standards use lamps for optical pumping [48, 49] and give a short-term stability around $4\times10^{-12}\ \tau^{-1/2}$. By employing lasers for optical-pumping, we expect to improve the short-term by more than one order of magnitude [22, 50]. The medium- to long-term clock stability is influenced by AC Stark shift, microwave power shift, temperature associated shifts and other related physical effects, and hence metrological quantitative measurements on these parameters are also of relevance to be studied in detail. We note a recent work by S. Micalizio and colleagues showing a state-of-the-art performance of a *pulsed* Rb standard exhibiting the stability as low as $1.7\times10^{-13}\ \tau^{-1/2}$ [51]. This clock was operated using Pulsed Optical Pumping (POP) principle with the physics package[1] containing a cylindrical cavity inside a *vacuum* enclosure.

We adopt the continuous-wave (CW) laser-pumped DR approach in our clock scheme. Our clocks are operated in ambient laboratory environment. Two different technologies towards a compact next generation rubidium cell standard are studied in this thesis: (i) use of wall-coating technology, and (ii) studies with a bigger cell (than that is used in the conventional Rb standards), using an improved and enlarged cavity towards a high-performance atomic standard. In the first approach, we characterize the wall-coated evacuated vapor cell filled with ^{87}Rb and implement it in a clock demonstrator. The detailed studies on the clock's short-term and medium- to long-term performances were done. The second, and novel approach involves the development of a new magnetron-type cavity resonator that has a compact volume, can hold a vapor cell larger than in existing rubidium standards and resonates around the ^{87}Rb ground state hyperfine frequency (ν_{Rb}). The well-defined field geometry in a given volume, competitive Q-factor, and power efficiency of these resonators make them ideal components for portable clock applications.

---

[1] The clock cell was fabricated in LTF.

The contents of this thesis are arranged in chapters as follows:

Chapter 1
This chapter gives the general basics required to understand a DR based rubidium standard. At first, a general clock principle is given. This is followed by the DR principle, and the ^{87}Rb "clock transition" explanation, along with theoretical description of the DR principle and the DR signal. The basics of determining the clock's frequency stability in terms of Overlapping Allan deviation is discussed and an overview on the underlying noise processes are given. Finally, the relevant perturbations on a Rb standard are disscussed in detail. A thorough experimental studies on these clock perturbations are done and explained in Chapters 5 and 6.

Chapter 2
The two main sources of electromagnetic radiation in DR clocks, one for *optical pumping* and second for *microwave interrogation* need to be abiding to certain stringent requirements in order to achieve the high-performance clock stabilities. Therefore, this chapter is dedicated on the details of these two sources, their requirements and measured characteristics.

Chapter 3
This chapter gives the details on the vapor cells and microwave resonator cavities used in this thesis work. The 14 mm diameter wall-coated cell, the enlarged 25 mm diameter buffer-gas cell, and their respective cavities are presented along with their simulated field modes and Zeeman measurements. Newly designed, fabricated, assembled and tuned cavity that can accommodate the 25 mm diameter cell is presented along with simulated field modes and Zeeman measurements. This cavity is emphasized towards the high-performance Rb clock. The results achieved using the first *prototype* of 25 mm cavity are published in 4, 11 (these numbers refer to *list of publications and presentations*, page xix). The design and performance results of the *optimized* cavity with an improved field mode are published in 2, 6, and 7.

Chapter 4
This chapter gives the details on experimental schematics, physics package(s) and breadboard(s) used to study the CW-DR spectroscopy and clock stabilites in this thesis.

Chapter 5

This chapter is dedicated to the studies on 14 mm diameter wall-coated cell. The characterization of wall coated cell was done by measuring the Rb ground-state T_1 and T_2 relaxation times. The systematic shifts, $\Delta\nu$ of the *clock transition* from the unperturbed hyperfine ground-state frequency, ν_{Rb}, due to intensity and frequency light shifts [52, 53], microwave power shift [54], temperature shifts [55] and spin-exchange shifts [56] are analyzed and discussed in detail. The influence of these parameters on the clock frequency instability is also evaluated. The results of this chapter are published in 1 and 13.

Chapter 6

We show that our CW-DR high-performance laser-pumped Rb standard using the 25 mm diameter BG cell outperforms laser pumped cesium (LPCs) standards [17], and is comparable to cold-atom portable clocks [57] and the space passive hydrogen maser (SPHM) [20], but from a compact physics package (PP) with volume of <1 dm^3 only. Similar to the spectroscopic analyses done on the wall-coated clock (see Chapter 5, Section 5.4), the perturbation measurements on the clock transition frequency affecting medium- to long-term time scales are measured and analyzed. With this clock, we achieve a state-of-the-art short-term stability adopting the CW DR principle. Parts of the work in this chapter are published in both peer reviewed articles (2, 4) and journal proceedings (5, 6, 7, 11).

Finally, the conclusions and future prospects are drawn based on the work presented in the thesis, towards the future high-performance clocks and their applications. The comparison of the high-performance clock presented in this thesis is made with presently existing portable clocks around the world.

Chapter 1 Double-Resonance Atomic Clock: Principle, Theory and Stability

Imagination is more important than knowledge.
-Albert Einstein

In general, the atomic frequency standards (atomic clocks) exploit a ground-state hyperfine transition to provide a stable atomic frequency reference to which the frequency of a quartz oscillator is stabilized [22, 32, 58]. A general interrogation and quartz stabilization scheme is shown in Fig. 1.1.

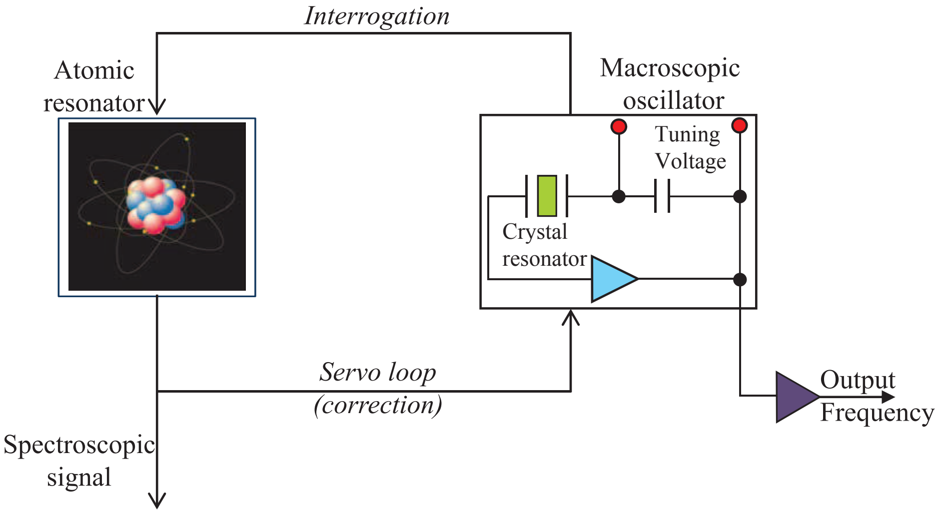

Figure 1.1: *General clock principle showing interrogation of atoms to give a spectroscopic signal and a servo correction feedback to stabilize the macro oscillator (quartz) to get the clock signal.*

This thesis is about vapor cell clocks [4]. Vapor cell clocks have multiple advantages. They are simple in operation, compact in size, no vacuum system required, many atoms contribute to the signal to give a good clock stability, they are portable and reliable (tested in deep space applications, eg. Cassini Huygens). Our studies are done with atomic ^{87}Rb confined in glass-blown cells (see Chapter 3 for details).

This chapter explains the DR principle - explaining the *interrogation* with *atomic resonator* (cf. Fig. 1.1), basic theoretical description and achievable frequency stabilities along with the perturbations involved in a typical DR clock. Later on, in Chapters 5 & 6 these aspects will be used to study, characterize and optimize the clock frequency stability performance.

1.1 Double-Resonance (DR) principle

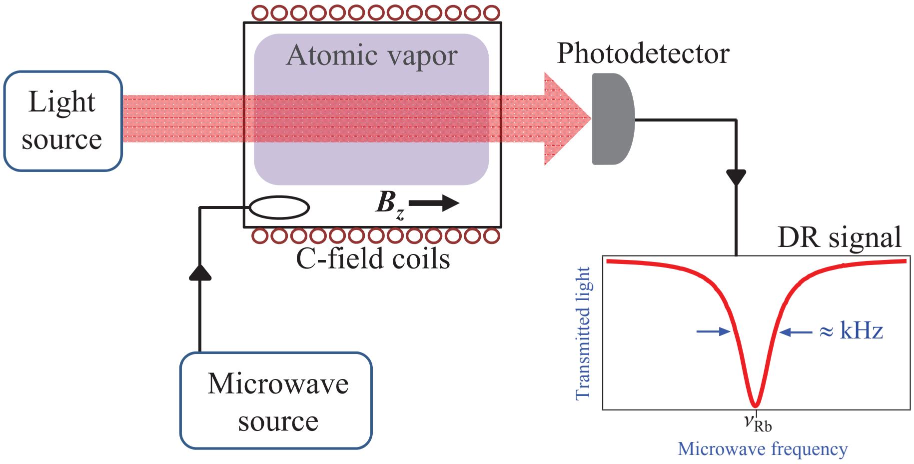

Figure 1.2: *Double-Resonance spectrocopic principle showing the interrogation of atoms confined in a vapor cell by optical and microwave fields to give a transmitted resonance curve.*

The studies in this thesis are based on the contiuous-wave (CW) laser-microwave double-resonance (DR) principle, explained as follows: Consider a three level system (cf. levels $|1\rangle$, $|2\rangle$, $|3\rangle$ in Fig. 1.3) at thermal equilibrium; both its ground states are equally populated. A laser-optical resonant field pumps the atoms to one of the atomic ground states via excited state by depleting the other ground state, thus creating a ground-state polarization. Simultaneously, a second resonant field interrogates at microwave frequency to drive the ground-state hyperfine *clock transition*: $5\,^2S_{1/2}|F_g = 1, m_F = 0\rangle \longleftrightarrow |F_g = 2, m_F = 0\rangle$ in the case of ^{87}Rb. The frequency of this transition is $\nu_{Rb} = 6834682610.90429(9)$ Hz [59]. The opacity of the vapor to the transmitted light signal as a function of microwave frequency is a measure of the atomic ground-state polarization known as *DR signal* (see Fig. 1.2). This signal typically has a Lorentzian shape as shown in Fig. 1.2, and the stabilization of the quartz oscillator to the centre of this reference signal, ν_{Rb}, realizes the clock [4, 22]. We adopt the

CW-DR interrogation scheme, as it is a simple method of operating the Rb standard. Whereas, the other techniques such as Pulsed Optical Pumping (POP) [60] require additional optical systems such as the Acousto Optical Modulator (AOM) for the clock operation increasing the operational complexity and volume of the clock. On the other hand, for POP operation, more stringent requirements on the microwave Local Oscillator (LO) phase noise is essential to avoid the Dick effect [61]. However, good improvements in the LO phase noise has helped the realization of excellent stabilities of the POP clocks [51].

1.1.1 Clock transition and perturbations

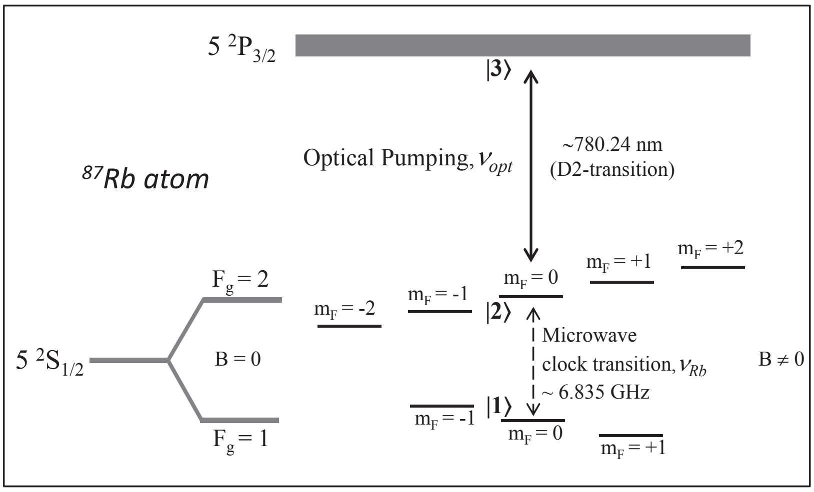

Figure 1.3: *DR principle for ^{87}Rb atom with energy level scheme showing the optical pumping and the clock-transition. The detailed energy level diagram and the properties of ^{87}Rb are given in Appendix A. The excited-state $5\ ^2P_{3/2}$ has the hyperfine structure that could be resolved, which is not shown here.*

Figure 1.3 shows the energy-level diagram of ^{87}Rb atom. The laser sources used in these studies emit around 780 nm (Rb D2-transition: $5\ ^2S_{1/2} \longleftrightarrow 5\ ^2P_{3/2}$). In the presence of a static, directional magnetic field, B_z (shown in Fig. 1.2), the ground-state degeneracy of ^{87}Rb atomic energy levels is lifted into their corresponding Zeeman-sublevels [62]. In presence of magnetic fields, the Zeeman energy level shift is explained by the Breit-Rabi formula [32] as,

$$\Delta\nu = -\frac{\nu_{hfs}}{2(2I+1)} - \frac{g_I m_F \mu_B}{h} B \pm \frac{\nu_{hfs}}{2}\sqrt{1 + \frac{4m_F}{2I+1}X + X^2}, \tag{1.1}$$

where, g_I is the Landé g-factor for the nucleus, ν_{hfs} is the hyperfine frequency difference, $X = (g_I + g_J)\mu_B B/h.\nu_{hfs}$, g_J the Landé g-factor for the valence electron with total angular momentum of **J**, and I=3/2 is the nuclear spin for Rb-87.

The first order dependence of Zeeman levels can be estimated by differentiating the above formula (Eqn. 1.1) with respect to the external magnetic field B as, $\partial\Delta\nu/\partial B$, shown in Fig. 1.4. The magnetic-dipole allowed transitions ($\Delta m_F = 0, \pm1$, see Fig. 1.4 for further details) are marked with circles.

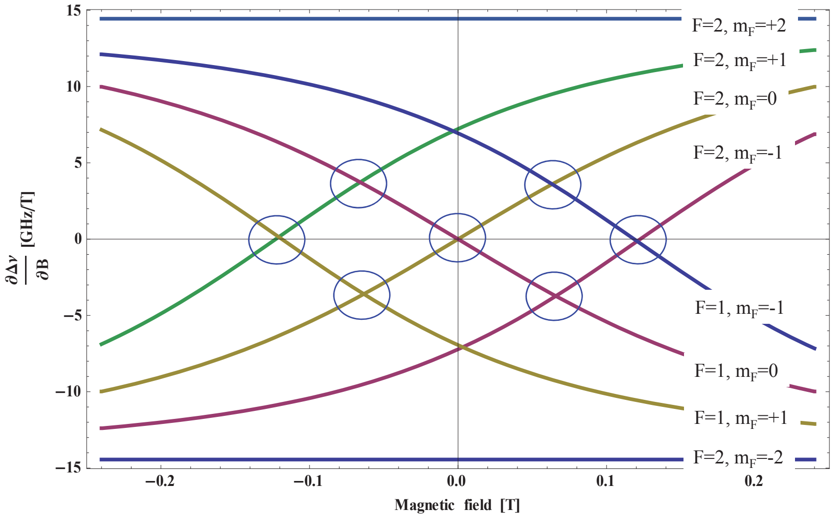

Figure 1.4: *The transition dependence on external magnetic field is shown for* ^{87}*Rb ground-state magnetic dipole-transitions. Magnetic dipole-allowed transitions that occur when* $\partial\nu_{hfs}(B)/\partial B$ *are equal but with opposite sign for both states of transitions are marked with circles.*

The magnetic dipole matrix elements values of the allowed Zeeman transitions between the two ground states are shown in Fig. 1.5. The relative strength of the interaction between ^{87}Rb and resonant microwave radiation is characterized by these magnetic dipole matrix elements. Similar to the optical dipole matrix element that couples the ground state to the excited state in an atom, the magetic dipole matrix element couples the two ground state hyperfine transitions via the spin operator S and can be computed as $\langle F, m_F|S|F', m_F'\rangle$ [32]. We are interested in the unperturbed transition for the first-order magnetic field variation, which is evident at the centre, known as the *clock transition.* Though the first order magnetic fields do not influence the clock transition, the second-order magnetic variations can however cause perturbations (see Section 1.5.1). It is important to minimize the effect of these magnetic variations on the clock transition, therefore magnetic shields are used. From Fig. 1.4, it is interesting to see that two other transitions: $5\ ^2S_{1/2}|F_g = 1, m_F = 1\rangle \longleftrightarrow |F_g = 2, m_F = 1\rangle$ and $5\ ^2S_{1/2}|F_g = 1, m_F = -1\rangle \longleftrightarrow |F_g = 2, m_F = -1\rangle$ are affected negligibly by the first order magnetic variations only in very high field B. Hence, in principle one can deduce that these transitions could also be used for the clock operation, but the magnetic field required for this is too high compared to the practical usage in typical Rb standards of few milli Gauss.

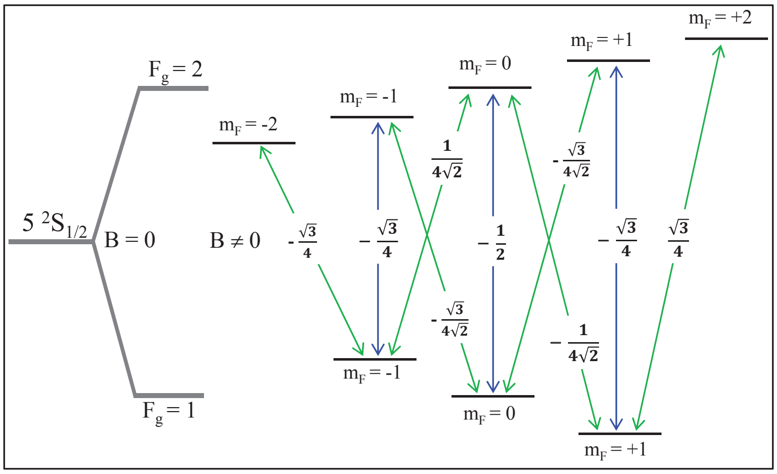

Figure 1.5: *Magnetic dipole matrix elements values computed for the ground state transitions of* ^{87}*Rb atom.*

The short-term stability of a clock (in terms of Allan deviation) is inversely proportional to the atomic quality factor (or line-Q) and to the signal-to-noise (S/N) ratio [22, 32]. The atomic quality factor is defined as,

$$Q_a = \frac{\nu_{Rb}}{\Delta\nu_{1/2}} \tag{1.2}$$

where $\Delta\nu_{1/2}$ is the full-width half-maximum of the DR signal with a line centre at ν_{Rb}. A narrow ^{87}Rb DR-signal with a line-width less than 1 kHz has the atomic Q-factor as large as 10^7. Therefore the parameter of the line-Q: the full-width half-maximum ($\Delta\nu_{1/2}$) is important to be controlled for a narrower signal that gives a better atomic Q-factor and hence a better clock short-term stability.

The sources of perturbations effecting ν_{Rb} and $\Delta\nu_{1/2}$ are important to be studied and understood in view of better clock performances. The fluctuations and noises of EM-fields (laser and microwave), temperature variations on the atoms, magnetic field fluctuations etc., cause the perturbations on the centre frequency, ν_{Rb} of the DR signal.

These perturbations are termed as systematic frequency shifts, $\Delta\nu$. These shifts include the constant buffer-gas shift [63], time dependent intensity and frequency light shifts [21, 64], microwave power shift [54, 65], temperature shifts [55], and cavity pulling shift [32]. However, the shift induced due to collisions of buffer gases with Rb atoms gives a static shift on ν_{Rb} known as *pressure shift* that is dependent on temperature (see Section 1.5.3). This net pressure shift is the main reason why vapor-cell clocks are secondary standards, which require calibration to correct for the initial inaccuracy and these collisions also result in frequency drifts in long-term [66]. A thorough understanding of the above shifts can help in controlling and minimizing the perturbing effects on the clock frequency instabilities.

1.2 DR Theory

The theory presented here is based on Vanier and Mandache's approach for laser pumped passive DR Rb frequency standards [22]. Here we present an overview of required theoretical basis and a more detailed analysis can be found in [22, 32, 50]. We follow a simplified three-level model for DR analysis, however in reality the laser interrogation (depending on laser line-width) happens with the excited state where more than one level is involved and with all the eight Zeeman levels in the ground state. The details on extending from three-level to multi-level treatement can be found in [56] and [50].

A. Buffer gas cell case

In our DR theoretical treatment we mainly consider the condition in which the vapor cells are filled with ^{87}Rb atoms and buffer gases. We however contrast these assumptions with wall-coated and the evacuated cell cases in the sections below.
The three-level model explained here has following assumptions:

1. Atomic ^{87}Rb and buffer gases are confined in a glass cell that is placed inside a microwave cavity. ^{87}Rb has two ground states for the clock transition and one excited state for optical pumping. In reality for D2-transition of ^{87}Rb atom, there are four excited state hyperfine levels (see [50]), but for simplicity we consider only one excited level in our treatment here.

2. The continuous wave scheme includes simultaneously operated optical pumping

laser field for creating a ground state population inversion and a microwave field for interrogating the clock transition.

3. The excited levels are overlapped due to buffer gas collisional broadening and Doppler broadening. Buffer gas-Rb atom collisions cause a homogeneous broadening of $P_{3/2}$ hyperfine levels ($\sim$ 18 MHz/torr) [67]. Due to this, the excited states overlap and the 3-level approximation considering only one excited state is justified. The Doppler broadening is 530 MHz (at the temperature of clock operation of 60 °C) and by considering the buffer gas pressure of 20 torr, the buffer gas broadening is 360 MHz and hence giving a total optical linewidth (in lab. frame) of 890 MHz. The excited state spontaneous emission (decay rate, due to BG collisions), Γ^* is of the order 2 - 5×10^9 s^{-1} (at the pressures considered in the present analysis), and is considered to be equally probable to all Zeeman sub-levels in one hyperfine ground state level.

4. The laser with linear polarization is tuned to ^{87}Rb D2-transition ($5\ ^2S_{1/2} \longrightarrow 5\ ^2P_{3/2}$). The laser beam intensity is uniform along its radius and the propogation direction of laser beam is considered in z-direction, i.e. along the cylindrical cell's symmetry axis and in the direction of the applied static magnetic field. The laser line-width ($\sim$ 5 MHz) is much less than the ground state hyperfine splitting.

5. Relaxations due to buffer gas collisions, spin exchange collisions and cell-walls collisions in both, ground and excited states are considered in a phenomenological way. Fractional population in the excited state is always small as compared to the decay rate, considering low light intensities.

B. Wall-coated cell case

To our knowledge the DR theoretical treatment with wall-coated cell does not exist. Here we consider the present DR theory to be closely matching to the wall-coated cell case with following modifications in the above assumptions. Only the differences with the above assumptions are contrasted here, and rest of them hold good for the wall-coated case also. In the assumption 1, instead of buffer gases in a glass cell, we consider the inner walls of the cell coated with an anti-relaxation material. Contrary to the case of buffer gas in assumption 3, the excited $P_{3/2}$ hyperfine levels of ^{87}Rb atom are not overlapped in a wall-coated cell ($\Gamma^* = 38\times10^6$ s^{-1}). In contrast to assumption 5, the relaxations and frequency shifts considered are due to wall-collisions and spin-exchange collisions. They are still considered in a phenomenological way and are treated in Chapter 5.

C. Evacuated cell case

A polarized atom in an evacuated (without buffer gases or wall-coating) vapor cell can depolarize by only one collision on the wall and hence the achievable DR-linewidth is several tens of kHz for a cm-scale cell, which corresponds to a clock short-term stability of approximately 1×10^{-9} at 1s. This assumes that the DR signal is not further degraded due to time-of-flight (TOF) effect (broadening due to the limited interaction time of an atom in the laser beam path). In contrast, a cell whose inner walls are coated with a high-quality anti-relaxation material preserves the polarized state of an alkali atom for more than a few hundred to few thousand collisions, depending on the size of the cell. The long-lived atomic polarization in turn increases the Q-factor of the atomic resonance line and thereby contributes to improve the short-term stability of the clock.

1.2.1 Three level model DR scheme

Figure 1.6 shows the three-level interrogation DR scheme, with $|g_1\rangle = |F=1, m_F=0\rangle$ and $|g_2\rangle = |F=2, m_F=0\rangle$ being the two clock transition ground states driven by microwave angular frequency of ω_μ and $|e\rangle$ is the excited state to which the laser of frequency ω_L is tuned for optical pumping. The *longitudinal* relaxation rate γ_1 and *transverse* relaxation rate γ_2 are responsible for *population* and *coherence* between two ground-states, respectively and are written as,

$$\gamma_1 = \gamma_{1BG} + \gamma_{1W} + \gamma_{1SE}, \tag{1.3a}$$

$$\gamma_2 = \gamma_{2BG} + \gamma_{2W} + \gamma_{2SE}, \tag{1.3b}$$

where, γ_{BG} is due to collisions with the buffer gas and γ_W is the diffusion to the cell walls and γ_{SE} is the spin-exchange relaxation rate, corresponding to both γ_1 and γ_2 alike. Further details on relaxation rates can be found in [32,50]. The *atom-radiation fields* system is analysed in density matrix formalism [68]. The time evolution of the atomic density matrix elements representing the population of energy levels and the coherences, under the action of Hamiltonian $\mathbf{H}$ is described by the quantum Liouville equation [69]:

$$\frac{\partial\rho}{\partial t} = -\frac{i}{\hbar}[\mathbf{H}, \rho] \tag{1.4}$$

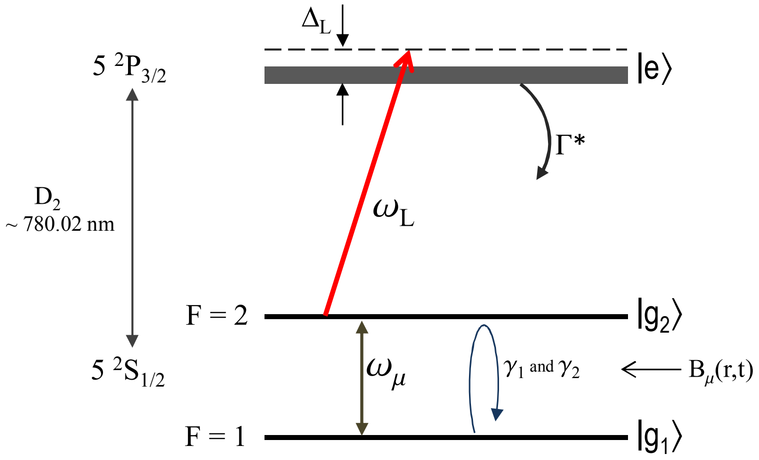

Figure 1.6: *A three-level model for DR interrogation in* ^{87}*Rb.* ω_L *is the laser angular frequency,* Δ_L *is the laser detuning with respect to the optical transition,* ω_μ *is the microwave angular frequency,* Γ^* *is the excited state decay rate and* γ_1 *and* γ_2 *are the population and coherence relaxation rates, respectively.*

The Hamiltonian $\mathbf{H}$ is the sum of several contributions in the interaction of atom with laser and microwave fields on the density matrices, ρ, and $\hbar$ is the Dirac's constant.

1.2.2 Atom-Laser interaction

The laser electric field $\mathbf{E}$ with an angular frequency ω_L and a definite polarization vector $\hat{\mathbf{e}}$ propagating in z-axis ($\mathbf{r} = (0, 0, z)$) with vector $\mathbf{k}$ can be written as,

$$\mathbf{E}(\omega_L, t, z) = E_0\ \hat{\mathbf{e}}\ cos(\omega_L t + \mathbf{k} \cdot \mathbf{r}), \tag{1.5}$$

where, E_0 is the amplitude of the laser radiation field. The interaction hamiltonian is written as $\mathbf{H_E} = \mathbf{d}.\mathbf{E}(\omega_\mathbf{L}, \mathbf{t}, \mathbf{z})$, where $\mathbf{d} = -e\mathbf{r}$ is the electric dipole operator. The optical Rabi angular frequency can then be written as,

$$\Omega_R = \frac{E_0}{\hbar}\langle e|e\mathbf{r} \cdot \hat{\mathbf{e}}|g_2\rangle = \frac{E_0}{\hbar} d_{eg_2}, \tag{1.6}$$

The terms within bra-c-ket are dipole matrix elements of D2 transition. Decay from the excited state is treated in a phenomenological method, i.e., at low light intensities the decay rate from P-state is always larger than the excited state fractional population. Then, the density matrices explaining atom-laser interactions: ρ_{ee} and ρ_{g_2e}, are written as [22]:

$$\frac{\partial \rho_{ee}}{\partial t} = -\Omega_R \ \mathrm{Im}\rho_{g_1 e} e^{-i\omega_L t} - \Omega_R \mathrm{Im}\rho_{g_2 e} e^{-i\omega_L t} - \Gamma^* \rho_{ee}, \tag{1.7a}$$

$$\frac{\partial \rho_{g_2 e}}{\partial t} = \mathrm{i}\omega_{g_2 e}\rho_{g_2 e} + i\frac{\Omega_R}{2}e^{i\omega_L t}(\rho_{ee} - \rho_{g_2 g_2}) + i\frac{b_R}{2}e^{i\omega_\mu t}\rho_{g_1 e} - i\frac{\Omega_R}{2}e^{i\omega_L t}\rho_{g_1 g_2} - \frac{\Gamma^*}{2}\rho_{g_2 e}, \tag{1.7b}$$

In the above equations, Γ^* is the excited state decay rate and b_R is the microwave Rabi frequency given by Eqn. 1.14. Note that the equation referring to laser coupling to $|g_1\rangle$ ground state ($\frac{\partial \rho_{g_1 e}}{\partial t}$) is omitted as we assume that our laser linewidth is much narrower than the ground-state hyperfine splitting.

From Fig. 1.2, we know that the measurable parameter is the intenstiy of the laser at the exit of the clock cell. This intensity on the detector causes a photocurrent and the voltage proportional to the load resistance is measured. The electric field $\mathbf{E}(\omega_L, t, z)$ is related to the electric polarization $\mathbf{P}$ by the relation [22],

$$\frac{\partial \mathbf{E}}{\partial z^2} - \epsilon_0 \mu_0 \frac{\partial^2 \mathbf{E}}{\partial t^2} = \mu_0 \frac{\partial^2 \mathbf{P}}{\partial t^2}. \tag{1.8}$$

where ϵ_0 is the vacuum dielectric constant and μ_0 is the permeability of free space. The above equation (cf. Eqn. 1.8) can be transformed in terms of optical Rabi frequency as [70],

$$\frac{\partial \Omega_R}{\partial z} = \alpha \ \mathrm{Im}\delta_{g_2 e}, \tag{1.9}$$

where $\delta_{g_2 e}$ is the complex amplitude of the optical coherence that is decomposed by excluding the fast oscillations from $\rho_{g_2 g_e}$ and the absorption coefficient α is given by,

$$\alpha = \left(\frac{\omega_L}{c\epsilon_0 \hbar} d^2_{eg_2} \right) n, \qquad [\mathrm{m}^{-1}\mathrm{s}^{-1}] \tag{1.10}$$

with c as the light speed in vacuum, ϵ_0 the permeability of free space and n the atomic number density.

Finally, the Laser pumping rate, Γ_p can be defined as,

$$\Gamma_p = \frac{|\Omega_R^2/2|^2 \ \Gamma^*}{(\Gamma^*/2)^2 + (\omega_L - \omega_\mu - \omega_{eg_2})^2}, \tag{1.11}$$

where $\omega_{eg_2} = \Delta_L$ in Fig. 1.6. When the laser is turned exactly to the transition $|g_2\rangle$ to $|e\rangle$, the above equation approximates to:

$$\Gamma_p = \frac{\Omega_R^2}{\Gamma^*}. \tag{1.12}$$

where Ω_R is function of z. A non-resonant coupling of the laser field with $|g_1\rangle$ state leads to off-resonant light-shift effect through virtual transitions (see Section 1.5.2).

1.2.3 Atom-Microwave interrogation

The microwave field is considered to be in resonance with the two ground states (see Fig. 1.6) and is given by,

$$B_\mu(r,t) = B_0\ cos(\omega_\mu t), \tag{1.13}$$

where B_0 is the microwave field amplitude and ω_μ is its angular frequency. Associated angular microwave Rabi frequency for the clock transition is written as,

$$b_R(r) = \frac{\mu_B}{\hbar} B_z(r), \tag{1.14}$$

where, μ_B is the Bohr magnerton. The matrix elements explaining these interactions are $\rho_{g_1g_1}$, $\rho_{g_2g_2}$ and $\rho_{g_1g_2}$, with the sum of populations of two ground states $\rho_{g_1g_1}+\rho_{g_2g_2} \approx 1$, and are written as:

$$\frac{\partial \rho_{g_2g_2}}{\partial t} = -b_R\ \mathrm{Im}\rho_{g_1g_2} e^{-i\omega_\mu t} + \Omega_R \mathrm{Im}\rho_{g_2e} e^{-i\omega_L t} + \frac{\Gamma^*}{2}\ \rho_{ee} - \gamma_1\ (\rho_{g_2g_2} - 1/2), \tag{1.15a}$$

$$\frac{\partial \rho_{g_1g_1}}{\partial t} = +b_R\ \mathrm{Im}\rho_{g_1g_2} e^{-i\omega_\mu t} + \Omega_R \mathrm{Im}\rho_{g_1e} e^{-i\omega_L t} + \frac{\Gamma^*}{2}\ \rho_{ee} - \gamma_1\ (\rho_{g_1g_1} - 1/2), \tag{1.15b}$$

$$\begin{aligned}\frac{\partial \rho_{g_1g_2}}{\partial t} = +\mathrm{i}\ \omega_{g_1g_2}\rho_{g_1g_2} + \frac{\mathrm{ib_R}}{2} e^{i\omega_\mu t}(\rho_{g_2g_2} - \rho_{g_1g_1}) + \mathrm{i}\frac{\Omega_R}{2} e^{i\omega_L t}\rho_{g_2e} \\ -\mathrm{i}\frac{\Omega_R}{2} e^{-i\omega_L t}\rho_{g_1e} - \gamma_2 \rho_{g_1g_2}.\end{aligned} \tag{1.15c}$$

In this model, it is also assumed that the optical Rabi frequency $\Omega_R \ll \Gamma^*$, the microwave Rabi frequency $b_R \ll \Gamma^*$ and the microwave detuning $\omega_{\mu'} \ll \Gamma^*$, where $\omega_{\mu'} = \omega_\mu - \omega_{g_1g_2}$. Typically, the values of Ω_R, b_R and Γ^* are of the order $10^6\ \mathrm{s}^{-1}$, $10^3\ \mathrm{s}^{-1}$ and $10^9\ \mathrm{s}^{-1}$, respectively. The values considered here are valid over a broad range of optical and microwave Rabi frequencies usually applied in DR clocks. Therefore, from above approximations one can eliminate the population in the excited state, and similar to the optical coherence (δ_{g_2e} in Eqn. 1.9) the ground state coherence $\delta_{g_1g_2}$ created by the microwave field can be written as,

$$\begin{aligned}\delta_{g_1g_2} = \mathrm{i}\ \frac{(b_R/2)\,(\gamma_2+\Gamma_p)}{(\gamma_2+\Gamma_p)^2 + (\omega_\mu + \Delta\omega_{LS} - \omega_{g_1g_2})^2}\Delta + \\ \frac{(b_R/2)(\omega_\mu + \Delta\omega_{LS} - \omega_{g_1g_2})}{(\gamma_2+\Gamma_p)^2 + (\omega_\mu + \Delta\omega_{LS} - \omega_{g_1g_2})^2}\Delta,\end{aligned} \tag{1.16a}$$

where, $\Delta\omega_{LS}$ is the light-shift given by Eqn. 1.43 (see Section 1.5.2) and Δ is the population difference between the two ground states given by,

$$\Delta = \frac{\Gamma_p}{(\gamma_2+\Gamma_p) + \frac{b_R^2(\gamma_2+\Gamma_p)}{(\gamma_2+\Gamma_p)^2+(\omega_R+\Delta\omega_{LS}-\omega_{g_1g_2})^2}}. \tag{1.17a}$$

On the other hand, the optical optical coherence δ_{g_2e} (cf. Eqn. 1.9) is given as,

$$\delta_{g_1e} = -i\frac{\Omega_R/2}{(\frac{\Gamma^*}{2} + i(\omega_L - \omega_{g_2e}))}\rho_{g_2g_2}. \tag{1.18a}$$

This means that the transition from $|e\rangle$ to $|g_2\rangle$ is mainly driven by the direct interaction of the laser and not by any feedback from the other transition $|g_1\rangle$ to $|e\rangle$.

The value of $\rho_{g_2g_2}$ is obtained from the set of equations, 1.7 and 1.15 within the frame of above approximations on Ω_R, b_R and Γ^*as explained in [22].

The saturation factor is defined as,

$$S = \frac{b_R^2}{\gamma_1^{'}\gamma_2^{'}}, \tag{1.19}$$

where, $\gamma_1^{'} = \gamma_1 + \Gamma_p/2$ and $\gamma_2^{'} = \gamma_2 + \Gamma_p/2$. Here optical pumping is considered as an added source of relaxation contributing for line broadening.

1.2.4 DR signal

The typical DR signal has approximately Lorentzian shape and hence by using the above saturation parameter it can be written as:

$$DR_L = -a_0\frac{S}{S+1}\frac{1}{[1 + x^2/(S+1)]}, \tag{1.20}$$

where a_0 is the maximum fractional signal amplitude at $x = 0$, and $x = \frac{\omega_{\mu}{'}}{\gamma_2^{'}}$. The full-width-half-maximum (FWHM) of the DR signal is given by,

$$\Delta\nu_{1/2} = \frac{1}{\pi}\gamma_2^{'}\sqrt{(S+1)}. \tag{1.21}$$

Hence, the FWHM ($\Delta\nu_{1/2}$) can be calculated at the exit of the cell by proper evaluation of the pumping rates and saturation factor. The important parameter in view of clock frequency stability is the Discriminator slope (D) that can be approximately written as,

$$D \approx \frac{A}{\Delta\nu_{1/2}}, \tag{1.22}$$

where, A is the amplitude of the DR signal. Similarly, another important parameter known as Figure-Of-Merit (FOM), which also considers the detected background noise (Bk) affecting the signal to noise (S/N) ratio can be defined as,

$$FOM = \frac{C}{\Delta\nu_{1/2}}, \tag{1.23}$$

where, C is the contrast of the DR signal given by $C = A/Bk$, with A as the DR signal amplitude and Bk the background level. Further more, the contrast of the DR signal depends on absorption coefficient α, microwave field intensity, laser light intensity (or pumping rate) and the length of the cell (L). Using Eqns. 1.9 & 1.16a by numerical evaluation, one can write the contrast C in terms of Rabi frequency as [22]:

$$C = \left| \frac{\Omega_R^2(z = L, \omega = \omega_\mu) - \Omega_R^2(z = L, \omega_{\mu'})}{\Omega_R^2(z = L, \omega_{\mu'})} \right| . \tag{1.24}$$

For instance, the microwave detuning, $\omega_{\mu'} = 2\pi \times 10000 \text{ s}^{-1}$ makes sure that the background is well outside the microwave resonance.

1.3 Buffer gas line broadening and relaxation mechanisms

By using buffer gases in the Rb cell it is possible to preserve the polarization-state of the atoms up to few milliseconds (by suppressing relaxation on the cell walls, the time-of-flight broadening and the Doppler broadening) to get a narrow ($\sim$ kHz) resonance line with an improved Q_a. However, the buffer gases also cause line broadening of the optical absorption [67]. Equations 1.3(a) & 1.3(b) give the possible relaxation mechanisms responsible for the change of *population* (γ_1) difference and *coherence* (γ_2) in the ground state clock transition. Below we outline these line-broadening mechanisms in some detail for the case of the 25 mm diameter cell used in this study.

1.3.1 Buffer gas collisional relaxations

Albeit the buffer gas prevents the atoms from colliding on to the glass walls of the vapor cell, the collisions between ^{87}Rb atoms and the buffer gases are unavoidable. The binary collisions of alkali atoms with buffer gases alter the electron density at the alkali nucleus and thereby a change in alkali's hyperfine coupling (i.e., $A\mathbf{I.S} \rightarrow (A + \delta A)\mathbf{I.S})$). This is known as Carver mechanism [71], and is explained in [72, 73]. These collisions are dependent on the collisional cross-sections between Rb atoms and buffer gases, the cell temperature in turn is responsible for the mean relative velocity between the Rb atoms and buffer gases, $\bar{v}_r$. P is the corresponding BG pressure inside the vapor cell. Thus, the buffer gas relaxations for population and coherence can be written as [56]:

$$\gamma_{1BG} = L_0\ \bar{v}_r\ \sigma_1 \frac{P}{P_0}, \tag{1.25a}$$

$$\gamma_{2BG} = L_0\ \bar{v}_r\ \sigma_2 \frac{P}{P_0}. \tag{1.25b}$$

where L_0 (= 2.686 7774(47)×10^{25} m^{-3} at 0 °C and 1 atm.) is Loschmidt's constant, σ_1 is the collisional cross-section responsible for population (i.e., $\rho_{g_1g_1}$-$\rho_{g_2g_2}$) relaxation, σ_2 is the collisional cross-section responsible for the coherence ($\rho_{g_1g_2}$) relaxation, $\bar{v}_r = \sqrt{8\mathrm{k_B} \cdot \mathrm{T}/\pi\mu}$ is the mean velocity of the colliding atoms and buffer gases at temperature T, with k_B the Boltzmann constant and μ the reduced mass of the colliding particles and P_0 is equal to 760 Torr. The collision cross-sections between Rb and respective buffer gas responsible for population and coherence relaxations are given in Table 1.1. The N_2 buffer gas also acts as a *quenching gas*; the excited rubidium atoms can transfer from one of the P states to the ground states without emitting or absorbing the radiation, since all the fluorescence is quenched by nitrogen gas [32].

Table 1.1: *Collisional cross-sections of Rb with Ar and N_2.*

Collision	σ_1 **[10^{-23} cm^2]**	σ_2 **[10^{-23} cm^2]**
Rb-Ar	37	37
Rb-N_2	8.3	350

For example, considering the temperature of 63 °C (336 K) (we get $\bar{v}_r$ = 286.4 m/s), and a typical buffer gas pressure (in our case) of 19.5 Torr and computing for the above equations (cf. 1.25(a) & 1.25(b)), we get γ_{1BG} = 8.94 s^{-1} and γ_{2BG} = 76.4 s^{-1}, respectively.

1.3.2 Cell-wall diffusion relaxations

The atoms diffuse through the buffer gases by the process of collisions and finally can reach the bare glass walls, where they lose the state of polarization, resulting in essentially zero population difference. The motion of atoms through buffer gases can be explained by diffusion equation. For a cylindrical cell (like the ones used in our clocks in this thesis), with radius a and length of the cell L, the diffusion equations responsible for the relaxations through binary (Rb-BG) collisions of *populations* and *coherence*, respectively, are given by [32]:

$$\gamma_{1W} = \left[\left(\frac{(2.405)^2}{a^2} + \frac{\pi^2}{L^2} \right) D_0 \frac{P_0}{P} \right], \tag{1.26a}$$

$$\gamma_{2W} = \left[\left(\frac{(2.405)^2}{a^2} + \frac{\pi^2}{L^2} \right) D_0 \frac{P_0}{P} \right]. \tag{1.26b}$$

The process of diffusion causes transitions among the atomic energy levels contributing for γ_1 and the phase shifts by affecting the coherence contributing for γ_2. However, note that the order of shift contribution for both the relaxations is same. Typical values of the diffusion constant D_0 for ^{87}Rb with the buffer gases Ar and N_2 are given in the Table 1.2. There are possibilities of molecule formation as explained in [32,72], which could also cause the relaxation.

Table 1.2: *Diffusion constants of Rb interacting with buffer gases. These values are calculated for a temperature of 63 ° C from [32] by considering D_0 is proportional to $T^{3/2}$ [74].*

Buffer gas	**Relaxation**	D_0 **[cm^2· s^{-1}]**
Ar	γ_{1W}	0.49
	γ_{2W}	0.53
N_2	γ_{1W}	0.45
	γ_{2W}	0.4

Now, by considering the typical cell dimensions in our case of radius $a = 1.15$ cm and length $L = 2.3$ cm and the diffusion constant values from Table 1.2 and computing for the Equations 1.26(a) & 1.26(b), we get $\gamma_{1W} = 228.5$ s^{-1} and $\gamma_{2W} = 226$ s^{-1}, respectively.

1.3.3 Spin exchange relaxations

The spin-exchange collisions between two atoms A and B in $S_{1/2}$ state with spin-up $|\uparrow\rangle$ ($|g_2\rangle$ = +1/2) and spin-down $|\downarrow\rangle$ ($|g_1\rangle$ = -1/2) can be represented as [75],

$$A|\uparrow\rangle + B|\downarrow\rangle \rightarrow A|\downarrow\rangle + B|\uparrow\rangle, \tag{1.27}$$

showing that after the collision the spin states of the two atoms are exchanged, but the total spin of a colliding pair of atoms is conserved. This effect is also a source of relaxation that causes broadening of the resonance line depending on the atomic density [32].

The spin exchange collision between two Rb atoms responsible for relaxation of populations is given as [56]:

$$\gamma_{1SE} = \bar{v}_s \, \sigma_{ex} \, n, \tag{1.28}$$

where σ_{ex} is the spin-exchange cross section responsible for broadening of the resonance signal and $\bar{v}_s = \sqrt{8\mathrm{k_B} \cdot \mathrm{T}/\pi\mu}$ is the mean velocity between the two colliding Rb atoms with reduced mass μ between them. Typically $\sigma_{ex} \approx 1.6\times10^{-14}$ cm^2 for ^{87}Rb [32, 76]. Whereas, the coherence spin-exchange relaxation rate γ_{2SE} is given as [56]:

$$\gamma_{2SE} = \frac{6I+1}{8I+4}\,\gamma_{1SE}. \tag{1.29}$$

where I is the nuclear spin, for ^{87}Rb it is 3/2. For a temperature of 63 °C, the rubidium density is 6.9×10^{11} cm^{-3} and $\bar{v}_s$ is calculated to be 2.86×10^4 cm·s^{-1}, substituting these values and σ_{ex}, we get $\gamma_{1SE} \approx 316$ s^{-1}, and $\gamma_{2SE} \approx 197.5$ s^{-1}.

Table 1.3 summarizes the population and coherence relaxations caused on ^{87}Rb atoms in a buffer gas vapor cell. The intrinsic linewidth of the DR signal is limited by the total relaxation, i.e. sum of the coherence relaxations of the above processes. The value of intrinsic linewidth is considered when there is no influence of light and microwave, i.e., at zero light intensity and zero microwave power. For our vapor cell with a buffer gas pressure of 26 mbar (19.5 Torr), operating at a temperature of 336 K, when there is complete absence of light and microwave, the saturation parameter (cf. Eqn. 1.19) becomes "zero", and hence the intrinsic linewidth using the Eqn. 1.21 is calculated to be ≈ 160 Hz.

Table 1.3: *Relaxation of population and coherence of the clock transition in ^{87}Rb calculated for 25 mm diameter BG cell.*

Parameter	**Symbol**	**Value [s^{-1}]**	**Symbol**	**Value [s^{-1}]**
BG collision relaxation	γ_{1BG}	8.94	γ_{2BG}	76.4
Cell-wall diffusion relaxation	γ_{1W}	228.5	γ_{2W}	226
Spin exchange relaxation	γ_{1SE}	316	γ_{2SE}	197.5
Total relaxation	γ_1	$\sim$ 553	γ_2	$\sim$ 500

1.4 Clock Frequency Stability

The frequency stability of a Rb standard can be divided into three regimes based on the averaging time scales: (i) the short-term stability, limited due to S/N ratio (typically 1-100 s in this thesis), (ii) the medium-term stability, limited due to random-walk or flicker noise (100-1000 s here) and (iii) the long-term stability, limited due to drift and ageing processes (1,000 s up to one day or more). However, in the studies done here, we consider the effects of (ii) and (iii) combined, and focus our attention on the clock behavior at 10,000 seconds, as this is at relevant time scales (6,000 s) that are essential in view of clock error prediction and synchronization [31, 77, 78].

In this section, at first, few basic concepts on accuracy, precision, stability, overlapping Allan deviation and noise processes are explained. This is followed by a discussion of short-term and medium- to long-term stabilities.

1.4.1 Accuracy, precision and stability

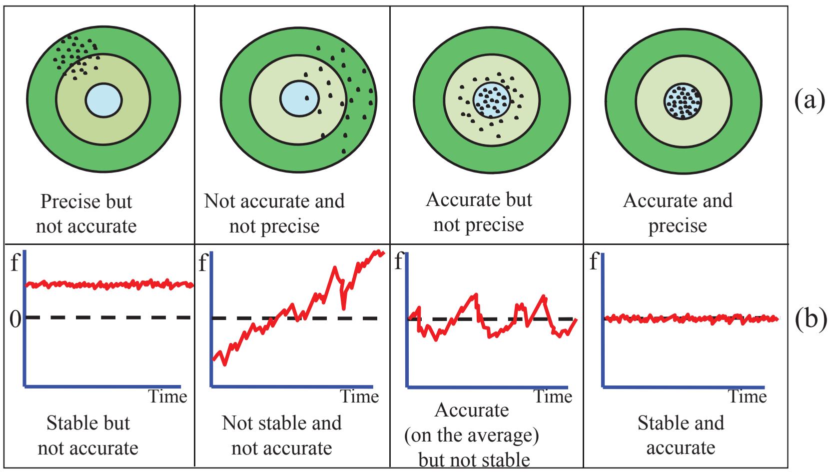

Figure 1.7: *(a) Conceptual illustration of the accuracy, precision and stability of an oscillator with a target analogy, (b) the corresponding frequency stability as a function of time. Courtesy: John R. Vig, A tutorial on quartz crystal resonators and oscillators, Frequency control and timing applications, November 2008.*

The instantaneous frequency of an oscillator at time t can be considered as:

$$f(t) = f_0[1 + \epsilon + y(t)], \tag{1.30}$$

where f_0 is the reference frequency or the unperturbed ground-state hyperfine frequency of an atom (e.g. ν_{Rb} in ^{87}Rb, shown in Fig. 1.3), ϵ is the systematic bias and $y(t)$ represent the statistical fluctuations. In an analytical measurement, it is the *accuracy* that gives a measure of how close is the measured value to the reference. In the Eqn. 1.30, if $\epsilon = 0$, then it is *accurate.* The *precision* is the reproducibility of multiple measurements and usually it is described by the standard deviation; if $y(t) = 0$, it is determined as 100% *stable* in terms of frequency. Figure 1.7 illustrates the accuracy, precision and stabilities of a target analogy. The centre circle of the target is considered as the reference point (or reference frequency) and the deviation of bullets from the centre is represented in terms of frequency as a function of time in the lower part of the illustration. Next sections explain the need and method of evaluation of $y(t)$, that is used to characterize a clock's performance in terms of Allan deviation.

1.4.2 Need for Allan deviation

The noises affecting an oscillator lead to its instabilities. In order to distinguish between the noises such as white frequency noise and flicker frequency noise, the conventional statistical tool such as standard deviation is not suitable as the output is divergent. Therfore, in order to characterize the variations of the oscillator over time due to different noise processes (see Fig.1.9), the two sample variance is used known as Allan variance [79]. The square root of Allan variance is known as Allan deviation. Below section gives the basics of Allan deviation and its variant known as overlapping Allan deviation. The overlapping Allan deviation takes more number of averages than the Allan deviation that helps to increase the confidence limits of the statistical analysis.

1.4.3 Overlapping Allan deviation and noise processes

An atomic standard's frequency or phase fluctuations are typically characterized in time domain, statistically in terms of Allan deviation [79–81]. A typical frequency output of an atomic standard is shown in Fig. 1.8. This frequency as a function of time can be divided into equal intervals of duration τ; such that, $\tau = t_{i+1} - t_i$, and $\overline{y_i}$ are the averages of $y(t)$ in each interval $[t_i; t_{i+1}]$.

In Fig. 1.8, $y(t)$ is the oscillator frequency normalized to the reference (cf. Eqn. 1.30). The mean frequency fluctuations $\overline{y_i}$ in the interval τ can be represented as,

$$\overline{y_i} = \frac{1}{\tau} \int_{t_i}^{t_{i+1}} y(t)dt, \tag{1.31}$$

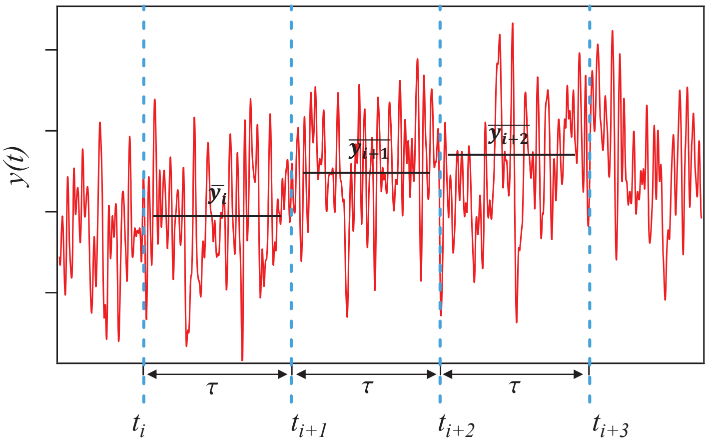

Figure 1.8: *Typical frequency fluctuations of an atomic standard or oscillator.*

And the Allan deviation for N number of intervals can be calculated as [79, 82]:

$$\sigma_y(\tau)_{Allan} = \sqrt{\frac{1}{2}\langle(\overline{y_{i+1}} - \overline{y_i})^2\rangle} = \sqrt{\frac{1}{2(N-1)}\sum_{i=1}^{N-1}(\overline{y_{i+1}} - \overline{y_i})^2}\,, \tag{1.32}$$

The confidence interval of an Allan deviation is estimated as $\pm\sigma_y(\tau)/\sqrt{(\mathrm{N}-1)}$, this is usually dependent on the noise type [83]. In order to improve the confidence of a stability estimation and to make the best use of the data set, the overlapping between the samples at each averaging time $\tau_0 < \tau$ is considered. Consider the overlapping samples at each averaging time τ, which is an integer multiple of τ_0. From a set of M frequency measurements, the averaging time $\tau = m\tau_0$, then the Overlapping Allan deviation can be expressed as,

$$\sigma_y(\tau) = \sqrt{\frac{1}{2m^2(N-2m+1)}\sum_{j=1}^{N-2m+1}\left\{\sum_{i=j}^{j+m-1}\left[\overline{y_{i+m}} - \overline{y_i}\right]\right\}^2}\,, \tag{1.33}$$

The confidence interval of an Overlapping Allan variance estimate is better than that of normal Allan variance as the additional overlapping intervals are taken in to consideration to improve the confidence estimation [83]. In performing the clock stability estimate for our clocks explained in this thesis, we use the overlapping Allan deviation because of better statistical estimate of the clock's performance.

It is also possible to calculate the stability in frequency domain in terms of power spectral density (PSD) by accounting for phase or frequency fluctuations as a function of Fourier frequency [79, 83]. The PSD of the random frequency fluctuations can be written in the form of power law spectral densities as,

$$S_y(f) = \sum_{\alpha} h(\alpha) f^{\alpha}, \tag{1.34}$$

where, $S_y(f)$ is one-sided PSD of y in Hz^{-1}, f the Fourier frequency in Hz, $h(\alpha)$ is the intensity coefficient and α the exponent of the power law noise process. The most commonly encountered behavior of $\sigma_y(\tau)$ for different noise process spectra in an atomic standard are shown in Fig. 1.9. The relation between α and μ (or $\mathrm{S}_y(\mathrm{f})$ and $\sigma_y(\tau)$) can be found in [84]. Note that in order to distinguish between the white PM noise and the Flicker PM noise, modified Allan deviation technique must be used [83].

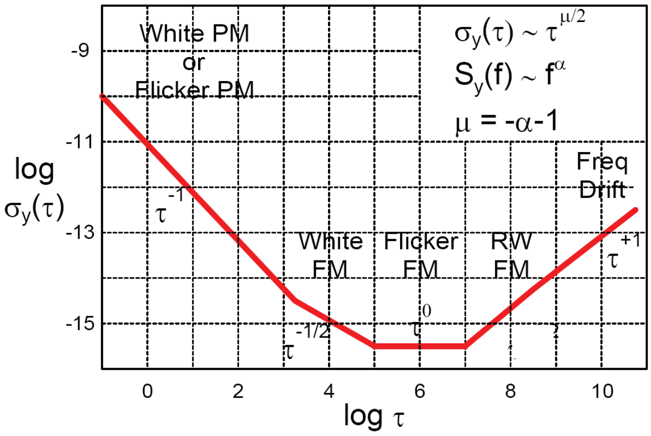

Figure 1.9: *The logσ versus logτ plot shows the power-law dependence of Allan Variance value and the type of noise associated with a particular slope, μ. FM: frequency noise, PM: phase noise, and RW: random walk noise. Modified Allan deviation must be used to distinguish between RW-FM (flicker phase) and Freq Drift (white phase) noises. Courtesy: This graph is taken from [83].*

1.4.4 Short-term stability

The short-term stability (1 to 100 s) of a passive rubidium frequency standard strongly depends on signal to noise ratio (S/N) [32, 85]. The instability caused due to this is termed as $\sigma_{S/N}$, and can be estimated [31] by,

$$\sigma_{S/N}(\tau) = \frac{N_{psd}}{\sqrt{2} \cdot D \cdot \nu_{Rb}} \cdot \tau^{-1/2} \tag{1.35}$$

where N_{psd} is the detection noise power-spectral-density when microwave and pump laser are switched on (in closed clock loop condition). D is the discriminator slope that can be approximated as the ratio of the signal amplitude (A) to the linewidth ($\Delta\nu_{1/2}$) of DR signal (see Fig. 1.10). The measured noise density, N_{psd} also includes

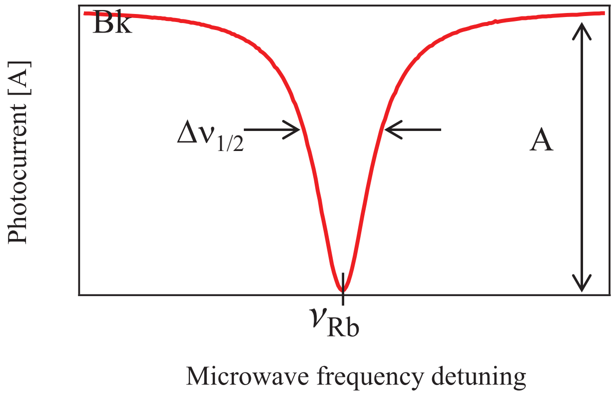

Figure 1.10: *A typical DR signal showing a Lorentzian line shape.*

the contribution of PM-to-AM (phase noise to amplitude noise) laser noise conversion in the clock cell [86, 87].

The error signal is generated by frequency modulating (f_m) the microwave at reasonably low frequencies of few hundreds of Hz with a depth of $\pm\delta f$ as depicted in Fig. 1.11(a). More precisely, the discriminator slope D is determined close to the centre of the error signal (see Fig. 1.11). The modulation depth is always considered to be less than the FWHM ($\Delta\nu_{1/2}$) of the DR signal here. We consider this modulation happens during a quasi-static state, meaning that the DR signal doesn't move during the modulation process. The optimized maximum discriminator slope D is obtained at a modulation depth $\pm\delta f = 0.3\times\Delta\nu_{1/2}$. On the other hand, the modulation frequency f_m is chosen such that it is lower than the γ_1 and γ_2 relaxation rates [32], thus giving enough time for the atom to respond for microwave interrogation in the quasi-static condition.

The modulated signal is detected using phase sensitive synchronous lock-in detection circuit to obtain the error signal as shown in Fig. 1.11(b). The extrema in the error signal show the points of the changing slope in the DR signal. The instability caused due to frequency modulation on the phase noise of the LO is denoted here as $\sigma_{PMnoise}(\tau)$. Phase noise of the microwave frequency synthesizer sets a limit on the clock frequency stability known as Dick effect [61, 88, 89]: the process of frequency modulation adds an extra noise to the closed clock loop via aliasing effect (or intermodulation induced effect) [90]. This noise depends on the modulation frequency used in the clock loop as explained in Section 2.6.2 (Table 2.2).

The intensity and frequency fluctuations of the laser also affect the short-term clock stability via light-shifts (see Section 1.5.2). We denote the instabilities caused due to both the light-shifts affecting the DR line centre to move as $\sigma_{LS}(\tau) = \sigma_\alpha(\tau) +$

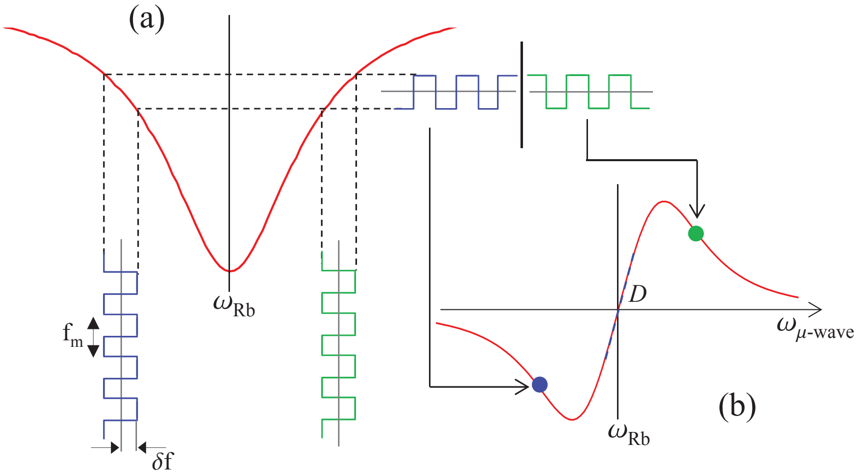

Figure 1.11: *(a) Sampling of the DR signal by frequency modulation (f_m) of the microwave with a depth of $\pm\delta f$ and (b) its corresponding error signal obtained by phase-sensitive detection. Dotted line at the centre of the error signal shows the discriminator slope D.*

$\sigma_\beta(\tau)$ that can be estimated as,

$$\sigma_\alpha(\tau) = \frac{|\alpha| \cdot \sigma_{\Delta I_L/I_L} \cdot I_L}{\nu_{Rb}} \cdot \tau^{-1/2}, \tag{1.36a}$$

$$\sigma_\beta(\tau) = \frac{|\beta| \cdot \sigma_{\Delta \nu_L/\nu_L} \cdot \nu_L}{\nu_{Rb}} \cdot \tau^{-1/2}. \tag{1.36b}$$

where $|\alpha|$ is the absolute value of the intensity light-shift coefficient (cf. Section 1.5.2), I_L is the input laser interrogating intensity, $\sigma_{\Delta I_L/I_L}$ is the relative intensity stability of the laser (cf. Section 2.4 and Fig. 2.7), $|\beta|$ is the absolute value of the frequency light-shift coefficient (cf. Section 1.5.2), $\nu_L = 384.23$ THz is the frequency of laser for the D2-transition and $\sigma_{\Delta\nu_L/\nu_L}$ is the relative frequency stability of the laser (cf. Section 2.4 and Fig. 2.6).

Eventually, the overall short-term clock frequency stability can be estimated from the sum of the squares of the individual limits by the following equation:

$$\sigma_y(\tau) = \sqrt{\sigma_{S/N}(\tau)^2 + \sigma_{PMnoise}(\tau)^2 + \sigma_{LS}(\tau)^2}. \tag{1.37}$$

The shot-noise limit of the clock occurring due to statistical nature of the photons arrival at the detector (time-energy uncertainty) [91, 92] is calculated using the noise spectral density as,

$$N_{shot} = \sqrt{2 \cdot e \cdot I_{dc}}, \tag{1.38}$$

where e is the charge of an electron and I_{dc} is the photocurrent of the DR signal at

$\Delta\nu_{1/2}$. By replacing N_{shot} in place of N_{psd} in the Eqn. 1.35, one can calcuate the shot-noise limited clock frequency stability, $\sigma_{shot}(\tau)$. This sets the potential limit of the clock's attainable short-term stability, provided the other technical noise contributions (eg. laser noise, LO phase noise etc.) are nullified.

1.4.5 Medium- to long-term frequency stability

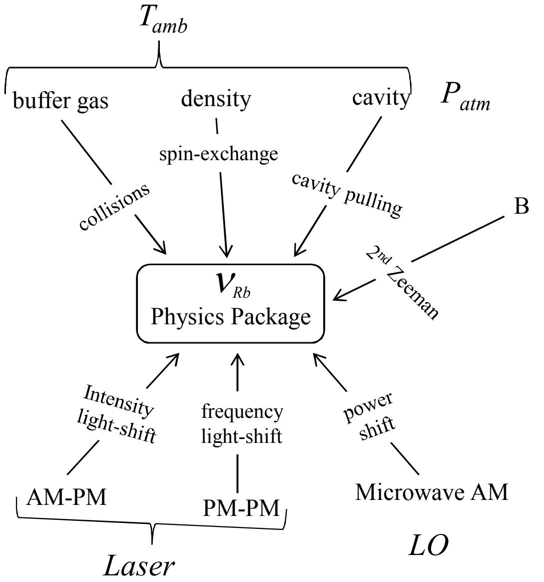

Figure 1.12: *Physical effects and their corresponding sources of fluctuations affecting the clock frequency stability in medium-long-term time scales.* T_{amb} *is the ambient temperature around the physics package (PP),* P_{atm} *is the atmospheric pressure and* B *is the external magnetic field.*

As explained in Section 1.4, the medium-term frequency stability is mainly affected by flicker and random walk noise types, whereas the long-term clock frequency stability is affected by drift and ageing (see Fig. 1.9). In laser pumped Rb standards, the frequency and amplitude instabilities of the laser are among the main causes of instabilities. The other physical environmental parameters, such as temperature variations, atmospheric pressure, magnetic field variations etc., also causes the limits on achievable stabilty [93].

Figure 1.12 shows physical effects and their corresponding sources of fluctuations affecting the clock frequency in medium-long-term time scales. Therefore, the perturbed output clock frequency can be estimated as,

$$\nu_{pert} = \nu_{Rb} + \Delta\nu_{Z} + \Delta\nu_{LS} + \Delta\nu_{BG} + \Delta\nu_{SE} + \Delta\nu_{\mu P} + \Delta\nu_{CP}, \tag{1.39}$$

where, ν_{Rb} is the frequency of the ^{87}Rb unperturbed hyperfine transition used as reference and $\Delta\nu_Z$ is the 2^{nd} order Zeeman shift, $\Delta\nu_{LS}$ is the light-shift, $\Delta\nu_{BG}$ is the shift caused due to collisions between ^{87}Rb and buffer gases, $\Delta\nu_{SE}$ is the spin-exchange shift (due to ^{87}Rb-^{87}Rb collisions), $\Delta\nu_{\mu P}$ is the microwave power shift and $\Delta\nu_{CP}$ is the shift due to cavity-pulling. Though the effect of light-shift in this work is compensated for by using the AOM laser head, the temperature variations are unavoidable as our clocks are operated in laboratory ambient conditions.

1.5 Clock Frequency Perturbations

In this section we will discuss the perturbations and the corresponding shifts caused on the centre frequency of the DR signal ν_{Rb} (cf. Fig. 1.11) in detail. In particular, the focus will be on the effects that are most relevant on the medium- to long-term frequency stability. The emphasis is to understand the underlying physical effects in view of having a better control on them in order to improve the medium- to long-term frequency stability in the clocks presented here.

1.5.1 Second order Zeeman shift

The second order Zeeman shift for the clock transition is given as,

$$\Delta\nu_Z = A_0|\mathbf{B}\cdot\hat{z}|^2, \qquad \textit{with}\ A_0 = 575.14\ \ \mathrm{Hz/G}^2, \tag{1.40}$$

where, $\hat{z}$ is the quantization axis direction. The magnetic field $\mathbf{B}$ includes the combination of contributions [93] from, the applied quantization magnetic field $\mathbf{B_0}$, the residual field $\mathbf{B_r}$ and the field related to the noise of the magnetic shields $\mathbf{B_s}$. $\mathbf{B_r}$ is the field that remains even after the shields are used to suppress the external flucuations. The fluctuations of these terms on clock frequency can be characterized by their respective variances, $\sigma^2_{B_0}(\tau)$, $\sigma^2_{B_r}(\tau)$ and $\sigma^2_{B_0}(\tau)$ as [93]:

$$\sigma^2_y(\tau) = \left(\frac{2A_0\mathbf{B_0}}{\nu_{pert}}\right)^2 \{\sigma^2_{B_0}(\tau) + \sigma^2_{B_r}(\tau) + \sigma^2_{B_s}(\tau)\}. \tag{1.41}$$

The calculations for our typical experimental conditions using Eqn. 1.41 are done in Section 4.5.1.

1.5.2 Light-shifts

Generally, the AC Stark shift effect is termed as light-shift (LS) in atomic clocks [52]. The LS effect of an electromagnetic field on the clock transition is usually encountered in Rb clocks when in continuous wave (CW) operation. This occurs by the light field initiating virtual transitions in the atoms, and in this sense is fundamentally related to the Lamb shift, which arises due to atom's interaction with the vacuum field [4]. The LS, $\Delta\nu_{LS}$, can be written as [53, 94],

$$\Delta_{LS} = \frac{1}{4}|\Omega_R|^2 \frac{(\omega_L - \omega_{opt})}{(\omega_L - \omega_{opt})^2 + \frac{(\Gamma^*)^2}{4}}, \tag{1.42}$$

where, Ω_R is the optical Rabi frequency proportional to laser intensity I_L, ω_L is the laser angular frequency, Γ^* is the width of the approximatively Lorentzian optical absorption broadened due to BG collisions that is centered at the optical atomic transition frequency ω_{opt}.

Incidentally, there is a minor contribution to the light-shift from the other ground state ($|g_1\rangle$) levels due to the spread of the wings of the dispersive LS profiles [21, 32]. This is important to be considered in evaluating the effect of LS on the ground-state hyperfine "clock transition" [21]. Therefore, the total LS contribution from Δ_{LS1} and Δ_{LS2} can be written as,

$$\Delta\nu_{LS} = \Delta_{LS2} - \Delta_{LS1}. \tag{1.43}$$

with $\Delta\nu_{LS} = \Delta\omega_{LS}/2\pi$. By detuning the laser frequency (ν_L) one can reduce the effect of intensity light-shift on the clock. To facilitate this, we have developed a laser head integrated with Acousto Optical Modulator (AOM) (cf. Section 2.2.2). The use of AOM LH is demonstrated to reduce the intensity LS coefficient as explained in Sections 5.4.1 & 6.3.1, respectively.

A. Intensity Light-shift coefficient, α

From Eq. (1.42), the intensity LS coefficient, α, can be derived as $\alpha = \frac{\partial\Delta\nu_{LS}}{\partial I_L}$ at a fixed laser frequency. This essentially gives the slope when the clock frequency is measured as a function of laser intensity. The limitation to the clock's stability due to intensity light-shift, α in medium-to long-term time scales can be estimated by the Eqn. 2.2 (explained in Section 2.4).

B. Frequency Light-shift coefficient, β

From Eq.(1.42), when the intensity of the light is kept constant, the frequency LS coefficient is written as $\beta = \frac{\partial\Delta\nu_{LS}}{\partial\nu_L}$. Frequency LS can be nullified, e.g. in pulsed mode [56]. In the continuous-wave operation discussed here, this is not possible, but we can reduce β by operating at low light intensities [95] (also see Chapters 5 & 6) or operating at high buffer gas pressures as studied by Camparo et al. [96]. The influence of β on clock instability can also be estimated similar to that of intensity LS, given by Eqn. 2.1 in Section 2.4.

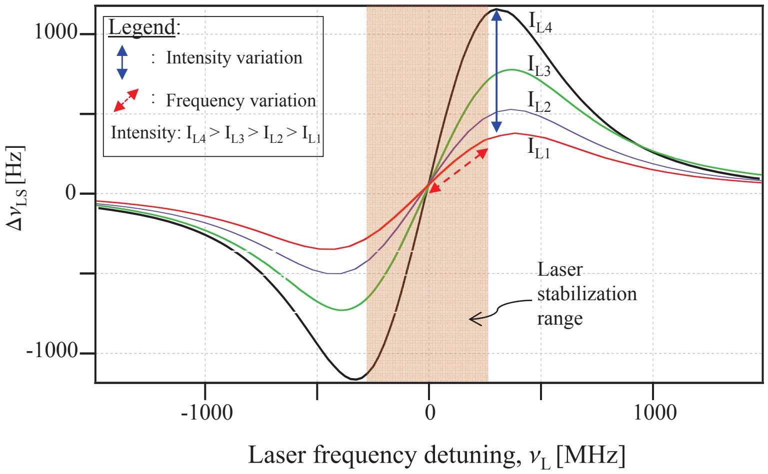

Figure 1.13: *Conceptual diagram depicting the intensity and frequency light shift effects. The x-scale shows the laser frequency detuning around the center of the optical transition in the clock cell.*

The plot of total LS $\Delta\nu_{LS}$ as a function of laser frequency detuning for different laser intensities when the laser frequency is varied around the $F_2 \to F_e$ transitions is shown in Fig. 1.13. The amplitude (or slope) of the curve in the shaded area increases as the laser intensity increases ($I_{L4} >> I_{L1}$) and vice versa, this effect as a function of laser intensity depicted by solid-line-arrows is the intensity light shift coefficient α. At a fixed laser intensity, the slope of the curve gives the frequency light shift coefficient β that is depicted by dashed-line-arrows. The nominal laser stabilization range studied in this thesis is shown by the shaded box.

1.5.3 Buffer gas shifts and Temperature Coefficient (TC)

The buffer gas (BG) is mainly used in order to prevent the atoms from colliding on to the walls of a glass cell. At reasonably high buffer gas pressures (> 15 Torr), during the interrogation time of ^{87}Rb atoms with the EM-fields, the atoms can be assumed to be almost stationary in space inside the vapor cell [34]. The collision cross-sections (σ_1 & σ_2 in Eqn. 1.25) of buffer gases with Rb atoms (for the Rb D2-transition), in particular, nitrogen N_2 is large enough (~43 Å^2) to keep the Rb atoms localized in space [32]. As said earlier, the N_2 buffer gas also acts as a *quenching gas*: the excited rubidium atoms can transfer from one of the P-states to the S-states without emitting or absorbing the radiation, since all the fluorescence is quenched by nitrogen gas. The buffer gas can also be used to reduce the intensity light-shift effect [21, 97]. This is achieved by filling the right amount of BG pressure inside the clock cell that due to collisions with the buffer gases shifts the excited state Rb transition line (ν_{opt} in Eqn. 1.42) to give a minimal effect on the clock frequency. In a conventional lamp-pumped Rb standard, the BG were used in the lamp in order to match the transition lines of ^{85}Rb with that of ^{87}Rb [32]. By first approximation, the observed collision frequency shift between the alkali atoms and BG gas molecules can be more appropriately termed as *density shift* [97].

The shift due to the ^{87}Rb-buffer gas collisions is dependent on the temperature of operation of the clock. A mixture of buffer gases can be used to reduce the temperature coefficient. For this purpose, we use an appropriate mixture of Argon (Ar) and Nitrogen (N_2); while N_2 produces the necessary fluorescence quenching, the Ar decreases the TC of nitrogen. The N_2 has a $+^{ve}$ TC with Rb, whereas Ar has $-^{ve}$ TC, therefore by mixing these two gases one can obtain a zero TC point. The equation that dictates this methodology can be written as [32, 98],

$$\Delta\nu_{BG}(T) = \nu_{Rb} + P_t(\beta' + \delta'\Delta T + \gamma'\Delta T^2), \tag{1.44}$$

where $P_t = P_{N_2} + P_{Ar}$ is the total gas pressure, $\Delta T = T - T_0$ is the difference between the working temperature and the reference temperature for which the coefficients are measured. Note that the total gas pressure P_t can increase during the cell sealing [98]. β', δ', γ' are the pressure coefficient, the linear temperature coefficient and the quadratic temperature coefficient of the mixture, respectively for the gas mixture. Further more: $\beta' = (\beta_{N_2} + r\beta_{Ar})/(1+r)$, $\delta' = (\delta_{N_2} + r\delta_{Ar})/(1+r)$ and $\gamma' = (\gamma_{N_2} + r\gamma_{Ar})/(1+r)$, with r as the pressure ratio P_{Ar}/P_{N_2}. Typical coefficient values for Ar and N_2 buffer gases are given in Table 1.4.

Table 1.4: *Pressure shift and temperature coefficients of* ^{87}*Rb in Ar and* N_2 *buffer gases. The values are referred from [32].*

Buffer gas	β_{BG} **[Hz·Torr^{-1}]**	δ_{BG} **[Hz·Torr^{-1}·°C^{-1}]**	γ_{BG} **[Hz·Torr^{-1}·°C^{-2}]**
Ar	-59.7	-0.32	-0.35x10^{-3}
N_2	546.9	0.55	-1.5x10^{-3}

For our case of gas mixture ratio of 1.6, the corresponding calculated coefficients are given in Table 1.5. At a total pressure P_t of 19.5 Torr (typically in our case), the offset shift on ν_{Rb} is calculated as $\beta' \times P_t = 3385$ Hz (see Fig. 6.3 for the measured value).

Table 1.5: *Calculated coefficients of Ar and N$_2$ BG mixture (with r = 1.6) contributing to the temperature coefficient of the Rb vapor cell.*

β' **[Hz·Torr^{-1}]**	δ' **[Hz·Torr^{-1}·°C^{-1}]**	γ' **[Hz·Torr^{-1}·°C^{-2}]**
173.6	1.46x10^{-2}	-0.8x10^{-3}

1.5.4 Spin-exchange shift

As explained before the spin-exchange collisions not only cause the line broadening, they also produce a small phase shift of the atomic magnetic moment, resulting in an average frequency shift of the clock transition [76, 93, 99], given as:

$$\Delta\nu_{SE} = -\frac{1}{8\pi} n\bar{v}_s\lambda_{se}\ \Delta. \tag{1.45}$$

where λ_{se} (= 6.9×10^{-15} cm^2 for ^{87}Rb [99]) is the frequency-shift related collisional cross-section, Δ is the population difference between the two hyperfine clock levels [76]. The value and sign of Δ thus depends on the optical pumping condition in which the atomic sample is prepared for clock operation, i.e. whether the optical pumping is done from either $5^2S_{1/2}$ F$_g$ = 1 or F$_g$ = 2 (cf. Fig. 1.3). For example, consider that the atoms are pumped from F$_g$ = 1 state, in which case $\Delta = +1/5$ and if the atoms are pumped from F$_g$ = 2 state, Δ = -1/3 [76]. The mean velocity between the two colliding Rb atoms with reduced mass μ, inside the cell volume with a temperature T$_v$ can be calculated by the formula,

$$\bar{v}_s = \sqrt{8\mathrm{k_B} \cdot \mathrm{T_v}/\pi\mu} \tag{1.46}$$

where, k_B is the Boltzmann constant.

The spin exchange frequency shift that is dependent on local temperature of the stem T$_s$ in the operating range that changes the atomic density correspondingly, can be calculated by the formula [76],

$$\Delta T_{SE} = \frac{\delta(\frac{\Delta\nu_{SE}}{\nu_{Rb}})}{\delta T} \tag{1.47}$$

At an operating cell volume temperature T$_v$ = 336 K, $\bar{v}_s \approx 2.86\times10^4$ cm·s^{-1}. And, at the stem temperature of T$_s$ = 321 K the Rb atomic density $n = 2\times10^{11}$ cm^{-3}. For the condition in which atoms are pumped from $F_g = 1$ state, $\Delta = +1/5$. Therefore, with the above values in Eqn. 1.45, one gets $\Delta\nu_{SE} \approx$ -0.3 Hz or $\frac{\Delta\nu_{SE}}{\nu_{Rb}}$ = -4.6×10^{-11}. The dependance on temperature in our stem operating range around 321 K, we can consider that the Rb density increases by 10% for every kelvin and thus we calculate $\Delta T_{SE} \approx$ -5×10^{-12}/K (see Section 6.2.3).

1.5.5 Microwave power shift

The light-shift varies continuously along the path of the light beam in a buffer gas cell thereby causing inhomogeneous broadening of the resonance signal [32, 54, 65, 100]. This happens due to the fact that atoms are relatively motionless during the microwave interaction time so that spatial gradients can cause line inhomogeneity effects inside a microwave cavity [54, 65]. Hence, in a DR signal, we can say that the measured resonance frequency is a function of the applied microwave (RF) power. This inhomogeneity causes the shift on the clock hyperfine frequency and is termed as *power shift*, $\Delta\nu_{P_\mu}$. More precisely, this shift arises due to the fact that different parts of the atomic sample that have different frequencies contribute less to the resonance signal upon saturation and hence the line-centre is shifted. On the other hand, the use of wall-coated cell (without buffer gases) reduces the effect of microwave power shift [54, 101]. But, the microwave power shift also includes the effect due to position of atoms inside the vapor cell, known as *position-shift.* Hence the observed shift is a weighted average of the ensemble of atoms that is dependent on each atom's position inside the cell [56, 93]. It is attributed to the field distribution (mode) inside the cavity and the variations of the microwave power [54], which couples the laser power with the microwave power. Hence, the observed shift is dependent on light intensity and mimics the light-shift behavior, known as pseudo-light-shift [56].

A detailed analytical theoretical analysis of this effect is not found in literature and needs to be formalized. However, the observed effects have been treated with numerical analysis and we focus our studies in this thesis on the basis of evaluating the observed shift and its influence on the clock's stability.

1.5.6 Cavity pulling

In a Rb standard, the vapor cell containing the atoms and buffer gases is placed inside a microwave cavity. Due to the feedback of the cavity on the atoms and because of detuning of the cavity from ν_{Rb}, the cavity pulling effect arises. The cavity pulling shift can be written as,

$$\Delta\nu_{CP} \approx \frac{Q_c}{Q_a}\frac{C}{(1+S)}\Delta\nu_c, \tag{1.48}$$

where Q_c is the quality factor of the cavity, $C \approx 10^{-2}$ [32] is the parameter dependent on oscillation threshold, $S = 2$ is the saturation parameter for which the discriminator slope D is maximum, and $\Delta\nu_c$ is the cavity detuning from ν_{Rb} as a function of temperature. Therefore, if the temperature varies, the cavity frequency also shifts, and so does $\Delta\nu_c$, which implies that $\Delta\nu_{CP}$ changes accordingly influencing the clock frequency (cf. see Fig. 1.12).

1.5.7 Other shifts and drifts

Although the buffer gases such as N_2 and Ar cannot penetrate the sealed borosilicate glass cells, the lighter gas such as Helium (He) can permeate and thus create a very slow shift (or drift) on clock long-term frequency [102,103]. It has a positive shift when He permeates into the glass cell in the normal atmospheric conditions and vice versa when the clock is in space. This is an equilibration process. For the clocks studied in this thesis, we have not made any quantitative measurements on this effect, but from Camparo et al. [102] we approximately estimate the equilibration time constant of $<$ 280 days for our cell sizes. All the other physical mechanisms responsible for medium- to long-term clock instabilities are responsible for the drift caused over a period of 1 day to few months.

1.5.8 Shifts and broadening summary

Tables 1.6 and 1.7 show the summary of the DR line-broadening mechanisms and the perturbing effects causing the shifts on the DR line-centre frequency ν_{Rb} for buffer gas and wall-coated cells, respectively. The values presented here are approximated typical ones, which are close to the measured values presented in Chapters 5 and 6.

1.6 Conclusions

The basic DR principle was explained along with the clock transition for a ^{87}Rb atom and the possible perturbations were discussed. A summary of DR theoretical description was given by pointing out the important aspects for the clock. The basics on clock frequency stability analysis were explained by giving the importance on Overlapping Allan deviation, as this will be used in characterizing our clocks studied

Table 1.6: *Summary of DR line-broadening and DR line-shift perturbing effects in buffer gas cells.*

Type	**Physical effect**	**Approx. value [Hz]**
Broadening *(BG interaction)*	Collisions $[\propto V_{cell}]$:	
	Wall collisions	70
	Buffer gas collisions	10
	Rb-Rb spin exchange	70
	Light broadening	100
	Microwave power broadening	100
	Total broadening	350
Shifts	Pressure shift *(constant shift)*	4000
	Zeeman 2nd order	< 1
	Intensity light-shift effect	< 0.1
	Frequency light-shift effect	< 0.1
	Cavity pulling shift	< 0.1
	Microwave power-shift effect	< 0.1
	Spin-exchange shift	< ±[a]0.5

---

[a] The sign depends on the pumping scheme, see Sections 1.5.4 & 5.4.4

Table 1.7: *Summary of DR line-broadening and DR line-shift perturbing effects in wall-coated cells.*

Type	**Physical effect**	**Approx. value [Hz]**
Broadening *(wall-coating -interaction, see Chapter 5)*	Wall-collisions $[\propto V_{cell}]$: *(adiabatic, temp. dependent)*	300
	Rb-Rb spin exchange	50
	Reservoir effect	50
	Light broadening	100
	Microwave power broadening	100
	Total broadening	600
Shifts	Wall-shift	-300
	Zeeman 2nd order	< 1
	Intensity light-shift effect	< 0.1
	Frequency light-shift effect	< 0.1
	Cavity pulling shift	< 0.1
	Microwave power-shift effect	< 0.1
	Spin-exchange shift	< ±[a]0.5

---

[a] The sign depends on the pumping scheme, see Sections 1.5.4 & 5.4.4

and presented in this thesis. The short term stability formula in order to predict the S/N limit was introduced. The medium to long-term frequency perturbations were explained along with the physical processes that are responsible for such effects. For the buffer gas cell, we estimated an overall (in presence of laser and microwave) line-boradening of about 350 Hz. The constant pressure shift due to BG, for a gas pressure of 26 mbar is estimated to be around 4000 Hz and all the other shifts are < 1 Hz from the Rb unperturbed frequency ν_{Rb}. We also estimated the line-broadening and shifts in wall-coated cell. The overall line-broadening in wall-coated cell is around 600 Hz with the wall-coated shift estimated to be around -300 Hz and all the other shifts are < 1 Hz from ν_{Rb}. The The intensity light-shift can be minimized by the use of laser detuning technique with AOM laser head (cf. Section 2.2.2). The frequency perturbing shifts and their contribution on the clock frequency instabilities have been evaluated and are explained in the Chapters 5 & 6.

Chapter 2 Laser Heads and the Local Oscillator (LO)

> *Time is really the only capital that any human being has, and the only thing he can't afford to lose.*
> *-Thomas Edison.*

In this chapter we give the details of two important sources required for the DR spectroscopy and clock operation. At first, the optical laser sources that are used for optical pumping and signal detection, and then the details on the microwave source (the Local Oscillator - LO)) responsible for driving the microwave resonance and for clock loop stabilization are presented along with the phase noise measurements.

The optical source used for this research is a Distributed Feedback (DFB) diode laser that was mounted in a compact in-house built Laser Head (LH) module. Two variants of the laser heads were fabricated for this study at LTF; one that has a compact design without Acousto Optical Modulator (AOM) and the other one which has an integrated AOM for frequency fine tuning (in order to minimize the light-shift effect on clock stability). The laser heads presented here were mainly realized thanks to the efforts of P. Scherler, F. Gruet and the author (T. Bandi) for design, construction and characterization, M. Pellaton for Rb cells. This was based on the previous work on External Cavity Diode Lasers (ECDL) [95]. The author mainly contributed for the AOM LH by providing the basic design, assembly integration and by performing the characterization measurements.

In order to avoid any ambiguity in distinguishing between the above mentioned two laser heads, we name them as follows: (i) the compact laser head without AOM as *"the clock laser head"* and (ii) the AOM-integrated module as *"the AOM laser head"*.

The LO was constructed at INRIM [51, 104] and was procured via a collaboration project [105]. The phase noise measurements performed at LTF by the author are presented here by detailed analysis of its influence on the clock loop and instability on clock's short-term frequency performance.

2.1 Requirements on laser and microwave sources

Our performance goal for the next generation clocks for satellite navigation is to achieve a short-term stability of $< 6\times10^{-13}\ \tau^{-1/2}$ between 1 to 100 s and reach $< 1\times10^{-14}$ (drift removed) between 10^4 s up to one day time scales, with an overall volume of < 3 liters, mass of < 4 kg and power consumption of < 20 W. These performance requirements set the limits on the laser and microwave sources explained as follows:

(i) Laser source: A collimated laser beam with a wavelength of 780 nm and a power output of at least few tens of microwatts (after passing through the optical components) is required to optically pump the D2 transition of ^{87}Rb atoms to one of the hyperfine ground states (thus creating an atomic ground-state polarization). The linewidth of the laser should be in few MHz range in order to resolve all the sub-Doppler transitions in a seperate, evacuated reference cell. This feature is required for laser frequency stabilization by locking to one of the sub-Doppler transitions (cf. Section 2.3). Locking to a sub-Doppler transition ensures a better laser frequency stability by minimizing the contribution via frequency light-shift coefficient β. The Relative Intensity Noise (RIN) and FM noise should be $< 10^{-12}$ Hz^{-1} and < 6 kHz/$\sqrt{\text{Hz}}$ at the modulation frequency, respectively to reach the clock goal of $< 6\times10^{-13}\ \tau^{-1/2}$. Desired power stability of the laser in order to avoid the clock drift is within 0.1 %/day, at fixed environmental conditions. Finally, the frequency stability of the laser should be $< 1\text{x}10^{-11}\ \tau^{-1/2}$ (1-1000 s) and $< 3\text{x}10^{-12}$ for 1,000 s to 1 day.

(ii) Local Oscillator: A synthesizer that can generate 6.835 GHz of microwave frequency and a power output level up to 0 dBm is required. However for the DR spectroscopic and clock measurements, the usage of power could be very well reduced down to the level of -10 dBm or even less. A typical tuning range of 2 MHz is ideal (to cover a broader range of associated clock frequency shifts) with steps of < 1 Hz resolution. An important factor is the phase noise of the LO. Typical clock modulation frequency is in the range 50-300 Hz. For our clock, referred to a 6.8 GHz carrier, a phase noise of $\leq$ -80 dBrad^2/Hz @ 100 Hz and $\leq$-100 dBrad^2/Hz @ 1 kHz is required. The LO should be capable of operating in two modes; a *sweep mode* - covering a range of 1 MHz to ensure the full Zeeman spectrum and *locked mode* - for the clock operation. The 10 MHz output of the crystal oscillator (OCXO) in the microwave synthesizer should give a power output up to 10 dBm to compare the clock with the active hydrogen maser.

2.2 Frequency stabilized laser heads

The 780 nm DFB laser sources were procured from Eagleyard photonics GmbH (EYP-DFB-0780-00080-1500-TOC03-0000). The laser diodes are mounted in TO-3 package along with integrated peltier thermo-electric cooler, in order to reduce the sensitivity to external thermal variations. Similar diodes emitting at ^{87}Rb D1 transition (795 nm) were also used and laser heads were fabricated. The details on 795 nm laser heads is out of the scope of this thesis (as we operate here only on D2-transition), and can be found in [106, 107]. An overview of the design is given in the below sections highlighting the important characteristics that are useful for clock operation.

2.2.1 The clock laser head

The clock laser head shown in Fig. 2.1 is built on the basis of previous works at Observatoire de Neuchâtel [95,108]. All the optical components are mounted on a thermally controlled baseplate. The 780 nm (∼384.6 THz) DFB diode is mounted next to the collimation assembly that includes an optical isolator to avoid any backscattered light on to the diode, that otherwise could invoke frequency instabilities. One part of the direct beam is incident on a photodetector, that can be used to measure the direct beam intensity variations (cf. Section 2.4). Another part of the direct beam is made to pass through a miniature evacuated cell (10 mm diameter, 19 mm long) filled with ^{87}Rb atoms. This beam is retro-reflected on its path to resolve the sub-Doppler transitions and is detected using the second photodetector for laser frequency stabilization (see Section 2.3). The space below the thermal baseplate is reserved for photodetector pre-amplification electronics. The evacuated Rb cell is fabricated at the LTF, with an in-house developed cell filling facility [106]. This cell is mounted inside an assembly that has two magnetic shields, a magnetic coil and heaters for thermal control. The magnetic shields reduce the influence of external magnetic fluctuations. A stabilized magnetic field is applied using the magnetic coil and the heater is used to increase the cell temperature in order to get a higher number of atoms participating in the interrogation to give better signal-to-noise ratio. This heater is temperature controlled at the mK level. The overall clock laser head assembly occupies a volume of 0.63 dm^3 and mass of 0.6 kg.

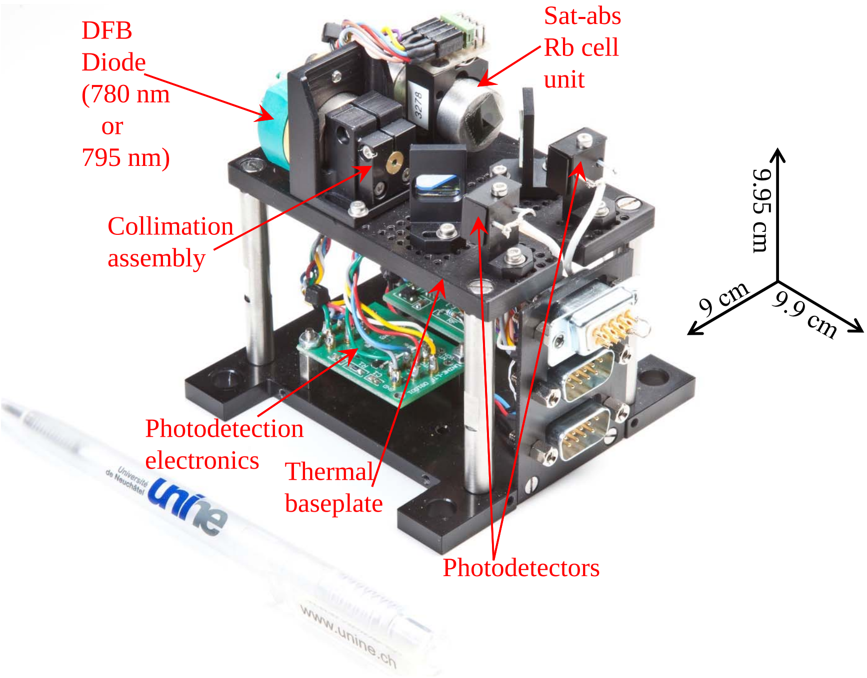

Figure 2.1: *Fully mounted compact clock laser head shown without the outer covering contrasting its dimensions with that of a pen. Dimensions are shown on the right hand side. A detailed schematic with laser beam path is presented in Appendix B*

2.2.2 The AOM laser head

The design of the AOM laser head is similar to the clock laser head, except for the implementation of the AOM and its relevant optical components (Fig. 2.2). A part of the beam is split-off after the collimation assembly and is directed towards the *physics package* for the clock interrogation. This feature of interrogating the direct beam from the Laser Head with atoms in the clock physics package is essential in order to avoid any laser instabilities arising due to detuning by the AOM. The other part of the beam is detuned using the AOM assembly and then is passed through the reference cell for sub-Doppler spectroscopy. The resolved sub-Doppler peaks are then utilized for the laser frequency stabilization. Note that the *detuning* used for laser frequency stabilization with the sub-Doppler peaks is with opposite sign to that as seen by the atoms in the clock physics package. The beam passes through the AOM in a double-pass configuration [109], depending on the detuning required, either the 1^{st}- or 2^{nd}-order is selected for frequency stabilization. Further details on the design and optical components can be found in [106]. The AOM laser head assembly has a volume of < 2.3 dm^3 and a mass of ~ 1.4 kg.

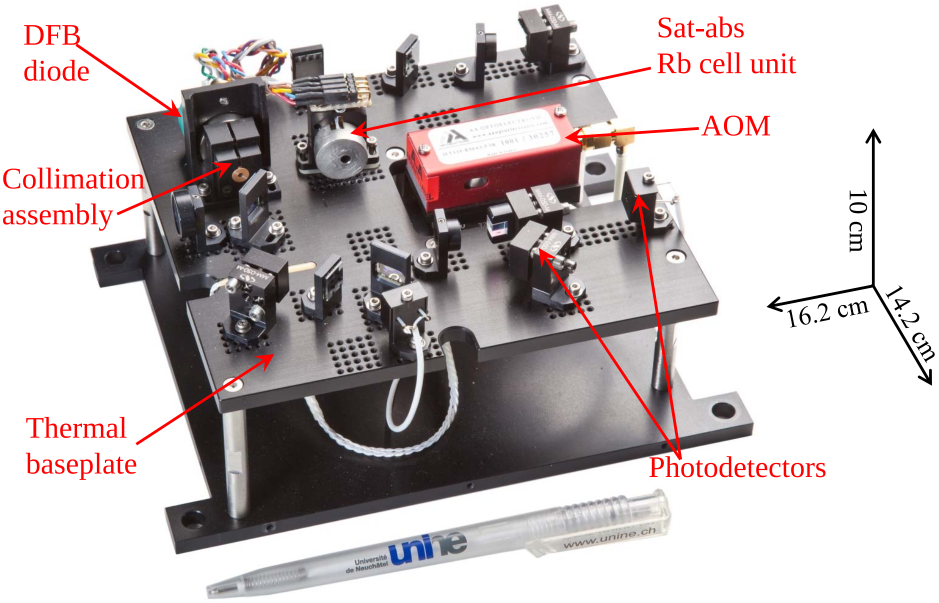

Figure 2.2: *Fully assembled AOM laser head shown contrasting its size to a pen. The top cover is not shown. The laser beam path is shown in Appendix B*

As mentioned above, the AOM laser head is helpful for detuning the laser frequency and thereby for reducing the intensity light-shift effect on the clock transition, inorder to improve the medium- to long-term clock frequency stability. We have also demonstrated such an implementation in a wall-coated cell clock [110] as further detailed in Chapters 5 & 6.

2.3 Saturated absorption spectroscopy and laser frequency stabilization

In this section, we will see the methods adopted to frequency stabilize the above introduced laser heads.

The reference cell filled with ^{87}Rb only is called as evacuated cell in this work. These cells are mounted in the respective laser heads (see Figs. 2.1 & 2.2) and are used for resolving the sub-Doppler transitions by the method of saturated-absorption spectroscopy; a technique that we describe shortly later. When the frequency of the laser is swept through transition lines of the atoms confined in the vapor cell, part of the beam is absorbed giving an absorption signal that is recorded using a photodetector. This signal is Doppler broadened due to the random thermal motion of atoms within the vapor cell. It has a Maxwell-Boltzmann distribution around the transition frequency ν_0 and the FWHM ($\sim$ 523 MHz for ^{87}Rb at 315 K in our case) of this distribution can be determined by, $\Delta\nu_{Dopp} = 2\frac{\nu_0}{c}\sqrt{2 \cdot ln2 \cdot k_B T/m}$, where k_B is the Boltzmann constant, T is the absolute temperature, c is the speed of light in vacuum and m is the mass of the absorbing atom. As the excited-state hyperfine splittings are of the same order and comparable to the Doppler broadening, the method of high-resolution spectroscopy (saturated absorption) is used to resolve the sub-Doppler (or hyperfine splitting) peaks [111–113].

Let's consider two counterpropagating laser beams with same frequency but differing intensities passing through the vapor cell; one intense beam is called "pump-beam" with propagation vector $+k$, which optically pumps the atoms, whereas the other beam is of low intensity known as "probe-beam" with the propagation vector $-k$ that is used to get the information on the pumped atoms. Both the beams are made to overlap along the full length of the cell. For a simpler description, we assume a two-level case having a ground-state $|g\rangle$ and an excited state $|e\rangle$. Let's call the number of atoms in ground state as Ng and that in the excite state as Ne. Assuming the laser frequency, ν_L detuned as $\nu_0 - \Delta\nu$, the atoms moving with a longitudinal velocity $v_l = c\Delta\nu/\nu_0$ towards the probe beam give rise to a simple absorption signal ($\sim$ N$_g$-N$_e$). These atoms perceive the probe-beam frequency as blue-shifted and that of the pump-beam as red-shifted (as it is propagating in the opposite direction), hence no effect due to pump-beam is observed if $\Delta\nu \geq$ intrinsic width. Now consider the class of atoms that are travelling *perpendicular* to the laser beam with velocities $v_l = 0$, such that $\nu_L = \nu_0$, the pump-beam is "on-resonance" and hence optically pumps the atoms, *say* δN from the ground-state to the excited-state. This depletes or creates a *hole burning* [114] in the ground state and populates the excited state. In this condition, the probe-beam absorption is reduced and a "dip" is seen, giving the information on the natural linewidth of that particular resonant transition. This is also known as sub-Doppler transition. As there are "dips" when the probe beam is *transmitted* without any absorption these are also called as *Lamb dips* [112]. Consider a case with more than one excite level: when the atoms are having velocities such that the pump-beam is in resonance with one transition and the probe-beam is in resonance with another transition, cross-over resonance dips appear. However, intuitively we see that there are *two* velocity classes of atoms for which this condition is satisfied - atoms travelling away from the pump laser and towards it. Finally, the probe-beam transmission (intensity) is recorded as a function of laser frequency ν_L when the pump and probe beams are in resonance with the transitions in order to obtain the sub-Doppler peaks. Typical Rb sub-Doppler peaks are shown in Fig. 2.3 on Doppler-broadened signal, obtained from our laser heads. The sub-Doppler peaks are having the FWHM of about 17 MHz compared with the Doppler width of 500 MHz. The sub-Doppler peaks' linewidth is a factor of three higher than its natural linewidth, mainly due to the probe beam intensity broadening [114]. However, a factor of '30' reduction in the sub-Doppler FWHM compared with that of the Doppler broadening signal improves the laser frequency stability, which in turn is useful to achieve a better clock stability. The polarization of the pump and probe beams also influences the sub-Doppler peaks (due to population redistribution among the Zeeman sublevels), in the sense either the probe beam is transmitted or absorbed based on the polarization used [111]. We use linear polarization that is parallel for both pump and probe beams (lin||lin configuration); hence we observe a sub-Doppler peak with increased absorption on the $F_g = 1$ component. The presence of this peak also indicates a good magnetic shielding ($< \mu$T level) of the reference cell [95].

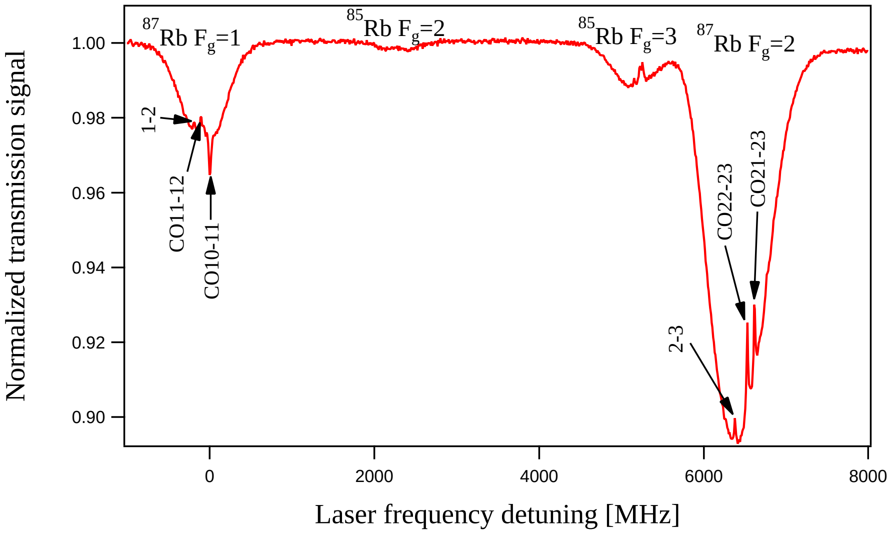

Figure 2.3: *Saturated absorption spectra of ^{87}Rb D_2 from the reference evacuated cell mounted in the laser head. The sub-Doppler lines are labelled and correspond as follows: 2-3: F_g=2→F_e=3, CO22-23: F_g=2→F_e=2,3 cross-over, CO21-23: F_g=2→F_e=1,3 cross-over, CO10-11: F_g=1→F_e=0,1 cross-over, CO11-12:F_g=1→F_e=1,2 cross-over, and 1-2: F_g=1→F_e=2 transition.*

A dedicated in-house made analog electronics for laser operation and frequency stabilization is used. This electronics assembly has the features for laser diode's temperature control (with NTC thermistor feedback), current control unit with a current noise of 1 nA/$\sqrt{\text{Hz}}$, the laser frequency stabilization module and the detector signal pre-amplifier module.

The laser injection current is frequency modulated at 50 kHz for stabilization using lock-in detection. The modulated saturated absorption signal obtained from the laser head is fed into the pre-amplifier module, which amplifies (settable gain) and filters the signal at 50 kHz with a bandwidth of 20 kHz. The laser stabilization module demodulates the amplified signal by multiplying it with the 50 kHz reference using phase-sensitive synchronous detection (which includes a low pass filter of < 5 kHz bandwidth) to give the dispersive error signal. For any deviation from the zero of the error signal, the dc correction voltage is generated and applied to the laser current using a servo-loop in order to have a controlled frequency stabilization onto any desired sub-Doppler peak. This module also includes a ramp generator for scanning the laser current with 20 Hz frequency to obtain full Rb spectra.

2.4 Laser linewidth, frequency and intensity stabilities

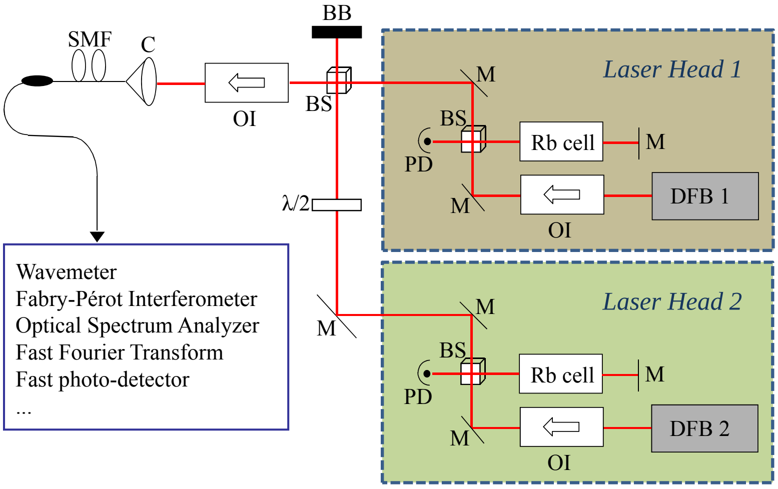

Figure 2.4: *Generalized laser spectral characterization setup. DFB: Distributed Feedback; M:Mirror; PD:Photodetector; BS:Beamsplitter; OI:Optical Isolator; BB:Beam Blocker; SMF:Single Mode Fibre, C:coupler, and $\lambda/2$:Half-wave plate. Bottom left box lists the devices used to measure different laser characteristics.*

The laser diodes were tested by measuring the relevant parameters such as frequency as a function of diode injection current ($\nu_L(I)$), frequency versus diode temperature $\nu_L(T)$, output power, modehop-free tuning range, Side Mode Suppression Ratio (SMSR), Relative Intensity Noise (RIN), FM noise, linewidth, frequency and intensity stabilities. Figure 2.4 shows a general setup that is used to characterize the laser diodes/heads. At a time, one of the laser head modules is characterized to measure most of the physical parameters mentioned above, except that the beat measurement is done using both the laser modules to measure the linewidth and frequency stability applying heterodyne detection. Various laboratory instruments used to measure different spectral parameters are mentioned in the bottom left box of Fig. 2.4.

The beat note between the two identical laser head units was performed by overlapping the beams using a beam-splitter. The superposed beam was detected (cf. 2.3) using a fast photodetector (Newport 1434-50) and the signal was measured with an rf spectrum analyzer (Agilent E4405B). The difference frequency between the two laser frequencies of few tens of MHz is seen as the beat signal (Fig. 2.5). The width of the Lorentzian beat signal corresponds to the sum of the linewidth of two laser heads. The measurement details are explained in [106]. The narrow laser linewidths of about 3 MHz are of particular relevance in order to resolve the sub-Doppler peaks in ^{87}Rb [22, 32].

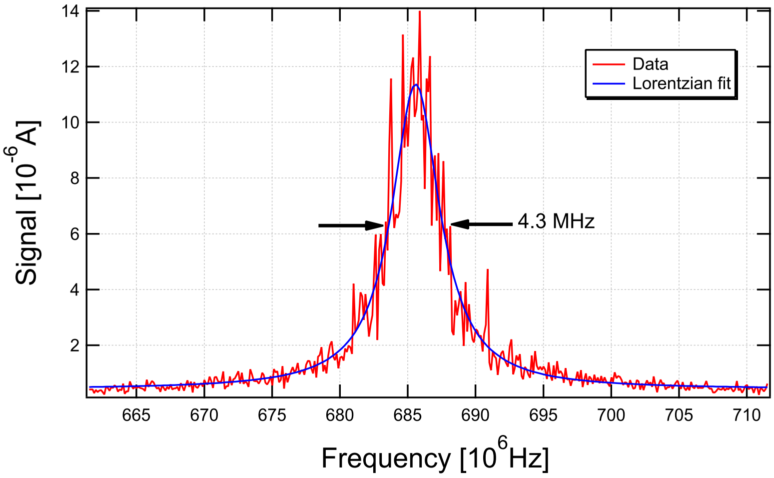

Figure 2.5: *Linewidth (FWHM) measured by beat-note method. The FWHM of individual clock laser head can be considered as FWHM/2 $\simeq$ 2.15 MHz.*

To measure the laser frequency stability either of the laser heads were locked to two different sub-Doppler peaks and the beat note signal detected using the fast photodetector is then fed to a frequency counter. The frequency counter is referenced to an active Hydrogen maser to guarantee that the counter doesn't degrade the laser frequency stability evaluation.

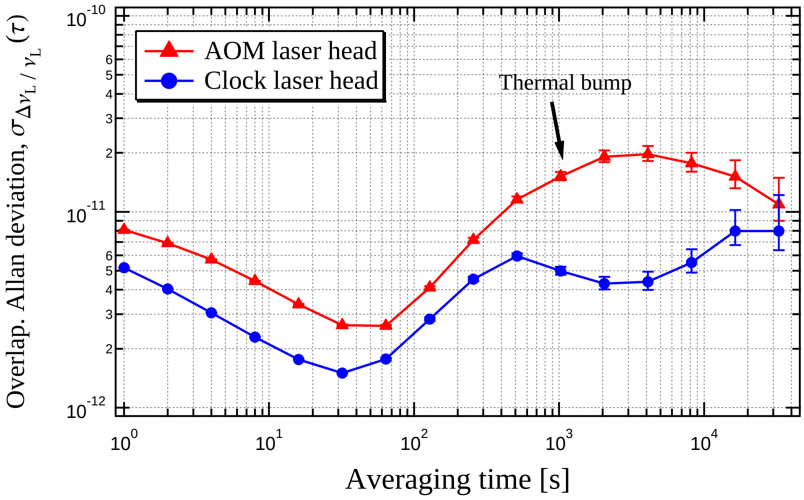

Figure 2.6: *Beat note stabilities of the two 780 nm laser heads. Closed triangles represent the beat between AOM LH and Clock LH, and closed circles represent the beat stability between two identical Clock LHs.*

Figure 2.6 gives the measured fractional frequency stability in terms of overlapping Allan deviation for both, clock and AOM laser heads. The AOM laser head shows slightly higher instability, possibly due to added frequency and intensity noises from the AOM itself. The bumps around 1000 seconds are due to temperature variations in the laboratory mainly because of the air conditioning cycle. Influence of the laser frequency instabilities affecting the clock medium- to long-term time scale via frequency light shift coefficient (β) [32, 52, 53] can be estimated from the formula giving the fractional clock instability due to β, $\sigma_\beta(\tau)$:

$$\sigma_\beta(\tau) = \frac{|\beta| \cdot \sigma_{\Delta\nu_L/\nu_L} \cdot \nu_L}{\nu_{Rb}}, \tag{2.1}$$

where, $|\beta|$ is the abolute value of the frequency light-shift coefficient (see Section 1.5.2), $\sigma_{\Delta\nu_L/\nu_L}$ is the instability value obtained from Fig. 2.6 and ν_L is the laser frequency.

The direct beam recorded using the photodetector shown in Figs. 2.1 and 2.2 is used to estimate the fractional intensity variations of the corresponding laser head. Figure 2.7 shows the clock laser head fractional intensity variations in terms of overlapping Allan deviation. The values are of particular relevance as they directly influence the clock frequency stability via intensity light-shift effect [32, 53, 110, 115]. The corresponding data set for the AOM LH could not yet be measured with the aquisition system used for the Clock LH. However, from the previous data on AOM LH, we estimate its upper limits (see Table 2.1).

Influence of the laser intensity instabilities on the clock medium- to long-term time scale that affects via intensity light shift coefficient (α) can be estimated by the formula,

$$\sigma_\alpha(\tau) = \frac{|\alpha| \cdot I_L \cdot \sigma_{\Delta I_L/I_L}}{\nu_{Rb}}, \tag{2.2}$$

where, $|\alpha|$ is the abolute value of the intensity light-shift coefficient (see Section 1.5.2), $\sigma_{\Delta I_L/I_L}$ is the fractional intensity instability value obtained from Fig. 2.7 and I_L is the interrogating beam intensity.

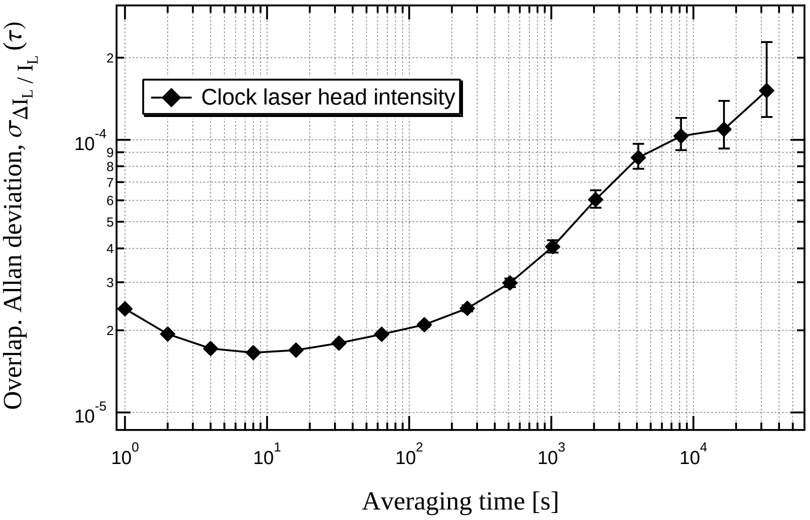

Figure 2.7: *Relative intensity stability of the Clock laser head beam.*

2.5 Measured characteristics of the Laser Heads

Each LH was extensively characterized. A summary of the obtained results is given in Table 2.1. The values of $\nu_L(I)$, $\nu_L(T)$, SMSR, output power, RIN and FM noise of both, the clock and the AOM laser heads are very similar. However, the frequency stability of the AOM LH is slightly degraded due to instabilities introduced by the AOM assembly and additional optical components. When measured with the same in-house built aquisition system, the intensity stabilities of both LHs are identical up to 100 s. After 1000 s, the AOM LH shows slightly larger drift in comparison resulting from additional thermal instabilities due to the larger base plate used in the AOM LH and also possibly due to thermal variations of the AOM itself. The values given in Table 2.1 will be used in the evaluation of the clock performance in Chapters 5 & 6.

Table 2.1: *Characteristics summary of 780 nm Clock and AOM laser heads.*

Parameter	**Clock laser head**	**AOM laser head**
$\nu_L(I)$ [GHz/mA]	-1	-0.875
$\nu_L(T)$ [GHz/K]	-25	-26.3
Single mode operation	Yes	Yes
Modehop-free tuning range [GHz]	$\sim$ 80	$\sim$ 80
Output power from DFB [mW]	$\sim$ 60	$\sim$ 60
Output power from LH [mW]	$\sim$ 5	$\sim$ 5
SMSR [dB]	$>$ 40	$>$ 40
RIN [Hz^{-1}] @75 mA	$<5\times10^{-14}$ @ 300 Hz	7×10^{-14} @ 300 Hz
FM noise [kHz/$\sqrt{\text{Hz}}$]	4 @ 300 Hz	5 @ 300 Hz
Linewidth [MHz] @ 75 mA	$\sim$ 2.2	$\sim$ 4.6
Frequency stability	$<5\times10^{-12}\ \tau^{-1/2}$ for <100 s $<8\times10^{-12}$ (100 s to 1 day) Drift $< 5\times10^{-12}$/day	$<8\times10^{-12}\ \tau^{-1/2}$ for <100 s $<2\times10^{-11}$ (100 s to 1 day) Drift $<$-4×10^{-11}/day
Intensity stability	$<3\times10^{-5}$ (1-100 s) 1×10^{-4} at 10^4 s Drift $\sim$ -1.6×10^{-4}/day	$<1\times10^{-4}$ (1-100 s) $<3\times10^{-4}$ at 10^4 s Drift $\sim +1\times10^{-3}$/day

2.6 The microwave Local Oscillator

The Local Oscillator (LO) produces the microwave radiation for interrogating the atoms by means of the synthesis chain [51]. Briefly, in the LO, the first stages multiply the 10 MHz signal (from the oven controlled crystal oscillator - OCXO) up to 180 MHz and this frequency is further multiplied to the microwave range by a non-linear transmission line (NLTL) to give a comb spectrum, out of which the 39^{th} harmonic at the value of 7.02 GHz is selected for further signal processing. Note that the NLTL is 20 dB less noisy compared to the Step-Recovery-Diode (SRD) used in previous designs [104, 116]. This frequency is filtered out by a coaxial filter and is used to phase-lock a Yttrium-Iron-Garnet (YIG) oscillator. In the phase lock loop, the 7.02 GHz is mixed with a 185.3 MHz to generate 6.835 GHz (for further details see [51]).

The output from the LO was measured using an rf spectrum analyzer (Agilent E4407B). Measured output frequency was 6.834686525 GHz. The frequency can be tuned with 1 μHz resolution with a span of 1.5 GHz. 50 Hz spurs were present at the -66 dB level. The measured output power of the locked OCXO at 10 MHz was 2 dBm. While comparing the clock signal with that of the H-maser, the output from the OCXO was amplified to 10 dBM using an rf amplifier (Mini-Circuits, ZHL-3A).

2.6.1 LO phase noise measurements

As mentioned before in the Section 1.4.4 of Chapter 1, the phase noise of the LO is an important parameter to be measured accurately, as it influences on the short-term clock stability via intermodulation effects. The schematic of the setup for the phase noise measurement using cross-correlation method is shown in Fig. 2.8. Cross-correlation is essentially a means for comparing two or more signals in order to determine the degree of similarity between them.

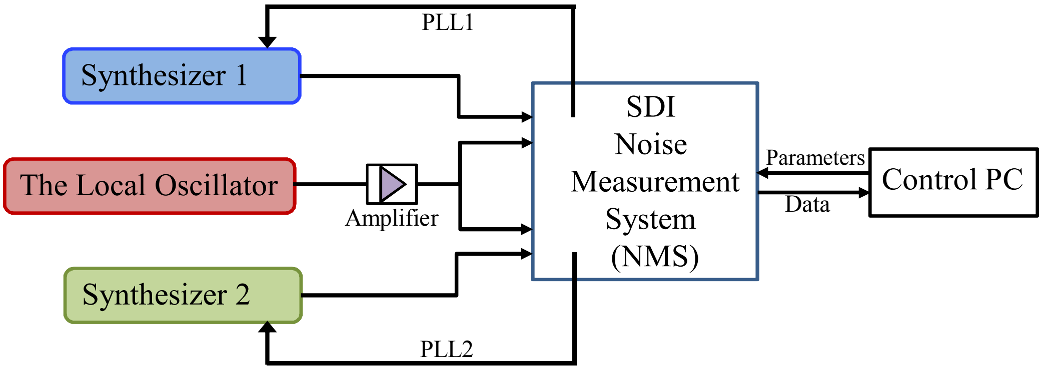

Figure 2.8: *Schematic diagram of the cross-correlation phase noise measurement of the LO. The LO is measured with a frequency difference between two reference oscillators. PLL: Phase Lock Loop (see text for details)*

A *cross-correlation* measurement was performed using two reference synthesizers (Synthesizer 1 & Synthesizer 2 in Fig. 2.8) at 6.835 GHz in order to determine the phase noise of *the LO* only. The 6.835 GHz and 20 dBm (amplified from 2 dBm using the microwave amplifier MITEQAFD3-040080-27) output from *the LO* was divided into two equal parts fed into the SDI Noise Measurement System (NMS) unit. One of the outputs was compared with that of *Synthesizer 1* by a Phase Lock Loop (PLL1), and the other output of *the LO* was compared with that of *Synthesizer 2* by the second PLL (PLL2). Both the PLLs are 90° out of phase with respect to the LO and were locked with a bandwidth of 5 Hz. The other parameters (such as high-pass filter, DC-coupling, span etc.) were set using the computer interface. Finally, the phase noise was measured and the results are shown in Fig. 2.9. The Synthesizer 1 will be used for the wall-coated cell clock operation in Chapter 5, whereas the LO is used for high-performance clock in Chapter 6.

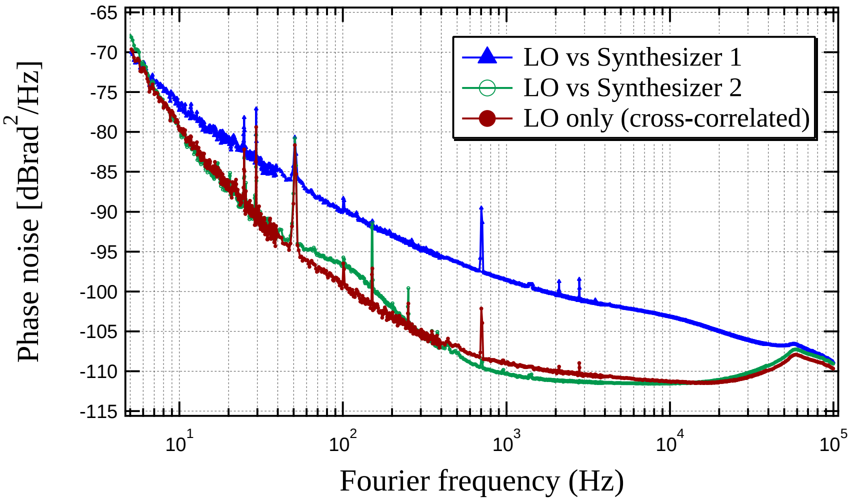

Figure 2.9: *Cross-correlated phase noise measurement at 6.8 GHz carrier frequency. Closed triangles (blue color) show the phase noise limited by Synthesizer 1, open circles (green color) show the stability limited due to the influence of Synthesizer 2 and the closed circles (brown color) represent the phase noise of the LO only.*

The phase noise of the LO (Fig. 2.9 brown color curve) at the carrier frequency of 6.8 GHz has a flicker level at -70 dBrad^2/Hz and noise floor at -111 dBrad^2/Hz.

2.6.2 LO phase noise influence on clock instability

The influence of the phase noise on clock instability depends on the modulation frequency f_m that is used to stabilize the DR signal to the LO. During the process of modulation, the aliasing effect influences the clock loop via higher even harmonics in the phase noise spectrum [61, 86, 117]. The phase noise limited short-term stability, $\sigma_y(\tau)_{PMnoise}$ in a quasi-static model for the square-wave modulation and sine-wave demodulation can be written in terms of phase noise spectral density [90,117], $S_\phi(f_m)$ as

$$\sigma_y(\tau)_{PMnoise} = \sqrt{\sum_{n=1}^{\infty} C_{2n}^2 \cdot S_\phi(2nf_m)} \cdot \tau^{-1/2}, \tag{2.3}$$

where

$$C_{2n} = \frac{2n}{(2n-1)(2n+1)} \frac{f_m}{\nu_{Rb}}. \tag{2.4}$$

Table 2.2: *Influence of* the LO *phase noise due to intermodulation effects on the clock short-term instability for the corresponding clock loop modulation frequencies by considering the even harmonics of the phase noise up to 100 kHz.*

Modulation frequency, f_m [Hz]	$\boldsymbol{\sigma_y(\tau)_{PMnoise} \cdot\tau^{-1/2}}$
10	6.82×10^{-14}
20	6.47×10^{-14}
30	6.77×10^{-14}
40	7.34×10^{-14}
44	7.46×10^{-14}
50	8.24×10^{-14}
60	8.55×10^{-14}
100	1.05×10^{-13}
150	1.22×10^{-13}
164	1.32×10^{-13}
200	1.43×10^{-13}
250	1.72×10^{-13}
300	1.89×10^{-13}

By considering the even harmonics of the phase noise spectrum up to 100 kHz, the estimated influence on the clock instability depending on the modulation frequency f_m = 164 Hz is estimated to be 8.98×10^{-14} $\tau^{-1/2}$. Detailed analysis on the LO phase noise influence on the clock instability to corresponding selected clock loop modulation frequencies are shown in Table 2.2. In the range of modulation frequency f_m considered here from 10 Hz to 300 Hz, nominally for every one Hz increase, an increment in the phase noise influence of 0.425×10^{-15} $\cdot\tau^{-1/2}$ occurs.

2.6.3 LO power stability

The power stability of the LO was measured by connecting the synthesis chain output to a microwave crystal power detector (Agilent 8472B), which was connected to a higher-resolution data aquisition system. Data were recorded using a computer interface. The aquired data are presented in terms of the relative power stability in Fig. 2.10. The data around 1000 s suffer from the influence of the laboratory air conditioning system.

The influence of the LO power instabilities on the clock stability is affected via microwave power shift as explained in Section 1.5.5. Influence of the microwave power instabilities on the clock medium- to long-term time scale that affects via microwave power shift(μ_{PS}) can be estimated from the formula,

$$\sigma_{\mu_{PS}}(\tau) = \frac{|\Delta\nu_{P_\mu}| \cdot \sigma_{\Delta P_\mu/P_\mu} \cdot P_\mu}{\nu_{Rb}}, \tag{2.5}$$

where, $|\Delta\nu_{P_\mu}|$ is the absolute value of the microwave power shift coefficient (cf. Section 1.5.5), $\sigma_{\Delta P_\mu/P_\mu}$ is the LO power instability value obtained from Fig. 2.10 and P_μ is the input microwave power to the cavity resonator.

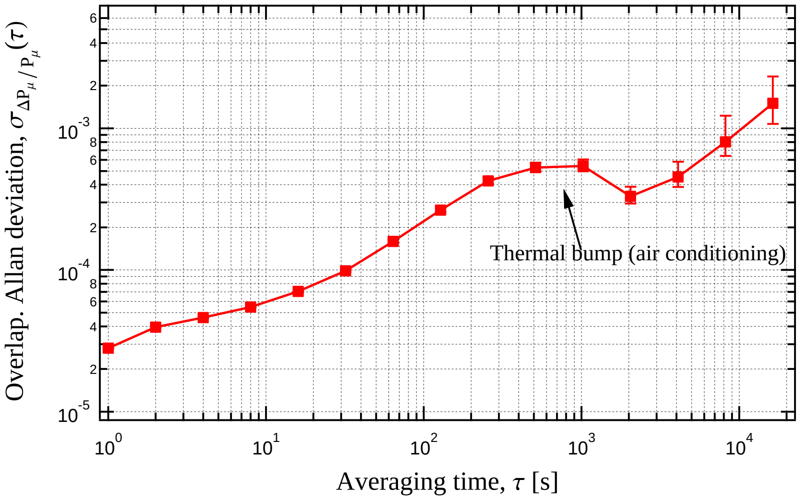

Figure 2.10: *Power stability of the local oscillator.*

2.7 The LO for wall-coated cell clock

In the previous section (cf. Section 2.6), we have seen the details of the LO and its phase noise measurements. For the experiments performed with wall-coated cell (cf. Chapter 5), we used the LO that was termed as *Synthesizer 1* in Section 2.6.1. For further details on this microwave synthesizer see [104, 116]. Figure 2.9 gives the phase noise of Synthesizer 1 at 6.835 GHz carrier frequency. A flicker level of -77 dBrad^2/Hz (at 6.8 GHz Fourier frequency) and a noise floor of -102 dBrad^2/Hz were measured. The phase-noise limited short-term stability, $\sigma_y(\tau)_{PMnoise}$ in a quasi-static model for the square wave modulation with frequency f_m in terms of spectral density is explained in Section 2.6.2 by Eqns. 2.3 & 2.4 [90].

2.8 Conclusions

Two main sources (the optical and microwave) required for DR spectroscopy and clock operation were presented with their respective characteristics. Two types of laser heads, namely - the clock laser head and the AOM laser head were described. The fully assembled clock laser head has an overall volume of < 0.7 dm^3 with a mass of 0.6 kg and the AOM laser head has a volume of < 2.3 dm^3 with a mass of 1.4 kg. Sub-Doppler (saturated absorption) spectroscopy and laser stabilization principles were discussed qualitatively. The complete characteristics of each laser head were detailed along with their influences on the clock instabilities. The laser linewidths of the clock LH and AOM LH are 2.2 MHz and 4.6 MHz, respectively. The frequency stability of these laser heads are $< 5\times10^{-12}\ \tau^{-1/2}$ and $< 8\times10^{-12}\ \tau^{-1/2}$ between 1-100 s. The microwave source was presented with the phase noise measurement technique of cross-correlation, and the influence of this phase noise on the clock especially in the short-term stability was presented quantitatively. For example, at a modulation frequency $f_m = 44$ Hz, the phase noise influence on clock instability is $7.5\times10^{-14}\ \tau^{-14}$. Also, the medium to long-term influence of the power flucutations of the LO was discussed. These sources will be further used in Chapters 5 & 6. The CAD drawings of the Laser Heads are shown in Appendix B.

Chapter 3 Vapor Cells and Magnetron Resonators

> *In science, the credit goes to the man who convinces the world, not to the man to whom the idea occurs.*
> *-Sir Francis Darwin*

At the heart of any Rb DR cell clock, including conventional lamp-pumped rubidium atomic frequency standards (RAFS) [32, 118, 119], a Rb vapor cell is implemented inside a microwave cavity resonator that is tuned to resonate at 6.835 GHz. These cells are usually filled with a droplet of metallic ^{87}Rb and a mixture of buffer gases (to avoid ^{87}Rb atoms in vapor phase from colliding onto the cell walls, as explained in sections 1.3 & 1.5.3) with known and controlled pressure.

In one of our studies, an alternative approach of wall-coating technology instead of buffer gases was adopted with the cells of 14 mm diameter. Cavities developed at Observatorie de Neuchâtel [119] were used in the studies of 14 mm diameter wall-coated cells. In the second approach, to improve the clock performance further, cells with increased dimensions ($\phi = 25$ mm) were evaluated. These cells were filled with buffer gases. In this thesis, new compact magnetron-type cavities that can hold these cells to resonate at the Rb ground state frequency ($\sim$ 6.835 GHz) were developed and studied in detail.

In this chapter we will discuss on the two kinds of aforementioned vapor cells and the microwave cavities.

Note that the evacuated cells ($\phi = 10$ mm) used in our laser heads (cf. Chapter 2) were fabricated at LTF.

3.1 General features of vapor cells

Vapor cells are usually made of borosilicate or quartz glass. In conventional RAFS, these cells are of cylindrical or spherical shape in order to facilitate the fabrication and inserting them in to the microwave cavity resonator. In principle, the two end windows of a cylindrical cell should be flat to avoid any lensing effect with the light propogating along the length of the cell. The cells are cleaned on the inside from any contaminants and are evacuated before filling them with liquid Rb droplet and a mixture of buffer gases (see section 1.5.3 for the explanation of the need of buffer gases). The procedure of cell filling is, in practice customized to particular laboratory or industry. The general techniques on cell fabrication for buffer gas cells can be found in [32, 120–122] and that of the wall-coated cells in [45, 123].

3.2 Vapor cells used in the physics packages

As mentioned above, we study two kinds of cells (wall-coated and BG filled) that are implemented in our clocks and are explained with details in the following sections.

3.2.1 Wall-coated cell

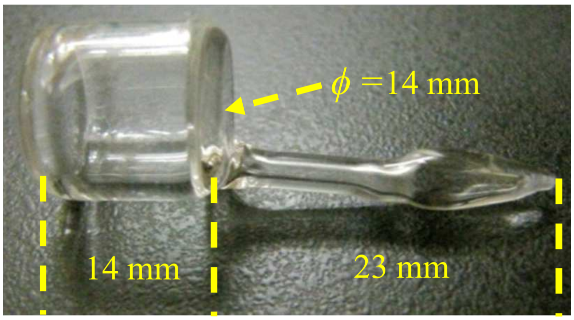

Figure 3.1: *Paraffin-coated cell (V_{WC} = 1.4 cm^3) with a reservoir stem on its right-hand side.*

Figure 3.1 shows the wall-coated cell with an inner volume of ~1.4 cm^3 that is used in our experiments. This cell's inner walls are coated with tetracontane ($C_{40}H_{82}$) [32, 124]. The cell has two distinctive regions; a cell-volume, which holds the vapor of interrogated Rb atoms, and the cell-stem that acts as a reservoir for metallic Rb. The usefulness of the stem is evident by the fact that one can avoid any metallic Rb from accumulating on to the cell walls, which otherwise can degrade the coating and degrade the life-time of the cell and secondly to control the vapor pressure inside the cell volume by controlling the stem temperature. This cell was procured in an external collaboration. In the mean time, LTF has upgraded its cell filling system for the production of wall-coated cells [125].

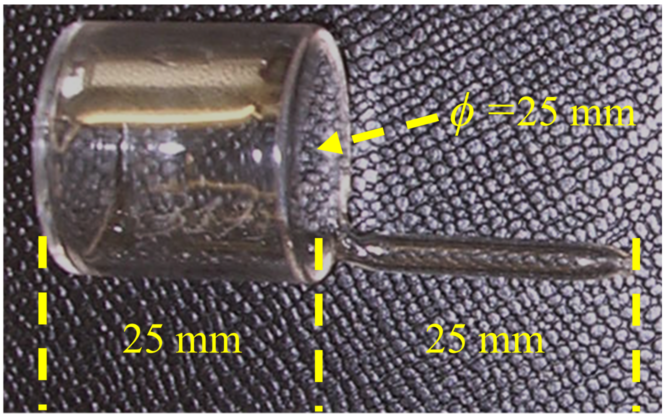

Figure 3.2: *Buffer-gas cell with an inner volume V_{BG} = 9.6 cm^3. The buffer gas mixture has the ratio Ar/N$_2$ = 1.6, with a total pressure of 26 mbar. The stem serves as a reservoir for metallic Rb.*

3.2.2 Buffer-gas cell

The short-term stability is related to the vapor cell size [126], and hence the motivation towards a bigger cell of 25 mm diameter was initiated [127]. Secondly, the buffer gas cell has been selected due to its reliability for long operation life times and success with the previous RAFS. The cells with enriched ^{87}Rb and buffer-gases (argon and nitrogen) were filled (courtesy: M. Pellaton, LTF) using the in-house LTF cell filling system. One ramp of six cells were cleaned and filled. The cells have good optical quality windows and a stem reservoir to have better control on the vapor density of atoms. Figure 3.2 shows a filled and sealed cell having the outer diameter of 25 mm that is used in the spectroscopy and clock studies presented in Chapter 6. The stem is useful to store the metallic Rb and hence to better control the vapor pressure of the Rb inside the cell volume, this also helps to increase the operation life-time of the clock. The design with a bending at the intersection of the stem and the cell allows a larger beam incidence to interrogate a higher number of atoms to get a better signal. An estimation of cell-size influence on clock's short-term stability is presented in the next section (3.2.3).

3.2.3 Cell size influence on clock short-term stability

We do a first approximation for the cell size and its influence on the clock stability *for buffer gas cells*. In this approximation, we consider the similar operating conditions for two different cell dimensions: i.e. the same cell temperatures and the input laser powers. With these considerations, we approximately evaluate the *ratio* of the attainable frequency short-term stability between the two cell dimensions as explained below.

At the clock operating conditions, the DR signal is power broadened due to laser and microwave input intensities, which in turn influences the short-term clock stability. From Eqn. 1.35, the discriminator slope D is inversely proportional to the short-term clock stability. The discriminator D is approximately equal to the ratio between the DR signal amplitude A and the linewidth $\Delta\nu_{1/2}$. With the above considerations, we can write that the linewidth is proportional to the input laser intensity I_L given as,

$$\Delta\nu_{1/2} \propto I_L \sim \frac{1}{a^2}, \tag{3.1}$$

where a is the radius of the vapor cell.

Similarly, the DR signal amplitude is proportional to the input laser intensity I_L and the number of atoms N_{at} in the vapor cell participating to give the signal and hence can be written as,

$$A \propto I_L \cdot N_{at} \sim \frac{1}{a^2} \cdot a^2 \cdot L, \tag{3.2}$$

where L is the length of the vapor cell.

Now, using the above equations 3.1 & 3.2 for discriminator D in the formula of short-term frequency stability, we get an approximated expression for the S/N limited short-term stability that depends on the vapor cell dimensions as,

$$\sigma_y(\tau) \propto \frac{1}{a^2 \cdot L} \tag{3.3}$$

It is important to note that due to the approximations, the above equation (3.3) does not aim to give the estimated short-term stability value, but is helpful only to find the ratios of expected short-term stability between two cell dimensions. Few calculated ratios (σ_A/σ_B) for different cell dimensions are shown in Table 3.1. The bigger cell is considered to be of 25 mm (external) diameter, which is kept constant (referred as Cell B (cf. Fig. 3.2) in Table 3.1) and different dimensions for the other cell (Cell A) are considered. Figure 6.18 shows the measured ratio between two buffer gas cell dimensions that matches well with our calculated value of ‘factor of 5.3’ (first row) in Table 3.1.

Table 3.1: *Short-term stability ratios based on vapor cell dimensions. Cell A's dimensions (inner radius and length) are varied, whereas we consider the fixed dimensions for Cell B (25 mm external diameter cell, cf. Fig. 3.2).*

Cell A		**Cell B**		σ_A/σ_B
a **[mm]**	L **[mm]**	a **[mm]**	L **[mm]**	
6	16	11.5	23	5.3
6	12	11.5	23	7
10	20	11.5	23	1.5
5	10	11.5	23	12.2

3.3 Magnetron resonator cavity theory

Microwave cavities or resonators have a wide array of applications ranging from frequency standards (or atomic clocks) [32, 128], Electron Spin Resonance (ESR) [129], Electron Paramagnetic Resonance (EPR) [130], to Nuclear Magnetic Resonance (NMR) [131]. The field homogeneity, robustness and reliability of these devices makes them well-suited for such applications. For example, in a rubidium standard, a basic cylindrical cavity having TE_{011} uniform mode [128] along the direction of the laser field and the quantization field in the atomic sample region guarantees a good atomic signal. A variant of the cylindrical cavity is a split-ring or slotted-tube resonator [132], which is also known as loop-gap-resonator (LGR) or a magnetron cavity [118, 133]. The volume of a magnetron cavity is at least a factor of three more compact in comparison to that of a traditional cylindrical cavity when using Rb cells of same size. First development of a magnetron cavity that can hold a vapor cell of 14 mm diameter for a portable rubidium cell standard was done at Observatorie Cantonal Neuchâtel (ON) [119, 134]. An LGR is an open-shield resonator whose shape, reminiscent of lump circuit model [129], provides a spatial separation between $\mathbf{E}$ and $\mathbf{B}$ fields on distances significantly shorter than the microwave wavelength. The number of gaps/slots can be increased, and its equivalent circuit can be described by a number of individual inductors and capacities, which is termed as lumped model. The resonator consists of an inner cylinder (i.e. inductor) of radius r and length Z with one or several slots (gap between these slots acts as capacitors). This is coaxially surrounded by a shield tube of radius R ($R > r$). The lumped elements model to estimate the resonance frequency, ν_r is given by [129] [135],

$$\nu_r = \frac{1}{2\pi}\underbrace{\sqrt{\frac{n}{\pi r^2 \varepsilon\mu}\frac{t}{W}}}_{\text{LC}}\underbrace{\sqrt{1+\frac{A_1}{A_2'}}}_{\text{shield}}\underbrace{\sqrt{\frac{1+\Delta Z/Z}{1+\Delta W/W}}}_{\text{fringing}} \tag{3.4}$$

where n is the number of gaps with thickness t, W is the width as illustrated in Fig. 3.3, ϵ and μ are electric permitivity and magnetic permeability of the free space coupling between the electrode gaps, respectively. $A_1 = \pi r^2$ is the cross-sectional area of the inner loop cylinder, $A_2' = \pi[R^2 - (r+W)^2] - nB$, is the area between the outer shield and the inner loop cylinder with B as the area of one support/slab holding an electrode. Z is the physical length of the electrode with ΔZ the equivalent length extension due to the magnetic fringing fields, similarly with a gap width of W, ΔW is the gap width extension due to the electric fringing fields. Mehdizadeh [135] gave simple approximations for the fringing fields as $\Delta Z = 0.18R$ and $\Delta W = 0.54(1 + 0.85\epsilon_r)t$, where ϵ_r is the dielectric constant of the glass cell inside the magnetron [134]. In Eqn. 3.4, we see the contribution due to basic inductor-capacitor (LC) equivalent model, the correction due to the outer shield and the factor influencing due to electric fringing fields extending out of the gap edges [135].

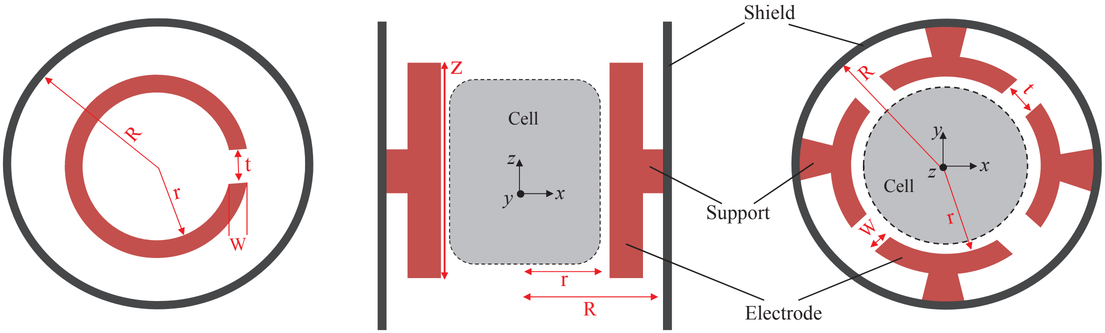

(a) (b) (c)

Figure 3.3: *(a) Basic Loop-Gap Resonator (LGR), (b) magnetron vertical cross section, (c) horizontal cross section with* $n = 4$ *gaps. The metallic electrode pieces and their supports (shown in brick-red) to the external shield are identified. Dashed line indicates the glass cell outer surface.*

The resonant mode electric field is mainly concentrated in the gaps and the magnetic field H_z is confined within the loop perpendicular to the electric field. We are interested in TE_{011}-like mode due to its magnetic field uniformity across the cell. In contrast to the TE_{011} mode in cylindrical cavities, our magnetron cavities have slightly different transverse field distributions, however maintaining the magnetic field uniformity along the cell length, therefore we name this mode from here on as “TE_{011}-like" mode. Equation 3.4 gives a *qualitative* picture to solve for the required resonance frequency, but fails to give a *quantitatively precise* picture. The lumped elements model fails to give a precise estimation of the resonating frequency when the dimensions of the electrodes structure approaches the limit $\approx \lambda/4$ [129]. Due to this, in our enlarged magnetron cavity structure, typically the computed frequency is off by > 3 %, which has to be considered in order to be precise in resonance frequency [136]. Two more characteristics that need to be considered include, the openings of the cavity at two ends of the cylinder to let the laser beam interact with the Rb atoms, and other modes that need to be suppressed at the resonance frequency to have pure TE_{011}-like mode. For a detailed treatment of the above issues the reader is directed to our recently published paper [136].

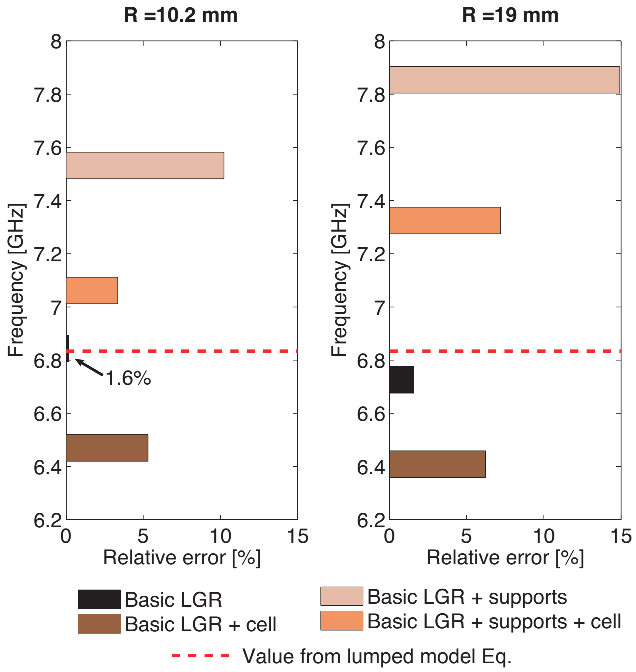

Figure 3.4: *Relative error of the simulated [137] eigenmode frequency of the TE_{011}-like mode with respect to the value calculated by (Eq. 3.4) for four different geometrical parameters. Taken from [136].*

Further analyses were done using the ANSYS high frequency numerical simulations (HFSS) [137] in a collaboration with Laboratory of Electromagnetics and Acoustics (LEMA) - EPFL, Lausanne, Switzerland. Figure 3.4 shows the above discussed effects on the resonant frequency for two different magnetron geometries considering the parameters: $R = 10.2$ mm & 18 mm; $n = 4$ & 6; $t = 0.841$ mm & 2.138 mm; $w = 1.8$ mm & 3.8 mm; $r = 7.5$ mm & 13.5 mm; for 14 mm and 25 mm diameter cells, respectively. The presence of the dielectric glass cell decreases the resonant frequency as expected from Eqn. 3.4, and that of the electrode supports increases the resonant frequency. From Fig. 3.4 one can conclude that the lumped elements model (cf. Eqn. 3.4) gives an estimation error around 10% between 1 to 10 GHz range over variations of t, w, r, R and Z [129], and the error increases with the increase in above dimensions of the cavity structure.

The microwave magnetic field distribution inside the cavity can be characterized by the *filling factor* $\eta^{'}$ and the *field orientation factor* (FOF) ξ. The filling factor – as used in the context of active hydrogen masers – is defined as [32],

$$\eta^{'} = \frac{1}{V_{\text{cell}}} \frac{\left(\int_{V_{\text{cell}}} H_z dV\right)^2}{\int_{V_{\text{cavity}}} |\mathbf{H}|^2 dV}, \tag{3.5}$$

where V_{cell} is the volume of the clock cell occupied by Rb atoms (excluding the reservoir, V_{stem}) and V_{cavity} is the total volume of the cavity. The z-axis is superposed with the external static dc magnetic field (C-field) that defines the quantization axis and is parallel to the laser propagation direction [4,22,115]. Hence, $\eta^{'}$ gives the efficiency ratio of magnetic field energy in H_z (that contributes to the clock signal) to the total microwave standing wave energy inside the cavity. However, for characterizing the Rb cell clock signal, it is more useful to evaluate the homogeneity of the H-field orientation in the cell volume. Therefore, in order to optimize the fraction of the magnetic field component useful for driving the clock transition with respect to the total field energy over the cell volume, we define *field orientation factor* ξ as the ratio of the magnetic field energy in H_z-direction to the total field energy over the entire cell volume as given in [136],

$$\xi = \frac{\int_{V_{\text{cell}}} H_z^2 dV}{\int_{V_{\text{cell}}} |\mathbf{H}|^2 dV}, \tag{3.6}$$

The maximum value of ξ is 1, which implies the absence of σ-Zeeman transitions. In contrast to $\eta^{'}$, ξ accounts only for the useful magnetic field components that are parallel to the C-field and light propagation vector in the interrogation cell volume. Therefore, ξ gives a good estimation for the DR signal quality, especially for buffer gas cells, where alkali atoms can be treated as localized in space during the interrogating time scales. The experimental evaluation of ξ is done for 14 mm wall-coated cell magnetron resonator cavity (cf. Section 3.4.4) and two versions of 25 mm BG-cell magnetron resonators (cf. Sections 3.5.4 & 3.5.5).

3.4 14 mm magnetron resonator cavity

As mentioned earlier, the basic design, construction and characterization of the compact magnetron cavity that can hold a cell of 14 mm diameter was done at ON [119, 134]. These compact cavities were later established for RAFS products of Spectratime, SA, Switzerland.

3.4.1 Cavity assembly

The 14 mm cavity was redesigned with minor modifications to the original prototype; such as direct injection of 6.8 GHz radiation to the cavity and an opening at the rear-end for laser radiation to propagate onto a detector placed outside the cavity. The re-designed cavity assembly is shown in Fig. 3.5.

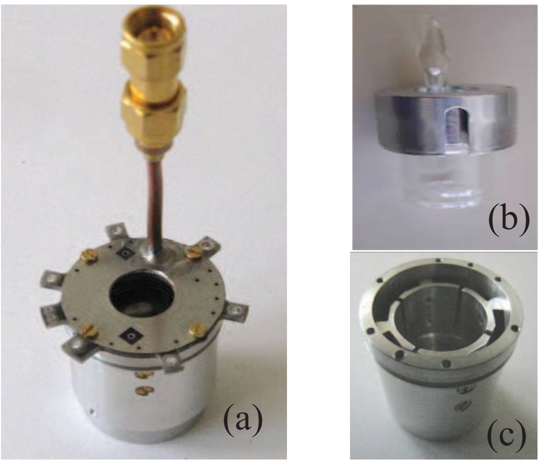

Figure 3.5: *(a) Cavity assembly with the co-axial cable for microwave injection, (b) 14 mm wall-coated cell attached to the tuning-cap and (c) the magnetron design with four electrodes.*

It was noticed that the hole in end cap did not affect the resonant signal, rather only the presence of the glass cell was crucial. Also, coupling efficiency for direct injection of 6.8 GHz was improved by several orders of magnitude, which reduces the power requirements for the microwave source. At a later stage, this cavity was further developed to integrate a lens at the rear-end opening and was used in high-performance clock developments [138].

3.4.2 Tuning and characterization

Tuning a cavity for the right atomic transition frequency is a step-by-step manual process. Influence of dielectricity (ϵ_r) of the glass material (in our case pyrex $\epsilon_r = 4.82$) on the fringing fields of ΔW decreases the resonance frequency ν_r (cf. Eqn. 3.4). Figure 3.6 shows the setup to measure the cavity's resonance frequency ν_r, the Q-factor and the reflection coefficient, $|\Gamma|^2$. The reflection coefficient is defined as the ratio of the reflected power (P_r) to the incident power (P_i), $|\Gamma|^2 = \frac{P_r}{P_i}$. These measurements were done in the ambient laboratory conditions (air) at room temperature of $\approx 21°$C. The RF sweeper gives the output of microwave frequency around 6.835 GHz with an adjustable sweep (maximum of ± 0.5 GHz) that is fed to the cavity through an attenuator and a directional coupler. The cell is positioned inside the cavity by threading inwards, such that the cavity resonates around 6.8 GHz. When the injected microwave frequency is in resonance with the cavity mode, more microwave power is coupled to the cavity, and thus less microwave power is reflected back to the directional coupler and detector. Finally the signal is displayed using an oscilloscope as shown in Fig. 3.6. Typical measured parameters with a 14 mm tuned cavity are: $\nu_r = 6.834$ GHz, Q $= 341$ and absorption coefficient, 1-$|\Gamma|^2 = 76\%$ and a tuned overall cavity height $h = 29$ mm.

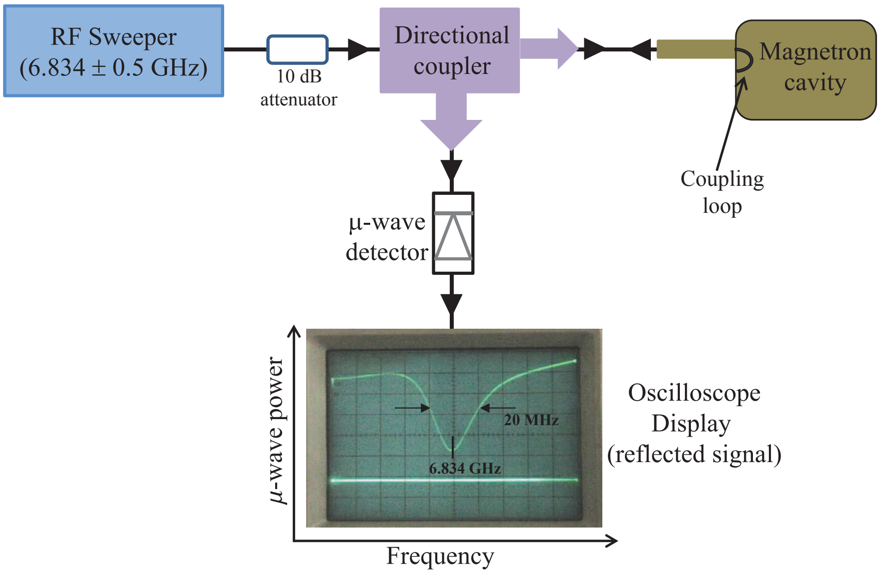

Figure 3.6: *Cavity tuning by reflection method. Oscilloscope display shows the measured parameters of the tuned 14 mm cavity using the wall-coated cell.* $\nu_r = 6.834$ *GHz, Q* $= 341$ *and absorption coefficient, 1-*$|\Gamma|^2 = 76\%$.

3.4.3 Cavity pulling

For the 14 mm magnetron-type cavity, the measured cavity quality factor $Q_c < 350$ (cf. Fig 3.6), the $Q_a \approx 1{\times}10^7$ (cf. Section 5.3.1). Our 14 mm magnetron cavities are made of Aluminum and the measured temperature sensitivity shift $\Delta\nu_c/\Delta T \approx$ +40 kHz/°C. The temperature variations of our cavity around 10^4 s is ≈10 mK and therefore the calculated fractional cavity pulling shift from Eqn. 1.48 is $\Delta\nu_{CP}/\nu_{Rb} < 6.8{\times}10^{-15}$.

3.4.4 Simulation and field mode

Figure 3.7 shows the simulated TE_{011}-like field mode inside the 14 mm magnetron cavity. The magnetron resonator cavity has cylindrical symmetry with two parts; the metallic cap to which the glass cell is attached and the cavity body as shown in Fig. 3.7. The field mode inside the cell is uniform along z-direction, i.e. the laser propagation direction to give a good S/N ratio for the clock signal. The irregularities in the field at the edges of the cell boundaries might influence the clock signal to a lesser extent in a buffer-gas cell and with that of the wall-coated cell, atoms in continuous motion give the average of the field distribution as a clock-signal.

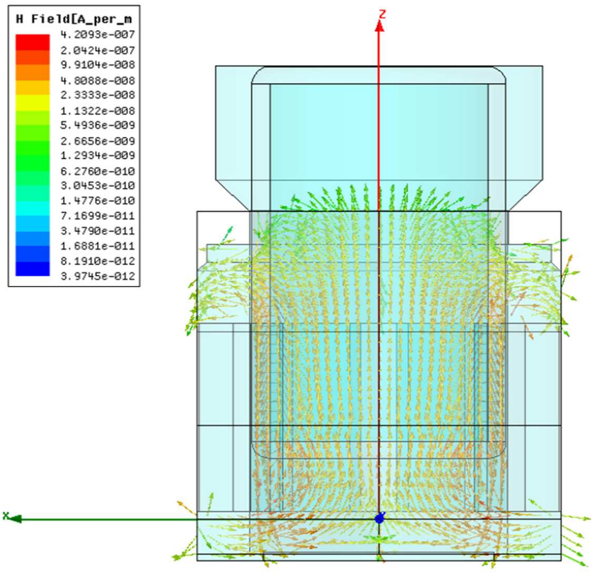

Figure 3.7: *Eigen mode simulation showing TE_{011}-mode. Courtesy: LEMA-EPFL.*

We assume that the applied static magnetic field (i.e. the C-field) is uniform and parallel to the laser propagation direction along z-axis throught the length of the cavity. In an external static (directional, z-axis) magnetic field, the hyperfine levels split into their corresponding Zeeman sub-levels according to Eqn. 1.1. Due to the selection rules ($\Delta \mathrm{m}_F = 0, \pm 1$) for the microwave transition, the projection of the H_z field inside the cavity on to the static C-field gives the π-transitions ($\Delta \mathrm{m}_F = 0$), whereas the σ-transitions ($\Delta \mathrm{m}_F = \pm 1$) are due to the projection of the transverse fields ($\mathrm{H_t} = \sqrt{\mathrm{H_x^2} + \mathrm{H_y^2}}$, radial field component) on to the C-field. We are mainly interested in the π-transitions that are obtained by the homogeneity of the H_z field over the cell volume.

In order to characterize the H_z field inside the cell, we quantify for the FOF (ξ) by measuring the Zeeman transitions of ^{87}Rb atoms in the clock cell situated inside the resonant magnetron cavity. The input microwave power needs to be low, such as not to saturate the microwave Zeeman transitions. Figure 3.8 shows a span of all possible ^{87}Rb Zeeman transitions between the two ground states ($^5S_{1/2}$ $\mathrm{F}_g = 1$ and $\mathrm{F}_g = 2$) (cf. Fig. 1.3). The laser was stabilized to ^{87}Rb $\mathrm{F}_g = 2 \rightarrow \mathrm{F}_e = 3$ transition (cf. Fig 2.3) with an incident intensity of 36 μW/mm^2, a z-directional C-field of ~40 mG was applied and a microwave power of -40 dBm was injected into the cavity.

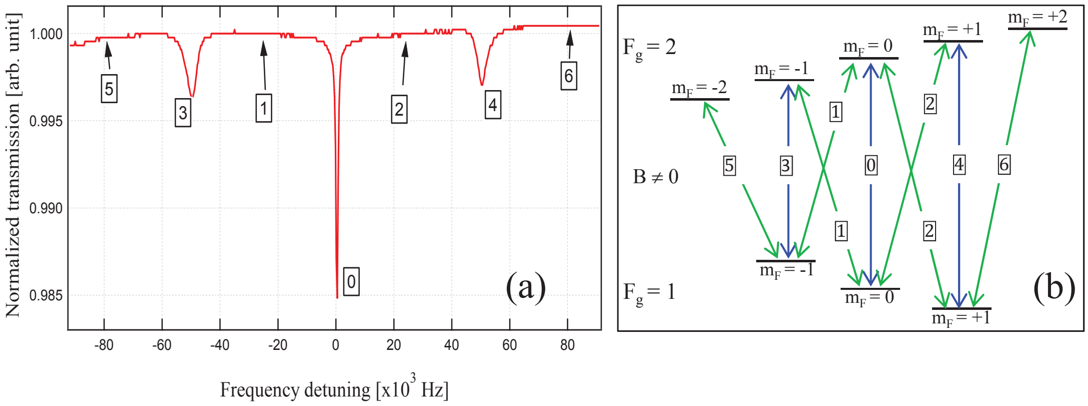

Figure 3.8: *(a) Zeeman transitions between ^{87}Rb ground states ($^5S_{1/2}$ $F_g=1 \leftrightarrow F_g=2$) in the 14 mm wall-coated cell inside the magnetron cavity. Suppression of sigma transitions (arrows) indicate the presence of uniform microwave magnetic field along the laser propogation axis (z-axis). (b) shows the Zeeman transitions for corresponding peaks in (a).*

The experimental field orientation factor, ξ_{exp} is determined using the equation:

$$\xi_{exp} = \frac{\int S_\pi}{\int S_\pi + \int S_\sigma} \tag{3.7}$$

where $\int S_\pi$ and $\int S_\sigma$ are the integrated signal strengths over all the corresponding Lorentzian peaks for $\Delta m_F = 0$ and $\Delta m_F = \pm 1$, respectively. These signal strengths

S_i are proportional to H_z^2, for small microwave powers [85] and thus Eq. 3.7 is an experimental measure of the FOF (Eq. 3.6). The value of FOF for 14 mm cavity with wall-coated cell calculated from the data of Fig. 3.8(a) is $\xi^W_{exp} = 0.993$. This proves that in 14 mm cavity, the TE_{011}-like cavity mode has a highly uniform magnetic field geometry oriented almost exclusively parallel to the laser propagating direction over the entire cell volume.

3.5 25 mm magnetron resonator cavities

Two 25 mm cavities were designed, fabricated and utilized in building the clocks. The first ***25 mm prototype*** cavity was designed and fabricated based only on the calculations using LGR lumped model (Eqn. 3.4). Furthermore, in order to crosscheck the field mode inside the cavity, numerical simulations were done (see Section 3.5.4) and found the mode is not TE, but a TM mode. Hence a new cavity was developed by first performing the geometrical optimization via simulations to get the desired TE_{011}-like mode, and then was fabricated accordingly, which we call as the ***25 mm optimized*** cavity. Both the cavities (prototype and optimized) are made of aluminum with alodine coating treatment (for better surface conductivity and corrosion resistance), and are similar in design, however they differ only in the value of gap-width thickness between the electrodes t, and hence in resonant frequencies of TE and TM modes as contrasted in Table 3.2.

Furthermore, in order to crosscheck the validity of the lumped model (Eqn. 3.4), the value of $t = 2.55$ mm was substituted in Eq. 3.4 and we found that the resonant frequency $\nu_r = 6.3$ GHz, giving an estimation error of 8 % from 6.834 GHz (the required Rb resonant frequency).

Table 3.2: *Geometrical parameters of the two 25 mm cavities. The values of* prototype cavity *were calculated using Eqn. 3.4 and the values of the* Optimized cavity *are the ones by HFSS numerical simulation.*

Cavity type	**n**	**R [mm]**	**r [mm]**	**t [mm]**	**W [mm]**	**TE [GHz]**	**TM [GHz]**
25 mm prototype	6	18	12.75	**3.48**	3.65	7.4	6.7
25 mm optimized	6	18	12.75	**2.55**	3.65	6.8	7.1

3.5.1 Cavity assembly

The cavity assemblies for both of the 25 mm cavities are similar, except for one prominent change of the gap-width thickness t. The fabricated parts of one of the cavities are shown in Fig. 3.9. The resonator cavity has a compact volume of < 45 cm^3 (with a cell of 12 cm^3), in comparison to a fundamental-mode cylindrical cavity that would have a volume of $\simeq 140$ cm^3 (to accommodate a similar vapor cell). In Fig. 3.9, the front- and rear-end caps have openings of ≈ 20 mm for the laser beam propogation in order to interact with maximum number of atoms covering the volume of the cell. The rear-end cap also holds a plano-convex lens (not shown in the figure) that focuses the laser beam on to a photodetector. The two end openings and the presence of the lens however influence the resonance frequency and the field mode inside the cavity (see Section 3.5.4). In the first 25 mm prototype, these details were not taken in to account as the design was based only on the lumped model approach. However, the further improvement of 25 mm optimized cavity considered these effects (see Section 3.5.5).

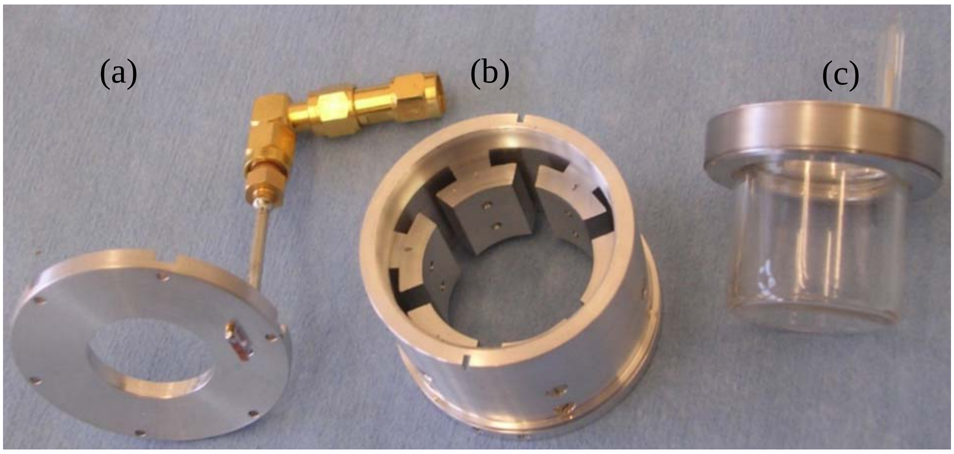

Figure 3.9: *(a) The rear-end cap with microwave coupling coaxial cable and microwave coupling loop, a plano-convex lens (not shown here) is mounted inside the hole for focussing the laser beam on to the detector (b) cavity structure with six-electrodes, and (c) 25 mm cell attached to the tuning cap.*

3.5.2 Tuning and characterization of 25 mm cavities

The experimental setup and method is similar to the tuning of the 14 mm cavity (cf. Section 3.4.2). Tuned parameters of the 25 mm prototype cavity and the 25 mm optimized cavity are given in Table 3.3. The cavity-Q < 100 ensures that the effect of cavity pulling is negligible for RAFS to reach the stability levels below 1×10^{-14} in medium to long-term time scales [32, 139].

Table 3.3: *Tuned parameters of 25 mm cavities.*

Cavity type	$\boldsymbol{\nu_r}$ [GHz]	**Cavity-Q**	1-$\|\boldsymbol{\Gamma}\|^2$ [%]	**h [mm]**
25 mm prototype	6.834	~79.6	35	33.1
25 mm optimized	6.834	~81.8	93	34.2

3.5.3 Cavity pulling

For the 25 mm magnetron-type cavities studied in this thesis, the measured cavity quality factor $Q_c < 100$ (cf. Table 3.3), the $Q_a \approx 2\times10^7$ (cf. Section 6.1.1). Our magnetron cavities are made of Aluminum, the measured temperature sensitivity shift $\Delta\nu_c/\Delta T \approx +7$ kHz/°C. The temperature variations of our cavity around 10^4 s is ≈5 mK and therefore the calculated fractional cavity pulling shift from Eqn. 1.48 is $\Delta\nu_{CP}/\nu_{Rb} < 1.5\times10^{-16}$.

3.5.4 Field mode and Zeemans: 25 mm prototype cavity

The HFSS eigen mode simulations for the 25 mm prototype resonator cavity gave us the insight into the resonating modes present in the cavity. At a tuned height of $h = 33.1$ mm, the H-field distribution around 6.8 GHz is shown in Fig. 3.10. This is a TM-like mode with field mostly oriented along H_t direction and is sensitive to external influences: for example, moving any object (or even hand) close to the aperture openings shifted the frequency upwards or downwards depending on the position of the hand with respect to the end-cap hole. We term this as "hand effect". This effect was more pronounced at the rear-end cap due to the presence of the lens, which has a high dielectric constant of 10.7. The simulations however revealed another mode around 7.4 GHz, which was TE_{011}-like mode. It was noticed that the hand effect was prominently influencing the TM-like mode but not that of the TE-like mode.

The Zeeman measurements (cf. Fig. 3.11) further validate the field mode and inhomogeneity inside the cavity. For these measurements, the laser was stabilized to $F_g=1 \rightarrow F_e=01CO$ transition (cf. Fig 2.3) with an input intensity of 60 μW/mm^2, a

C-field of ∼80 mG was applied and a microwave power of -10 dBm was input into the cavity. From Fig. 3.11 we compute the experimental FOF for the 25 mm *prototype* cavity as, $\xi^{P}_{exp} = 0.26$. This low value reflects the TM mode with prominent H_t components. The inhomogenous broadening observed at the extreme sigma transitions are due to the C-field inhomogenites.

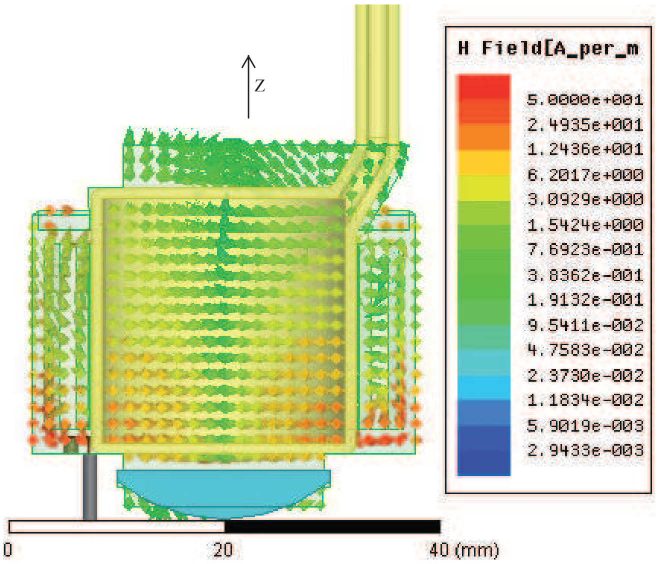

Figure 3.10: *Simulation of the field mode inside the 25 mm cavity, showing the inhomogeneous TM-like mode along the laser propogation direction (z-axis).*

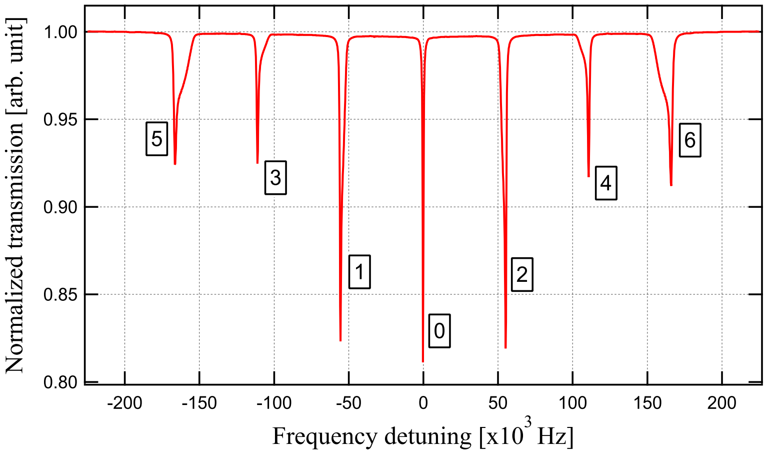

Figure 3.11: *The Zeeman signals showing the inhomogeneity in the microwave field inside the 25 mm prototype cavity. The labels associated for particular transitions are as defined in Fig. 3.8.*

3.5.5 Field mode and Zeemans: 25 mm optimized cavity

Table 3.4: *Simulated microwave performance of the optimized magnetron cavity.*

Parameter	**Symbol**	**Value**
Resonant frequency [GHz]	ν_r	6.831
Filling factor	$\eta^{'}$	0.136
Field orientation factor	ξ	0.877
Volume [dm^3]	V_{cavity}	0.044
Q-factor (unloaded)[a]	Q_{o}	488
Q-factor (loaded)[b]	Q_{l}	185

---

[a] From eigenmode simulation

[b] Excitation, holes and reservoir included

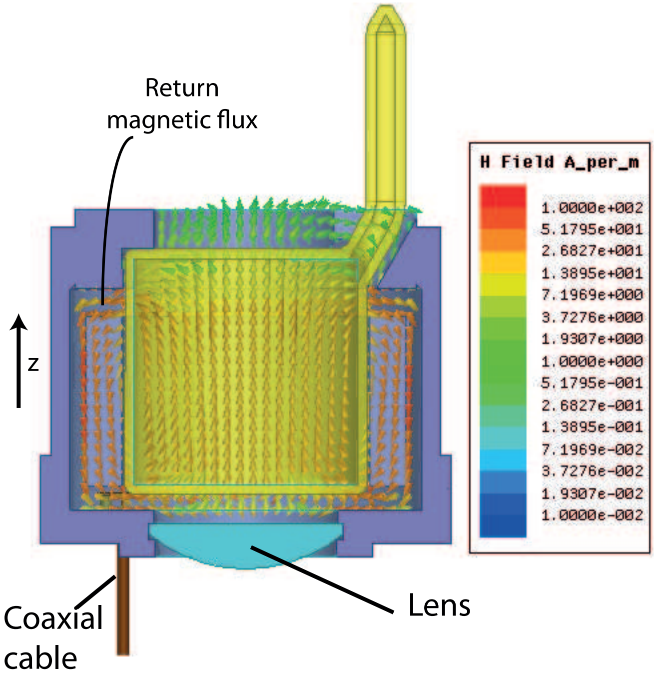

Figure 3.12: *25 mm cavity simulation of the modified structure by increasing the electrode gap widths.*

As shown before in Table 3.2, the proper dimensions of the cavities were chosen by optimizing the geometrical parameters, such that the TE-like mode resonating around 7.4 GHz was moved to resonate at 6.8 GHz. The simulated results of the performances of the optimized cavity are shown in Table 3.4. In fact, the value of

η' can be improved by increasing the return flux cross-section (see Fig. 3.12), but at the price of a larger shield radius. However, our design focuses on the compactness of the structure, and also provides an excellent working behavior because of its high ξ as shown in Fig 3.13. Finally, the loaded Q-factor ($Q_l < 200$) meets the passive atomic clocks requirements [32] and ensures a negligible cavity pulling contribution on the atomic signal [139]. The loaded Q-factor Q_l is less than half the value of the unloaded Q-factor because of the presence of the apertures for the optical interaction that induce losses for the microwave power. Figure 3.12 shows the TE$_{011}$-like mode resonating at 6.834 GHz with the overall cavity height $h = 33.7$ mm and $t = 2.5$ mm.

For further validation of the TE$_{011}$-like cavity mode, the Zeeman measurements were done (cf. Fig.3.13). For these measurements, the laser was stabilized to F$_g$ = 2 → F$_e$ = 13CO transition (cf. Section 2.3) with an input intensity of ~25 μW/mm^2, a C-field of ~44 mG was applied and a microwave power of -28 dBm was input into the cavity. From Fig. 3.11, the experimental value of FOF for the *optimized* cavity is $\xi^O_{exp} = 0.868$. The inhomogenous broadening observed at the extreme sigma transitions are due to the C-field inhomogenities. Notice that the required input micowave power in the optimized cavity as compared to the prototype cavity is reduced by about a factor of three at comparable signal contrast. This is due to exclusive orientiation of the microwave magnetic field along the C-field and that of the laser propagation z-direction.

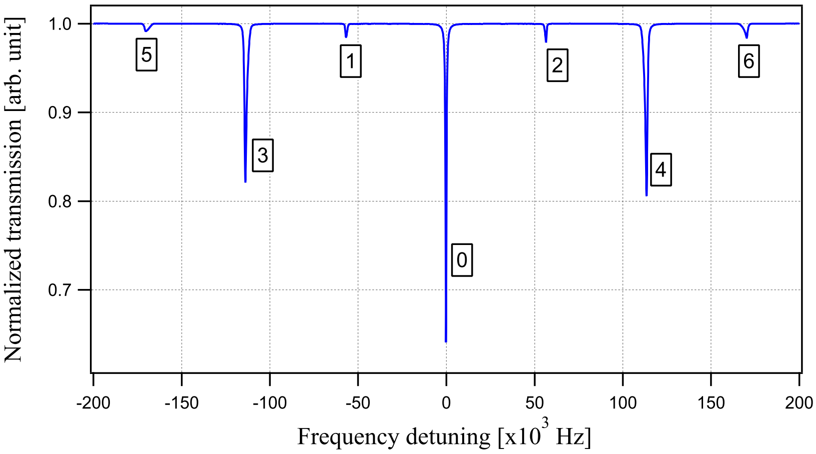

Figure 3.13: *Zeeman transitions for an applied C-field of 44 mG. Suppression of sigma transitions indicate the uniform TE$_{011}$-mode.*

3.6 Field modes comparison and influence on the clock stability

We compare two similar 25 mm cavities; the protoype cavity and the optimized cavity. Two cavities differ in their field modes with one having a TM-like mode and the other having the required TE-like mode. The characterization of these two cavities by Zeeman measurements also gave us the FOF (ξ) values that one can compare directly to know the field orientation along the Z-direction inside the cavity. The FOF of the optimized cavity, $\xi^{O}_{exp} = 0.868$ is more than a factor of three better compared with that of the FOF of the prototype cavity with $\xi^{P}_{exp} = 0.26$. As a first approximation, with a linear influence of the FOF on the clock stabilities (Allan deviation), we expect to have a difference of a factor of three between the two phyiscs packages. In Chapter 6 we do a quantitative treatment of the stabilities and compare the results between two cavities.

3.7 Conclusions

In this chapter, we have seen the vapor cells used in the thesis for spectroscopic and clock studies: 14 mm diameter wall-coated with an overall volume of $\sim$ 2.1 cm^3, and 25 mm diameter buffer-gas cell with an overall volume of $\sim$ 12 cm^3. Two types of compact magnetron cavities, one accommodating the 14 mm cell with four electrodes with a volume of 8 cm^3 and the other that was newly developed with six-electrodes having a volume of only 45 cm^3, which can hold the enlarged 25 mm cells and resonates at the ^{87}Rb ground state frequency, were presented. The field modes of these cavities with the aid of simulations were shown, and then were also characterized by Zeeman measurements introducing a new terminology of Field Orientation Factor (ξ). The 14 mm cavity Zeemans measured with a wall-coated cell shows the ξ = 99% and the optimized 25 mm cavity measured with a BG cell shows the ξ = 87%. The 25 mm prototype cavity however does not posses the required TE mode (uniform field along the Z-axis), but thanks to the simulations this was rectified in the 25 mm optimized cavity, thereby improving the FOF by approximately a factor of three. The input power required for the optimized cavity (-28 dBm) is also improved by a factor of three as compared to the power required by the prototype cavity (-10 dBm). The CAD drawings of the magnetron-type microwave resonator cavities are shown in Appendix B.

The next chapter explains how these components are integrated in a physics package and used in DR spectroscopic and clock experiments.

Chapter 4 The Experimental Setup

> *An experiment is a question which science poses to Nature and a measurement is the recording of Nature's answer.*
> *-Max Planck*

This chapter gives the details on the general clock and spectroscopic experimental setup used in this thesis. In Chapter 2, we have seen the two important sources required for double-resonance scheme: (i) the laser head(s) (in Section 2.2) and (ii) the Local Oscillator (or 6.8 GHz microwave synthesizer, in Section 2.6). Here, we will see how these two sources are integrated in an overall experimental scheme (cf. Section 4.1). Another important component of the setup is the Physics Package, which includes: (a) the ^{87}Rb cells (either with inner walls coated (cf. Section 3.2.1) or filled with buffer gases (cf. Section 3.2.2) and (b) these cells are mounted inside the microwave cavities resonating at $\sim$ 6.835 GHz (cf. Sections 3.4 & 3.5). The details on two physics packages are explained in Section 4.2. Furthermore, in order to minimize the impact of external magnetic fluctuations on the clock transition, magnetic shields were required and the characterization of these shields are explained in Section 4.5). Finally, the setup breadboard is shown in Section 4.6.

4.1 Schematic

The schematics of the clock experimental setup is shown in Fig. 4.1 and is explained as follows:

In total five modules are used: Laser Head (LH) module, Physics Package (PP) module, Local Oscillator (LO) module, Detection module and clock stability measurement module. The LH module[1] represents mainly the clock laser head, whereas, the AOM laser head is optional when detuning is required to suppress the light-shift effect in the clock cell.

---

[1] The LHs use reference ^{87}Rb evacuated cell for laser frequency stabilization as explained in Section 2.3.

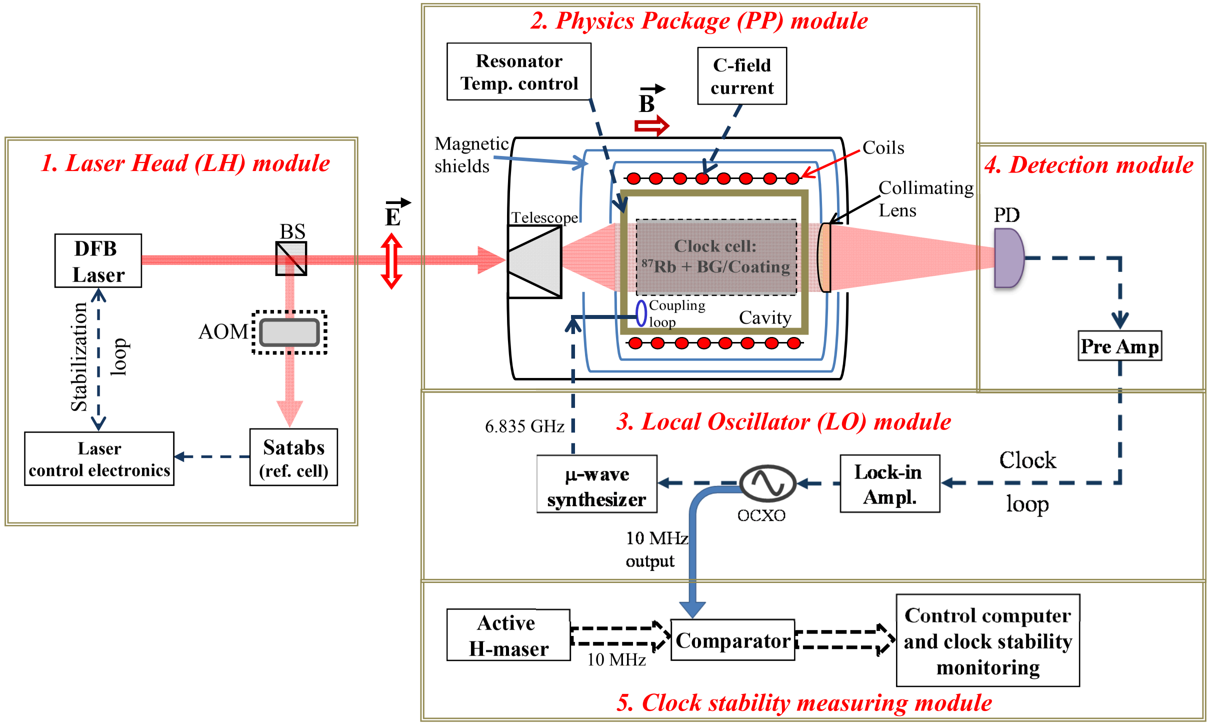

Figure 4.1: *Schematic of the clock experimental setup. Five modules include: Laser Head (LH), Physics Package (PP), Local Oscillator (LO), Detection and clock stability measuring module. The LH module includes clock laser head and the AOM laser head is optional when detuning is required to suppress the light-shift effect. At the heart of the PP module is the clock cell:* ^{87}*Rb atoms either in wall-coated cell or buffer-gas cell. The LO module generates 6.835 GHz for* ^{87}*Rb clock transition interrogation. The detection module has a photodetector and preamplifier electronics. Once the clock loop is closed, the 10 MHz signals from the LO module and the active Hydrogen maser are compared and the stability is recorded using a computer interface. For DR spectroscopy, the "clock loop" is not closed, instead the output of the detection module is directly monitored using an oscilloscope. The laser electric field,* $\vec{E}$ *(linearly polarized) and the dc magnetic field,* $\vec{B}$ *directions are indicated. The dashed-line arrows indicate the electrical connections.*

The PP module consists of the clock cell (^{87}Rb atoms either in wall-coated cell (Chapter 5) or buffer-gas cell (Chapter 6)), the magnetron resonator cavity, C-field coils in order to lift the degenerancy of hyperfine ground states and magnetic shields to suppress the perturbation due to external magnetic fluctuations (cf. Section 4.5). The LO module consists of an Oven Controlled Crystal Oscillator (OCXO), and the microwave synthesis chain to generate 6.835 GHz for ^{87}Rb clock transition interrogation. The detection module has a photodetector and preamplifier electronics. The amplified signal is fed to a synchronous detector that generates an error signal by operating at the modulation frequency f_m, which is used to lock the crystal oscillator to the atomic resonance frequency. Once the clock loop is closed, the stabilized 10 MHz output from the LO module is compared with the 10 MHz signal from an active Hydrogen maser and the stability is recorded using a computer interface in the clock stability measuring module. For DR spectroscopy, the “clock loop" is not closed, instead the output of the detection module is directly monitored using an oscilloscope.

Though the experimental setup is generic, it is worth clarifying here that two PPs were studied in this thesis: (i) 14 mm wall-coated cell PP (Chapter 5), (ii) 25 mm cell in the optimized cavity PP (Chapter 6). Two microwave synthesizers were used (i) one for the wall-coated cell studies (characteristics is given in Chapter 5 (Section 2.7)) and (ii) the second for 25 mm cell studies (the characteristics of this LO was already explained in Chapter 2 (Section 2.6). The basic differences between these two LOs is that the one used for 25 mm cell studies is an improved version with a lower phase noise [51, 107] as compared with the one used for 14 mm wall-coated studies [116]. This improvement was required as we aim at the high-performances with 25 mm cell PPs.

4.2 Assembled physics packages (PP)

Here we discuss the two physics packages: one for the wall-coated cell and the other for the enlarged buffer gas cell.

4.3 Wall-coated cell PP

Figure 4.2 shows the details of wall-coated cell PP. The 14 mm wall-coated cell along with the tuned magnetron cavity is mounted inside a thermal isolation and the delrin holder and the C-field coils are wound around this assembly. At the rear end of the PP, the microwave coupling co-axial cable with the SMA connector for the direct 6.8 GHz coupling, and the electrical connections for the control heater and the C-field coils are shown. This entire assembly is mounted inside the first magnetic shield that is held inside a delrin holder surrounded by the second magnetic shield (cf. Fig. 4.2(c)). This picture also shows the stem heater and the electrical control connections. The laser beam has a Gaussian profile with an area of ≈ 2.8 mm^2 that enters the clock cell in the PP through the stem side and exits at the microwave cable side.

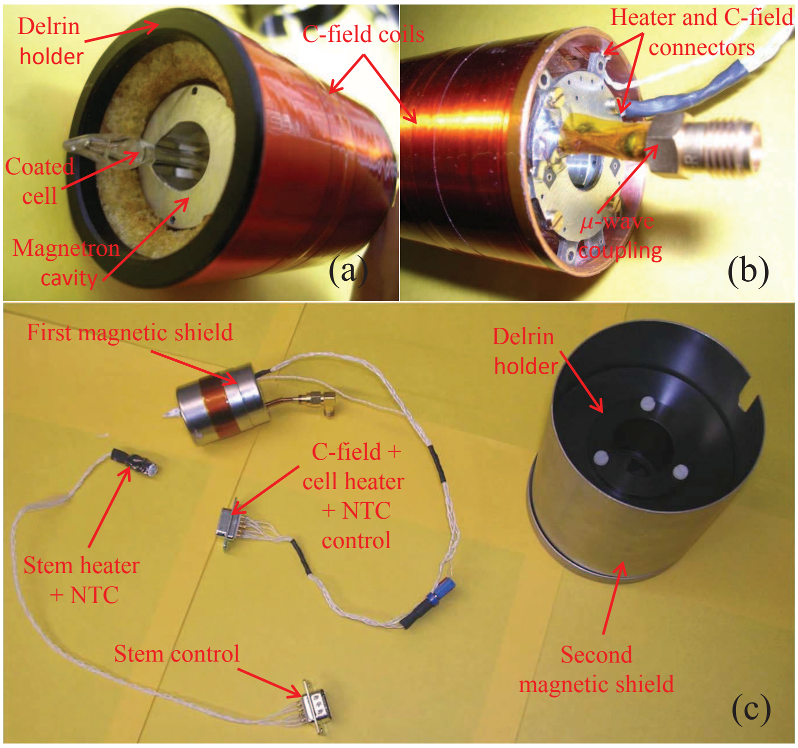

Figure 4.2: *Assembled wall-coated physics package (PP). (a) 14 mm wall-coated cell inside the magnetron cavity that is mounted inside the delrin holder and the C-field coils are wound around this assembly. (b) The rear end of the PP showing the electrical connectors and the microwave coupling co-axial cable, and (c) The clock wall-coated cell and the cavity along with C-field coils are mounted inside the first and second magnetic shields. The control electrical connections for cell volume and stem temperatures and C-field current are shown. The laser beam enters the clock cell through the stem side and exits at the microwave cable side.*

4.4 Buffer gas cell PP

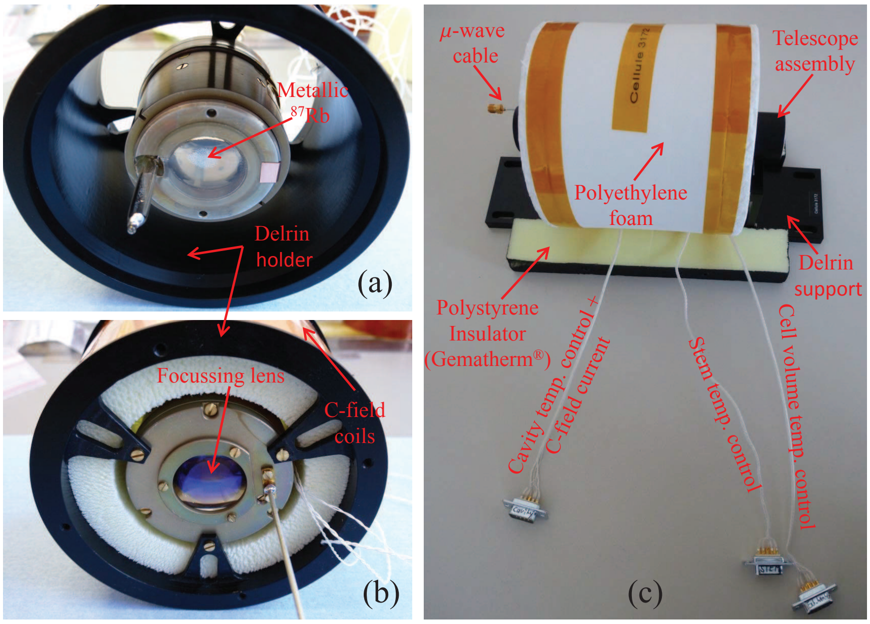

Figure 4.3: *Assembled enlarged buffer gas cell physics package (PP). (a) The assembled and tuned 25 mm cavity. Notice the Rb droplets at the cell window. This influences the clock stability, especially in the long-term equilibrium (cf. Section 6.4.3). The delrin holder is used to reduce the thermal conductivity. (b) The rear end of the cavity showing the focussing lens that helps in focussing the laser beam on to the photodiode and (c) Assembled PP with C-field coils and magnetic shields. Control electrical connections for cell volume and stem temperatures and C-field current are shown. At the laser entrance side, a telescope assembly expands the beam to interrogate the atoms in the entire cell area.*

Figure 4.3 shows the fully assembled Physics Package (PP) with 25 mm prototype cavity. The design and construction for 25 mm optimized cavity is identical to this. This includes the Rb cell, the compact magnetron cavity, the C-field coils and μ-metal magnetic shields. The electrical connections in order to control the temperatures and C-field current are also seen. In Fig. 4.3, the telescope assembly expands the laser beam uniformly to have a flat beam to interrogate the atoms covering almost the entire area of the cell cross-section ($\approx$ 4.91 cm^2). The μ-wave coaxial cable serves to inject the 6.834 GHz microwaves. A polyethylene foam having the thermal conductivity of 39$\times$10^{-3} W/m.K is wound around the second magnetic shield (see Fig. 4.3(c)) to maintain good thermal homogeneity across the physics package. The outer polystyrene insulator (Gematherm®) covering ensures a thermal homogeneity, also serves as a thermal insulator for external variations and attenuates the air currents that occur, for example due to air conditioning effects. For a thickness of 20 mm at 283 K, the thermal conductivity of this insulator is only 36×10^{-3} W/m.K and almost similar compared with the thermal conductance of air 25×10^{-3} W/m.K, however the air convection losses are reduced by this insulator. The base part of the 3D box alone is shown here. The overall physics package (excluding the polystyrene insulator) has a volume of < 0.8 dm^3 and mass of < 1.4 kg.

4.5 Magnetic shielding factor

Though the clock transition frequency in first order is unaffected by fluctuations of magnetic fields, the second order fluctuations do perturb its frequency and hence it is necessary to suppress them as explained in Section 1.5.1. In each of our physics packages, one for the wall-coated cell clock (Chapter 5) and other for buffer-gas cell clock (Chapter 6), two layers of magnetic μ-metal shieldings were used. The measured values of the longitudinal shielding factors for both the PPs are approximately the same. Here we explain the procedure to measure the longitudinal shielding factor by considering the case of 25 mm PP.

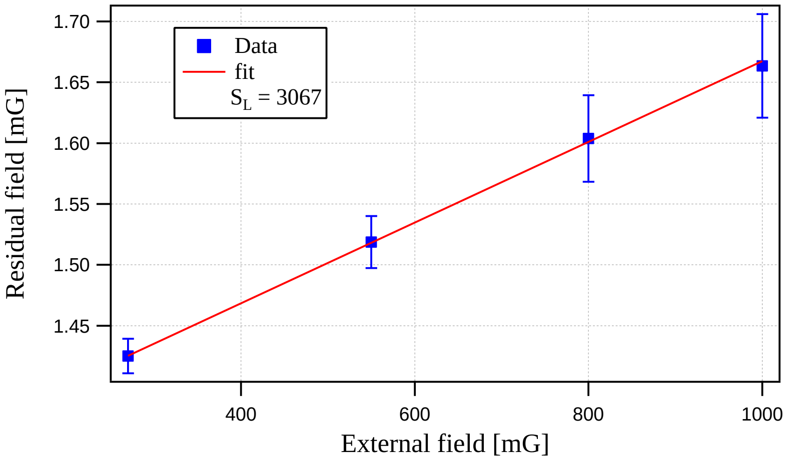

Figure 4.4: *Measured shielding factor for two μ-metal cylindrical shields using Helmholtz coils. Inverse of the slope gives the attenuation factor or the shielding factor.*

The inner shield has the dimensions of radius $r = 44$ mm, thickness $t = 0.8$ mm and length $L = 52$ mm and the second (outer) shield has the dimensions of $r = 49$ mm, $t = 0.8$ mm and the length $L = 100$ mm. The shielding factor measurements were done with the aid of Helmholtz coils. Three set of coils mutually orthogonal to eachother (in x-, y- and z-axes) were used to apply a known external field on the physics package. The zeeman spectra were then recorded as a function of C-field values. By extrapolating the shift of zeemans to the zero C-field value, one gets the shift and the associated remnant (or residual) field acting on the atoms; this gives the indication of the suppression of the external field by the magnetic shields. Repeating this procedure for different external field values, the longitudinal shielding factor, S_L can be known, which has a linear behaviour as shown in Fig. 4.4. Measured longitudinal shielding factor S_L=‘3067’ or $\approx$ 70 dB, which implies that the external magnetic variations are attenuated by this factor.

4.5.1 Influence on clock instability

From Section 1.5.1, we know that the perturbation to the clock signal can occur due to fluctuations in the applied quantization magnetic field $\mathbf{B}_0$, the residual field $\mathbf{B}_r$ (at zero external field) and the noise field of magnetic shields $\mathbf{B}_s$. We apply, typically a quantization field (C-field) of $\mathbf{B}_0 \approx 40$ mG, and the measured relative stability of this field due to resonator control electronics is $\sigma_{\Delta B_0/B_0}(\tau) < 10^{-6}$ for time averages up to 10^5 s, which implies $\sigma_{B_0}(\tau) = 40$ nG. We measured a residual magnetic field $\mathbf{B}_r \approx 1.3$ mG at zero external field and with a measured shielding factor of 3067, we can assume $\sigma_{B_r}(\tau) \approx 0.4$ μG. From [93] and [140], for our external shield with radius $r = 49$ mm and thickness $t = 0.8$ mm, the influence due to the magnetic shield noise is estimated as $\sigma_{B_s}(\tau) \approx 132$ pG. From Eqn. 1.41, and the above values, the total influence due to magnetic variations on clock frequency due to second order magnetic variation is $\sigma_y(\tau) \approx 2.7\times10^{-15}$ up to $\tau = 10^5$ s, however this value can degrade to the level of 10^{-14} in pertrubed geomagnetic conditions.

4.6 Setup breadboard

A complete clock breadboard is shown in Fig. 4.5. The physics package shown in this breadboard is that of 25 mm prototype cavity. However, the 25 mm optimized cavity PP also has the same overall dimensions. The PP control electrical connections to the Resonator Control Electronics (RCEs) and the 780 nm laser beam (linearly polarized) path of the clock laser head are shown. Optional AOM laser head is not in operation (in the picture). During its usage, the optics (mirrors and attenuators) can be arranged to align the beam output from AOM LH to interrogate the atoms in the PP.

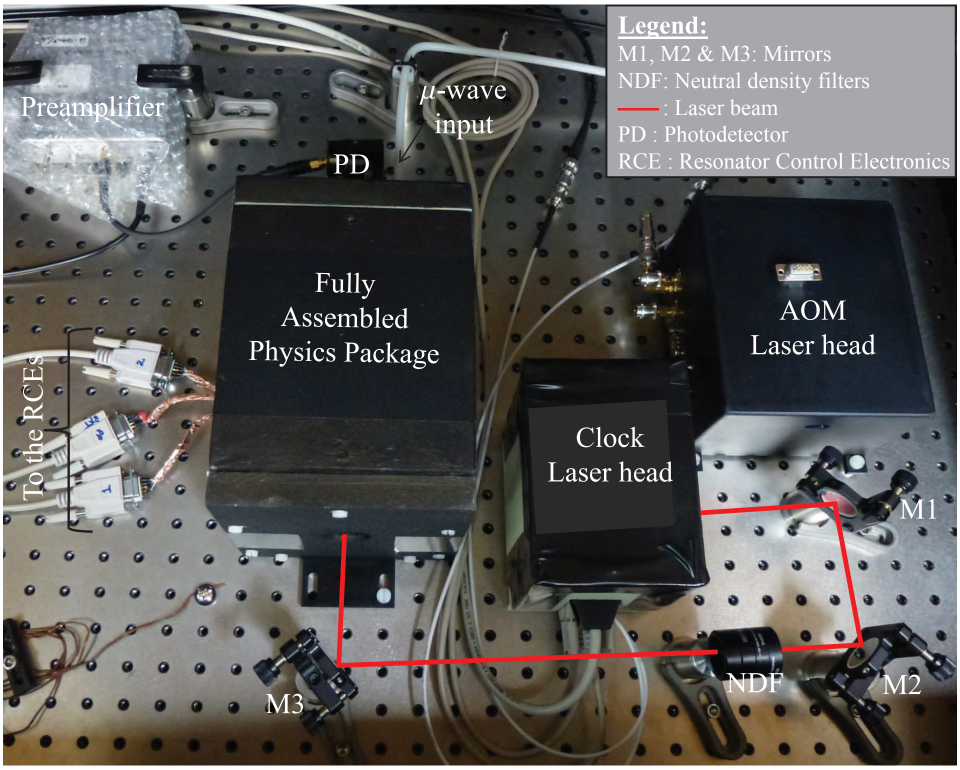

Figure 4.5: *Experimental breadboard showing the Physics Package, the clock laser head and the AOM laser head. The laser beam path is seen along with neutral density filters in order to reduce the laser intensity to the optimized value. The preamplifier electronics box connects the photodetector and the microwave synthesizer (not in the picture). This setup corresponds to the block scheme presented in Fig. 4.1.*

4.7 Conclusions

In this chapter, we have seen the longitudinal shielding factor measurements with two μ-metal shields and the estimation of the influence of magnetic variations on the clock transition. Two shields give a longitudinal magnetic shielding factor of about 3000 and the overall influence on clock transition due to second order magnetic variations is estimated to be at the level of $\sim 3\times10^{-15}$ at the time scales up to one day. The fully assembled PP for the 25 mm diameter cell has an overall volume of < 0.8 dm^3 with a mass of < 1.4 kg. A generic experimental schematic (for DR clock and spectroscopy) with all the components was shown and explained along with the overall setup breadboard. This experimental schematic will be used for the studies of 14 mm wall-coated cell and the 25 mm buffer gas cells in Chapter 5 and Chapter 6, respectively. The CAD drawings of the Physics Packages are shown in Appendix B.

Chapter 5 Spectroscopy and Clock with Wall-Coated Cell

Everything in the Universe takes time to be the way it is, even the time!
-Thejesh Bandi

We recall here that although the idea to use wall-coated cells in an atomic frequency standard was suggested by Robinson [35] in the late 1950's, it was not realized due to the limitations in operating temperatures of such cells (incompatible with the use of lamps for optical pumping) and other technological difficulties, such as control of the coating quality. Part of these drawbacks is overcome with laser optical pumping, however a reliable commercial product is yet to be realized. Recently, the interest in wall-coated cells for high-precision spectroscopy and metrology is growing again, because coated cells represent good candidates to realize high-performance or micro-fabricated devices, such as miniaturized atomic clocks and/or atomic magnetometers [41,42]. Basic studies on the application of wall-coated cells for Rb frequency standards are reported in [43–47].

In this work (chapter), we take a step ahead to investigate and demonstrate the clock along with detailed metrological studies using a ^{87}Rb vapor cell whose inner walls are coated with anti-relaxation material (cf. Section 3.2.1). This cell is situated inside a compact magnetron cavity (cf. Section 3.4) that resonates around ν_{Rb}. The entire PP assembly for this cell was discussed in Section 4.3.

At first a brief theory of atom interaction with wall-coating is presented in Section 5.1. The experimental characterization of wall-coating is done by measuring the hyperfine population relaxation (T_1) and the coherence relaxation (T_2) times, respectivey in Section 5.2.2. Following to this, in Section 5.3.1, the optimization of double resonance signals as a function of laser intensity, microwave power and the cell temperatures is presented. The metrological characterization of medium- to long-term perturbations on the clock frequency by measuring the AC Stark shifts (light-shifts), the microwave power shift and temperature coefficients of the coating material is explained in Section 5.4. The reduction of intensity light-shift coefficient by the detuning method using the AOM LH is also demonstrated. The S/N limited short-term clock stability is demontrated in Section 5.5.1 along with detailed evaluation on the above perturbing parameters on medium- to long-term frequency of the clock.

5.1 Theory of atom interaction with wall-coating

In a Hydrogen maser, the inner walls of the bulb are coated by Teflon (a flurocarbon polymer) to prevent the polarized atoms from losing their state by colliding on to bare glass walls [32]. However, with the alkali metals like rubidium, the chemical reaction occurs with flurocarbon polymer surfaces, therefore coating materials such as paraflint ($CH_3(CH_2)_nCH_3$, with $40 \leq n \leq 60$), Dri-film ($(CH_3)_2SiCl_2$) and tetracontane ($C_{40}H_{82}$) are used [32]. In our studies we used a wall-coated cell with tetracontane coating that is filled with ^{87}Rb atoms (seen in Section 3.2.1).

Atoms inside the cell are in constant motion with an average velocity depending on the cell volume temperature given by $\bar{v} = \sqrt{8\mathrm{k_B T}/\pi \mathrm{M}}$, where k_B is the Boltzmann constant and M the mass of ^{87}Rb atom. Due to this motion, the ^{87}Rb atoms *collide* with the coating material mainly in three different ways [141]. Though, an elaborate theory would consider many other mechanisms involved in relaxation processes, we confine ourselves to the following main interactions:

(i) adiabatic collisions causing the hyperfine frequency shift and decoherence,

(ii) strong collisions, responsible in randomizing the electron spin but not affecting the nuclear spin, hence retaining a certain degree of polarization and,

(iii) the inelastic collision by *adsorption* on to the coated-walls and eventually diffuse into the coating material itself,

Additionally, due to continuous exchange of Rb atoms in the vapor phase in an equilibrium from the reservoir stem, we consider another important effect called

(iv) the reservoir effect.

In the processes (i) and (ii), the atom gets *adsorbed* onto the coated wall for a short duration (order of few pico-seconds [32, 36]) and may hop on to neighboring sites during this time. The (iii) type of collision not only causes the atom to lose its polarized state but to also reduce the density of atoms on long-time operation of the cell. A novel technique to improve the density of atoms by removing them from the trapping potentials of the coating material is known as Light-Induced Atomic Desorption (LIAD). This was first demonstrated independently by Budker and colleagues in paraffin coated cells [142, 143] and Burchianti et al., from porous silica [144]. This technique uses a non-resonant light source, usually in the ultra violet (UV) region in order to liberate the atoms that are adsorbed (or trapped) on the walls. Adaptation of LIAD for atomic clocks requires a separate dedicated study to accurately determine its advantages and impacts on the clock frequency stability. The reservoir effect (iv) mainly accounts for the interaction of polarized atoms with that of the metallic Rb through the reservoir hole, which will completly randomize the atomic spin.

During the process of *adsorption*, the alkali atom electronic cloud is deformed by the van der Waals force of attraction towards the surface and hence reducing the hyperfine interaction. This produces a negative frequency shift, known as the "wall-shift" [32]. The wall-shift, $\Delta\nu_w$, of the clock frequency due to the coating, associated with the temperature and geometry of the cell can be written according to Rahman and Robinson [145] as,

$$\Delta\nu_w = (\Delta\nu_d)\frac{\tau_a}{\bar{\tau}_c}, \tag{5.1}$$

where $\Delta\nu_d$ is the difference between the resonant hyperfine frequency while the Rb is adsorbed on the surface and that in free space, τ_a is the adsorption time and τ_c is the correlation time for atom-wall collisions, in other words this characterizes the average time between collisions with the coating surface inside the cell. Considering a cylindrical geometry (in our case the length and diameter are same), $\bar{\tau}_c$ depends on the cell radius, R, and the mean velocity, $\bar{v}$, of the Rb atoms inside the cell and can be written as

$$\bar{\tau}_c = 4R/3\bar{v} \tag{5.2}$$

The adsorption process of the alkali atoms on the coated walls also has a temperature dependance. Assuming a uniform (or average) adsorption energy, E_a, in the overall cell volume, the adsorption time, τ_a, of an atom on the walls can be calculated by a simple formula [141, 145–147],

$$\tau_a = \tau_0 \cdot e^{\frac{E_a}{k_B T}}, \tag{5.3}$$

where τ_0 is the period of vibration of the adsorbed atom in the wall potential typically having a value $\approx 10^{-12}$ s, k_B is the Boltzmann constant, and T is the absolute temperature. If the temperature increases, Rb atom spends less time on the wall, which results in a smaller frequency shift and broadening, and vice versa. From Eqn. (5.3) and Eqn. (5.1), the fractional change in frequency shift due to a fractional change in adsorption time by the influence of the temperature can be written as [141],

$$\frac{d\Delta\nu_w}{\Delta\nu_w} = -\frac{E_a}{k_B \cdot T}\frac{dT}{T} \tag{5.4}$$

The temperature coefficient of the cell volume is then, $TC_v = d\Delta\nu_w/dT$. This allows to extract the average adsorption energy of Rb on the coating material as shown in Section 5.4.3.

Each collision of an atom with the wall-coating causes the phase shift ϕ between the hyperfine states [32, 141, 147] and hence an average phase shift $\bar{\phi}$ is given by,

$$\bar{\phi} = 2\pi\bar{\tau}_c\Delta\nu_w. \tag{5.5}$$

The wall-shift $\Delta\nu_w$ can be measured experimentally (see Section 5.4.1). The statistical nature of the collisions gives rise to a spread in the phase-shift attained by the atoms. This adiabatic relaxation contributes to the line width given by,

$$\nu_a = 2\frac{\bar{\phi}^2}{\pi\bar{\tau}_c}. \tag{5.6}$$

5.1.1 Broadening mechanisms

A. Wall-coating collisional broadening

As discussed above, collisions of the polarized atoms with the coated walls give rise to broadening of the DR linewidth. From Eqn. 5.5, by using the experimentally measured wall-shift value of -370 Hz at a cell volume temperature T_v = 329 K (see Section 5.4.3, and internal cell volume radius R = 6 mm, we calculate an average wall shift per collision $\bar{\phi}$ = -65 mrad. For our cell dimensions, at the above temperature, we get $\bar{\tau}_c = 2.8\times10^{-5}$ s (from Eqn. 5.2). By substituting this value in Eqn. 5.6 we get the linewidth contribution due to collisions with the wall-coating, ν_a = 302 Hz.

B. Spin-exchange collisional broadening

On the other hand, due to the density of Rb atoms (corresponding to the temperature) the spin-exchange collisions occur (similar to as explained in Section 1.3(c)), which is also a source of relaxation and contributes to the observed width. With a single isotope of the alkali metal present (as in our case, only ^{87}Rb), having a nuclear spin I, the spin-exchange contribution to the line-width of the DR signal is given by the formula [75, 141],

$$\nu_{se} = \frac{1}{\pi}R(I)n\bar{v}_{rel}\sigma_{se}, \tag{5.7}$$

where σ_{se} is the spin-exchange-collision cross section ($\sigma_{se} = 1.6\times10^{-14}$ cm^2 for ^{87}Rb), n is the atomic number density that is controlled by stem/reservoir temperature (at the stem temperature T_s = 313 K, $n = 8.5\times10^{10}$ cm^{-3}) and the relative velocity of atoms $\bar{v}_{rel} = \sqrt{8\mathrm{k_B T}/\pi\mu_{\mathrm{red}}}$ = 39085 cm/s, with μ_{red} as the reduced mass of the colliding atoms and $R(I) = \frac{6I+1}{8I+4}$ is known as the nuclear slow-down factor (see [75]) for the

0-0 (clock) transition. For instance, with $I = 3/2$ (for ^{87}Rb), one gets $R(I) = 5/8$. By using the above values in Eqn. 5.7, we get $\nu_{se} \approx 11$ Hz.

C. Reservoir effect broadening

The intrinsic linewidths of the DR signal is also affected due to the Reservoir effect (or hole effect) [32, 125]. The polarized atom vanishes through the hole (connecting the cell volume and the stem) and gets replaced by a non-polarized atom from the reservoir, equivalent to a non-coated wall surface area that completely depolarizes the Rb by collisions. The linewidth contribution due to reservoir effect can be characterized by the formula,

$$\nu_{Res} = \bar{v}\frac{a}{\pi \cdot V}, \tag{5.8}$$

where a is the surface area of the hole intersection between the cell volume and the stem, V the volume of the cell. For our wall-coated cell, with $a = 0.8$ mm^2 and $V = 1.4$ cm^3, we get $\nu_{Res} \approx 51$ Hz.

C. Total broadening

Table 5.1 summarizes all the above broadening mechanisms. Therefore, the total contribution to the line-width is then the sum due to adiabatic collisions γ_a, the spin-exchange collisions γ_{se} and the broadening due to the reservoir effect γ_{Res}, which is equal to 372 Hz (or $T_2 = 0.88$ ms by using the Eqn. 1.21 at zero light intensity and zero microwave powers).

Table 5.1: *Summary of the broadening mechanisms in a wall coated cell.*

Broadening mechanism	**Parameter**	**Value [Hz]**
Wall collisions	ν_a	302
Spin-exchange collisions	ν_{se}	11
Reservoir effect	ν_{Res}	51
Total broadening	$\sum_i \nu_i$	364

5.2 Characterization of wall-coating

A paraffin-coated ($C_{40}H_{82}$) cell shown in Fig. 3.1 with an inner volume of ~ 1.4 cm^3 was used in the DR spectroscopic and clock measurements. At first the presence of wall-coating was tested by linear absorption spectroscopy (see Fig. 5.1). We note that in a separate parallel study by Pellaton et al., the tetracontane coated cells were fabricated at LTF and a thorough studies on ripening process of such cells were done [125]. In these studies it was seen that the coating undergoes a *curing process* to attain a state of stable equilibrium [125].

5.2.1 Absorption spectroscopy

Linear absorption spectroscopy was performed simultaneously in both, the wall-coated cell and an evacuated ^{87}Rb enriched cell by scanning the laser frequency (around D2-line). The schematics of optical pumping is shown in Fig. 5.1(a) corresponding to the laser scan as shown in Fig. 5.1(b).

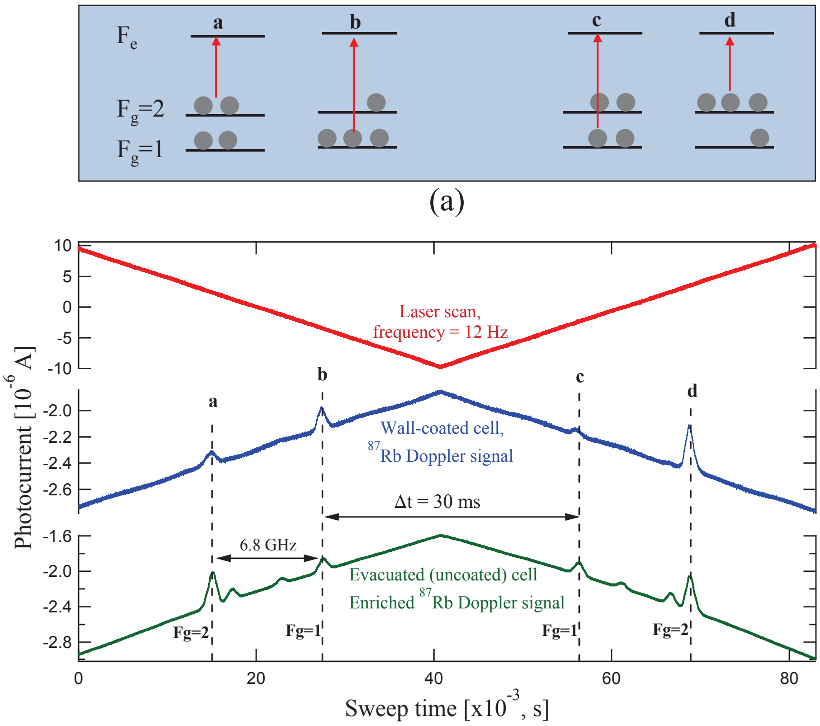

(a)

(b)

Figure 5.1: *(a) Schematics of optical pumping absorption spectroscopy and (b) absorption of wall-coated cell in comparison with an evacuated non-coated cell. The labels a, b, c, d show the absorption peaks for ^{87}Rb, corresponding to the optical pumping from either of the ground states with reference to schematics as shown in (a) above. Typical optical pumping time is 2.4 μs for each peak with an intensity of 28 $\mu W/mm^2$ [50, 92].*

This discussion focuses only on the ^{87}Rb lines (labelled: a, b, c and d in the

Fig.5.1). The laser frequency was scanned in such a manner that at first it optically pumps the atoms from $F_g = 2$ state to $F_g = 1$ state (peak-a) via the excited state F_e. This increases population in $F_g = 1$, which leads to enhanced laser absorption at peak b. Optical pumping during peak-b also depletes $F_g = 1$ population. Due to the coating this population imbalance survives during the time $\Delta t \approx 30$ ms. After that, reversing the direction of laser scan, when $F_g = 1$ is sampled again, population of this state is still low, leading to a very small peak-c. In the uncoated cell, population is not preserved over Δt, thus peaks- b and c have same amplitudes. Furthermore, the laser at peak-c optically pumps more number of atoms into $F_g = 2$ that is evident in peak-d corresponding to wall-coated cell absorption. This gives a clear indication of the anti-relaxation property of the wall-coating. A quantitative measurement of the relaxation time (or the atomic polarization retaining time) is done by relaxation in the dark method as explained in the next section (cf. Section 5.2.2).

5.2.2 Relaxation times (T_1 & T_2) measurements

Further detailed characterization of the wall-coating was done by measuring the longitudinal (T_1) and transverse (T_2) (or the coherence) relaxation times. Here, the longitudinal and transverse terminologies are used in analogy with the nuclear magnetic resonance.

The clock laser head (cf. Fig 2.1) emitting at the Rb D2-line (780 nm) optically pumps the atoms from ^{87}Rb, $F_g = 2$ hyperfine state as shown in Fig. 5.2(a) (using a linear light polarization). The excited state (F_e) manifold is not resolved due to Doppler broadening, however the strongest contribution to the pumping process mainly comes via the $F_e = 2$ state. The laser beam passes through an Acousto Optical Modulator (AOM), which was used as an optical switch as shown in Fig. 5.2(b). Note that this external AOM is not the same as one that is integrated in the AOM laser head (cf. Fig 2.2). The optical pumping time was kept constant, but the dark time was varied using the *on* and *off* time durations of the AOM rf-drive. During the dark time, τ_d, the atoms undergo relaxation mainly because of random electronic depolarization by collisions with the walls [148], and also due to the reservoir effect [146].

The absorption voltage levels of the laser passing through the wall-coated cell were recorded as a function of the dark time using the photodetector. This gives a measure of the number of atoms, N2, in the $F_g = 2$ state at the end of the dark time, as a function of τ_d, and eventually reaching a saturation termed as $N2_{eq}$ in Fig. 5.3. The longitudinal relaxation time, T_1, is extracted by a single exponential fit function

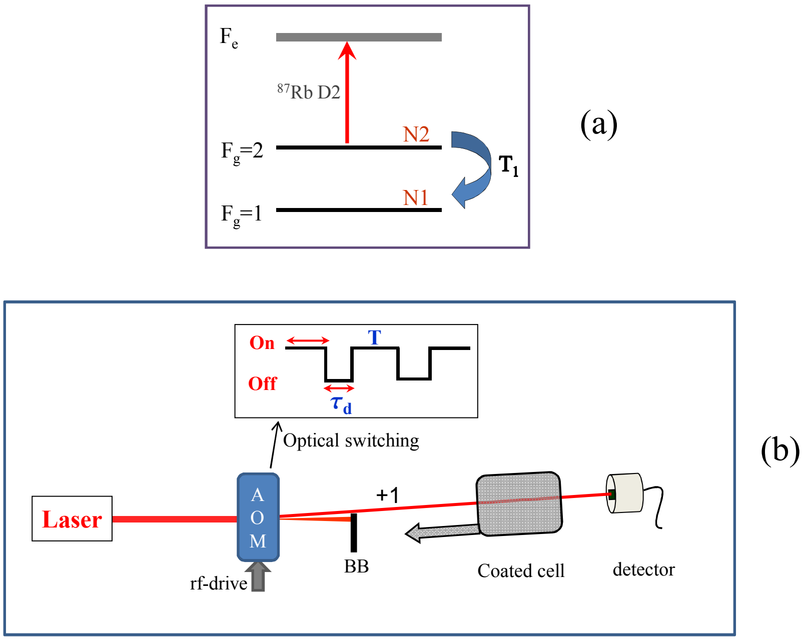

Figure 5.2: *(a) Conceptual diagram of relaxation of population in the ground-state hyperfine components, and (b) the schematic setup for measuring the T_1 by relaxation in the dark method, BB: beam blocker. The inset shows the optical switching time.*

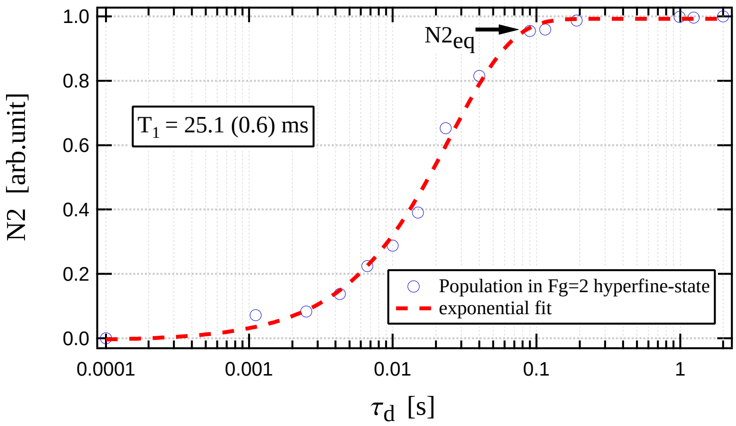

Figure 5.3: *The experimental T_1 extracted by the exponential fit.*

given by [148],

$$N2(\tau_d) = N_0 + N2_{eq}(1 - e^{-\tau_d/T_1}) \tag{5.9}$$

where τ_d is the dark time, N_0 is measured to be zero within the experimental errors, and $N2_{eq}$ is normalized to 1 (arb. unit). To the first-order approximation, we calculate the number of wall collisions, N as,

$$N = T_1 \frac{A}{V} \sqrt{\frac{8 k_B T}{\pi M}}, \tag{5.10}$$

where k_B is the Boltzmann constant, M is the mass of ^{87}Rb atom and $\frac{V}{A} = \frac{R}{2(1+R/L)}$ is the ratio of volume to area of the cell considering the cylindrical geometry, where R and L are the internal radius and length of the cell, respectively [32]. Here the T_1 relaxation time is measured for the total hyperfine ground state, which includes the contribution from all the Zeeman levels. The fitted value of $T_1 = 25.1(0.6)$ ms (at T = 300 K) gives an estimate of about 2,255 wall collisions before an atom loses its polarized state.

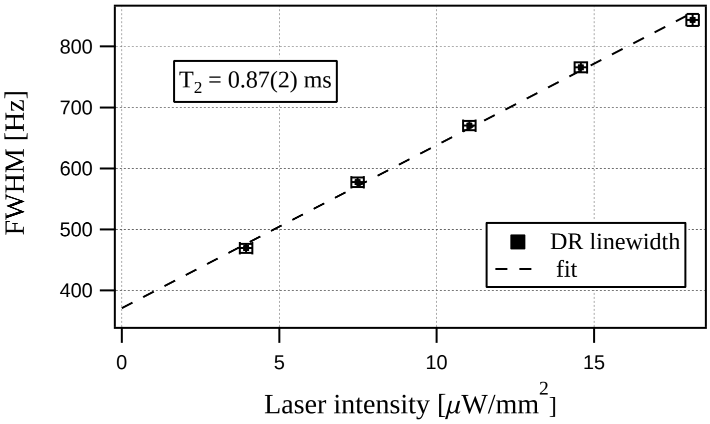

Figure 5.4: *The DR linewidth as a function of laser intensity for determination of coherence relaxation time, T_2.*

The coherence between two states, measured by the transversal relaxation time, T_2, contributing the linewidth is also an influencing parameter for the clock short-term stability. Here, the T_2 relaxation time is measured only for *the clock transition*, by the double-resonance mechanism (explained in Section 1.2). Extrapolation of the clock transition linewidth (FWHM) $\Delta\nu_{1/2}$ to zero pump-light intensity allows one to extract T_2 from 1.21 [149],

$$\Delta\nu_{1/2} = 1/(\pi T_2), \tag{5.11}$$

A relaxation time of coherences, $T_2 = 0.87(2)$ ms is obtained from the line-fit as shown in Fig. 5.4. This is in excellent agreement with the theoretical calculation giving the value of 0.87 ms (cf. Section 5.1, Eqns. 5.5 –5.8).

5.3 DR signals

5.3.1 Optimization of DR signals

In these DR experiments, the clock laser head was stabilized to the $5^2S_{1/2}F_g = 2 \rightarrow 5^2P_{3/2}F_e = 3$ (cf. 2-3 in Fig. 2.3) direct transition on the ^{87}Rb D2-line.

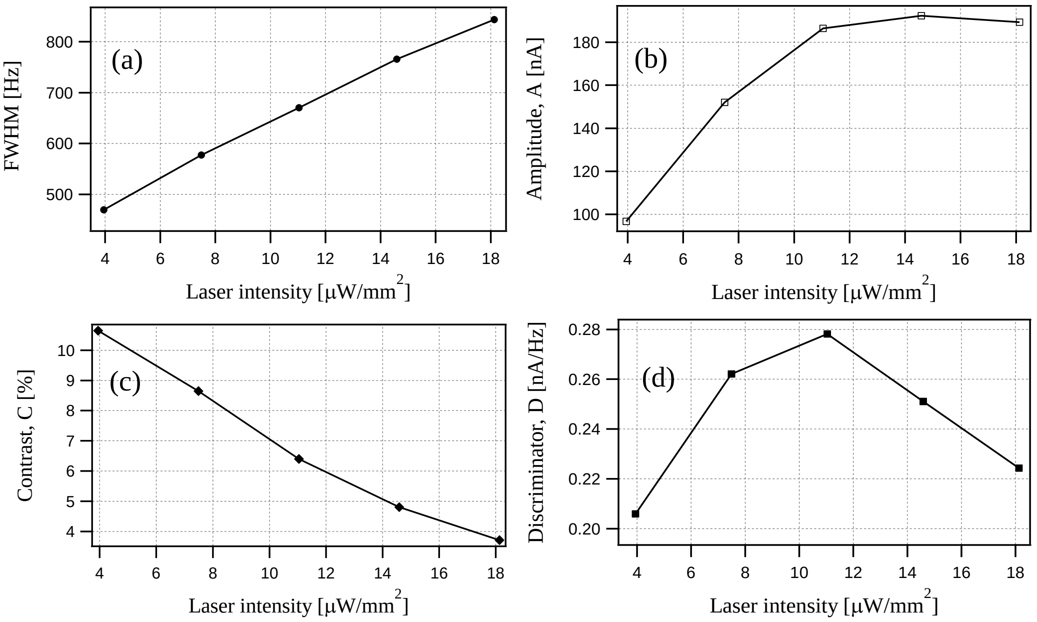

Figure 5.5: *Typical DR parameters as a function of laser intensity. Fixed microwave power P_μ=-40 dBm, cell volume temperature, T_v=323 K and stem temperature, T_s=313 K. (a) DR linewidth as a function of laser intensity, (b) DR amplitude as a function of laser intensity, (c) DR signal contrast (amplitude/background) as a function of laser intensity and (d) the DR signal discriminator slope (estimated as amplitude/FWHM) as a function of laser intensity.*

Primarily, it is worth studying the DR signal parameters and optimize for the best possible signal-to-noise-ratio (S/N), which in turn determines the clock's short-term stability [32, 115]. In this view, at first, the DR signal parameters were studied as a function of laser intensity, while all other parameters were unvaried (constant) as shown in Fig. 5.5. A laser intensity of 11 μW/mm^2 was chosen based on this optimization.

Then, the DR signal parameters were studied as a function of microwave power (cf. Fig. 5.6). Here, an useful definition of Figure of Merit (FOM), which is a ratio of the DR signal contrast to the linewidth gives a better estimate of the optimization

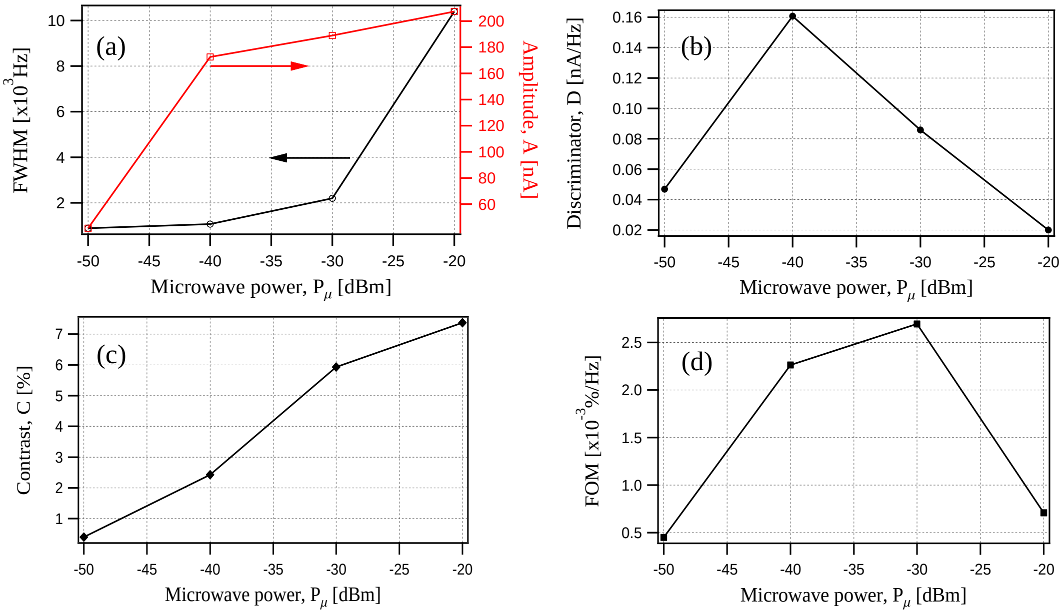

Figure 5.6: *Typical DR parameters as a function of microwave power. Fixed laser intensity* I_L*= 11* μ*W/mm*^{2}*, cell volume temperature,* T_v *= 323 K and stem temperature,* T_s *= 313 K. (a) DR signal linewidth (open circles) as a function of laser intensity on left axis, and the right axis indicate DR amplitude (open squares) as a function of laser intensity, (b) Discriminator (amplitude/linewidth) as a function of microwave power, (c) Contrast (amplitude/background) as a function of microwave power, and (d) Figure of Merit (FOM) (contrast/FWHM) as a function of microwave power.*

as it also considers the background noise level. A similar FOM could also be used for laser intensity. The microwave power input at the cavity coupling of P_μ=-30 dBm (or 1 μW) was selected from the optimization.

Finally, the DR signal discriminator was measured as a function of the cell volume temperature T$_v$ and the cell stem temperature, T$_s$ as shown in Fig.5.7. The optimized cell volume and stem temperatures for maximum signal are T_v = 329 K and T_s = 321 K, respectively. Note that the T$_v$ could have been increased further, but it was not done in order to be absolutely below melting point ($\approx$ 253 K) of the tetracontane coating material. It is important to note that this optimization was started by first varying the laser intensity and so on. However, it is now clear that the better approach would be to first study the DR signal as a function of cell volume and stem temperatures, this is adopted for studying the enlarged cell in the next chapter (cf. Section 6.1.1). The above optimized parameters were set: an optical intensity of about 11 μW/mm^2 on the clock cell; a microwave power of 1 μW

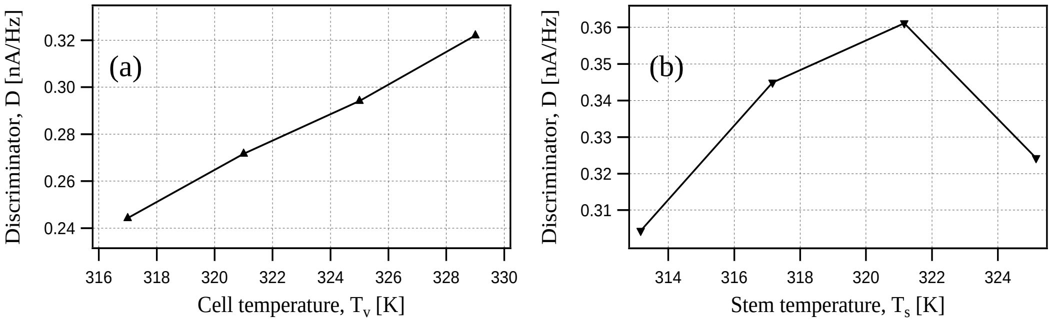

Figure 5.7: *Optimization of DR discriminator signal as a function of, (a) cell volume temperature, T_v at T_s=313 K and, (b) cell stem temperature, T_s at T_v=329 K. The laser intensity and microwave power were set at 11 μW/mm^2 and -30 dBm, respectively.*

injected into the cavity; T_v = 329 K and T_s = 321 K, respectively. The DR signal in these conditions is shown in Fig. 5.8. It has a narrow linewidth of 642 Hz with an amplitude and contrast of 0.62 μA and 11%, respectively. The center frequency is $\nu_{DR} = \nu_{Rb} + \Delta\nu$ = 6.834682330 GHz here, giving an atomic Q-factor of 10^7 (from Eqn. 1.2). These values are in good agreement with the estimated ones in Table 1.7. A narrow DR signal gives a better discriminator slope D and hence a better short-term stability (see Section 5.5.1). In our DR signals, we do not observe any Doppler-broadened pedestal, that would be expected when using a travelling microwave field due to the phase variations over the cell volume [36, 141]. In contrast to the use of a typical cylindrical cavity having TE$_{111}$ mode [101] (where the cell volume occupies different microwave phase regions), in our magnetron cavity the cell only occupies regions of same microwave phase; therefore the broad pedestal is suppressed.

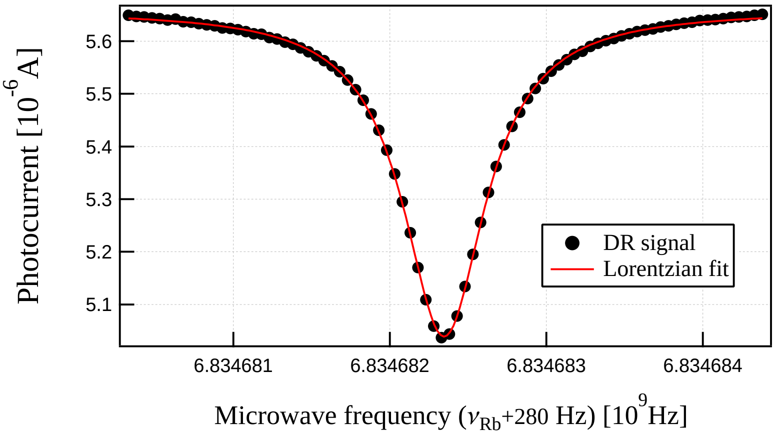

Figure 5.8: *Double-Resonance signal with a linewidth of 642 Hz and a contrast of 11%.*

In the following sections we will see the measurements on the physical effects causing perturbations on the centre frequency of the DR signal, ν_{DR}.

5.4 Perturbation studies on clock transition

As we came across in Chapter 1.5 in detail, though first-order shifts due to magnetic field variations are absent on the clock transition frequency, the other parameters, such as, the 2nd order Zeeman shift, variations in laser intensity and frequency, the power fluctuations of microwave, and the residual temperature fluctuations can induce shifts on the clock transition and degrade the clock stability on medium- to long-term time scales. Therefore, control or suppression of the influence of these effects is needed for improving the clock performance. In Section 4.5.1 we have seen that the magnetic shields reduce the 2nd order magnetic variations on the clock transition to a level of $< 3\times10^{-15}$. In this Section, we present quantitative measurements of AC Stark shift (cf. Section 1.5.2) (also referred to as intensity or frequency light-shift), microwave power shift (cf. Section 1.5.5) and temperature shifts due to the temperature dependence of the cell's volume and stem. The temperature shifts occuring in a wall-coated cell are due to interaction of atoms with the wall as explained in Section 5.1. This is different to the atom interaction with buffer gases that was explained in Section 1.5.3. The experimental studies of atom interaction with coated walls is presented in a dedicated Section 5.4.3. Influences of these perturbations on the clock instability are also evaluated quantitatively.

5.4.1 Light-shifts

The light-shift (LS) of an electromagnetic field on the clock transition was discussed in Section 1.5.2. The measurements relevant to the wall-coated cell physics package are done and presented in the sections below.

(i) Intensity light-shift coefficient (α) and its reduction by laser detuning method

The intensity LS coefficient, α, can be written as $\alpha = \frac{\delta\nu_{LS}}{\delta I_L}$ at a fixed laser frequency. Experimentally, we determine α by measuring the clock frequency as a function of laser intensity, for the laser frequency stabilized to three different sub-Doppler transitions on the ^{87}Rb D2-line $F_g = 2$ state (see Fig. 2.3), the LS data is shown in Fig. 5.9(a). The fitted slopes give the intensity LS coefficients α for the particular laser frequency as explained in Fig. 1.13. The lowest value, obtained for the laser stabilized to the $F_g = 2 \rightarrow F_e = 3$ direct transition in the LH evacuated reference cell, is $\alpha = +2.3(1)$ Hz·mm$^2/\mu$W.

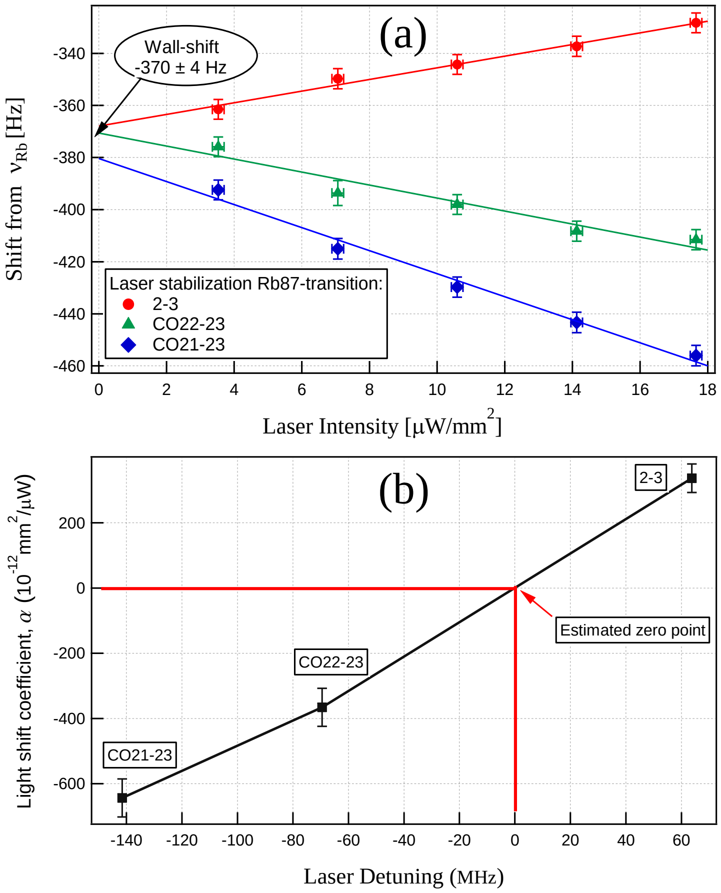

Figure 5.9: *(a)* ^{87}*Rb frequency shift as a function of the interrogating laser intensity, slope gives the intensity LS coefficient, α, (b) dependence of α on laser frequency detuning is shown with reference to the locked transitions using an evacuated Rb cell. The inset labeling of the* ^{87}*Rb transitions correspond as follows; 2-3:F_g=2 $\rightarrow$ F_e=3, CO22-23:F_g=2 $\rightarrow$ F_e=2,3 cross-over, and CO21-23:F_g=2 $\rightarrow$ F_e=1,3 cross-over.*

Extrapolation to zero laser intensity gives the value of the clock frequency shift, $\Delta\nu = \nu_{DR} - \nu_{Rb}$, corrected for LS effects, and which is mainly determined by the wall-coating, in this case it is $\Delta\nu$ = -370(4) Hz (see Section 5.4.3 for details). The dependence of the intensity LS coefficient, α, on the laser frequency is shown in Fig. 5.9(b). One can reduce the effect of intensity LS by detuning the laser frequency, ν_L closer to ν_{opt}, where α is small [21]. In our experiment, we adopt the AOM laser head (cf. Section 2.2.2) for detuning the laser frequency by -131 MHz before stabilizing the frequency-shifted beam to the $F_g = 2 \rightarrow F_e =$ 1,3 cross-over resonance. Using the unshifted laser frequency for the clock (i.e. detuned by +131 MHz with respect to $F_g = 2 \rightarrow F_e =$ 1,3 cross-over), a reduced coefficient $\alpha_{redu} =$ -0.057(4) Hz·mm^2/μW was measured, which is a reduction in α by a factor of '40'.

Influence on clock instability:

Though the intensity LS influences the clock instability at all integration times, main limitations result on the medium- to long-term time scales. Hence, we estimate the LS contribution to clock instability at 10^4 s. When the laser frequency is stabilized to the $F_g = 2 \rightarrow F_e = 3$ direct transition, the intensity LS, is measured to be $|\alpha| = 2.3(1)$ Hz·mm^2/μW (cf. Fig. 5.9(a)). The intensity LS contribution on the clock frequency can be estimated by,

$$\sigma_\alpha = \frac{|\alpha| \cdot \sigma_{\Delta I_L/I_L}(\tau) \cdot I_L}{\nu_{Rb}}, \tag{5.12}$$

where the relative stability of the laser intensity in terms of Allan standard deviation at 10^4 s is measured to be $\sigma_{I_L} = 5\times10^{-3}$. At the operating laser intensity, $I_L = 11$ μW/mm^2 (chosen for optimized short-term clock stability, see Section 5.5.1), the contribution to the clock instability, σ_α is estimated as 1.8×10^{-11} at 10^4 s. Using the AOM for reduction of the intensity-LS (α) results in a stability limit of 4.5×10^{-13}.

(ii) Frequency light-shift coefficient (β) and dependence on laser intensity

The frequency LS coefficient is explained in Section 1.5.2(B), as $\beta = \frac{\delta\nu_{LS}}{\delta\nu_L}$. At different fixed light intensities, the value of β is evaluated as the slope of the line-fits is shown in Fig. 5.10(a). The zoom-inset at the zero laser detuning frequency again shows the measure of the clock frequency shift, $\Delta\nu \approx$ -372±4 Hz, when unperturbed by LS. Dependence of the frequency LS coefficient β as a function of pump-light intensity is shown in Fig. 5.10(b) and is linear in I_L, as expected from Eqn. 1.42. Frequency LS can be nullified, e.g. in pulsed mode [56]. In the continuous-wave operation discussed here, this is not possible, but we can reduce the effect of β by operating at low light intensities as the optical Rabi frequency is reduced (cf. 1.42) [95] or high buffer gas pressures [96].

Influence on clock instability:

We estimate the influence of the frequency LS on the clock's instability at 10^4 s. At a light intensity of 11 μW/mm^2, the value of $\beta = 413.8(4)$ mHz/MHz. The stability of

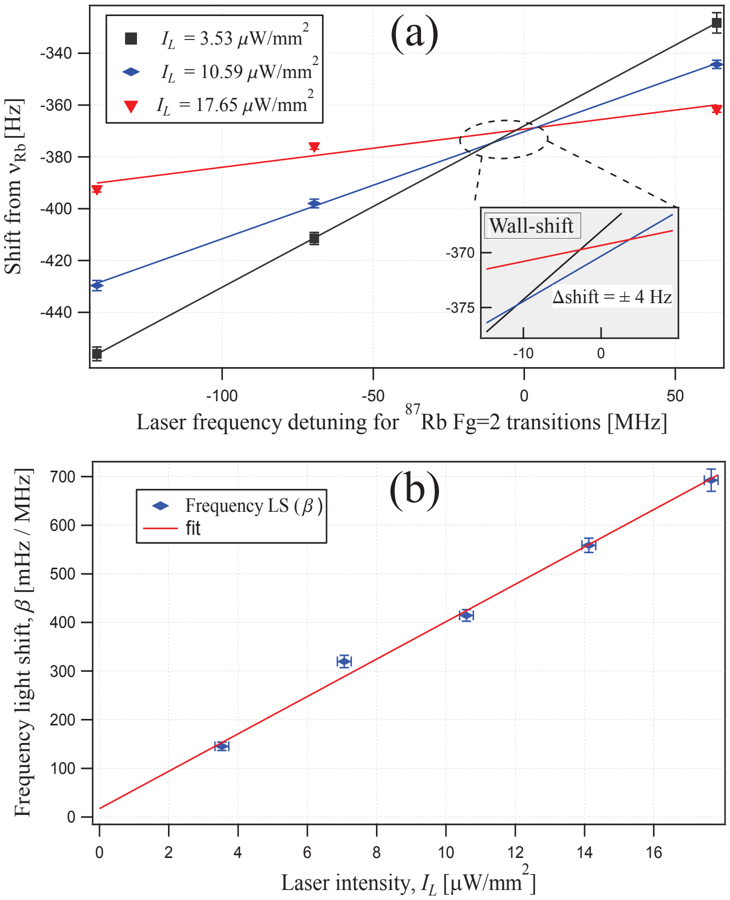

Figure 5.10: *(a) Clock frequency shifts as a function of the laser frequency detuning corresponding to optical transitions as shown in Fig. 5.9(b). The slopes give the frequency LS, β, and (b) the dependence of β on laser intensity.*

the laser frequency, σ_{LF}, at 10^4 s measured by beat note method [106] is $< 5\times10^{-12}$ and $\nu_L = 384.23$ THz. Similar to Eqn. (5.12), we find a contribution of frequency LS to the clock instability as $\sigma_\beta = 1.2\times10^{-13}$ at 10^4 s (also see Table 5.5).

5.4.2 Microwave power shift (preliminary)

The microwave power shift on the clock frequency was measured as a function of microwave power input into the cavity with the laser stabilized to $F_g = 2 \rightarrow F_e = 3$ direct transition. From Fig. 5.11, a linear-fit gives a shift rate or power-shift coefficient, $\delta_\mu = 3.4(2)$ Hz/dBm ($\simeq 7.8(4)$ Hz/μW at $P_\mu = 1$ μW). This shift is not negligible, thus requiring a good power stability of the microwave synthesizer.

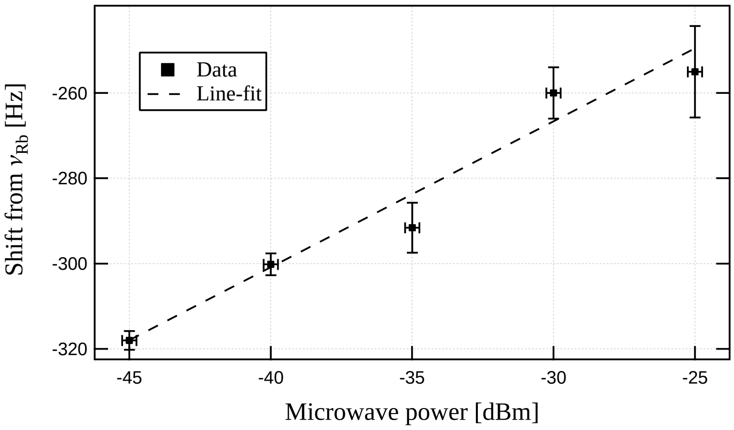

Figure 5.11: *Frequency shift as a function of microwave power.*

Influence on clock instability:
The power stability of our synthesizer is measured to be $\sigma_p = 1\times10^{-4}$ at 10^4 s. With an input power of $P_\mu = 1\ \mu$W, the instability contribution on the clock at 10^4 s is estimated to be $\sigma_\mu = 1.1\times10^{-13}$ (see also Table 5.5).

We note that the work of Risely et al. [54] shows that the use of wall-coated cells reduces the microwave power shift to ≤ 0.2 Hz/dBm, which is not observed here. This discrepancy is yet to be studied in detail in wall-coated cells, but as a first approximation, we attribute this to the contribution from light intensity effects. Furthermore, in Chapter 6 we observe that the microwave power shift is influenced by light intensity, i.e., the value obtained as microwave power shift also includes the effect of light shift in it. The value at *zero* light intensity can give a pure microwave power shift in the *ligh-shift free* regime; such a measurement was done in Section 6.2.2. A further validation of this influence of light-shift on the microwave power shift value is clearly evidenced and presented in detail in Section 6.3.2.

5.4.3 Temperature coefficients

As shown in Fig. 3.1, the wall-coated cell has two regions (T_v and T_s) that are separately controlled in temperature. The temperature coefficient (TC) of a wall-coated cell is an intrinsic property of the coating material [55], where the variations in temperature determine the interaction of atoms with the wall-coating and its impact on their polarization state (see Section 5.1). The TC experiments were performed below the paraffin melting point (~353 K) [145]. The laser was stabilized to $F_g = 2 \rightarrow F_e = 3$ (see Fig. 2.3) at an input fixed light intensity of $\approx 11\ \mu$W/mm^2 and microwave power of - 40 dBm. Dependence of the clock frequency shift on T_v is shown in Fig. 5.12(a), its linear-fit slope gives the cell-volume temperature coefficient, $TC_v = +1.39(5)$ Hz/K $\approx 2\times10^{-10}$/K. This behavior is related to the adsorption process of the alkali atoms on the coated walls according to Eqn. 5.3. Therefore, the temperature coefficient of the cell volume from Eqn. 5.4, $TC_v = \frac{d\Delta\nu_w}{dT} = -\frac{E_a\cdot\Delta\nu_w}{k_B\cdot T}$. The wall shift depends on the cell temperature, and can vary for different coating materials and this shift can change over time depending on the modifications in the coating material [141, 150].

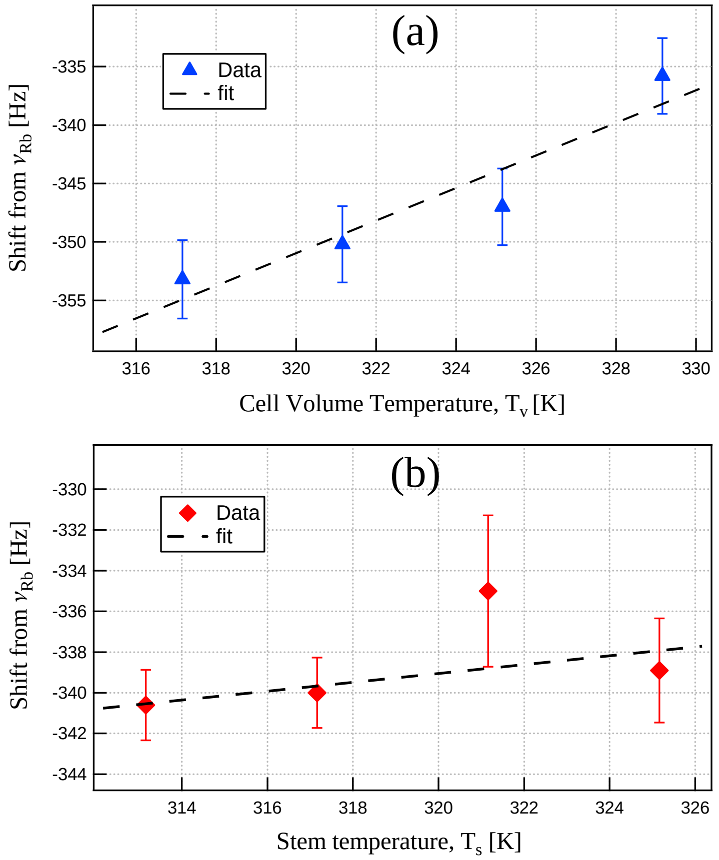

Figure 5.12: *(a) Clock frequency shift from ν_{Rb} as a function of cell volume temperature, T_v, when T_s is kept constant at 313 K. The closed triangles depict the measured data and the dashed line shows the fit to the data with a cell volume temperature coefficient of TC_v = +1.39(5) Hz/K, and (b) Clock frequency shift from unperturbed level as a function of stem temperature, T_s, when T_v is kept constant at 329 K. Closed diamonds show the experimental data and the dashed line is a linear fit, with a stem temperature coefficient of TC_s = +0.22(3) Hz/K. The laser intensity and the microwave power were kept constant during both measurements of the temperature coefficients.*

In our case, the wall shift extracted from Fig. 5.9 is $\Delta\nu_w$ = -370 Hz. The average adsorption energy of Rb on the coating is calculated as, $E_a = 0.036$ eV. This value is in close agreement with previously reported studies [141,145] (see Table 5.2). Part of TC_v might be due to the Rb-Rb spin-exchange effect due to any metallic Rb present in the cell volume, but as we have not observed any Rb droplets in the cell volume, this effect can be neglected. On the other hand, the effect of spin-exchange due to change of Rb density with the stem acting as reservoir is 10-times smaller in comparison with TC_v (see below).

Table 5.2: *Comparison of the adsorption energy values with other works.*

Reference	E_a [eV]
[141]	0.06
[145]	0.062
This work	0.036

A similar shift of the clock frequency due to the stem temperature is measured to be $TC_s = +0.2(2)$ Hz/K $\approx 3(3) \times 10^{-11}$/K as shown in Fig. 5.12(b). Because the cell stem contains the reservoir of liquid Rb, we mainly attribute this shift to the influence of the atomic density and the related spin-exchange effect, as explained in Section 1.5.4 (also see [75, 76, 141] and references therein). The shift of the clock frequency due to spin-exchange can be calculated according to Micalizio et al. [76] by the Eqn. 1.45 (see Section 5.4.4).

Influence on clock instability:

From measured variations in the cell's temperature control ($\sigma_T = 10$ mK at 10^4 s), the clock instability due to the temperature coefficient of the cell-volume is estimated as $\sigma_{TC}^{volume} = 2\times10^{-12}$, and the contribution on the clock frequency instability due to stem temperature coefficient is $\sigma_{TC}^{stem} = 3.2\times10^{-13}$. The limit due to the TC of the cell-volume is thus the dominating one for the clock instability, with the stem's TC being one order of magnitude smaller. The influences of physical parameters on the clock instability in medium to long-term time scales are summarized in Table 5.5.

5.4.4 Spin exchange frequency shift

The spin-exchange collisions that are responsible in giving rise to the frequency shift of the clock transition were explained in Section 1.5.4 (Eqn. 1.45), as function of temperature. In our wall-coated cell, the temperature of the stem T_s determines the density of Rb atoms inside the cell volume and the velocity of atoms in the cell volume are dictated by the temperature T$_v$. At a fixed T$_v$ = 329 K, the velocity of the atoms inside the cell calculated by the formula 1.46 is ≈ 28300 cm/s and the atomic density at 313 K is $n = 8{\times}10^{10}$ cm^{-3}. In our case, the atoms are pumped from F$_g$ = 2 state, therefore the population difference between two clock levels is Δ = -1/3 [76, 99]. We calculate the spin-exchange frequency shift from Eqn. 1.45, $\Delta\nu_{SE} \approx 0.2$ Hz or $\frac{\Delta\nu_{SE}}{\nu_{Rb}} \approx 3{\times}10^{-11}$.

The relative shift dependent on temperature locally in our operating range can be calculated from the Eqn. 1.47. In the temperature range of T$_s$, between 313 K to 325 K (cf. Fig.5.12(b)), the increase in every kelvin temperature increases the atomic density by 6%. Therefore, the calculated temperature related spin-exchange $\Delta T_{SE} \approx 7{\times}10^{-12}$/K.

5.5 Wall-coated cell clock stability

5.5.1 Short-term noise budget

(i) Signal to noise estimation

The short-term stability (1 to 100 s) of a passive rubidium frequency standard can be predicted [31] by Eqn. 1.35, with a known, total detection noise power-spectral-density N_{psd} when microwave and pump laser are switched on (in closed clock loop condition) and the discriminator slope D of the clock error-signal close to the line centre. The typical measured parameters, estimated signal-to-noise (S/N) limit and shot-noise limit are presented in Table 5.3. Measured noise density, N_{psd} includes the contribution of PM-to-AM noise conversion in the clock cell [86,87]. Using Eqn. 1.35, the S/N limited short-term stability is calculated as $1.3{\times}10^{-12}\ \tau^{-1/2}$. The shot-noise limit of the clock occurring due to the statistical nature of the photons arriving at the detector [91] can be given by Eqn. 1.38 is calculated as $3.3{\times}10^{-13}\ \tau^{-1/2}$.

(ii) Phase noise estimation

The limit due to LO intermodulation effect is given by Eqn. 2.3 and for the clock loop modulation frequency, f_m = 193 Hz, considering its even harmonics up to 100 kHz it is calculated as $\sigma_y(\tau)_{PMnoise} = 6{\times}10^{-13}\ \tau^{-1/2}$.

Table 5.3: *Noise budget and estimation of signal-to-noise and shot-noise limits. The discriminator slope D is measured from the error signal of the DR curve.*

Parameter	**Value**
FWHM	642 Hz
Contrast	11.3%
Discriminator, D	0.41 nA/Hz
N_{psd}	5.1 pA/$\sqrt{\text{Hz}}$
S/N limit	$1.3\times10^{-12}\ \tau^{-1/2}$
Shot-noise limit	$3.3\times10^{-13}\ \tau^{-1/2}$

(iii) Light-shift estimation

The intensity and frequency light-shifts also influence the short-term stability of the clock (as explained in Section 1.4.4), *via* the laser's intensity and frequency instabilities, which perturb the clock transition on short-time scales. Table 5.4 summarizes these effects and resulting limits on the short-term clock stability.

Table 5.4: *Intensity and frequency light-shift contribution to the clock's short-term instability.*

Physical effect	**Coefficient**	**Variation**	**Formula**	**Inst.** $[\tau^{-1/2}]$
Intensity- LS effect, $\|\alpha\|$	2.3(1) Hz·mm^2/μW	Laser int. instab.: $\sigma_{\Delta I_L/I_L}(\tau)< 3\times10^{-5}$	1.36a	1.1×10^{-13}
Frequency- LS effect, $\|\beta\|$	413.8(4) mHz/MHz	Laser freq. instab.: $\sigma_{Lf}=4\times10^{-12}$ (1-100 s)	1.36b	9.3×10^{-14}
Total LS instab., σ_{LS}				2×10^{-13}

(iv) Sum of contributions on short-term stability

Eventually, the overall short-term clock stability can be estimated from the sum of the squares of the individual limits by Eqn. 1.37 as 1.5x$10^{-12}\ \tau^{-1/2}$.

5.5.2 Measured short-term stability

The experimentally measured short-term stability of the DR clock using the paraffin-coated cell is shown in Fig. 5.13. The measured short-term stability of $2.75\times10^{-12}\tau^{-1/2}$

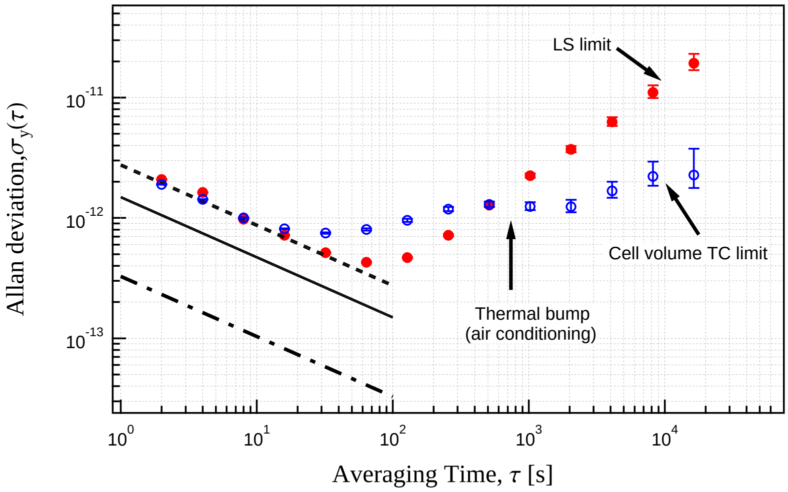

Figure 5.13: *Measured clock stability using the wall-coated Rb cell. Closed (red) circles show clock stability data without intensity LS compensation; open (blue) circles denote the clock stability with intensity LS compensation by the detuning method. The dotted line represents the measured clock short-term stability of* $2.75\times10^{-12}\tau^{-1/2}$*, the solid line indicates the estimated total limit, and dash-dotted line shows the shot-noise limit of* $3.3\times10^{-13}\tau^{-1/2}$*.*

is in reasonable agreement with the estimated stability of $\simeq 1.5\times10^{-12}\ \tau^{-1/2}$. The short-term stability is mainly limited due to the S/N limit that includes the contribution of laser PM-to-AM noise conversion in the clock cell [87].

5.5.3 Medium- and long-term stabilities

The medium-term stability is influenced by the sensitivities measured before, such as, the light-shift, and temperature coefficients. The light-shift coefficient is suppressed by the use of AOM detuning method, however the clock stability is limited to around 2×10^{-12} at 10^4 s by the temperature coefficient of the coating material (1.39(5) Hz/K). This limitation is an intrinsic property of the coating material and hence gives the ultimate limit for this particular clock, unless improvements on the temperature control of the cell are implemented. Figure 5.13 shows the clock medium-to long-term stability without laser detuning (closed circles) limited to 1.8×10^{-11} due to intensity light-shift effect and the second run (open circles) where intensity light-shift effect is reduced by a factor of '40' by using the AOM LH, as predicted (see Table 5.5).

A linear drift of $+8.5\times10^{-12}$/day was measured, including also the ageing of the coating material. In order to reach the level of $< 1\times10^{-14}$ after one day integration

Table 5.5: *Summary of instability contributions of physical perturbations on the clock transition in medium to long-term time scales.*

Physical effect	**Coefficient**	**Variation**	**Instab. at 10^4 s**
Intensity LS effect $\lvert\alpha\rvert$	2.3(1) Hz·mm^2/μW	53×10^{-3} μW/mm^2	1.8×10^{-11}
Redu. int. LS $\lvert\alpha_{redu}\rvert$	0.057(4) Hz·mm^2/μW	53×10^{-3} μW/mm^2	4.5×10^{-13}
Frequency LS effect, $\lvert\beta\rvert$	413.8(4) mHz/MHz	<1.93 kHz	1.2×10^{-13}
Cell volume TC $\lvert TC_v\rvert$	1.39(5) Hz/K	10 mK	2×10^{-12}
Stem TC $\lvert TC_s\rvert$	0.22(3) Hz/K	10 mK	3.2×10^{-13}
Microwave PS [a] $\lvert\mu_{PS}\rvert$	7.8(4) Hz/μW	2×10^{-4} μW	2.2×10^{-13}
Spin ex. shift $\lvert\Delta T_{SE}\rvert$	7×10^{-12}/K	10 mK	7×10^{-14}
Cavity pulling $\lvert\Delta\nu_{CP}\rvert$	4.6 mHz/K	10 mK	$<$ 6.8×10^{-15}

---

[a] This is to be confirmed. However, it will not be a limiting factor as in wall-coated cells the microwave PS is reduced [54], and already this reported instability contribution is lower than the limits arising from the cell's TC or intensity LS coefficient.

time, further suppression and control on the light-shift effect, and that of the TC to $\leq$ 6.8 mHz/K is required. A linear drift possibly due to degradation of the coating was measured in the D1-line (795 nm, in a parallel study), and -7×10^{-10}/month (or -2.4×10^{-11}/day) was observed [151].

5.6 Conclusions

Investigations on the paraffin coating material characteristics were performed by measuring the T_1 = 25 ms and T_2 = 0.9 ms relaxation times for a wall-coated Rb cell, and have shown that a polarized Rb atom undergoes about 2,255 wall collisions (at 300 K) before losing its polarized state. The optical-microwave double-resonance spectroscopic studies with a paraffin coated cell inside a TE$_{011}$ magnetron cavity showed a narrow linewidth of $<$ 650 Hz with a large signal contrast $>$ 11%. Systematic studies of the parameters that influence the medium to long-term stability - notably by the perturbations due to intensity and frequency light-shift effects, microwave power shift and shifts on clock transition due to temperature variations that occurs due to the atom-wall interactions were quantified and their instability contributions on the clock were estimated.

We showed that wall-coated cells can be used for realization of high-performance

Rb clocks even when using small cells (1.4 cm^3 volume) in view of compact clocks exhibiting the short-term frequency stability of $<3\times10^{-12}\ \tau^{-1/2}$. Measured clock stabilities are in agreement with the calculated limits on both the short-term and medium-term time-scales. Using detuning of the laser frequency, the limitation to medium-term clock stability arising from the intensity light-shift effect was suppressed, which results in the clock stability being limited by the temperature coefficient of the coating at 2×10^{-12} level. This temperature coefficient could in principle be compensated by adding a small amount of suitable buffer-gas to the cell. This possibility was discussed previously [152, 153] for linewidth studies, but not for compensation of the temperature coefficient of the coating.

Use of wall-coatings also is of high interest to achieve narrow line-widths from cells of smaller dimensions or even microfabricated cells [154], but better coating materials allowing for a higher number of wall collisions at higher cell temperatures are required. Recent work of Seltzer et al. [153] on octadecyltrichlorosilane (OTS) shows that the coating can sustain higher temperatures up to 170 °C. Surface science techniques help to characterize the quality of the coating materials to the precision of monolayers [155,156]. However, the influence of this coating's temperature coefficient on the clock transition is not yet known and may be expected to have an important impact on the achievable clock stability.

Chapter 6 Spectroscopy and Clock with Enlarged Buffer-Gas Cell

If I have seen further than others, it is by standing upon the shoulders of giants.
-Issac Newton

The short-term frequency stability of a clock (in terms of Allan deviation) is inversely proportional to the atomic quality factor and to the signal-to-noise (S/N) ratio [32]. This implies that a narrow linewidth of the atomic clock signal increases the atomic quality factor and thereby improves the short-term clock stability (cf. Section 3.3). A larger dimension of the rubidium cell results in a higher atomic quality factor and allows interrogating more atoms with the standing microwave field, and gives a better S/N ratio (see Section 3.2.3). The number of active atoms participating in giving the DR signal could be increased by increasing the cell volume (considering the operation at similar temperatures as the conventional clocks).

With the above motivation, this chapter investigates the possibility and potential of using an enlarged cell of 25 mm diameter (cf. Section 3.2.2) filled with ^{87}Rb and a mixture of buffer gases. The magnetron cavity that accommodates this cell and resonates at 6.835 GHz was especially developed in this work that was seen in Section 3.5.1 and the overall physics package assembly was shown in Section 4.3.

This chapter is dedicated for metrological investigations of the 25 mm cell physics package and its clock performance studies in short- medium- and long-term time scales using the *clock laser head* (cf. Section 2.2.1). Similar experiments were done using the prototype and the optimized cavities (cf. Section 3.5). Here we present the results of the optimized cavity with the clock laser head. However, a comparison will be made in short-term performance with that of *the prototype cavity* results. Also, use of the *AOM laser head* with prototype cavity is demonstrated in this chapter.

6.1 Studies using the clock laser head

6.1.1 DR signals

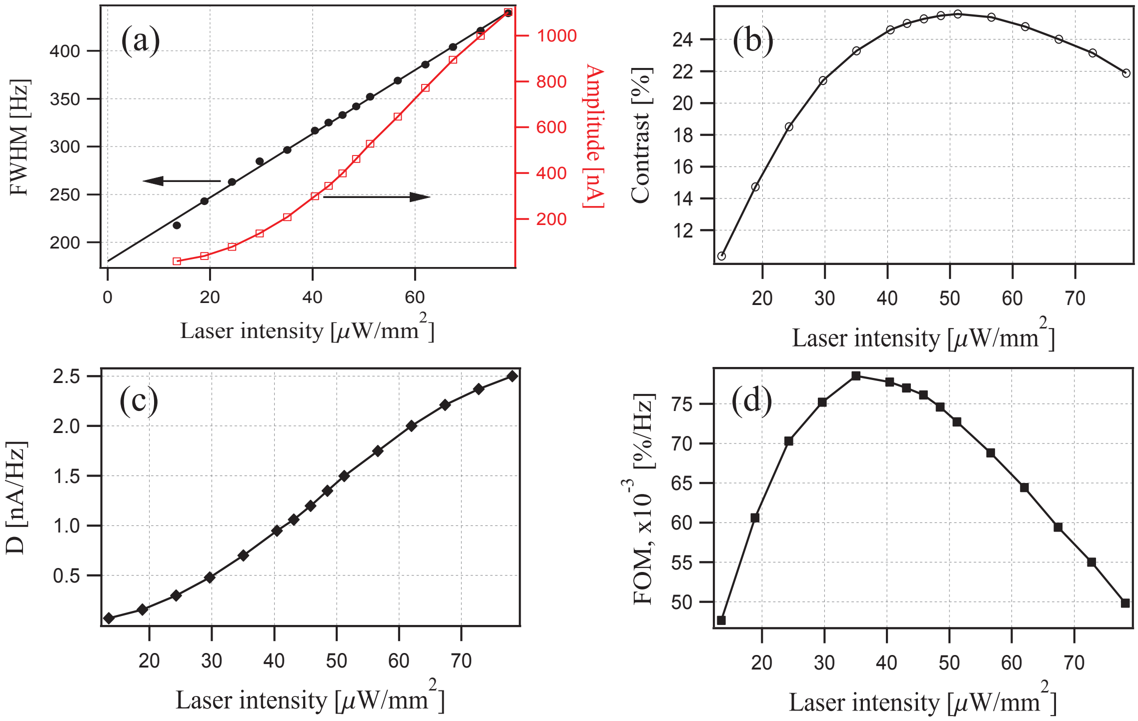

Figure 6.1: *Typical DR parameters as a function of laser intensity (I_L). Fixed microwave power P_μ = -34 dBm, cell volume temperature, T_v = 336 K and stem temperature, T_s = 321 K. (a) left axis: DR linewidth (open circles) as a function of I_L, and right axis: DR amplitude (open squares) as a function of I_L, (b) DR signal contrast (Amplitude/background) as a function of I_L, (c) Discriminator slope as a function of I_L, and (d) the Figure-of-Merit - FOM (Contrast/FWHM) as a function of I_L. Note that the laser intensity values on x-scaling is not calibrated after the telescope assembly, rather it is the intensity at the input of the telescope assembly. The values seen by atoms after the telescope assembly is approximately two orders of magnitude less.*

The characterization of 25 mm buffer gas cell was performed as a function of laser intensity and microwave power, similar to the procedure explained in Section 5.3.1. The laser frequency was stabilized to CO10-11 transition (cf. Fig. 2.3). At first, the cell temperature coefficients were measured (cf. Section 6.2.3) and the cell volume temperature was regulated at the minimum TC condition, i.e. at the inversion temperature value of $T_v = 336$ K and the stem temperature was set at $T_s = 321$ K. The

Rb atomic density inside the cell volume is mainly determined by the stem temperature T_s, however if there are any Rb metallic droplets present inside the cell volume, they contribute strongly to the Rb atomic density. Because we temperature regulate our clock vapor cell, such that $T_s < T_v$, depending on the amount of metallic Rb present inside the cell volume, it will take up to a duration of few days to couple of months for this metallic Rb in cell volume to move into the stem (reservoir). This effect is studied in Section 6.4.5.

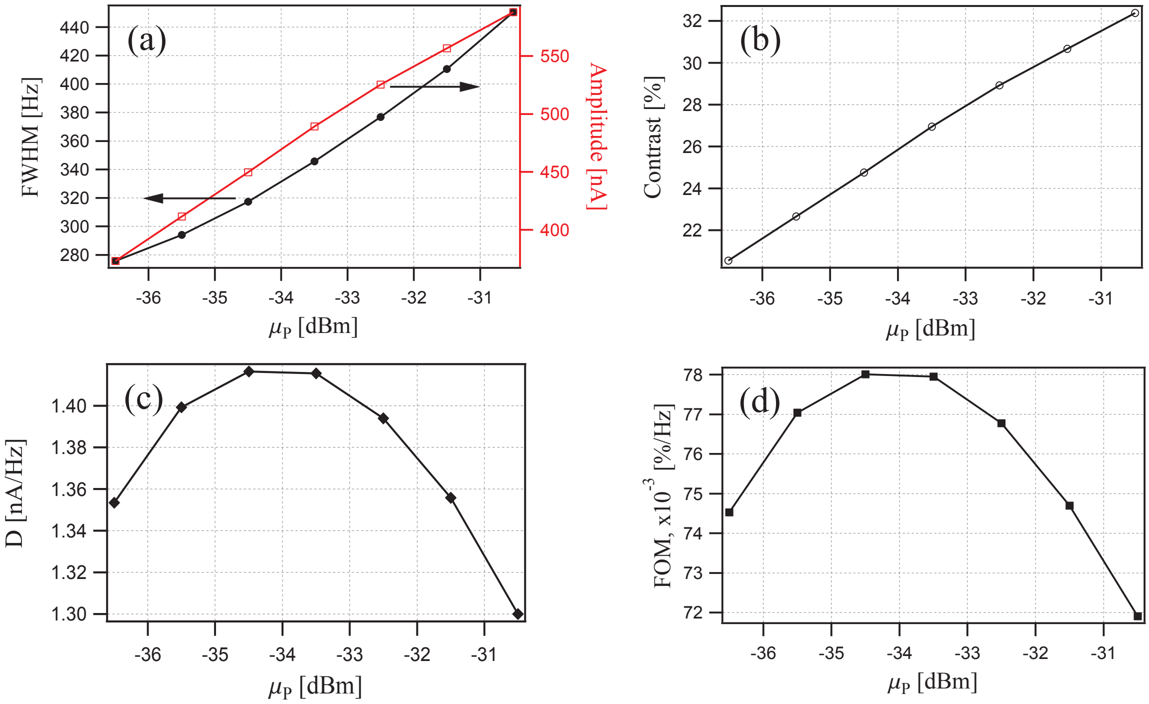

Figure 6.2: *Typical DR parameters as a function of microwave power. Fixed laser intensity* $I_L = 35\ \mu W/mm^2$*, cell volume temperature,* $T_v = 333$ *K and stem temperature,* $T_s = 321$ *K. (a) DR signal linewidth (open circles) as a function of input microwave power (*μ_P*) into the cavity on left axis, and the right axis indicates the DR amplitude (open squares) as a function of input* μ_P*, (b) Contrast (Amplitude/background) as a function of* μ_P*, (c) Discriminator (Amplitude/linewidth) as a function of* μ_P*, and (d) FOM as a function of* μ_P*.*

The DR signal parameters as a function of laser intensity is shown in Fig. 6.1, the microwave input power was approximately set around -34 dBm. Note that the laser intensity values on x-scaling is not calibrated after the telescope assembly, rather it is the intensity at the input of the telescope assembly. The values seen by atoms after the telescope assembly is approximately two orders of magnitude less. Throughout chapter 6 the laser intensity values are considered at the telescope input. In

Fig. 6.1(a), extrapolation of the linewidth (FWHM = $\Delta\nu_{1/2}$) to zero laser intensity, we get the value of intrinsic linewidth as 180 Hz. This determines the linewidth that is broadened by the mechanisms discussed in Section 1.3 and compares well with our calculated value of 160 Hz in Table 1.3, which is approximately two times narrower than coated 14 mm cell. The coherence relaxation time of the clock transition can thus be calculated using Eqn. 1.21 as 1.8 ms; this value is a factor of two higher than that obtained for the wall-coated cell of 14 mm diameter (cf. Section 5.2.2).

Once the optimum value for input laser intensity was obtained, for instance in the above optimization (Fig. 6.1) it is I_L = 35 μW/mm^2, this parameter is fixed (kept constant) and then the DR signal optimization was done as a function of input microwave power as shown in Fig. 6.2.

The optimized laser intensity of 35 μW/mm^2 and microwave power of -34 dBm were input to the physics package and the measured optimized DR signal is shown in Fig. 6.3. The DR signal has an amplitude of 0.48 μA, a linewidth (FWHM, $\Delta\nu_{1/2}$) of 334 Hz, and a contrast of 26 %. The theoretically estimated total broadening of 350 Hz (cf. Table 1.6) matches well with the measured value of $\Delta\nu_{1/2} = 334$ Hz (cf. Fig. 6.3). The shift of the Rb-hyperfine centre frequency ν_{Rb} due to buffer gas pressure (19.5 torr) is measured as 3390 Hz, this is in excellent agreement to the estimated value of 3385 Hz (see Section 1.5.3). The error signal corresponding to the DR lorentzian is shown in the inset of Fig. 6.3. This is obtained by frequency modulating the DR signal as explained in Section 1.4.4. A linear fit to the error signal gives a discriminator slope of 1.52 nA/Hz, this is in good match to $>$ 90% with the estimated value of D ($\sim A/\Delta\nu_{1/2}$) = 1.44 nA/Hz.

6.2 Perturbation studies on clock transition

Similar to the perturbation effects studied in Section 5.4, we experimentally evaluate the effects due to light, microwave and temperatures on the clock's frequency in medium- to long-term time scales. The experiments presented in this section were performed using *the clock laser head* (D_2-line, no AOM, cf. Section 2.2.1).

6.2.1 Light-shifts

The AC Stark shift of the electromagnetic field on the clock transition is an unavoidable phenomenon when in CW operation as explained in Section 1.5.2. Further, we measure the effect separately as a function of laser intensity, known as intensity

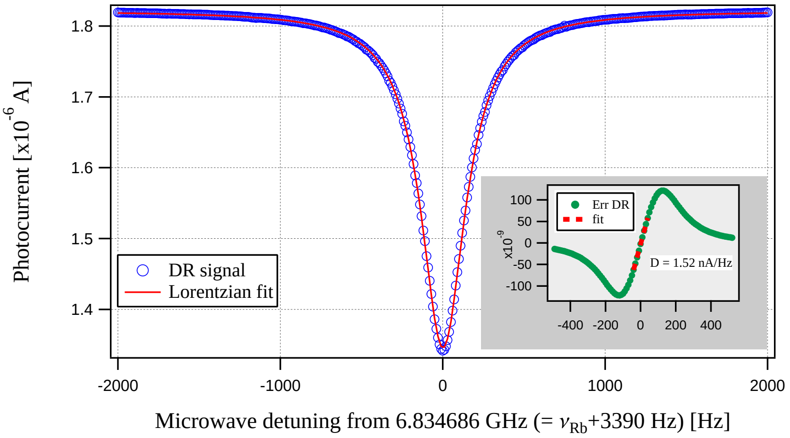

Figure 6.3: *DR spectroscopic signal with the 25 mm BG cell. It exhibits an amplitude A = 0.48 µA, background level Bk = 1.82 µA and contrast C = 26% and linewidth $\Delta\nu_{1/2}$ = 334 Hz. The microwave centre frequency was set to 6.834686 GHz that is higher than ν_{Rb} by 3390 Hz due to a buffer gas pressure of 19.5 torr. The inset shows the demodulated error signal with a discriminator slope of D = 1.52 nA/Hz, to which the microwave synthesizer is stabilized at the centre.*

light-shift coefficient, α and as a function of laser frequency, the frequency light-shift coefficient, β.

(i) Intensity light-shift coefficient, α

Figure 6.4(a) shows the relative clock frequency shift as a function of laser intensity impinged on the physics package. The intensity light shift coefficient was measured for the laser stabilized to three optical reference lines in the evacuated reference cell, i.e., 2-3; CO22-23; and CO21-23 on $F_g = 2$ and one transition CO11-01 of $F_g = 1$ (see Fig. 2.3). The clock shift (y-scaling) is in relative frequency units referred to active H-maser. Note that the y-scaling of all the graphs in this chapter are in relative frequency shift; referred to the active H-maser reference frequency. The lowest value obtained for CO11-01 transition is -2.85(2)$\times10^{-12}$ mm^2/μW.

Figure 6.4(b) shows the intensity light-shift coefficient, α as a function of laser frequency detuning. This quantifies the detuning required in laser frequency from a given sub-Doppler transition, in order to reduce the effect of intensity light shift, α on the clock transition (similar to as discussed in Section 5.4.1). For example, for the CO22-23 transition, a detuning of 102±5 MHz is required to substantially reduce the effect of intensity LS. Furthermore, the detuning of laser frequency has been experimentally demonstrated using the AOM laser head in Section 6.3.1. It is also possible to tune the optical line by buffer gas pressure [21,96]. From Fig. 6.4(b), we need a negative detuning of $\sim$ 23 MHz to CO21-23 line in order to reach almost zero intensity LS coefficient α, this can be achieved by reducing the BG pressure by $\approx$ 1.3 torr [67]. This reduction in pressure would also impact in reducing the FWHM and β (by operating at lower light intensities to get similar DR signal). The contribution due to α on clock's frequency is evaluated in Table 6.4.

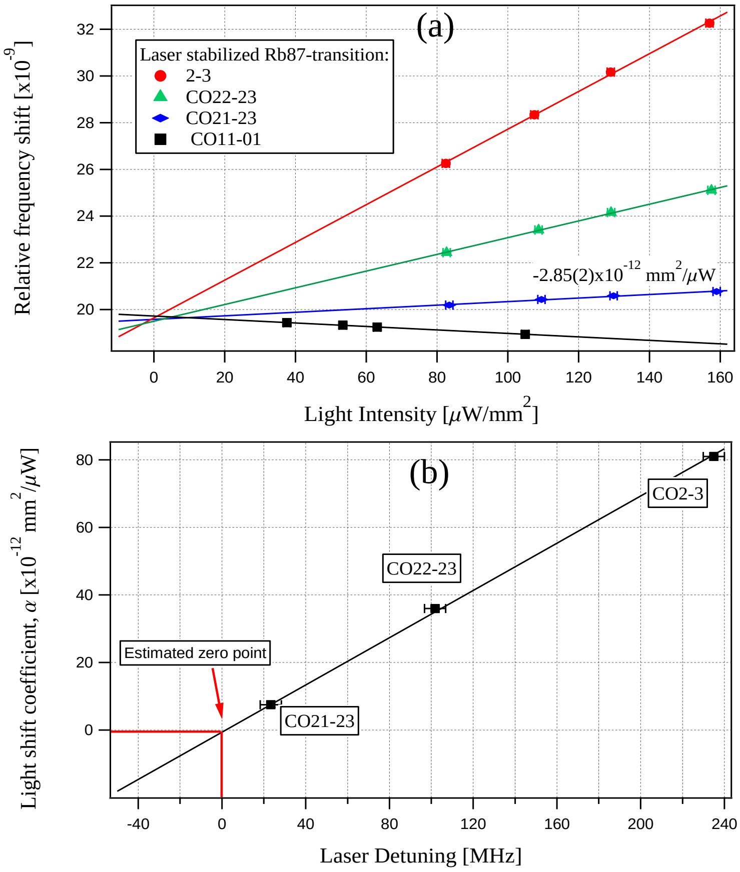

Figure 6.4: *(a) Clock frequency shift as a function of laser intensity for different Rb sub-Doppler transitions (see Fig. 2.3). The y-scaling shows relative frequency shift as the clock is referred to active H-maser. (b) Estimated detuning required to suppress the intensity LS. Zero on the x-scale represents the zero on Fig. 1.13 and defines the reference point to which the detuning from optical transitions is required to get zero LS coefficient α.*

(ii) Frequency light-shift coefficient, β

The frequency LS coefficient is explained in Section 1.5.2(B), as $\beta = \frac{\delta\nu_{LS}}{\delta\nu_L}$. By fixing the laser intensity, the value of β evaluated as the slope of the line-fit is shown in

Fig. 6.5(a). The frequency LS can be nullified, e.g. in pulsed mode [56]. In the continuous-wave operation discussed here, this is not possible. However, one can reduce the effect of β by operating at low light intensities as shown in Fig. 6.5(b), which is linear in I_L, as expected from Eqn. 1.42. Unlike the wall-shift explained in Fig. 5.10, here the zoom-inset at zero laser detuning frequency shows the uncertainty in measuring the BG shift. At the operating intensity of $I_L = 35\ \mu\text{W/mm}^2$, the value of $\beta = 12{\times}10^{-18}\ \text{Hz}^{-1}$ (or 82 mHz/MHz), and its effect on clock frequency instability is evaluated in Table 6.4

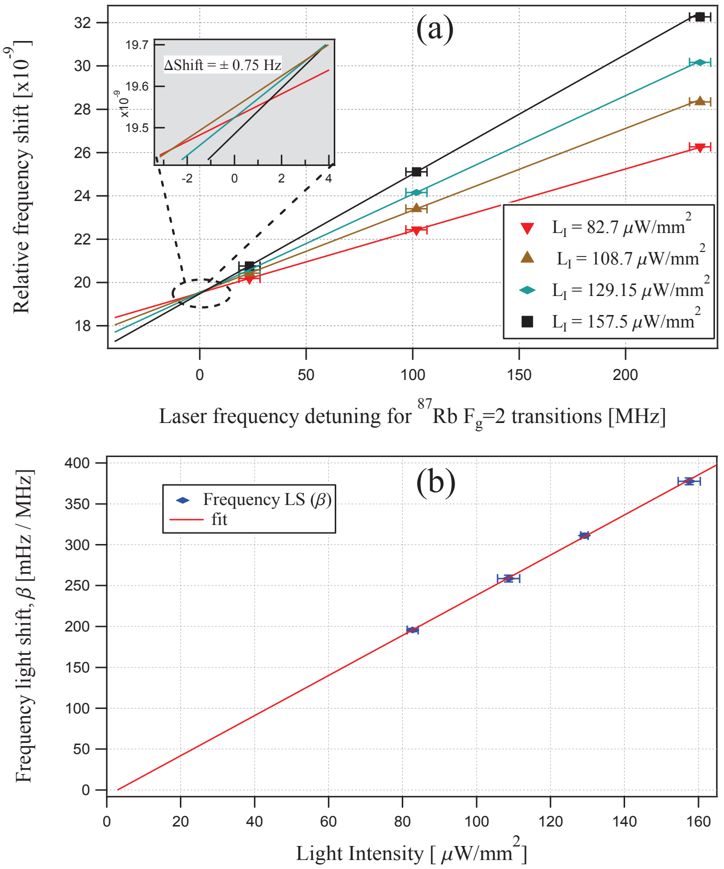

Figure 6.5: *(a) Clock frequency shift as a function of laser frequency. Zero on the x-axis denotes the same reference point as represented in Fig. 6.4(a), the inset shows the uncertainty in estimating the BG shift and (b) the frequency light-shift coefficient, β as a function of input laser intensity. The value will be approximately similar for $F_g = 1$ to excited state transitions [21].*

6.2.2 Microwave power shift

The microwave power shift in buffer gas cell is an unavoidable phenomenon, because the atoms are relatively motionless during the interaction, thereby causing the detected overall signal to be an inhomogeneous integration over the occuring spatial gradients (cf. Section 1.5.5). This is measured by fixing the laser intensity and by quantifying the dependence of clock frequency as a function of the microwave power input to the cavity. The process is repeated for different laser intensities and at each microwave power, the value was extrapolated to zero laser intensity, I_L, hence it is *light-shift free* measurement. Finally, the slope of these values as a function of microwave power gives the *pure microwave power shift* on the clock frequency. A shift of $< 5{\times}10^{-13}$/dBm was measured, as shown in Fig. 6.6. Its effect on medium to long-term clock frequency is evaluated in Table 6.4.

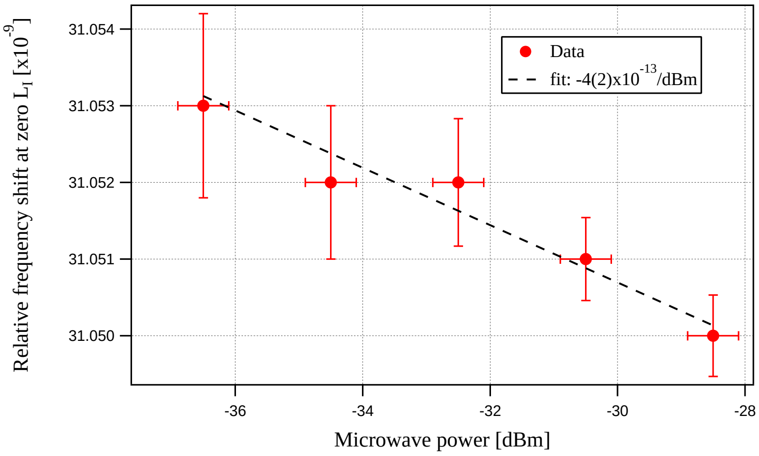

Figure 6.6: *Clock frequency variation as a function of injected microwave power into the cavity (MWR).*

This value of microwave PS (reported in Fig. 6.6) is three orders of magnitude lower than that reported for wall-coated cell (cf. Section 5.4.2), where we had not nullified the effect due to the light shift. Also, note that the intensity light shift value for wall-coated cell (e.g. $\alpha = 2.3$ Hz·mm$^2/\mu$W) is two orders of magnitude higher than that for the buffer gas cell case ($\alpha = 19.5$ mHz·mm$^2/\mu$W). At this reduced intensity light-shift coefficient (α), the microwave PS coefficient (in Hz/dBm) depends on the interrogating laser light intensity as shown in Fig. 6.7. For instance, at an input laser intensity of ≈ 8 μW/mm^2, one can nullify the effect of microwave power shift. A clear experimental validation of this dependance of LS on microwave PS is done using the AOM LH at reduced light-shift values in Section 6.3.2.

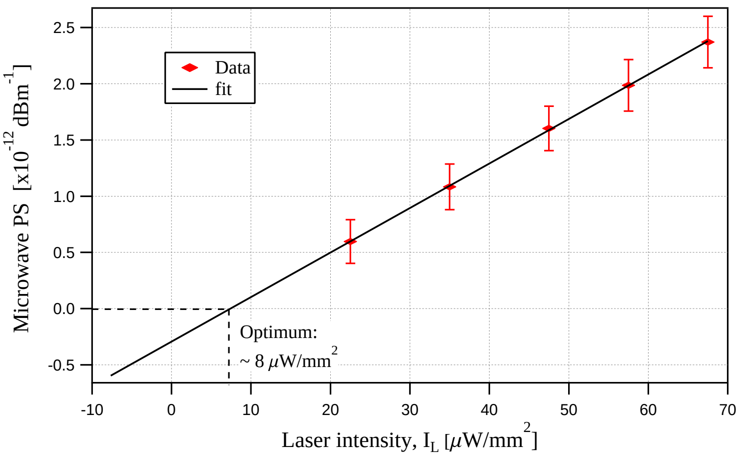

Figure 6.7: *Microwave PS dependance on input light intensity with a slope of +3.9(6)×10^{-14} mm$^2\mu$W$^{-1}\cdot$dBm^{-1}. The laser was stabilized to the CO11-01 transition (cf. Fig.2.3) and had an intensity LS α = -19.5 mHz·mm$^2/\mu$W.*

6.2.3 Temperature coefficients

A major drawback of the use of paraffin coated cells to get a better medium and long-term stability was the temperature coefficient due to the coating material (tetracontane, in our case). In the 25 mm cell studied here, the mixture of argon and nitrogen are used as buffer gases with a ratio, $r = \frac{P_{Ar}}{P_{N_2}} = 1.6$, and a total pressure of 26 mbar (19.5 torr). From Table 1.4, argon has a negative linear temperature coefficient, whereas nitrogen has a positive linear temperature coefficient and due to their (much smaller) quadratic temperature coefficients, the mixture of these two at a certain temperature can give, in principle a “zero” (or inversion point) temperature coefficient [32, 98]. For our gas mixture we calculate a zero temperature coefficient around 63±1 °C (or 336±1 K) from Eqn. 1.44. The inaccuracy in determining the TC value is because of practical reasons that when sealing the cell, the pressure can vary by about 5% and also due to the uncertainties of the BG coefficients [157].

When the stem temperature was fixed (T$_s$ = 321 K), a good temperature coefficient value of TC_v = -1(1)×10^{-12}/K has been achieved at the inversion temperature point by a linear fit (cf. Fig. 6.8(a)), and the quadratic TC gives a value of -4.34(4)×10^{-12}/K^2. The temperature coefficient was also measured as a function of the stem temperature changes (cf. Fig. 6.8(b)), at fixed T$_v$ of 336 K. Table 6.1 shows the measured temperature coefficients for the Ar/N$_2$ buffer gas mixture in our enlarged 25 mm cell having a total pressure of 26 mbar (19.5 Torr).

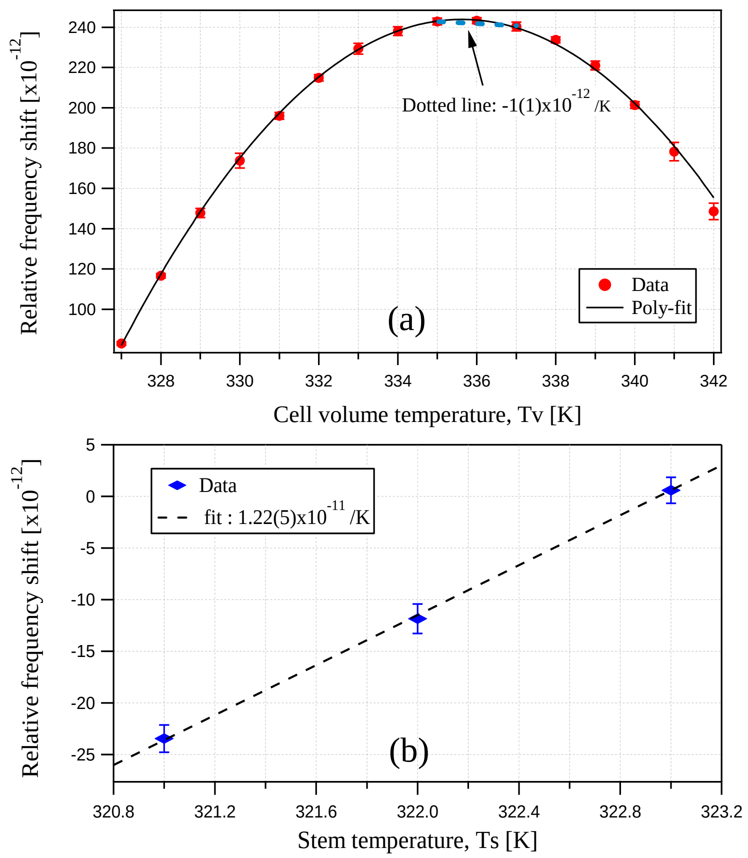

Figure 6.8: *(a) Temperature coefficient of the 25 mm BG cell as a function of the cell volume temperature, and (b) Temperature coefficient as a function of stem temperature.*

Table 6.1: *Measured coefficients (from Fig. 6.8) of Ar and N_2 BG mixture contributing to the temperature coefficient of the Rb vapor cell. This measured data matches well with the calculated ones in Table 1.5.*

	β' [Hz·Torr^{-1}]	δ' [Hz·Torr^{-1}·°C^{-1}]	γ' [Hz·Torr^{-1}·°C^{-2}]
Measured	175.25	9×10^{-2}	-0.74$\times10^{-3}$

6.2.4 Spin exchange frequency shift

The spin-exchange collisions that are responsible in giving rise to the frequency shift of the clock transition were explained in Section 1.5.4 (Eqn. 1.45), as function of temperature. In our BG cell PP, at an operating cell volume temperature T_v = 336 K, $\bar{v}_s \approx 2.86\times10^4$ cm·s^{-1}, and at the stem temperature of T_s = 321 K the Rb atomic density $n = 2\times10^{11}$ cm^{-3}. For the condition in which atoms are pumped from $F_g = 1$ state, $\Delta = +1/5$. Therefore, with the above values in Eqn. 1.45, one gets an absolute frequency offset of $\Delta\nu_{SE} \approx$ -0.3 Hz or $\frac{\Delta\nu_{SE}}{\nu_{Rb}}$ = -4.6$\times10^{-11}$. The dependance on temperature in our stem operating range around 321 K, we can consider that the Rb density increases 10% for increase in every kelvin, hence we calculate $\Delta T_{SE} \approx$ -5$\times10^{-12}$/K. This value is about a factor of two smaller than the observed stem TC shift of $TC_v = \sim 1.2\times10^{-11}$/K (cf. Fig. 6.8(b)) and also has an opposite coefficient. We call the observed effect, which is not due to Rb density changes as stem "fast" effect and analyze by attributing it to the geometrical effect of the cell and stem as discussed briefly below and quantified in Section 6.4.4.

This "fast" effect may be interpreted as a standard temperature coefficient resulting from the unavoidable overall cell temperature gradient, resulting from any temperature change in the stem. This effect could also occur due to the presence of any metallic Rb in the cell volume. The TC effect observed due to stem is termed as "fast effect" to distinguish the effect that will be observed further over long-time scales (cf. Section 6.4.3). A change in Rb density was recorded by measuring the Doppler absorption profiles by changing the stem temperatures. It was verified that at the short timescales (few minutes to 1 hour), no change in the Rubidium density was observed. Such a change in Rb density was however seen by waiting sufficiently long (> few hours to days) as shown in Fig. 6.9. This we term as "slow effect" due to stem temperature changes, which will be explained in Section 6.4.3.

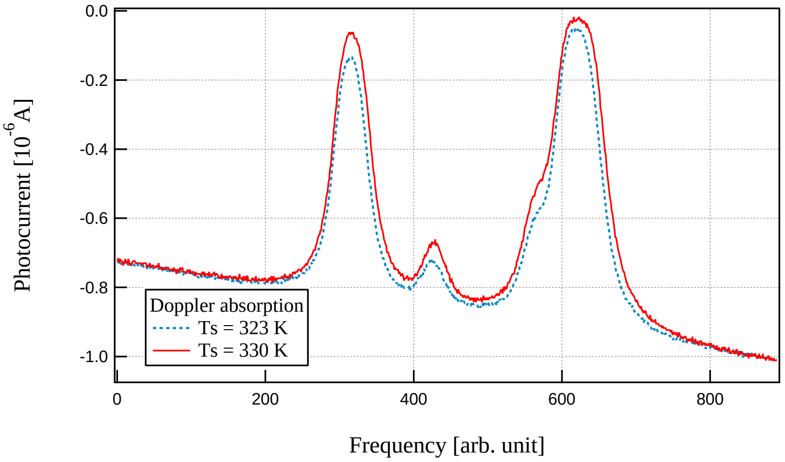

Figure 6.9: *Change of Doppler absorption of the clock cell by changing the stem temperature from 323 K (dotted line) to 330 K (solid line). The trace of 330 K was measured 1.5 days after the change of stem temperature was made.*

The above analyzed perturbing parameters and their influence on the clock's stability at 10^4 s is summarized in Table 6.4. The consideration of 10^4 s is optimal in view of accessing the medium- to long-term stability of clock, and is also accesible via relatively short data sets of one to few days only.

6.3 Studies using the AOM laser head

The spectroscopic studies using the AOM laser head are presented in this section. We have not used the AOM laser head for the clock stability studies, as the intensity light-shift value obtained by the clock laser head (cf. Section 6.2.1) is sufficiently small to reach medium- to long-term time scales below $1{\times}10^{-14}$ level (cf. Table 6.4). *The prototype cavity* was used in these studies (purely due to logistical reasons of the availability of the cavities). This however will not affect the kind of studies done here, except for the microwave power shift, which can have values further reduced by using *the optimized cavity.*

6.3.1 Reduction of intensity LS effect by detuning method

The intensity LS contribution can be significantly reduced to a negligible value by detuning the laser frequency using an Acousto Optical Modulator (AOM). To facilitate this possibility, a stabilized laser head with integrated AOM was developed (cf. Section 2.2.2). The detuning required from a particular sub-Doppler transition was estimated in Fig. 6.4(b). The α LS coefficient measured for different laser frequency fine detunings with respect to the CO22-23 atomic transition using the AOM laser head is shown in Fig. 6.10(a). At a detuning of 108.5 MHz, we observe a minimal value of α giving $6.6(4){\times}10^{-14}$ mm$^2/\mu$W. This value is lower by a factor of ‘43’ compared to that measured with the clock laser head (cf. Section 6.2.1). By carefully adjusting the frequency detuning, one can reduce the intensity LS coefficient α value to be even less.

Figure 6.10(b) shows the laser frequency light shift, β as a function of the laser input intensity. Here, for example, the value at 35 μW/mm^2 is increased by a factor of ‘1.5’ in contrast to the value obtained by the clock laser head (cf. Fig. 6.5(b)). This could be due to the tricky task of precisely measuring the incident intensities in the two cases studied. It is useful to quantify for this additional noise at future stages, when AOM is required for the clock operation.

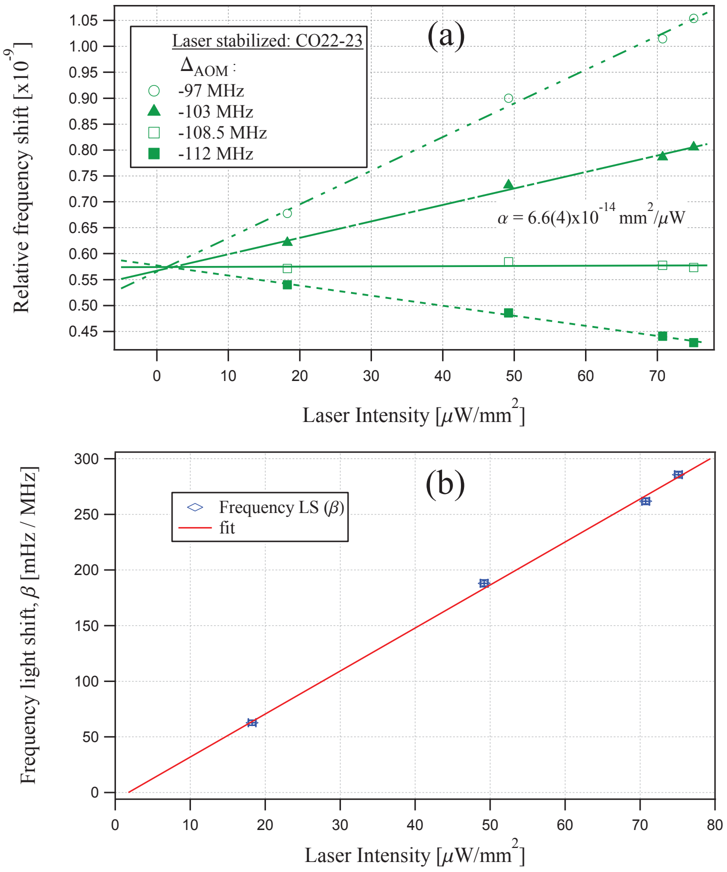

Figure 6.10: *(a) Intensity LS, α measured using the AOM laser head for CO22-23 transition corresponding to estimation done (see Fig. 6.4(b)), and detunings are shown in the inset. (b) Frequency LS, β as a function of input laser intensity, extracted from graph (a).*

6.3.2 Microwave power shift

At a reduced intensity light-shift condition, it was appropriate to study the dependence of clock frequency shift upon the microwave power. Figure 6.11(a) gives the microwave power shift coefficients μ_{PS} (clock frequency change as a function of injected microwave power into the cavity).

The dependence of microwave power shift on light intensity is clearly demonstrated in Fig. 6.11. At an input laser intensity of 68 μW/mm^2 we get a positive microwave PS of 1.56(5)$\times10^{-11}$/dBm and for 29 μW/mm^2, we get a negative microwave PS of -1.1(5)$\times10^{-11}$/dBm. In this case, with AOM LH the intensity LS α is reduced by a factor of '40' compared to that of the α obtained by the clock laser head (cf. Section 6.2.1). Therefore, the dependance of the microwave PS on input light intensity of $\sim$29 μW/mm^2 is clearly demonstrated and seen that it is possible to operate the clock at higher input light intensity to reach the condition of zero microwave PS (compare Fig. 6.7 and Fig. 6.11(b)).

Because the intensity light-shift contribution is substantially reduced, this behavior we believe is similar to the “pseudo light-shift” effect, as observed in pulsed optical pumped clocks [56, 158]. This is also called as the “position shift”, as it is dependent on the microwave field inhomogeneites in the physics package. This inhomogeneous behavior is due to the reason that the resonant frequencies of Rb atoms inside the cavity depend on their position inside the cell during their interrogation with the microwave field. Hence, the observed microwave PS is a weighted average of the individual frequencies along the length of the cell, and this weighted average is dependent on the laser intensity, hence mimicking the off-resonant light-shift behavior [56].

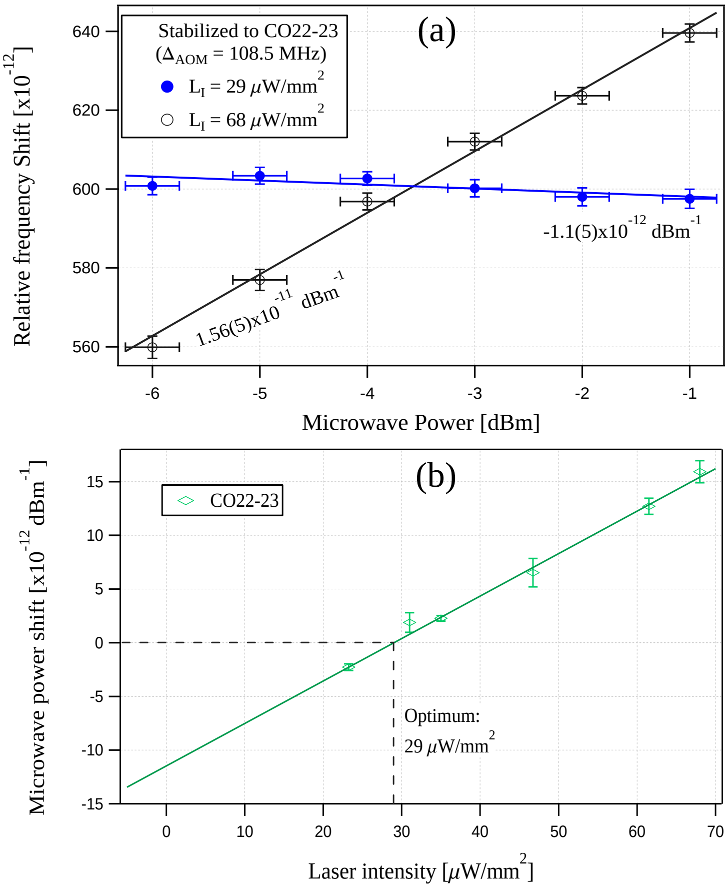

Figure 6.11: *(a) Microwave power shift for CO22-23 transition at reduced intensity light shift detuning of 108.5 MHz and (b) its dependence on light intensity with a slope of +3.9(2)×10*$^{-13}$ *mm*$^2\mu W^{-1}\cdot dBm^{-1}$.

It is important to recall that the measurements with AOM LH were made using the *prototype cavity* physics package, where the microwave PS will have higher values due to field inhomogenities compared to the values obtained with *optimized cavity* physics package. This higher inhomogeneity effect can be clearly observed in the microwave PS values of Fig. 6.7 and Fig. 6.11(b). However, the effect of light-shift dependance is quite strong that it can be observed even in a cavity with inhomogeneous field mode.

6.3.3 Temperature coefficients

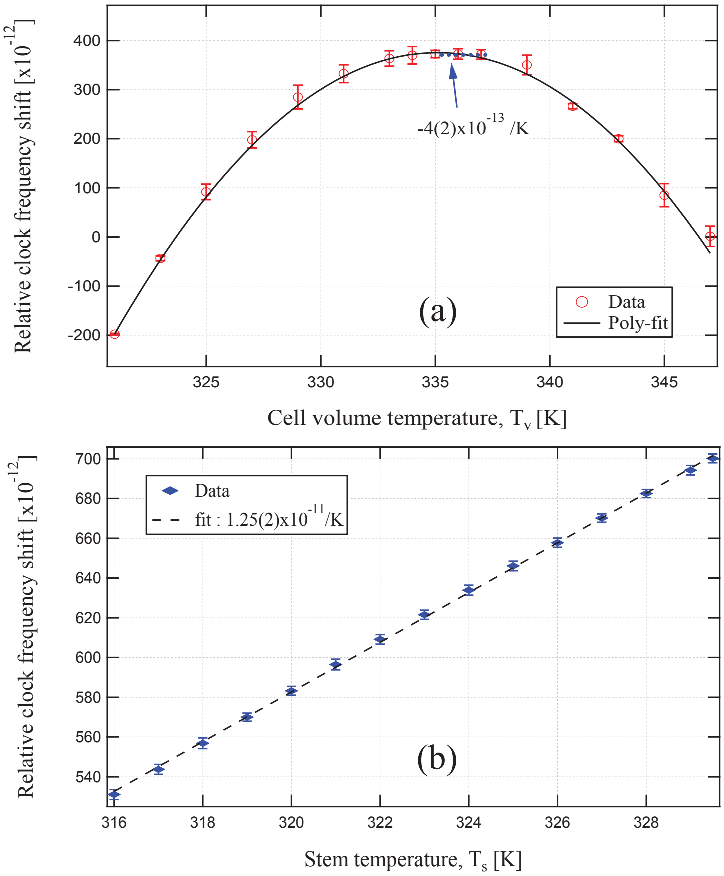

Figure 6.12: *(a) TC of the cell by reducing the LS and microwave effects, (b) similar studies on the TC of the stem.*

Exploiting the reduced light-shift and microwave power shift conditions, the temperature coefficient of the resonance cell was evaluated with improved accuracy. The clock's frequency shift as a function of the cell volume temperature is shown in Fig. 6.12(a). And, Fig. 6.12(b) shows the stem (fast) temperature coefficient. The TCs of cell volume and stem are measured to be almost the same as with the clock laser head (within the error bars). In principle, one can conclude that there is no substantial effect due to the light-shift coefficients (α and β) and microwave power shift on the cell and stem's temperature coefficients.

6.4 25 mm buffer-gas cell clock

In this section, we present the frequency stability results of the 25 mm optimized cavity physics package obtained by closing the clock loop (see Section 4.1). Here, we used the clock LH.

6.4.1 Short-term noise budget

As mentioned in Section 1.4, we consider 1 to 100 s averaging time range for short-term analysis. The noise budget analysis is done in few steps as explained below. At first, the discriminator slope of the clock error signal is measured (cf. inset of Fig. 6.3). This will be useful in estimating the contribution of the instability caused by the respective sources on the clock's frequency. The shot-noise limit is estimated by considering the dc photocurrent, I_{dc} = 1.585 μA at the FWHM of the DR signal by using the formula shown in Eqn. 1.38. In the following section, the complete noise budget analysis is presented, by estimating the contributions of the S/N and shot-noise limits.

(i) Signal to noise estimation

Table 6.2 gives the details of the noise sources and their contribution to the clock frequency instability. *Detector dark noise* was measured when the laser and microwave were off. The *shot-noise limit* was estimated by using the Eqns. 1.38 and 1.35. Impact of the *microwave noise* on the photodetection noise was measured using the FFT (SR770) in the following condition: the difference in noise was taken between two measurements - when microwave was on and microwave was off, the laser was kept on in both cases. This noise includes detector dark noise + stray light between physics package and detector assembly. *LO input noise* was measured by recording the Allan stability. This was done by using dividers (100 and 1000) before feeding the clock signal input to the LO, and the corresponding Allan stabilities were measured using picotime comparator referenced to 10 MHz H-maser. It was also important to change the gain of the clock loop accordingly with the divider used. Finally, knowing the stability at 1 s for each measurement (once using 100x divider and then with 1000x divider), we estimate the contribution to the clock by the LO. This will give

Table 6.2: *Signal to noise (S/N) short term budget of the 25 mm cell clock with, FWHM ($\Delta\nu_{1/2}$) = 334 Hz, C = 26%, D = 1.5 nA/Hz (cf. Fig 6.3).*

Sl. no.	**Source**	**Noise (pA/$\sqrt{\text{Hz}}$)**	**Inst. σ_{inst}(y) $\tau^{-1/2}$**
1	Detector dark noise	0.362	2.49×10^{-14}
2	Shot-noise limit	0.712	4.91×10^{-14}
3	Microwave noise	0.736	5×10^{-14}
4	LO input noise	0.075	5.17×10^{-15}
5	Total due to microwave (3+4)	0.74	5.1×10^{-14}
6	Laser noise (microwave off)	1.46	1×10^{-13}
7	Total S/N limit (1+5+6)	1.676	1.15×10^{-13}
8	S/N measured (clock loop)	1.7	1.17×10^{-13}

the noise not only by the microwave loop but it takes into consideration of all the other electronics used in the microwave synthesizer. The *laser noise* was measured, when the microwave was off. Eventually, the *total noise* is estimated by taking the square root of the sum of the squares of all the above noises (detector dark noise + microwave noise + LO input noise + laser noise). The total *signal-to-noise (S/N)* limit was measured when the clock loop was closed at a modulation frequency of f_m = 44 Hz (see Fig. 6.13). The optimum modulation depth is set to 100 Hz (i.e. 0.3 times the FWHM [157]).

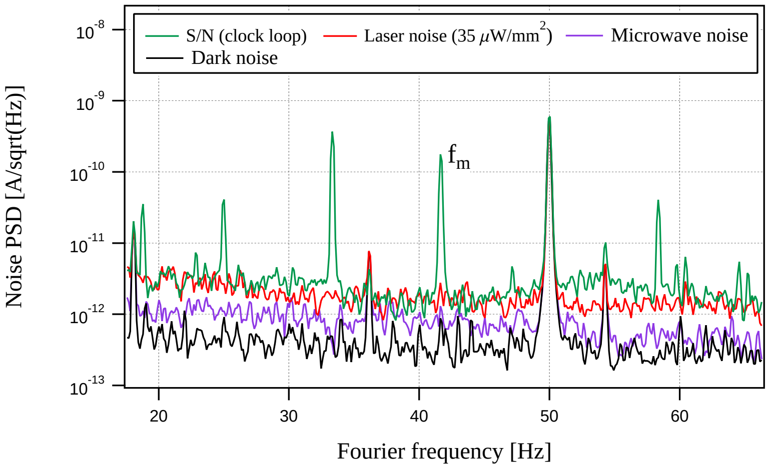

Figure 6.13: *Noise power spectral densities measured using an FFT analyzer (SR770).*

Fig. 6.13 shows the measured noises corresponding to the values given in Table 6.2. One can clearly distinguish the peaks at beat frequencies between the f_m and 50 Hz electronics noise.

(ii) Phase noise estimation

Additional instability arises from the LO PM noise, see Section 2.6.2. By using the Eqns. 2.3 and 2.4, at $f_m = 44$ Hz and considering the even harmonics up to 100 kHz, we estimate the contribution of the phase noise due to aliasing effect to be $\sigma_y(\tau) = 7.46\times10^{-14}\ \tau^{-1/2}$.

(iii) Light-shift estimation

The intensity and frequency light-shift coefficients also influence the short-term stability of the clock (as explained in Section 1.4.4), *via* the laser's intensity instability and laser frequency instability, which perturb the clock transition on short-time scales. Table 6.3 summarizes these effects and resulting limits on the short-term clock stability.

Table 6.3: *Intensity- and frequency light-shift contribution to the clock's short-term instability.* I_L *= 35* $\mu W/mm^2$ *and* ν_L *= 384.23 THz.*

Physical effect	**Coefficient**	**Variation**	**Formula**	**Inst.** $[\tau^{-1/2}]$
Intensity- light shift,$\lvert\alpha\rvert$	19.5 mHz·mm^2/μW	Laser int. instab.: $\sigma_{\Delta I_L/I_L}(\tau) < 3\times10^{-5}$	1.36a	3×10^{-15}
Frequency- light shift, $\lvert\beta\rvert$	82 mHz/MHz	Laser freq. instab.: $\sigma_{Lf} =< 8\times10^{-12}$(1 - 100 s)	1.36b	3.7×10^{-14}
Total LS instab., σ_{LS}				4×10^{-14}

(iv) Sum of contributions on Short-term stability

The overall short-term clock stability can be estimated from the sum of the squares of the individual limits of S/N, LO phase noise and LS by Eqn. 1.37 as $\sim 1.4\times10^{-13}\ \tau^{-1/2}$. The major contribution comes from the S/N limit, mainly due to laser FM-to-AM noise conversion in the atomic vapor [86, 159] (see laser noise in Table 6.2).

6.4.2 Measured short-term stability

The LO output microwave frequency was locked to the center of the clock discriminator signal (slope of inset error signal in Fig. 6.3) with an optimized modulation frequency $f_m = 44$ Hz and a modulation depth of 100 Hz, satisfying the quasi-static model ($1/f_m > T_1 \approx T_2$) by giving enough time for the atoms to interact (adjust

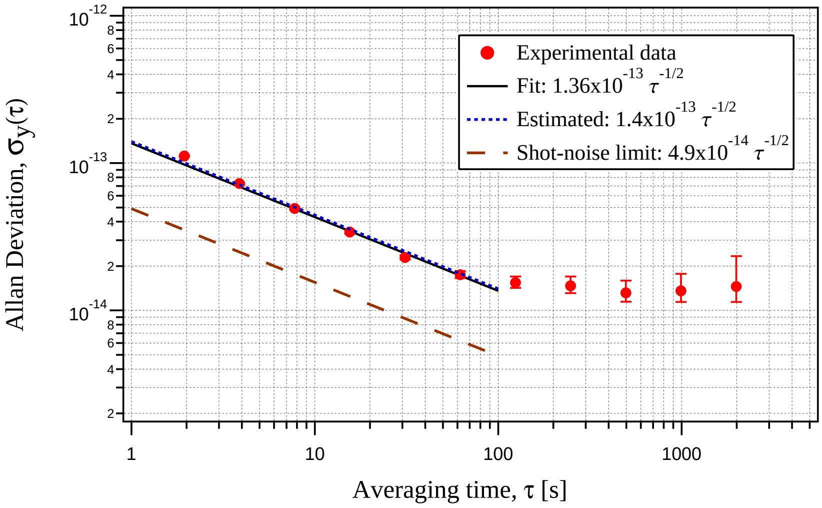

Figure 6.14: *Short-term frequency stability with the optimized cavity having TE_{011}-like mode. This stability is approximately a factor of '3' better than previously measured result of $4\times 10^{-13}\ \tau^{-1/2}$ with the prototype cavity [31].*

to the changing conditions) [32]. The modulation frequency was adjusted depending on the coherence life-time T_2 of the optically pumped polarized atoms. For measurements of the clock stability, the 10 MHz output from the LO's Oven Controlled Crystal Oscillator (OCXO) stabilized to the atomic clock transition is compared with a 10 MHz reference signal from an active H-Maser [160] using a frequency comparator (cf. Fig. 4.1). The clock frequency is recorded using a computer interface and the Overlapping Allan deviation plot of the frequency data is shown in Fig. 6.14. Short-term clock stability dominated by white frequency noise (cf. Fig. 1.9) is seen between 1-100 s. The solid line shows the fit to the experimental data (red dots) exhibiting an excellent clock stability of $1.36\times 10^{-13}\ \tau^{-1/2}$. Dotted line ($1.4\times 10^{-13}\ \tau^{-1/2}$) and the dashed line ($4.9\times 10^{-14}\ \tau^{-1/2}$) show the short-term S/N and the shot-noise limits, respectively. It is worthwhile to mention that the above stability result was achieved in a good equilibrium condition of the PP temperature.

This clock was operated in standard laboratory conditions (no vacuum enclosure or thermal chambers used). This short-term stability is comparable to the pulsed-optical-pumping clock operated under vacuum [107], is about a factor of five better than for a passive H-maser [20], a factor of 'two' better than previously reported state-of-the-art CW DR clock [86], and is approximately one order of magnitude better than the best lamp-pumped Rb clocks [161].

The stability of $< 1.4\times 10^{-13}\ \tau^{-1/2}$ is in excellent agreement with the estimated short-term limit (cf. Section 6.4.1). This stability is approximately a factor of 'three' better than the previously reported result [31], using *the prototype cavity.* The improvement is clearly due to the improvement of electromagnetic field distribution along the C-field (z-axis) in *the optimized cavity* (i.e., high field orientation factor (FOF)). This comparison matches well with our prediction by the ratio of the FOF (ξ^O_{exp}/ξ^P_{exp}) in Section 3.6.

6.4.3 Medium- and long-term studies

Figure 6.14 also shows the medium-term stability ranging from 100 s to 1000 s reaching the level of 1.5×10^{-14} due to flicker noise (cf. Fig. 1.9), after this the dominant noise sources cause limitation in the stability also giving rise to frequency drifts. In order to account for the overall range of medium-term and long-term stabilities, we estimate the influences of the perturbations due to light shift, microwave and temperatures at 10^4 s, as explained in Section 1.4. Especially, this time scale of 10^4 s, is essential in view of clock error prediction and synchronization for navigation clocks [31].

Table 6.4: *Summary of instability contributions of physical perturbations on the clock transition in medium to long-term time scales. The estimation is done for 10^4 s. The intensity and frequency stabilities of the laser heads are taken from Table 2.1.*

Physical effect	**Coefficient**	**Variation**	**Instab. at 10^4 s**
Intensity LS effect, $\lvert\alpha\rvert$	19.5(2) mHz·mm^2/μW	3.5×10^{-3} μW/mm^2	9.9×10^{-15}
Reduced int. LS,[a] $\lvert\alpha_{redu}\rvert$	0.45(3) mHz·mm^2/μW	10.5×10^{-3} μW/mm^2	6.9×10^{-16}
Frequency LS effect, $\lvert\beta\rvert$	82 mHz/MHz	<3.1 kHz	3.7×10^{-14}
Microwave PS, $\lvert\mu_{PS}\rvert$	15.3 mHz/μW	0.4×10^{-3} μW	8.9×10^{-16}
Cell volume TC $\lvert TC_v\rvert$ *(linear fit)*	1×10^{-12}/K	3.5 mK	3.5×10^{-15}
Cell volume TC $\lvert TC_v\rvert$ *(quadratic fit)*	4.34×10^{-12}/K^2	3.5 mK^2	5.3×10^{-17}
Stem TC $\lvert TC_s\rvert$	1.2×10^{-11}/K	4.6 mK	5.52×10^{-14}
Spin ex. shift $\lvert\Delta T_{SE}\rvert$	$<5\times10^{-12}$/K	~5 mK	$<2.3\times10^{-14}$
Cavity pulling $\lvert\Delta\nu_{CP}\rvert$	0.2 mHz/K	~5 mK	$< 1.5\times10^{-16}$

---

[a] Using AOM LH, refer table 2.1

The influences due to intensity-LS (α), frequency-LS (β), microwave power shift (μ_{PS}), and temperature coefficients due to cell volume (TC_v) and cell stem (TC_s) are summarized in Table 6.4. This detailed analysis of each effect gives the limits reached in the clock stability. From Table 6.4, we see that the clock instabilities arising due to frequency light-shift coefficient (β) and cell stem TC (TC_s) are the main limiting factors for the clock's performance to go below 1×10^{-14} over medium to long-term time scales. The influence due to β can be reduced by operating the clock with a lower light intensity (cf. Fig. 6.5(b)). For instance, at an input laser intensity of 17 μW/mm^2, one can estimate the influence of β on clock instability to be 9.6×10^{-15}. However, the present limitation is due to the TC_s. This effect is further studied quantitatively as explained in below Section 6.4.4.

6.4.4 Vapor cell geometric effect

As pointed out recently by Calosso et al., [162] a simple model of ideal gas law vindicates that the temperature fluctuation in the stem results in redistribution of buffer gas particles in the entire cell, they call this effect as Enhanced Temperature Sensitivity (ETS). This effect is not due to changes of interaction between Rb and buffer gas atoms, rather because of the buffer gas density variations between the cell body and the stem volumes, which is purely a geometrical effect (the stem part stays outside the microwave cavity and hence does not contribute in the microwave interrogation). In other words, one can say that the temperature gradient between the cell volume and the stem is responsible for this effect of ETS. We quantify the "fast stem effect" according to [162] as,

$$\frac{\partial \nu_s/\nu_{Rb}}{\partial T_s} = \frac{n_s a_0^{'}}{\nu_{Rb}} \cdot \frac{v_s}{T_s}, \tag{6.1}$$

where, the total volume of the cell (including stem and cell body) is given as $V = V_s{+}V_c$, defining $v_s{=}V_s/V$ and the average buffer gas density $n_s = N/V$. T_s is the stem operation temperature. At the cell filling temperature in our case of 293 K with a total buffer gas pressure of 26 mbar, we obtain $n_s \approx 1.5\times10^{17}/\text{cm}^3$, and $v_s = 0.029$. From [162], the $a_0^{'}$, denotes the buffer gas mixture in the cell volume and is related to $\beta^{'}$ coefficient in Eqn. 1.44 and is estimated as $\approx 5\times10^{-15}$ Hz·cm^3.

Using the above values in Eqn. 6.1, we obtain $\frac{\partial \nu_s/\nu_{Rb}}{\partial T_s} \approx 1.1\times10^{-11}$/K, matching well with the measured value (cf. Fig. 6.8(b)). It is clear from Eqn. 6.1, by reducing the stem volume v_s (e.g. the reservoir length), we can reduce the fast stem effect [162].

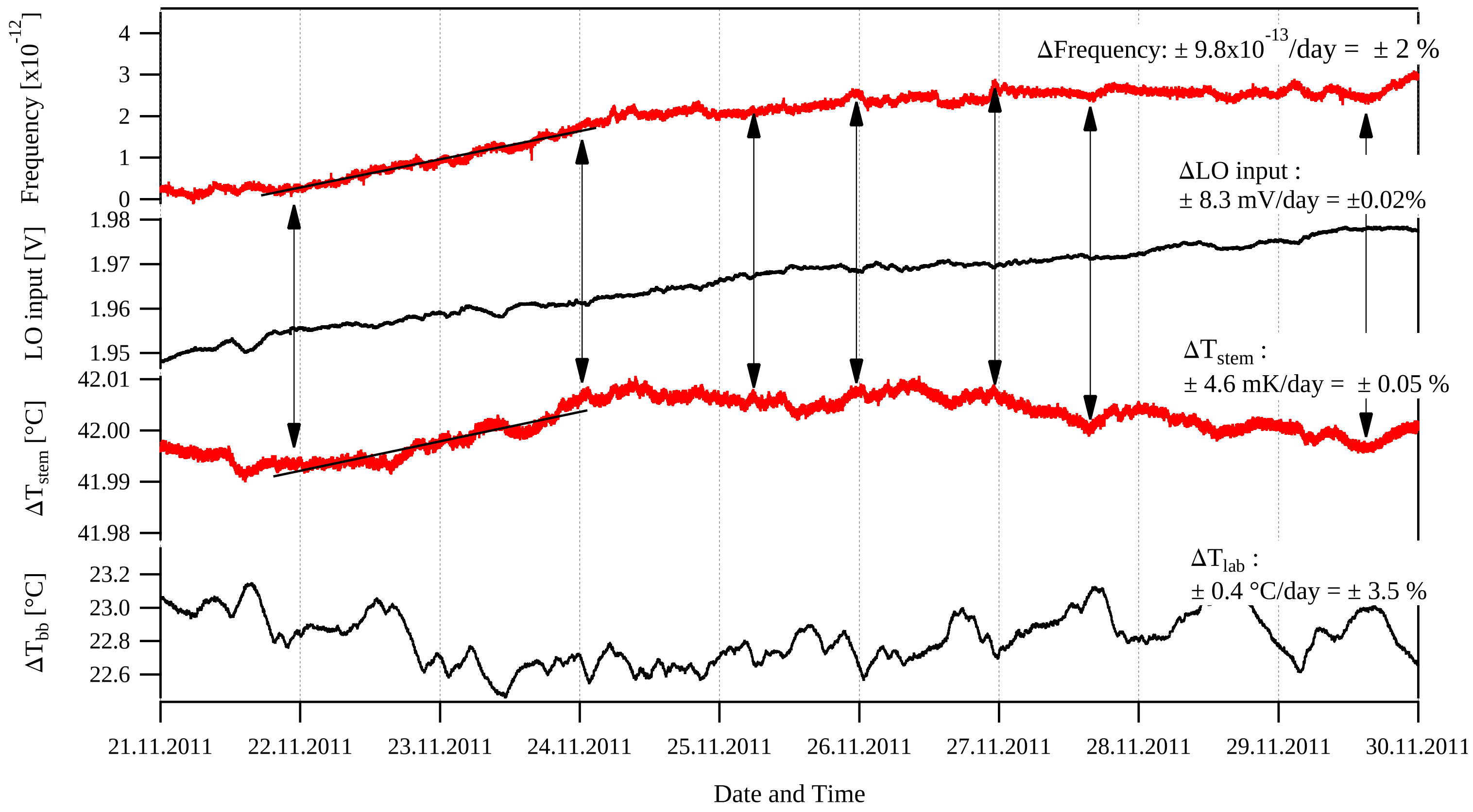

Figure 6.15: *Measured varying parameters affecting the clock frequency stability in medium- to- long-term time scales. Tlab: The laboratory temperature variations;* ΔT_{stem}*: the Stem temperature variations; LO input: transmitted light voltage measured at the clock detector after the pp; and Frequency: measure of the clock frequency against active H-MASER. Correlation between the* ΔT_{stem} *and Frequency are shown at selected points by arrows including the correlation in the drift between 22.11.2011 and 24.11.2011 data.*

It is important to note that in Fig. 6.15 the LO input voltage (or the measure of light intensity transmitted through the clock cell) does not exactly follow the fast stem fluctuations and hence does not correlate with clock frequency. This is because the changes in light intensity through the cell require variations in the density of Rb atoms inside the cell volume. However, in the fast effect the density changes of Rb atoms do not take place, therefore we treat this effect separately and call it as "slow stem effect" (as treated in Section 6.4.5). The experimentally measured clock frequency long-term stability in terms of Allan deviation is shown in Fig. 6.16. The limit at 10^4 s of $\sim 5{\times}10^{-14}$ is in excellent agreement with the limit due to $|TC_s|$ in Table. 6.4. The clock frequency was measured over a period of 9 days along with other relevant parameters that could affect the instability of the clock. It is to be noted that the clock was operated in typical ambient laboratory conditions; in air and *not* under vacuum. The stem temperature coefficient (TC_s or "fast effect") had a strong effect on the clock frequency affecting the medium- to long-term stability. This is evident by a well-matched correlation between the stem temperature changes and that of the clock frequency in Fig. 6.15. In [162], Calosso and colleagues operate their physics package under vacuum in well-controlled laboratory conditions, the stability level of their active temperature control is 100 μK, where as in our case (in air, or ambient laboratory conditions) this is measured to be 4.6 mK (factor of '46' higher) as shown in Fig. 6.15.

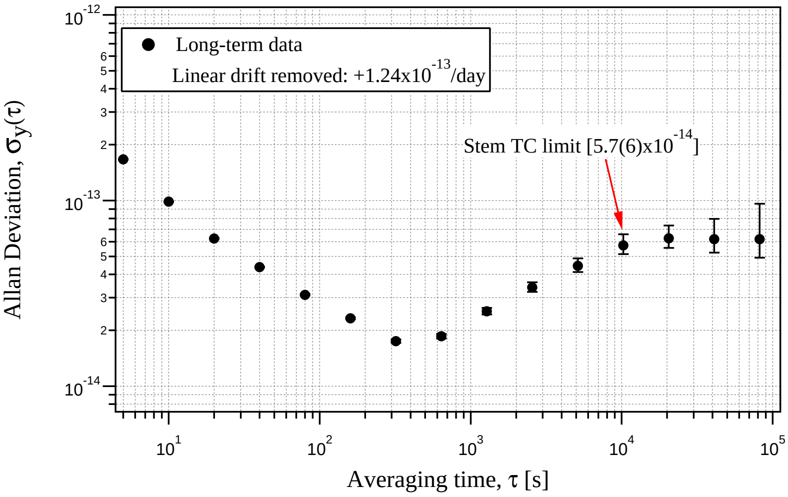

Figure 6.16: *Medium- to long-term clock frequency (Fig. 6.15 data) in terms of Allan deviation, showing the limit due to the stem TC as estimated in Table. 6.4.*

6.4.5 Stem slow effect

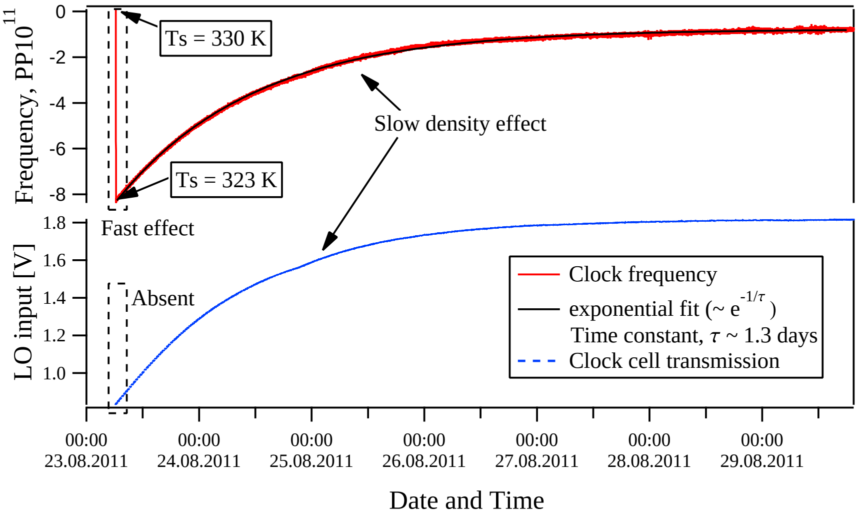

Figure 6.17: *Clock frequency and transmitted light through the clock cell, after a temperature step of the resonance cell stem. The "fast" and "slow" stem effects are demonstrated. The slow stem effect has a time constant of 1.3 days. Note absence of the "fast effect" in LO input voltage substantiating that there is no "fast" change in Rb atomic density in the cell volume.*

Further investigation was done to quantify the effect of stem temperature on the clock frequency instability over a period of one day or more. By keeping the cell volume temperature, T_v constant at 336 K, the stem temperature, T_s was changed from 330 K to 323 K and the transmitted intensity through the clock cell along with the clock frequency were recorded (cf. Fig. 6.17). The "fast" (almost instantaneous) and the "slow" (over one day) stem temperature coefficients are clearly demonstrated in this better controlled situation where, for instance, the light-shift and the microwave power shift related effects are almost one order of magnitude smaller than the observed clock frequency changes. The fast stem effect is due to stem geometric influence as discussed in Section 6.4.4. In Fig. 6.17, note absence of the "fast effect" in LO input voltage substantiating that there is no "fast" change in Rb atomic density in the cell volume and thus indicating that this effect is due to BG atoms. Hence, it is clear that the influence of day cycles on clock frequency is due to the stem "slow" temperature effect. The slow stem effect has a time constant of $\sim$ 1.3 days (30 hours). For any change in stem temperature, the Rb atomic density in the cell volume takes about 4 days to reach equilibrium, but in principle this steady state is never reached due to thermal fluctuations on the stem temperature control. The effect in Fig. 6.17 over a period of one day timescale has an influence on the clock frequency stability. This effect plays a major role in influencing the density of the Rb atoms in the cell and hence over a period of one day a change in the clock frequency by ≈ $\pm 1\times10^{-12}$ (see Fig. 6.15). This could be improved by: (i) a better stem temprature control and/or (ii) a better thermal isolation of PP (for example, by operating the PP inside a vacuum chamber).

6.5 Conclusions

As demonstrated in this chapter, increasing the number of "active" atoms is immediately obtained considering a bigger cell of 25 mm diameter inside a newly developed magnetron-type microwave cavity, in contrast to the 14 mm vapor cells used in previous studies [157, 163] while operating at same cell temperature. This results in larger volume where the light, microwave field and atoms can successfully interact.

A comparison graph of estimated and measured stabilites as a function of cell radius are presented in Fig. 6.18: measured ratios between two buffer gas cells of different dimensions- $cellA$ ($a = 6$ mm, $L = 16$ mm from [163]) and $cellB$ ($a = 6$ mm, $L = 23$ mm, this work) of a factor of '6.4' (ratios of S/N limits) is in reasonably good agreement with our estimated factor of '5.3' in Table 3.1 (see values in first row).

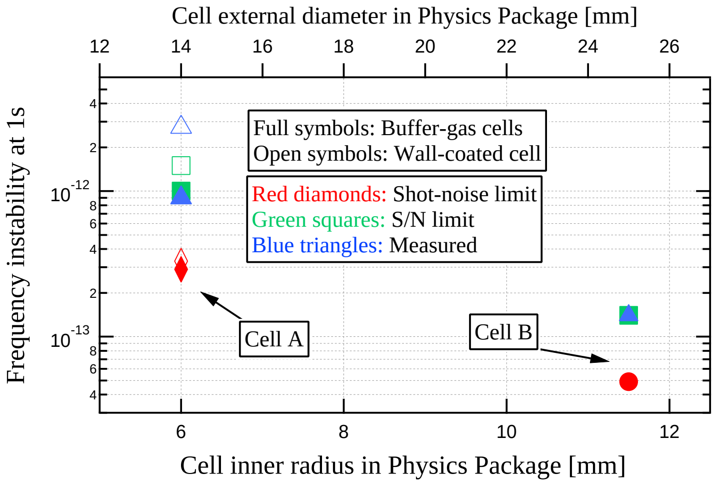

Figure 6.18: *Comparison of stability values obtained with PPs using different cells: 14 mm diameter wallcoated cell (cf. this work Chapter 5), 14 mm buffer-gas cell (from [163]), and 25 mm buffer-gas cell (this work Chapter 6).*

The spectroscopy of DR optimized signal, and the perturbing effects such as light shifts, microwave power shift and temperature coefficients were studied in detail using both the laser heads (clock and AOM). It is to be noted that the stability we have shown in this chapter 6 was obtained after several days of temperature stabilization. Excellent state-of-the-art short-term stability, typically achievable with our high-performance clock of $<1.4\times10^{-13}\ \tau^{-1/2}$ using the *clock laser head* was presented here. A clock stability of $6\times10^{-13}\ \tau^{-1/2}$ was achieved using the AOM integrated laser head and was presented elsewhere [164]. Medium- to long-term responsible physical sensitivities were quantified and their influence on the clock was discussed. An important effect of the temperature gradients and stem "fast" geometric effect dominating the medium-term stability of the clock was demonstrated. This leads us to the conclusion of having a smaller stem volume to have a better thermal control [162]. On the other hand, the diurnal cycles affect the clock frequency stability in long-term over one day time scales due to stem "slow" effect by changing the density of Rb atoms in the clock cell. This limitation could also be overcome by a smaller stem volume and a better thermal control of the stem.

We conclude that the best clock performances were obtained using the Laser Head without integrated AOM, but the Laser Head with integrated AOM proved very useful for reducing the intensity LS effect, as well as the independent optimization of some parameters such as the dependence of microwave power on input light intensity. Eventhough the AOM Laser Head allows higher resolution studies, the AOM itself is also a source of instabilities, particularly in medium and long term, in CW-optical pumping approach. A better control of the thermal conditions for AOM-related elements and overall optical system should be aimed to reduce this effect.

Summary, prospects and potential applications

> *For a successful technology, reality must take precedence over public relations, for nature cannot be fooled.*
> *-Richard Feynman*

This thesis presented detailed spectroscopic and clock studies on high-performance state-of-the-art improved rubidium cell standards for next generation applications, by adopting the Continuous-Wave (CW) Double-Resonance (DR) principle in two variants: wall-coated cells ($\phi = 14$ mm) and enlarged buffer-gas cells ($\phi = 25$ mm).

The 14 mm wall-coated (tetracontane) cell was characterized by measuring T_1 and T_2 relaxation times; quantifying the hyperfine population relaxation time $\mathrm{T}_1 = 25$ ms during which atoms undergo about 2300 collisions with the coated wall before losing their ground-state polarization, and a coherence relaxation time of the clock transition $\mathrm{T}_2 = 0.9$ ms, during which the phase of the polarized atoms is retained. The DR spectroscopic studies and optimization of DR signals were presented. Metrological characterization of the clock was performed by quantitatively measuring the important sensitivities such as the intensity and frequency light-shifts, microwave power shift and temperature coefficients. Limitations of these perturbing effects on the clock's short- and medium- to long-term frequency stabilities were quantified. Finally, the clock stability was measured that exhibits a short-term stability of $< 2.8\times10^{-12}\ \tau^{-1/2}$. To our knowledge, this constitutes the first ever wall-coated clock stability reported with laser pumping, and also shows a good short-term stability. Though the wall-coated cells give intrinsically a narrow DR signal [36], there is no significant improvement on the S/N ratio and therefore we cannot expect to have better clock performance compared to the similar sized buffer gas cell clock. The dominating effect on S/N is the laser PM-AM converted noise, by reducing this one can get closer to the shot-noise limit. The wall-coated cells are advantageous for spectroscopic studies, for instance the spin-exchange relaxation measurements etc. It was found that the limitation in medium- to long-term stability of this tetracontane coated cell clock is due to the temperature coefficient introduced by the coating that limits the stability to 2×10^{-12} at 10^4 s time scale, which is an intrinsic property of the coating material itself [110].

The drift of clock's frequency due to degradation of the coating material was quantitatively measured to be an additive limitation for the paraffin (tetracontane) coating making it difficult to reach a long-term stability below 10^{-14}/day, that is relevant for next generation navigation applications in order to reach the accuracy of < 1 ns/day.

The compact magnetron-type microwave cavities that can hold the cell with a diameter of 25 mm and resonate at the Rb ground state frequency of 6.835 GHz were designed, manufactured, assembled, tuned and tested. The field modes inside these cavities were presented, both by simulations and spectroscopic Zeeman measurements. A cavity characterizing factor, called as Field Orientation Factor (FOF), ξ was introduced and corresponding values by simulations and Zeeman measurements agree to within $< 1\%$. Finally, the influence of field modes on clock stability was seen with a quantitative picture by matching the ratio of FOF $\xi^{O}_{exp}/\xi^{P}_{exp} = 3.3$ to the short-term stability ratio of ∼'3' obtained between the prototype cavity ($4\times10^{-13}\ \tau^{-13}$, [31]) and the optimized cavity ($1.4\times10^{-13}\ \tau^{-13}$, Chapter 6) .

The spectroscopic and clock studies on the enlarged 25 mm vapor cell filled with ^{87}Rb and buffer gases (Ar+N2) were presented. Similar to the wall-coated cell studies, the DR signal optimization was presented along with the studies on medium- to long-term instabilities, such as, the intensity and frequency light-shifts, microwave power shift and the temperature coefficients of the cell volume and stem. The limitations to the clock stability due to these perturbing effects were analyzed and discussed. A detailed short-term noise budget analysis was established by estimating the limits due to signal-to-noise ratio (laser AM and FM-AM converted noise), shot-noise, the LO phase noise and the light-shift contributions. A state-of-the-art short-term stability for cell standards exhibiting $< 1.4\times10^{-13}\ \tau^{-1/2}$ was demonstrated. It is to be noted that the stability we have shown here was obtained after several days (> 10 days) of temperature stabilization. An important effect of the temperature gradient across the clock cell was identified, mainly due to the stem "slow" temperature coefficient, which is dominating the long-term stability of the clock over a period of one day due to diurnal cycles. This leads us to the conclusion that having a shorter stem will result in a better thermal control. However, in a good equilibrium condition of the stem temperature, a stability of $< 1\times10^{-14}$ has been achieved at 10^4 s integration time using a similar clock setup [31]. It is important to note that the clock studied in this thesis was operated under ambient laboratory conditions (not under vacuum). The operation of just the physics package under vacuum ($\approx 10^{-5}$ torr) can substantially reduce the dependence on ambient temperature fluctuations by cutting down on conduction losses. This eventually can improve the clock stability by at least a factor of five and hence is possible to reach below 1×10^{-14} level at $\tau = 10^4$ to 10^5 s.

Table C1: *Comparison between the wall-coated cell and buffer gas cell results.*

Parameters	**Wall-coated cell clock**	**Buffer-gas cell clock**
Cell external diameter	14 mm	25 mm
Cell internal volume	1.4 cm^3	9.6 cm^3
Intrinsic FWHM	366 Hz	180 Hz
Optimized FWHM	642 Hz	334 Hz
Optimized D	0.41 nA/Hz	1.5 nA/Hz
Background level	5.65 μA	1.82 μA
Total noise, N$_{psd}$	5.1 pA/$\sqrt{Hz}$	1.7 pA/$\sqrt{Hz}$
Short-term stability	$<3\times10^{-12}\ \tau^{-1/2}$	$<1.4\times10^{-13}\ \tau^{-1/2}$
Shot-noise limited stability	$<3.3\times10^{-13}\ \tau^{-1/2}$	$<5\times10^{-14}\ \tau^{-1/2}$
Intensity LS effect, $\|\alpha\|$	2.3 Hz·mm^2/μW	19.5 mHz·mm^2/μW
Reduced int. LS, $\|\alpha_{redu}\|$	57 mHz·mm^2/μW	0.45 mHz·mm^2/μW
Frequency LS effect, $\|\beta\|$	413.8 mHz/MHz	82 mHz/MHz
Microwave PS, $\|\mu_{PS}\|$	7.8 Hz/μW [a]	15.3 mHz/μW
Cell volume TC $\|TC_v\|$	1.39 Hz/K	6.84 mHz/K
Stem TC $\|TC_s\|$	0.22 Hz/K	0.082 Hz/K
Spin ex. shift $\|\Delta T_{SE}\|$	<48 mHz/K	<34 mHz/K

---

[a] This is to be confirmed. However, it will not be a limiting factor as in wall-coated cells the microwave PS is reduced [54], and already this reported instability contribution is lower than the limits arising from the cell's TC or intensity LS coefficient.

Table C1 gives the summary comparing the results obtained from two different approaches studied in this thesis; the wall-coated cell case and the buffer-gas cell case. Note that the cell sizes for these two cases are different. It is evident that the enlarged vapor cell used for BG approach gives an improved stability as compared with the wall-coated cell, due to the active participation of more number of atoms in the cell volume. The background level is higher in case of the wall-coated cell as compared with the buffer gas cell. This is partly due to the fact that in a buffer gas cell (as explained in Section 1.2) due to the buffer gas collisions with the ^{87}Rb atoms, the excited state relaxation rate Γ^* is more than two orders of magnitude higher as compared with the relaxation rate in the wall-coated cell. The perturbing effects due to laser intensity and frequency variations, microwave power fluctuations and the temperature influences on the buffer gas and wall-coated vapor cells that affect the clock's medium- to long-term stabilites are quantified by metrological analysis. Due to lower input laser intensities for an optimized DR signal in the BG cell case, the values of intensity and frequency LS coefficients obtained are smaller than that for the wall-coated cell case. The TC in BG cell case is determined by the ratio of the buffer gases whereas, in the wall-coated cell it is the coating material that determines the value of the TC.

Table C2 compares the work presented in this thesis on 25 mm diameter BG cell high-performance clock (highlighted in yellow) to other kinds of reported compact, portable clocks around the world, including both, commercial and laboratory-based ones.

Table C2: *Budget analysis on volume, mass, power and clock stabilities for different types of other reported clocks realizations, compared to the clock developed in this thesis.*

Clock[a]	**Stability at 1 s**	**Stability at 10^4 s**	**Volume ($\mathbf{dm^3}$)**	**Mass (Kg)**	**Power (W)**
Galileo RAFS [20]	3×10^{-12}	4×10^{-14}	2.4	3.3	<18
Galileo SPHM [20]	7×10^{-13}	$<1\times10^{-14}$	28	18	80
LPCs beam [17]	1.5×10^{-12}	$<3\times10^{-14}$	<5	7	<30
Active H-maser [167]	2×10^{-13}	2×10^{-15}	∼ 540	90	150
Laser-Rb (LARC) [168]	5×10^{-13}	$<4\times10^{-14}$	<3	<4	<18
PHARAO [169]	1×10^{-13}	1×10^{-15}	1200	227	450
HORACE [57]	$<3\times10^{-13}$	$<1\times10^{-14}$	>20	NA[b]	NA
Optical-POP [107]	1.6×10^{-13}	$<4\times10^{-15}$	2.1 (PP only)	3.86 (PP only)	< 25
5071A Cs-beam [170]	6×10^{-12}	$<6\times10^{-14}$	34	30	40
GPSII Rb [171]	3×10^{-12}	$<3\times10^{-14}$	4.6	<6	<15
This work	$<1.4\times10^{-13}$	$<4.2\times10^{-14}$	<1.5 (LH+PP)	<2 (LH+PP)	<18

---

[a] Note: The Integrated Miniature Primary Atomic Clock Technology (IMPACT) clocks are being developed at NIST [165], Symmetricom [166] and JPL [27] under Defense Advance Research Projects Agency (DARPA) contracts aiming the best accurate miniature clocks with V< 5 cm^3, power < 50 mW and timing error of < 32 ns/month ($\approx 1\times10^{-14}$ @ 2.7×10^6 s).

[b] Not available

I. Future prospects

A. Wall-coated cell approach

Alternative coating materials have to be studied especially by measuring their temperature coefficient limits. Adding a small amount of buffer gases (eg. ~ 1.5 torr of N_2) in the wall-coated cell in order to counter-balance the coating's TC could also improve the performances of the wall-coated based vapor cell clocks. Potential implementation of large (~ 25 mm ϕ) vapor cells with integrated approach of wall-coating and mixture of buffer gases may be very promising line to be studied, as the short-term stability could be improved due to reduced reservoir-effect (hole effect).

B. Buffer gas cell approach

The 25 mm BG cell clock's medium- to long-term stability can be improved by: (a) shortening the stem length, (b) improving the PP's temperature control/thermal design or alternatively operating the physics package under vacuum, as discussed above and (c) increasing the Ar/N_2 ratio (in new batch of cells) to operate at reduced temperature will have multiple advantages. For instance, operating the clock around 45 °C could reduce the temperature dependent spin-exchange relaxation and this also allows operating the clock at reduced input laser intensities which in turn reduces the frequency light-shift coefficient β.

As a new possible line of investigation for the future, a combination of both the above approaches may prove valuable: the Pulsed Optical Pumping (POP) with a magnetron-type microwave cavity. The future avenues for such a compact pulsed optical pumping (POP) clock have a strong potential. First possibility is to use the 14 mm TE_{011} mode cavity with BG cell for POP operation. Simulations have shown that there is a possibility of interrogating with 12 mm beam width for achieving good signal contrast and reaching excellent short-term stability [172]. The second possibility is to use the larger cavity with an enlarged cell (25 mm) for POP operation to have even better performances. Improvement of the field mode (TE_{011}) of the larger cavity has made this option more reliable for POP operation.

In parallel, the space qualification of key components such as the laser diode and the Acousto-Optical Modulator (for POP approach) needs to be pursued, in view of space qualified clocks for future satellite navigation applications. A recent elaborate long-term study of DFB laser performance has shown positive signs of reliability under vacuum operation conditions [173]. The *clock laser head* used in the studies of this thesis work is also in constant operation from over a period of *three years* in ambient laboratory conditions.

The theoretical and experimental studies on microwave power shift and its dependance on input light intensity and the intensity light shift-coefficient α is interesting to be pursued. This will be important in the view of further improving the medium to long-term stabilites of Rb standards.

Finally, it is worthwhile to mention the high potential of combining the vapor-cell standards technologies developed in this work with the technology of optical combs that may result in various configurations providing, for instance, as compact optical frequency references or synthesizers. This high-performance reference oscillator will be useful for portable applications in contrast to the active H-masers which are bulky and non-portable.

II. Potential applications

Compact high-performance clocks have a wide range of applications from telecommunications, satellite navigation, and basic science experiments to space probes [2, 4, 174, 175]. In particular, the next generation navigation systems such as, GALILEO, where the level of $< 1\times10^{-14}$ (equivalent to 1 ns) around 6000 s and up to 1 day is relevant for precise positioning due to the synchronization times involved [20, 31]. Timing accuracy of 1 ns is equivalent to locating the position on ground to 30 cm distance. Other aspects of everyday life also have numerous uses with precise time and frequency synchronization requirements [176]. Power companies require precise time for power regulation and phase adjustments in system grids and thereby to reduce the power losses [8]. Radio and television broadcasting stations need the precise time and frequency for broadcasting the programs. Mobile phone base stations need stable and accurate references to handle the massive amount of data receiving and transmission in a synchronous way [177]. Interplanetary and deep space travel missions need reliable and accurate time monitoring, either for scientific experiments or in order to position the space probe precisely [174]. The basic studies on understanding the Einstein's special theory of relativity, fine structure constant etc., need more stable and accurate clocks [175]. The further development of work presented in this thesis by improving mainly on the thermal control towards a device can essentially address many of the needs of aforementioned applications to a reasonable extent, in terms of clock stability performance, cost, reliability and portability.

Bibliography

[1] J. Jerspersen and J. Fitz-Randolph. *"From sundials to atomic clocks"*. Dover, 1982. 1

[2] W. M. Itano and N. F. Ramsey. "Accurate measurement of time". *Scientific American*, 269:56–65, 1993. 1, 140

[3] D. W. Allan, N. Ashby, and C. C. Hodge. "The Science of Timekeeping". Technical report, Hewlett-Packard, 1997. 1

[4] J. Camparo. "The rubidium atomic clock and basic research". *Physics Today*, 60(33), 2007. 1, 2, 7, 8, 31, 64, 140

[5] L. A. Mallette, P. Rochat, and J. White. "An introduction to satellite based atomic frequency standards". In *IEEE Aerospace Conference*, pages 1–9, Big Sky, MT, May 2008. 1

[6] L. A. Mallette. "Atomic and quartz clock hardware for communication and navigation satellites". In *39^{th} Annual Precise Time and Time Interval (PTTI) Meeting*, 2007. 1

[7] P. Waller, S. Gonzalez, S. Binda, I. Sesia, I. Hidalgo, G. Tobias, and P. Tavella. "The in-orbit performances of GIOVE clocks". *IEEE Trans. Ultrason. Ferroelctr. Freq. Control.*, 57:738, 2010. 1

[8] M. Rohden, A. Sorge, M. Timme, and D. Witthaut. "Self-Organized Synchronization in Decentralized Power Grids". *Phys. Rev. Lett.*, 109(064101):1–5, 2012. 1, 140

[9] M. Bird, M. Allison, S. Asmar, D. Atkinson, I. Avruch, R. Dutta-Roy, Y. Dzierma, P. Edenhofer, W. Folkner, D. Johnston, D. Plettemeier, S. Pogrebenko, R. Preston, and G. Tyler. "The vertical profile of winds on Titan". *Nature*, 438:800–802, 2005. 1

[10] J. D. Prestage, R. L. Tjoelker, and L. Maleki. "Atomic clocks and variations of the fine structure constant". *Phys. Rev. Lett.*, 74(18):3511–3514, 1995. 1

[11] J.-F. Pascual-Sánchez. "Introducing relativity in global navigation satellite system". *Annalen der Physik*, 16:258–273, 2007. 1

[12] M. Antonello et al. "Measurement of the neutrino velocity with the ICARUS detector at the CNGS beam". *Phys. Lett. B*, 713:17–22, 2012. 1

[13] I. I. Rabi. "Radiofrequency Spectroscopy". In *Richtmyer Memorial Lecture, delivered at Columbia University in New York, New York*, volume 67 of *Meeting at New York, January 19 and 20, 1945*, pages 199–204. Phys. Rev., 20th January 1945. 1

[14] I. Rabi, J. Zacharias, and P. Kusch. "A new method of measuring nuclear magnetic moment". *Phys. Rev.*, 53:318, 1938. 1

[15] L. Essen and J. V. L. Parry. "An Atomic Standard of Frequency and Time Interval". *Nature*, 176:280–282, 1955. 1

[16] J. Terrien. "News from the international beureau of weights and measures". *Metrologia*, 4(41), 1968. 1

[17] S. Lecomte, M. Haldimann, R. Ruffieux, P. Berthoud, and P. Thomann. "Performance demonstration of a compact, single optical frequency cesium beam clock for space applications". In *IEEE Frequency Control Symp. and 21st European Frequency and Time Forum*, pages 1127–1131, Geneva, Switzerland, 2007. 1, 5, 138

[18] R. Wynands and S. Weyers. "Atomic fountain clocks". *Metrologia*, 42(S64), 2055. 1

[19] G. Busca, L.-G. Bernier, and P. Rochat. "Active hydrogen maser frequency standard", United States Patent 5,838,206, Nov. 1998. 1

[20] P. Rochat, F. Droz, P. Mosset, G. Barmaverain, Q. Wang, D. Boving, L. Mattioni, M. Belloni, M. Gioia, U. Schmidt, T. Pike, and F. Emma. "The onboard Galileo rubidium and passive maser, status and performance". In *IEEE Frequency Control Symp.*, pages 26–32, Vancouver, BC, USA, 2005. 1, 5, 127, 138, 140

[21] C. Affolderbach, F. Droz, and G. Mileti. "Experimental demonstration of a compact and high-performance laser-pumped rubidium gas cell atomic frequency standard". *IEEE Trans. Instrum. Meas.*, 55(429), 2006. 1, 12, 31, 33, 98, 114, 115

[22] J. Vanier and C. Mandache. "The passive optically pumped Rb frequency standard: the laser approach". *Applied Physics B: Lasers and Optics*, 87:565–593, 2007. 1, 2, 3, 7, 8, 11, 12, 16, 18, 19, 47, 64

[23] M. Takamoto, F-L Hong, R. Higashi, and H. Katori. "An optical lattice clock". *Nature*, 435:321–324, 2005. 1

[24] S. A. Diddams, Th. Udem, J. C. Bergquist, E. A. Curtis, R. E. Drullinger, L. Hollberg, W. M. Itano, W. D. Lee, C. W. Oates, K. R. Vogel, and D. J. Wineland. "An optical clock based on a single trapped 199Hg+ ion". *Science*, 293(5531):825–828, 2001. 1

[25] J. D. Prestage, R. L. Tjoelker, and L. Maleki. "Mercury-Ion clock based on a linear multi-pole ion trap". TMO Progress Report 42-143, Jet Propulsion Laboratory, National Aeronautics and Space Administration, November 2000. 1

[26] J. C. Bergquist, S. R. Jefferts, and D. J. Wineland. "Time measurement at the millennium". *Physics Today*, pages 37–42, 2001. 1

[27] Y.-Y. Jau, H. Partner, P. D. D. Schwindt, J. D. Prestage, J. Kellogg, and N. Yu. "Low-power, miniature ^{171}Yb ion clock using an ultra-small vacuum package". *Appl. Phys. Lett.*, 101(253518), 2012. 1, 138

[28] P. Treutlein, P. Hommelhoff, T. Steinmetz, T. W. Hänsch, and J. Reichel. "Coherence in microchip traps". *Phys. Rev. Lett.*, 92, 2004. 1

[29] D. M. Farkas, A. Zozulya, and D. Z. Anderson. "A compact microchip atomic clock based on all-optical interrogation of ultra-cold trapped Rb atoms". *Appl. Phys. B*, 101:705–721, 2010. 1

[30] J. Reichel and V. Vuletić. *"Atom chips: Chapter 8– Microchip-based trapped-atom clocks"*. Wiely-VCH Verlag GmbH & Co., 2011. 1

[31] T. Bandi, C. Affolderbach, C.E. Calosso, and G. Mileti. "High-performance laser-pumped rubidium frequency standard for satellite navigation". *Electronics Letters*, 47(12):698–699, 2011. 2, 3, 23, 26, 104, 127, 128, 136, 140

[32] J. Vanier and C. Audoin. "The Quantum Physics of Atomic Frequency Standards". *Adam Hilger*, 1:365, 1989. 2, 7, 9, 10, 11, 12, 14, 20, 21, 22, 26, 27, 31, 32, 33, 35, 36, 47, 48, 57, 58, 61, 64, 71, 74, 86, 87, 88, 89, 93, 94, 109, 117, 127

[33] G. Mileti and C. Affolderbach. "Laser optical pumping in Rb vapor-cell atomic clocks". In Proc. of SPIE, editor, *13th International school on Quantum Electronics: Laser Physics and Applications*, volume 5830, pages 159–169, Bellingham, WA, 2005. 2

[34] R. H. Dicke. "The Effect of Collisions Upon the Doppler Width of Spectral Lines". *Phys. Rev.*, 89:472, 1952. 2, 32

[35] H. G. Robinson, E. S. Ensberg, and H. G. Dehmelt. *Bull. Am. Phys. Soc 3*, page 8, 1958. 2, 85

[36] H. G. Robinson and C. E. Johnson. "Narrow ^{87}Rb Hyperfine-structure Resonances in an Evacuated Wall-coated Cell". *Appl. Phys. Lett.*, 40(9):771–773, 1982. 2, 86, 96, 135

[37] H. G. Robinson and C. E. Johnson. "A New Heart for Rb Frequency Standards: The Evacuated, Wall-coated Sealed Cell". *IEEE Trans. Instrum. Meas.*, 32(1):198, 1983. 2

[38] M. A. Bouchiat and J. Brossel. "Relaxation of optically pumped rb atoms on paraffin-coated walls". *Phys. Rev.*, 147(1):41–54, 1966. 2

[39] W. Franzen. "Spin Relaxation of Optically Aligned Rubidium Vapor". *Phys. Rev.*, 115:850–858, 1959. 2

[40] M. V. Balabas, T. Karaulanov, M. P. Ledbetter, and D. Budker. "Polarized alkali vapor with minute-long transverse spin-relaxation time". *Phys. Rev. Lett.*, 105(070801), 2010. 2

[41] D. Budker and M. Romalis. "Optical magnetometry". *Nat. Phys.*, 3(4):227–234, 2007. 2, 85

[42] V. Shah, S. Knappe, P. D. D. Schwindt, and J. Kitching. "Subpicotesla atomic magnetometry with a microfabricated vapour cell". *Nature Photonics*, 1(649), 2007. 2, 85

[43] D. Budker, L. Hollberg, D. F. Kimball, J. Kitching, S. Pustelny, and V. V. Yashchuk. "Investigation of microwave transitions and nonlinear magneto-optical rotation in anti-relaxation-coated cells". *Phys. Rev. A*, 71(012903), 2005. 3, 85

[44] R. P. Frueholz and C. H. Volk. "Analysis of Dicke Narrowing in Wall Coated and Buffer Gas Filled Cells with Application to Gas Cell Atomic Clocks". *Proc. 38th Annual Frequency Control Symposium*, 1984. 3, 85

[45] G. Singh, P. Dilavore, and C. O. Alley. "A technique for preparing wall coated cesium vapor cells". *Rev. Sci. Instrum.*, 43(9):1388–1389, 1972. 3, 58, 85

[46] C. Szekely and R. E. Drullinger. "Improved rubidium frequency standards using diode lasers with AM and FM noise control". In *Proc. SPIE*, pages 299–305, Boston, MA, 1992. 3, 85

[47] E. Breschi, G. Kazakov, C. Schori, G. Di Domenico, G. Mileti, A. Litvinov, and B. Matisov. "Light effects in the atomic-motion-induced Ramsey narrowing of dark resonances in wall-coated cells". *Phys. Rev. A*, 82(063810), 2010. 3, 85

[48] A. Kastler. "Applications of polarimetry to infra-red and micro-wave spectroscopy". *Nature*, 166(4211):113, 1950. 3

[49] A. Kastler. "Optical methods for studying Hertzian resonances". *Science*, 158(3798):214–221, 1967. Nobel Lecture. 3

[50] G. Mileti. *"Etude du pompage optique par laser et par lampe spectrale dans les horloges á vapeur de rubidium"*. Phd thesis, Université de Neuchâtel - Faculté des Sciences, Observatoire Cantonal de Neuchâtel, September 1995. 3, 12, 14, 90

[51] S. Micalizio, C. E. Calosso, A. Godone, and F. Levi. "Metrological characterization of the pulsed Rb clock with optical detection". *Metrologia*, 49:425–436, 2012. 3, 9, 39, 50, 79

[52] B. S. Mathur, H. Tang, and W. Happer. "Light Shifts in the Alkali Atoms". *Phys. Rev.*, 171(1):11–19, Jul 1968. 5, 30, 48

[53] C. Affolderbach, C. Andreeva, S. Cartaleva, T. Karulanov, G. Mileti, and D. Slavov. "Light shift suppression in laser optically-pumped vapour-cell atomic frequency standards". *Appl. Phys. B*, 80(841), 2005. 5, 31, 48

[54] A. Risley, S. Jarvis, and J. Vanier. "The Dependence of Frequency Upon Microwave Power of Wall-coated and Buffer-gas-filled Gas Cell Rb87 Frequency Standards". *J. Appl. Phys.*, 51(9):4571–4576, 1980. 5, 12, 35, 101, 107, 137

[55] A. Brisson J. Vanier, R. Kunski and P. Paulin. "Progress and prospects in rubidium frequency standards". *J. de Physique*, 12:c8–139, 1981. 5, 12, 101

[56] S. Micalizio, A. Godone, F. Levi, and C. Calosso. "Pulsed optically pumped ^{87}Rb vapor cell frequency standard: A multilevel approach". *Phys. Rev. A*, 79(013403), 2009. 5, 12, 20, 22, 31, 35, 99, 115, 122

[57] F.X. Esnault, N. Rossetto, D. Holleville, J. Delporte, and N. Dimarcq. "HORACE: a compact cold atom clock for Galileo". *J. Adv. Space Res.*, 47(5):854–858, 2011. 5, 138

[58] M. A. Lombardi, T. P. Heavner, and S. R. Jefferts. "Nist primary frequency standards and the realization of the SI second". *Journal of Measurement Science*, 2(4):74–89, 2007. 7

[59] S. Bize, Y. Sortais, M. S. Santos, C. Mandache, A. Clairon, and C. Salomon. "High-accuracy measurement of the ^{87}Rb ground-state hyperfine splitting in an atomic fountain". *Europhys. Lett.*, 45:558, 1999. 8, 160

[60] A. Godone, S. Micalizio, and F. Levi. "Pulsed optically pumped frequency standard". *Phys. Rev. A*, 70(023409), 2004. 9

[61] G. J. Dick, J. D. Prestage, C. A. Greenhall, and L. Maleki. "Local oscillator induced degradation of medium-term stability in passive atomic frequency standards". In *22nd Precise Time and Time Interval (PTTI) meeting*, pages 487–508, Vienna, VA, 1990. 9, 27, 52

[62] A. Corney. *"Atomic and laser spectroscopy"*. Clarendon Oxford university press, 1977. 9

[63] J. Vanier, R. Kunski, P. Paulin, J.Y. Savard, M. Tetu, and N. Cyr. "On the Light Shift and Buffer Gas Shift in Passive Rubidium Frequency Standard". In *36th Annual Symposium on Frequeny Control*, pages 348–354, 1982. 12

[64] F. Levi, C. Novero, A. Godone, and G. Brida. "Analysis of the ligh shift effect in the ^{87}Rb frequency standard". *IEEE Trans. Instrum. Meas.*, 46:126–129, 1997. 12

[65] G. Mileti, I. Ruedi, and H. Schweda. "Line inhomogeneity effects and power shift in miniaturized rubidium frequency standards". In *Proc. of 6th European Frequency and Time Forum*, page 515, 1992. 12, 35

[66] J. Levine. "Invited review article: The statistical modeling of atomic clocks and the design of time scales". *Rev. Sci. Instrum.*, 83(021101), 2012. 12

[67] M. D. Rotondaro and G. P. Perram. "Collisional broadening and shift of the rubidium D_1 and D_2 lines ($5^2S_{1/2} \rightarrow 5^2P_{1/2}$, $5^2P_{3/2}$) by rare gases, H_2, D_2, CH_4 and CF_4". *J. Quant. Spectrosc. Radiat. Transfer*, 57(4):497–507, 1997. 13, 19, 114

[68] U. Fano. "Description of States in Quantum Mechanics by Density Matrix and Operator Techniques". *Rev. Mod. Phys.*, 29:74–93, 1957. 14

[69] C. Cohen-Tannoudji. *"Quantum Mechanics"*. Herman and John Wiley & Sons. Inc., 1977. 14

[70] A. Godone, F. Levi, S. Micalizio, and J. Vanier. "Dark-line in optically-thick vapors: inversion phenomena and line width narrowing ". *Eur. Phys. J. D*, 18:5–13, 2002. 16

[71] D. K. Walter, W. M. Griffith, and W. Happer. "Magnetic slowing down of spin relaxation due to binary collisions of alkali-metal atoms with buffer-gas atoms". *Phys. Rev. Lett.*, 88(093004), 2002. 19

[72] J. C. Camparo. "Semiempirical theory of Carver rates in alkali/noble-gas systems". *J. Chem. Phys.*, 126(244310), 2007. 19, 21

[73] P. J. Oreto, Y. Y. Jau, A. B. Post, N. N. Kuzma, and W. Happer. "Buffer-gas-induced shift and broadening of hyperfine resonances in alkali-metal vapors". *Phys. Rev. A*, 69(042716), 2004. 19

[74] F. A. Franz and C. E. Sooriamoorthi. "Spin relaxation within the $6^2\mathrm{P}_{1/2}$ and $6^2\mathrm{S}_{1/2}$ states of cesium measured by white-light optical pumping ". *Phys. Rev. A*, 10(126), 1974. 21

[75] W. Happer. "Optical Pumping". *Rev. Mod. Phys.*, 44(2):169, 1972. 21, 88, 103

[76] S. Micalizio, A. Godone, F. Levi, and J. Vanier. "Spin-exchange frequency shift in alkali-metal-vapor cell frequency standards". *Phys. Rev. A*, 73(033414), 2006. 22, 34, 103, 104

[77] G. Mileti, C. Affolderbach, F. Droz, and E. Murphy. "Navigating more precisely with laser clocks". ESA bulletin 122, May 2005. 23

[78] C. Affolderbach, R. Matthey, F. Gruet, T. Bandi, D. Miletic, P. Scherler, M. Durrenberger, and G. Mileti. "Gas cell laser clock technologies for atomic frequency standards". Executive summary 19392/05/NL/CP: LTF-01598-REP-0002, Université de Neuchâtel, October 2010. 23

[79] D. W. Allan. "Statistics of Atomic Frequency Standards". In *Proceedings of the IEEE*, volume 54, pages 221–230, February 1966. 24, 25

[80] IEEE-NASA symposium on the definition and measurement of short-term frequency stability. "Short-term frequency stability". In *Proceedings of the IEEE-NASA symposium on the definition and measurement of short-term frequency stability held at the Goddard Space Flight Center, Greenbelt, Maryland*, number 1078923 in NASA SP; 80, November 1964. 24

[81] IEEE. "Special Issue on Frequency Stability". In *Special Issue on Frequency Stability*, volume 54, 1966. 24

[82] J. A. Barnes et. al. "Characterization of Frequency Stability". *IEEE Trans. Instrum. Meas.*, IM-20(2):105–120, 1971. 25

[83] W. H. Riley. "Handbook of frequency stability analysis". Hamilton Technical Services, Beaufort, SC 29907, USA, July 2007. 25, 26

[84] E. Rubiola. *"Phase Noise and Frequency Stability in Oscillators"*. Cambridge university press, 2009. 26

[85] G. Mileti and P. Thomann. "Study of the S/N performance of passive atomic clocks using a laser pumped vapour". In *Proc. of 9th European Frequency and Time Forum (EFTF)*, pages 271–276, Besançon, France, March 1995. 26, 69

[86] G. Mileti, J. Deng, F. L. Walls, D. A. Jennings, and R. E. Drullinger. "Laser pumped rubidium frequency standards: new analysis and progress". *IEEE J. Quantum Electron.*, QE-34:233, 1998. 27, 52, 104, 126, 127

[87] J. G. Coffer, M. Anderson, and J. C. Camparo. "Collisional dephasing and the reduction of laser phase-noise to amplitude-noise conversion in a resonant atomic vapor". *Phys. Rev. A*, 65(033807), 2002. 27, 104, 106

[88] G. J. Dick. "Local oscillator induced instabilities in trapped ion frequency standards". In *Proc. of 19th Precise Time and Time Interval (PTTI) meeting*, pages 133–147, Redondo beach, CA, 1987. 27

[89] C. A. Greenhall and G. J. Dick. "Local oscillator limited frequency stability for passive atomic frequency standards using square wave frequency modulation". *IEEE Trans. Ultrason. Ferroelctr. Freq. Control*, 47(6):1593–1600, 2000. 27

[90] J. Q. Deng, G. Mileti, R. E. Drullinger, D. A. Jennings, and F. L. Walls. "Noise considerations for locking to the center of a Lorentzian line". *Phys. Rev. A*, 59(773), 1999. 27, 52, 54

[91] R. Menzel. *"Photonics: Linear and nonlinear interactions of laser light and matter"*. Springer, 2007. 28, 104

[92] B. E. A. Saleh and M. C. Teich. *"Fundamentals of photonics"*. John Wiley & Sons., Inc., 1991. 28, 90

[93] S. Micalizio, A. Godone, F. Levi, and C. Calosso. "Medium-Long Term Frequency Stability of Pulsed Vapor Cell Clocks". *IEEE Trans. Ultrason. Ferroelctr. Freq. Control.*, 57(7), 2010. 29, 30, 34, 35, 83

[94] D. Miletic, C. Affolderbach, M. Hasegawa, R. Boudot, C. Gorecki, and G. Mileti. "AC Stark-shift in CPT-based Cs miniature atomic clocks". *Appl. Phys. B: Lasers and Optics*, 109(1):89–97, 2012. 31

[95] C. Affolderbach and G. Mileti. "A compact laser head with high frequency stability for Rb atomic clocks and optical instrumentation". *Rev. Sci. Instrum.*, 76(073108), 2005. 31, 39, 41, 45, 99

[96] J. Camparo, J. Coffer, and J. Townsend. "Laser-pumped atomic clock exploiting pressure-broadened optical transitions". *J. Opt. Soc. Am. B*, 22(3):521–528, 2005. 32, 99, 114

[97] M. Arditi and T. R. Carver. "Pressure, Light, and Temperature Shifts in Optical Detection of 0-0 Hyperfine Resonacnce of Alkali Metals". *Phys. Rev.*, 124(3):800–809, 1961. 33

[98] J. Vanier, R. Kunski, N. Cyr, J. Y. Savard, and M. Têtu. "On Hyperfine Frequency Shifts Caused by Buffer Gases: Application to the Optically Pumped Passive Rubidium Frequency Standard". *J. Appl. Phys.*, 53(8):5387–5391, 1982. 33, 117

[99] S. Micalizio, A. Godone, F. Levi, and J. Vanier. "Erratum: Spin-exchange frequency shift in alkali-metal-vapor cell frequency standards". *Phys. Rev. A*, 73(033414), 2006. 34, 104

[100] A. Risely and G. Busca. "Effect of Line Inhomogeneity on the Frequency of Passive Rb^{87} Frequency Standards". In *Proc. 32nd Annual Symp. on Frequency Control*, 506-513. Electronic Industries Association, Washington DC, 1978. 35

[101] R. P. Frueholz, C. H. Folk, and J. C. Camparo. "Use of Wall Coated Cells in Atomic Frequency Standards". *J. Appl. Phys.*, 54(10):5613Ű5617, 1983. 35, 96

[102] J. C. Camparo, C. M. Klimcak, and S. J. Herbulock. "Frequency equilibration in the vapor-cell atomic clock". *IEEE Trans. Instrum. Meas.*, 54(5):1873–1880, October 2005. 36

[103] M. Bloch, O. Manchini, and T. McClelland. "Performance of rubidium and quartz clocks in space". In *IEEE Int. Freq. Control Symp.*, pages 505–509, 2002. 36

[104] C. E. Calosso, S. Micalizio, A. Godone, E. K. Bertacco, and F. Levi. "Electronics for the pulsed rubidium clock:design and characterization". *IEEE Trans. Instrum. Meas.*, 54:1731–1740, 2007. 39, 50, 54

[105] Laboratoire Temps-Fréquence. "European Space Agency (ESA) Project: contract 21504/08/NL/GLC". Technical notes and reports, 2008–2011. 39

[106] F. Gruet, M. Pellaton, C. Affolderbach, T. Bandi, R. Matthey, and G. Mileti. "Compact and frequency stabilized laser heads for rubidium atomic clocks". In *Proc. of International conference on Space Optics*, 9-12th, October 2012. 41, 42, 47, 100

[107] S. Micalizio, A. Godone, C. Calosso, F. Levi, C. Affolderbach, and F. Gruet. "Pulsed optically pumped rubidium clock with high frequency-stability performance". *IEEE Trans. Ultrason. Ferroelctr. Freq. Control.*, 59(3):457–462, 2012. 41, 79, 127, 138

[108] C. Affolderbach and G. Mileti. "Tunable, stabilised diode lasers for compact atomic frequency standards and precision wavelength references". *Optics and Lasers in Engineering*, 43:291–302, 2004. 41

[109] E. A. Donley, T. P. Heavner, F. Levi, M. O. Tataw, and S. R. Jefferts. "Double-pass acousto-optic modulator system". *Rev. Sci. Instrum.*, 76(063112), 2005. 42

[110] T. Bandi, C. Affolderbach, and G. Mileti. "Laser-pumped wall-coated cell rubidium frequency standard". *Journal of Applied Physics*, 111(124906), 2012. 43, 48, 135

[111] O. Schmidt, K.-M. Knaak, R. Wynands, and D. Meschede. "Cesium saturation spectroscopy revisited: How to reverse peaks and observe narrow resonances". *Appl. Phys. B*, 59:167–178, 1994. 44, 45

[112] T. W. Haensch, A. L. Schawlow, and G. W. Series. "The spectrum of atomic hydrogen". *Scientific American*, 240(94), 1979. 44

[113] K. B. MacAdam, A. Steinbach, and C. Wieman. "A narrow-band tunable diode laser system with grating feedback, and a saturated absorption spectrometer for Cs and Rb". *Am. J. Phys.*, 60:1098–1111, 1992. 44

[114] W. Demtröder. *"Laser spectroscopy: Basic concepts and instrumentation"*. Springer-Verlag Berlin Heidelberg, 1996. 44, 45

[115] D. Miletic, T. Bandi, C. Affolderbach, and G. Mileti. "AC Stark-shift in double resonance and coherent population trapping in a wall-coated cell for compact Rb atomic clocks". *Physica scripta*, T149(014012), 2012. 48, 64, 94

[116] C. E. Calosso, F. Levi, E. K. Vertacco, A. Godone, and S. Micalizio. "Low-noise electronic design for the 87Rb coherent population trapping maser". *IEEE Trans. Ultrason. Ferroelctr. Freq. Control.*, 52(11):1923–1930, 2005. 50, 54, 79

[117] C. Audoin, V. Chandelier, and N. Dimarcq. "A limit to the frequency stability of passive frequency standards". *IEEE Trans. Instrum. Meas.*, 40:121–125, 1991. 52

[118] P. Rochat, H. Schweda, G. Mileti, and G. Busca. "Developments of rubidium frequency standards at Neuchatel Observatory". In *Proc. of the 1994 IEEE International 48th Frequency Control Symposium*, page 716Ű723, 1994. 57, 61

[119] H. S. Schweda, G. Busca, and P. Rochat. "Atomic frequency standard", United States Patent 5387881, 1995. 57, 61, 65

[120] H. L. Hoyt. "Some fabrication techniques of spectral lamps and gas absorption cells for rubidium magnetometers". In *Proc. of the 22nd symposium on the art of glassblowing.* Wilmington, Delaware, 1978. 58

[121] D. J. Clack and J. M. Stanley. "The manufacture of alkali vapour cells for optical pumping experiments". *J Phys. E: Scientific Instruments*, 4:758–760, 1971. 58

[122] P. Violino. "Comment on ‘The manufacture of alkali vapour cells for optical pumping experiments’". *J Phys. E: Scientific Instruments*, 5:384–385, 1972. 58

[123] N. Castagna, G. Bison, G. Di Domenico, A. Hofer, P. Knowles, C. Macchione, H. Saudan, and A. Weis. "A large sample study of spin relaxation and magnetometric sensitivity of paraffin-coated Cs vapor cells". *Appl. Phys. B*, 96:763–772, 2009. 58

[124] M. Bouchiat and J. Brossel. "Relaxation of Optically Pumped Rb Atoms on Paraffin-Coated Walls". *Phys. Rev.*, 147:41–54, 1966. 58

[125] M. Pellaton, C. Affolderbach, R. Straessle, D. Briand, N. F. de Rooij, and G. Mileti. "Wall-coated cells for Rb atomic clocks: Study of the ripening process by double-resonance spectroscopy". In IEEE conference publications, editor, *Proc. of the 26th European Frequency and Time Forum (EFTF), Gothenburg, Sweden*, 2012. 58, 89, 90

[126] J. Kitching, S. Knappe, and L. Hollberg. "Atomic Vapor Cells for Miniature Frequency References". *Appl. Phys. Lett.*, 81:553, 2002. 59

[127] T. Bandi, C. Affolderbach, C. Calosso, and G. Mileti. "Studies on an improved compact physics package for Rb cell standards". In *Proc. of 42nd Precise Time and Time Interval (PTTI) meeting*, pages 329–342, Virginia, USA, 2010. 59

[128] A. Godone, S. Micalizio, F. Levi, and C. Calosso. "Microwave cavities for vapor cell frequency standards". *Rev. Sci. Instrum.*, 82(074703), 2011. 61

[129] W. Francisz and J. S. Hyde. "The loop-gap resonator: a new microwwave lumped circuit ESR sample structure". *Journal of Magnetic Resonance*, 47:515–521, 1982. 61, 62, 63, 64

[130] G. A. Rinard and G. R. Eaton. *"Biomedical EPR - Part B: Methodology, Instrumentation, and Dynamics"*, volume 24/B. Springer USA, 2005. 61

[131] W. N. Hardy and L. A. Whitehead. "Split-ring resonator for use in magnetic resonance from 200-2000 MHz". *Rev. Sci. Instrum.*, 52(2):213–216, 1981. 61

[132] T. Sphicopoulos and F. Gardiol. "Slotted tube cavity: a compact resonator with empty core". In *Microwaves, Antennas and Propagation*, volume 134, pages 405–410. IEEE, 1987. 61

[133] B. Xia, D. Zhong, S. An, and G. Mei. "Characteristics of a novel kind of miniaturized cavity-cell assembly for rubidium frequency standards". *IEEE Trans. Instrum. Meas.*, 55(3):1000–1005, 2006. 61

[134] H. Schweda. "Development of a miniature microwave loop-gap resonator with improved quality factor". ESA tech. report WP1, Observatoire Cantonal de Neuchatel, 7 1991. 61, 62, 65

[135] M. Mehdizadeh and T. Ishii. "Electromagnetic field analysis and calculation of the reesonance characteristics of the loop-gap resonator". *IEEE Trans. Microwave Theory Tech.*, 37(1113), 1989. 62

[136] C. Stefanucci, T. Bandi, F. Merli, M. Pellaton, C. Affolderbach, G. Mileti, and A. K. Skrivervik. "Compact microwave cavity for high performance rubidium frequency standards". *Rev. Sci. Instrum.*, 83(104706), 2012. 63, 64

[137] "High frequency structure simulator (HFSS)", version 13.0, 2011. 63

[138] C. Affolderbach, T. Bandi, R. Matthey, F. Gruet, M. Pellaton, and G. Mileti. "Compact, high- stability Rb atomic clocks for space". In *Proc. of the 3^{rd} International Colloquium -Scientific and Fundamental Aspects of the Galileo Programme, Copenhagen, Denmark*, volume 2. ESA special publication, 2011. 65

[139] C. Affolderbach, F. Gruet, D. Miletic, and G. Mileti. "Optimizing a high-stability cw laser-pumped Rubidium gas-cell frequency standard". In L. Maleki, editor, *Proceedings of the 7^{th} Symposium on Frequency Standards and Metrology*, pages 363–367, USA, 5-11 October 2008 2009. World Scientific. 71, 74

[140] T. W. Kornack, S. J. Smullin, S.-K. Lee, and M. V. Romalis. "A low-noise ferrite magnetic shield". *Appl. Phys. Lett.*, 90(223501), 2007. 83

[141] D. Budker, L. Hollberg, DF Kimball, J. Kitching, S. Pustelny, and V. V. Yashchuk. "Microwave Transitions and Nonlinear Magneto-Optical Rotation in Anti-Relaxation-Coated Cells". *Phys. Rev. A*, 71(1):012903, 2005. 86, 87, 88, 96, 102, 103

[142] E. B. Alexandrov, M. V. Balabas, D. Budker, D. S. English, D. F. Kimball, C.-H. Li, and V. V. Yashchuk. "Light-Induced Desorption of Alkali Atoms from Paraffin Coating". *Phys. Rev. A*, 66(042903), 2004. 86

[143] E. B. Alexandrov, M. V. Balabas, D. Budker, D. S. English, D. F. Kimball, C.-H. Li, and V. V. Yashchuk. "Erratum: Light-Induced Desorption of Alkali Atoms from Paraffin Coating". *Phys. Rev. A*, 70(e049902), 2004. 86

[144] A. Burchianti, C. Marinelli, A. Bogi, and al. "Light-Induced Atomic Desorption from Porous Silica". *Euro. Phys. Lett.*, 67(6):983Ű989, 2004. 86

[145] C. Rahman and H. G. Robinson. "Rb 0-0 Hyperfine Transition in Evacuated Wall-coated Cell at Melting Temperature". *IEEE J. Quantum Electron*, 23:1533–1539, 1987. 87, 101, 103

[146] M. Stephens, R. Rhodes, and C. Wieman. "Study of Wall Coatings for Vapour-cell Laser Traps". *J. Appl. Phys.*, 76:3479, 1994. 87, 91

[147] H. M. Goldenberg, D. Kleppner, and N. F. Ramsey. "Atomic Beam Resonance Experiments with Stored Beams". *Phys. Rev.*, 123(530), 1961. 87, 88

[148] M. V. Balabas, M. I. Karuzin, and A. S. Pazgalev. "Experimental investigation of the longitudinal relaxation time of electronic polarization of the ground state of potassium atoms in a cell with an antirelaxation coating on the walls". *JETP letters*, 70(3), 1999. 91, 92

[149] M. V. Balabas, K. Jensen, W. Wasilewski, H. Krauter, L. S. Madsen, J. H. Miller, T. Fernholz, and E. S. Polzik. "High quality anti-relaxation coating material for alkali atom vapor cells". *Opt. Express*, 18(5825), 2010. 93

[150] D. Budker and M. Romalis. "Optical Magnetometry". *Nat. Phys.*, 3:227, 2007. 102

[151] T. Bandi, D. Miletic, F. Gruet, M. Pellaton, C. Affolderbach, P. Scherler, M. Durrenberger, and G. Mileti. "Final report: Next generation compact

atomic clocks". ESA technical note LTF-01603-FR-0001, Laboratoire Temps-Fréquence, Université de Neuchâtel, September 2011. 107

[152] S. Knappe and H. G. Robinson. "Double-resonance lineshapes in a cell with wall coating and buffer gas". *New J. Phys.*, 12(065021), 2010. 108

[153] S. J. Seltzer and M. V. Romalis. "High-temperature alkali vapor cells with antirelaxation surface coatings". *J. Appl. Phys.*, 106(114905), 2009. 108

[154] S. Knappe, P. D. D. Schwindt, V. Gerginov, V. Shah, L. Liew, J. Moreland, H. G. Robinson, L. Hollberg, and J. Kitching. "Microfabricated atomic clocks and magnetometers". *J. Optics: Pure and Appl. Optics*, 8(S318), 2006. 108

[155] Y. W. Yi, H. G. Robinson, S. Knappe, J. E. Maclennan, C. D. Jones, C. Zhu, N. A. Clark, and J. Kitching. "Method for characterizing self-assembled monolayers as antirelaxation wall coatings for alkali vapor cells". *J. Appl. Phys.*, 104(023534), 2008. 108

[156] S. J. Seltzer, D. J. Michalak, M. H. Donaldson, M. V. Balabas, S. K. Barber, S. L. Bernasek, M.-A. Bouchiat, A. Hexemer, A. M. Hibberd, D. F. Jackson Kimball, C. Jaye, T. Karaulanov, F. A. Narducci, S. A. Rangawala, H. G. Robinson, A. K. Shmakov, D. L. Voronov, V. V. Yashchuk, A. Pines, and D. Budker. "Investigation of antirelaxation coatings for alkali-metal vapor cells using surface science techniques". *J. Chem. Phys.*, 133(144703), 2010. 108

[157] C. Affolderbach. "Performance verification of atomic resonator and electronics for initial evaluations, including gas cell production and evaluation (TN3)". ESA technical report LTF-01427-TN-0003, Université de Neuchâtel, July 2008. 117, 125, 133

[158] T. C. English, E. Jechart, and T. M. Kwon. "Elimination of the light shift in rubidium gas cell frequency standards using pulsed optical pumping". In L. J. Rueger, editor, *10th Precise Time and Time Interval Forum*, pages 147–165. NASA, Maryland, 1978. 122

[159] J. C. Camparo. "Conversion of laser phase noise to amplitude noise in an optically thick vapor". *J. Opt. Soc. Am. B*, 15:1177–1186, 1998. 126

[160] R. F. C. Vessot. "The atomic hydrogen maser oscillator". *Metrologia*, 42(S80), 2005. 127

[161] J. Vanier. "Atomic clocks based on coherent population trapping: a review". *Appl. Phys. B*, 81:421–442, 2005. 127

[162] C. E. Calosso, A. Godone, F. Levi, and S. Micalizio. "Enhanced temperature sensitivity in vapor-cell frequency standards". *IEEE Trans. Ultrason. Ferroelctr. Freq. Control.*, 59(12), 2012. 129, 131, 134

[163] C. Affolderbach, R. Matthey, F. Gruet, T. Bandi, and G. Mileti. "Realisation of a compact laser-pumped Rubidium frequency standard with $< 1{\times}10^{-12}$ stability at 1 second". In *Proc. of 24th European Frequency and Time Forum (EFTF)*, 2010. 133

[164] T. Bandi, C. Affolderbach, and G. Mileti. "Studies on an improved compact physics package for Rb cell standards". In *Proc. of the 42nd annual Precise Time and Time Interval (PTTI) systems and applications meeting, Reston, Virginia*, November 2010. 134

[165] F.-X. Esnault, J. Kitching, and E. A. Donley. "A compact cold-atom frequency standard based on coherent population trapping". In *Proc. of 2012 IEEE International Frequency Control Symposium*, Baltimore, USA, 2012. 138

[166] V. Shah, R. Lutwak, R. Stoner, and M. Mescher. "A compact and low-power cold atom clock". In *Proc. of 2012 International Frequency Control Symposium*, Baltimore, USA, 2012. 138

[167] Symmetricom. "MHM 2010: active hydrogen maser for applications that require extreme frequency stability, low phase noise and long service life", 2013. 138

[168] C. Affolderbach, T. Bandi, R. Matthey, F. Gruet, M. Pellaton, and G. Mileti. "Compact, high- stability Rb atomic clocks for space". In ESA special publication, editor, *Proc. of the 3rd International Colloquium – Scientific and Fundamental Aspects of the Galileo Programme*, number 1400, page 326, Copenhagen, Denmark, 2011. 138

[169] L. Cacciapuoti. "Atomic clock ensemble in space (ACES)". In *International workshop on Advances in Precision Tests and Experimental Gravitation in Space*, Firenze, 2006. 138

[170] Symmetricom. "5071A: Accuracy, stability and reliability for demanding laboratory and field applications", 2013. 138

[171] T. Dass, G. Freed, J. Petzinger, and J. Rajan. "GPS clocks in space: current performance and plans for the future". In *Proc. of 34^{th} Annual Precise Time and Time Interval (PTTI) meeting*, Reston, Virginia, 2002. 138

[172] T. Bandi, P. Scherler, C. Affolderbach, and G. Mileti. "WP3200- Auxiliary unit phyiscs package subsystems design and breadboarding". Technical Report LTF-01427-TN-0003A1, Laboratorie Temps-Fréquence (LTF), 2010. 139

[173] R. Matthey, C. Affolderbach, and G. Mileti. "Methods and evaluation of frequency aging in DFB laser diodes for Rubidium atomic clocks". *Optics Letters*, 36(17):3311–3313, 2011. 139

[174] J. D. Prestage and G. L. Weaver. "Atomic clocks and oscillators for deep-space navigation and radio science". In *Proc. of IEEE: Technical advances in deep space communications and tracking*, volume 95, page 2235, 2007. 140

[175] S. A. Diddams, J. C. Bergquist, S. R. Jefferts, and C. W. Oates. "Standards of time and frequency at the outset of the 21st centuary". *Science*, 306:1318–1324, 2004. 140

[176] M. A. Lombardi. "The use of GPS disciplined oscillators as primary frequency standards for calibration and metrology". *Measure: The Journal of measurement science*, 3:56–65, 2008. 140

[177] M. A. Lombardi. "Microsecond accuracy at multiple sites: Is it possible without GPS". *IEEE Instrumentation & Measurement Magazine*, pages 14–21, 2012. 140

[178] P. J. Mohr, B. N. Taylor, and D. B. Newell. "CODATA Recommended Values of the Fundamental Physical Constants: 2010". *Rev. Mod. Phys.*, 84:1527–1605, 2012. 159

[179] D. A. Steck. "Rubidium 87 D line data", September 2011. 159, 160, 161, 162

[180] J. Ye, S. Swartz, P. Jungner, and J. L. Hall. "Hyperfine structure and absolute frequency of the ^{87}Rb $5P_{3/2}$ state". *Optics Letters*, 21:1280, 1996. 160

APPENDIX A: Fundamental physical constants and ^{87}Rb properties

This appendix gives essential values of fundamental physical constants and important physical, optical and chemical properties of the ^{87}Rb atom.

Fundamental physical constants [178]. Table taken from [179]

Speed of Light	c	$2.997\ 924\ 58 \times 10^{8}$ m/s (exact)
Permeability of Vacuum	μ_0	$4\pi \times 10^{-7}$ N/A^2 (exact)
Permittivity of Vacuum	ϵ_0	$(\mu_0 c^2)^{-1}$ (exact) $= 8.854\ 187\ 817\ldots \times 10^{-12}$ F/m
Planck's Constant	h	$6.626\ 068\ 96(33) \times 10^{-34}$ J·s $4.135\ 667\ 33(10) \times 10^{-15}$ eV·s
	$\hbar$	$1.054\ 571\ 628(53) \times 10^{-34}$ J·s $6.582\ 118\ 99(16) \times 10^{-16}$ eV·s
Elementary Charge	e	$1.602\ 176\ 487(40) \times 10^{-19}$ C
Bohr Magneton	μ_B	$9.274\ 009\ 15(23) \times 10^{-24}$ J/T $h \cdot 1.399\ 624\ 604(35)$ MHz/G
Atomic Mass Unit	u	$1.660\ 538\ 782(83) \times 10^{-27}$ kg
Electron Mass	m_e	$5.485\ 799\ 0943(23) \times 10^{-4}$ u $9.109\ 382\ 15(45) \times 10^{-31}$ kg
Bohr Radius	a_0	$0.529\ 177\ 208\ 59(36) \times 10^{-10}$ m
Boltzmann's Constant	k_B	$1.380\ 6504(24) \times 10^{-23}$ J/K

Rubidium-87 physical properties. Table taken from [179].

Atomic Number	Z	37
Total Nucleons	$Z + N$	87
Relative Natural Abundance	$\eta(^{87}\mathrm{Rb})$	27.83(2)%
Nuclear Lifetime	τ_n	4.88×10^{10} yr
Atomic Mass	m	86.909 180 520(15) u $1.443\ 160\ 648(72) \times 10^{-25}$ kg
Density at 25°C	ρ_m	1.53 g/cm^3
Melting Point	T_M	39.30 °C
Boiling Point	T_B	688 °C
Specific Heat Capacity	c_p	0.363 J/g·K
Molar Heat Capacity	C_p	31.060 J/mol·K
Vapor Pressure at 25°C	P_v	$3.92(20) \times 10^{-7}$ torr
Nuclear Spin	I	3/2
Ionization Limit	E_I	33 690.804 80(20) cm^{-1} 4.177 127 06(10) eV

Energy level diagram of the ^{87}*Rb atom [59, 180]. Table taken from [179].*

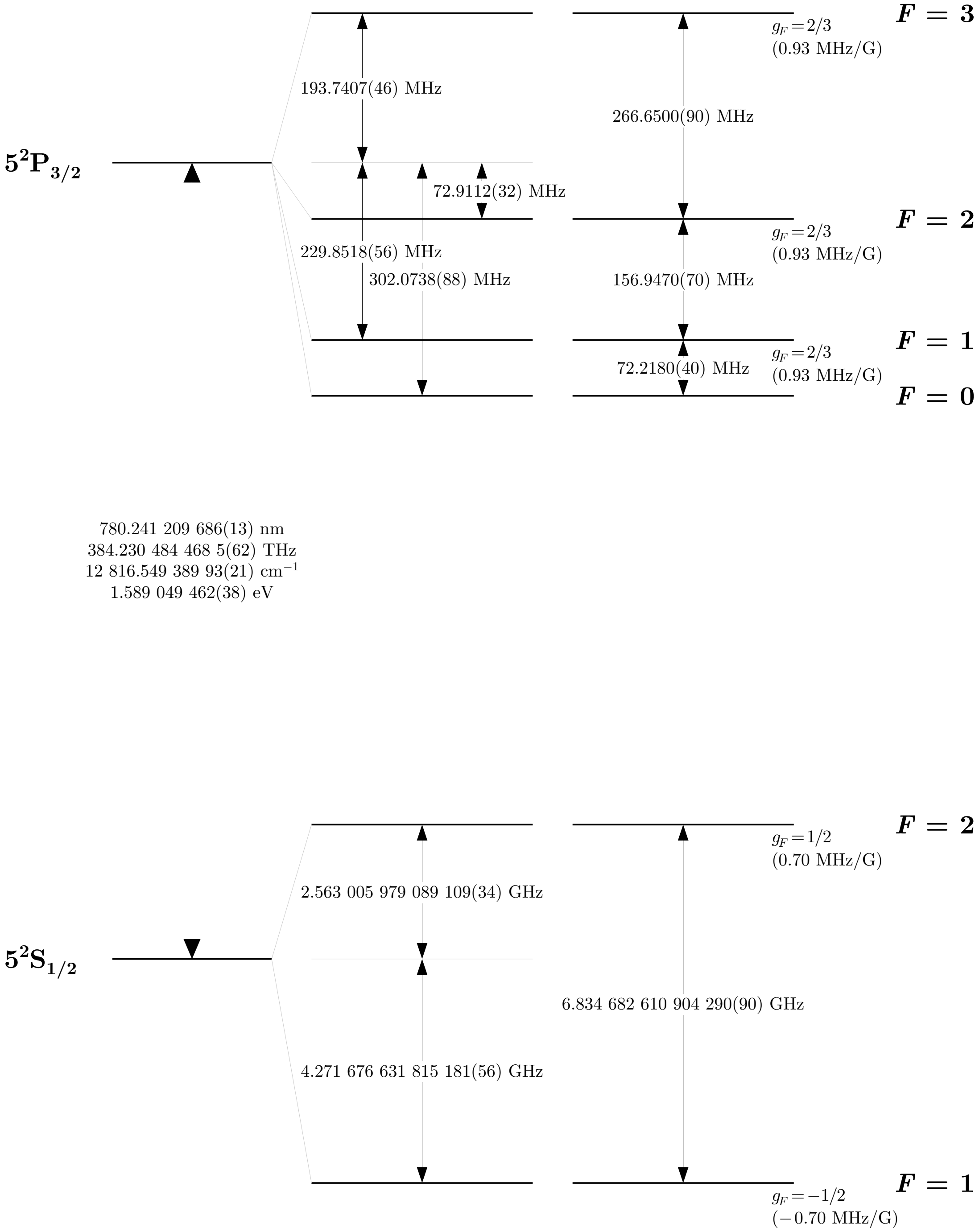

Rubidium 87 D_2 transition optical properties. Table taken from [179].

Frequency	ω_0	$2\pi \cdot 384.230\,484\,468\,5(62)$ THz
Transition Energy	$\hbar\omega_0$	$1.589\,049\,462(38)$ eV
Wavelength (Vacuum)	λ	$780.241\,209\,686(13)$ nm
Wavelength (Air)	λ_{air}	$780.033\,330(23)$ nm
Wave Number (Vacuum)	$k_{\mathrm{L}}/2\pi$	$12\,816.549\,389\,93(21)\ \mathrm{cm}^{-1}$
Isotope shift	$\omega_0(^{87}\mathrm{Rb}) - \omega_0(^{85}\mathrm{Rb})$	$2\pi \cdot 78.095(12)$ MHz
Lifetime	τ	$26.2348(77)$ ns
Decay Rate/ Natural Line Width (FWHM)	Γ	$38.117(11) \times 10^6\ \mathrm{s}^{-1}$ $2\pi \cdot 6.0666(18)$ MHz
Absorption oscillator strength	f	$0.695\,77(29)$
Recoil Velocity	v_{r}	5.8845 mm/s
Recoil Energy	ω_{r}	$2\pi \cdot 3.7710$ kHz
Recoil Temperature	T_{r}	361.96 nK
Doppler Shift ($v_{\mathrm{atom}} = v_{\mathrm{r}}$)	$\Delta\omega_{\mathrm{d}}(v_{\mathrm{atom}} = v_{\mathrm{r}})$	$2\pi \cdot 7.5419$ kHz
Doppler Temperature	T_{D}	$145.57\ \mu$K
Frequency shift for standing wave moving with $v_{\mathrm{sw}} = v_{\mathrm{r}}$	$\Delta\omega_{\mathrm{sw}}(v_{\mathrm{sw}} = v_{\mathrm{r}})$	$2\pi \cdot 15.0839$ kHz

Rubidium 87 D_2 transition dipole matrix elements, saturation intensities and resonant scattering cross sections. Table taken from [179].

$\mathrm{D}_2(5^2\mathrm{S}_{1/2} \longrightarrow 5^2\mathrm{P}_{3/2})$ Transition Dipole Matrix Element	$\langle J = 1/2 \Vert er \Vert J' = 3/2 \rangle$	$4.227\,52(87)\ ea_0$ $3.584\,24(74) \times 10^{-29}$ C·m
Effective Dipole Moment, Saturation Intensity, and Resonant Cross Section ($F = 2 \rightarrow F' = 3$) (isotropic light polarization)	$d_{\mathrm{iso,eff}}(F = 2 \rightarrow F' = 3)$	$2.042\,09(42)\ ea_0$ $1.731\,35(36) \times 10^{-29}$ C·m
	$I_{\mathrm{sat(iso,eff)}}(F = 2 \rightarrow F' = 3)$	$3.577\,13(74)\ \mathrm{mW/cm}^2$
	$\sigma_{0(\mathrm{iso,eff})}(F = 2 \rightarrow F' = 3)$	$1.356\,456\,704\,270(31) \times 10^{-9}\ \mathrm{cm}^2$
Effective Far-Detuned Dipole Moment, Saturation Intensity, and Resonant Cross Section (D_2 line, π-polarized light)	$d_{\mathrm{det,eff,D_2}}$	$2.440\,76(50)\ ea_0$ $2.069\,36(43) \times 10^{-29}$ C·m
	$I_{\mathrm{sat(det,eff,D_2)}}$	$2.503\,99(52)\ \mathrm{mW/cm}^2$
	$\sigma_{0(\mathrm{det,eff,D_2})}$	$1.937\,795\,291\,814(44) \times 10^{-9}\ \mathrm{cm}^2$
Dipole Moment, Saturation Intensity, and Resonant Cross Section $\vert F = 2, m_F = \pm 2\rangle \rightarrow \vert F' = 3, m'_F = \pm 3\rangle$ cycling transition ($\sigma^{\pm}$-polarized light)	$d_{(m_F = \pm 2 \rightarrow m'_F = \pm 3)}$	$2.989\,31(62)\ ea_0$ $2.534\,44(52) \times 10^{-29}$ C·m
	$I_{\mathrm{sat}(m_F = \pm 2 \rightarrow m'_F = \pm 3)}$	$1.669\,33(35)\ \mathrm{mW/cm}^2$
	$\sigma_{0(m_F = \pm 2 \rightarrow m'_F = \pm 3)}$	$2.906\,692\,937\,721(66) \times 10^{-9}\ \mathrm{cm}^2$

Vapor pressure of rubidium as a function of temperature. The vertical line shows the melting point. Table taken from [179].

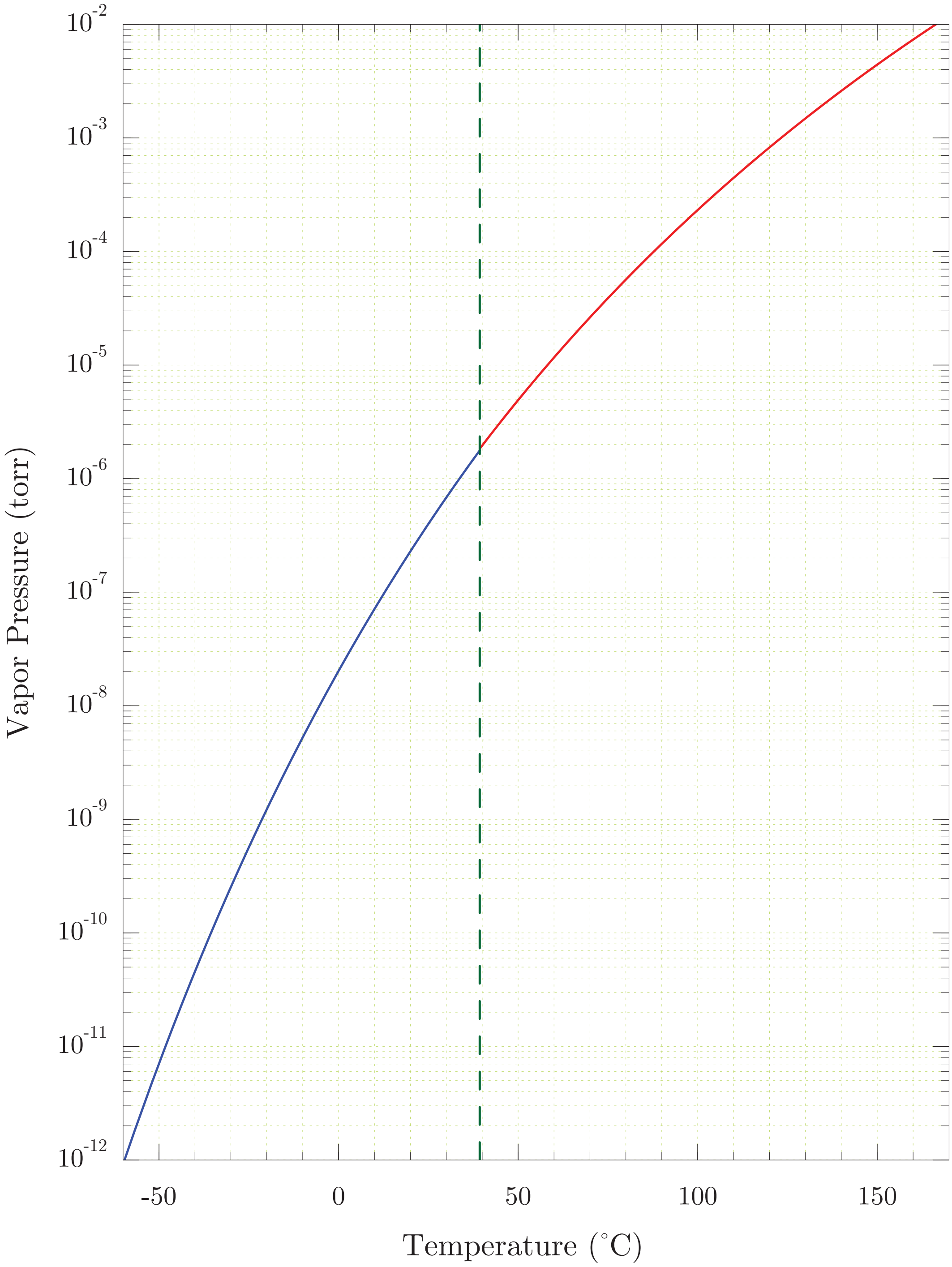

APPENDIX B: CAD designs of laser heads, cavities and physics packages

CAD designs (courtesy: P. Scherler, LTF) of the laser heads, assembled cavities and phyiscs packages that were used in this thesis are presented in this appendix with details on the components in each of them.

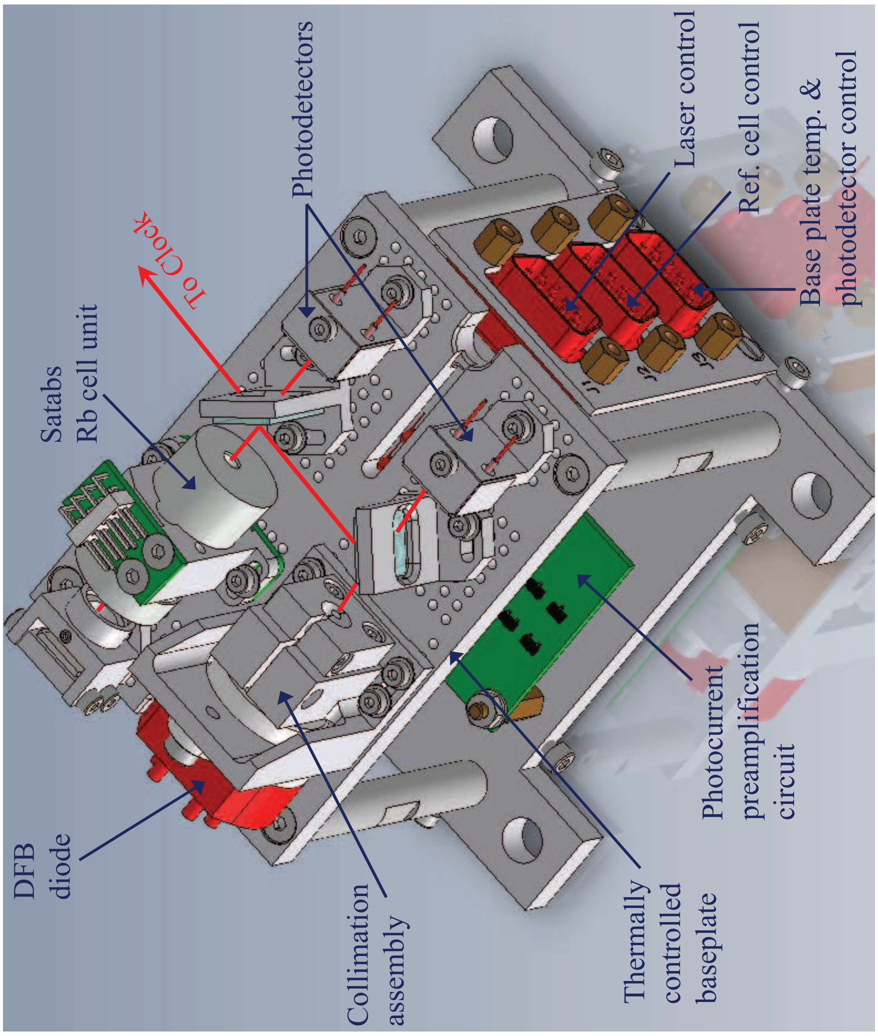

Figure 6.19: *CAD diagram of the clock laser head indicating important components and the laser beam paths (red lines).*

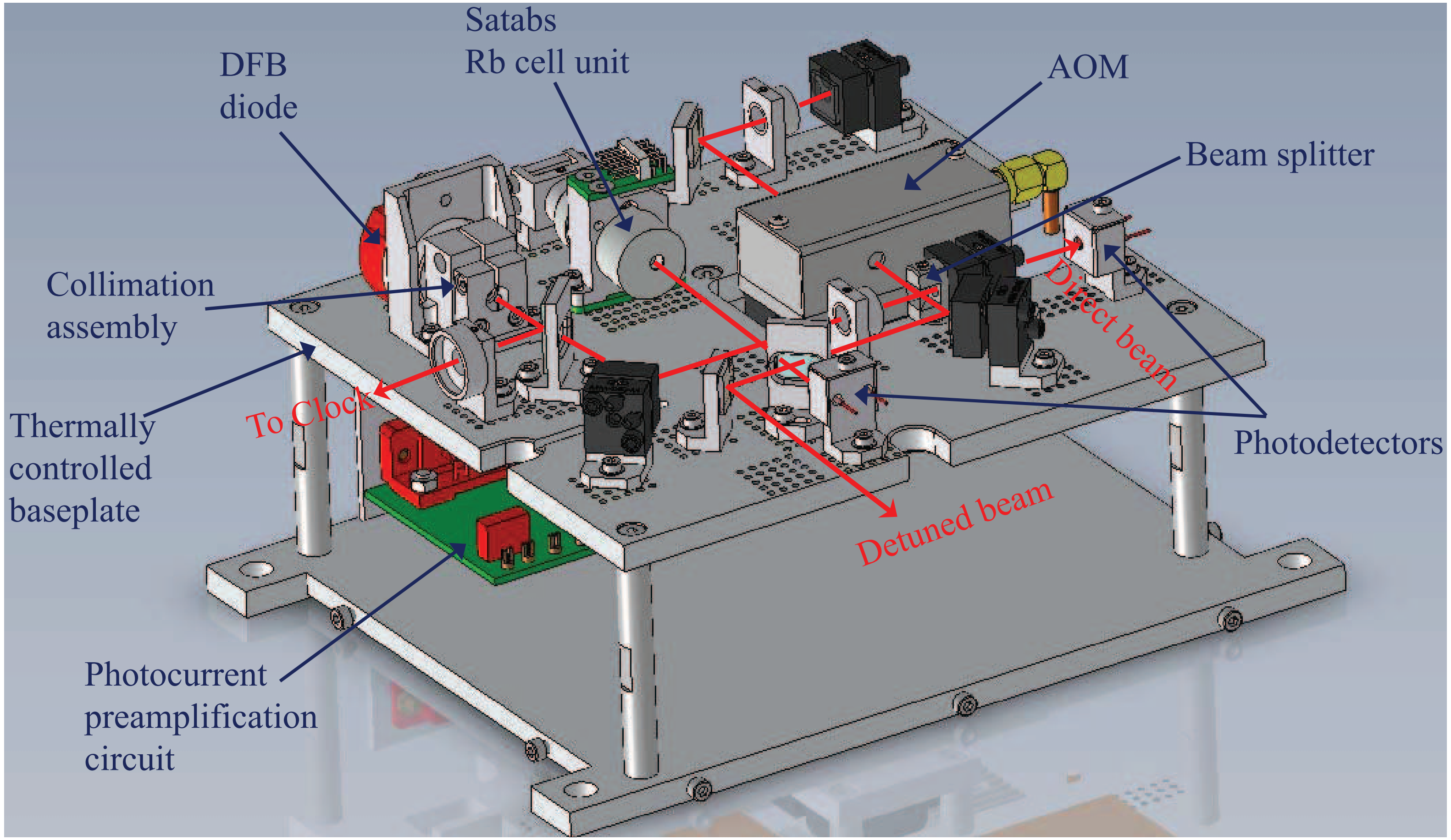

Figure 6.20: *CAD diagram of the AOM laser head indicating important components and the laser beam paths (red lines).*

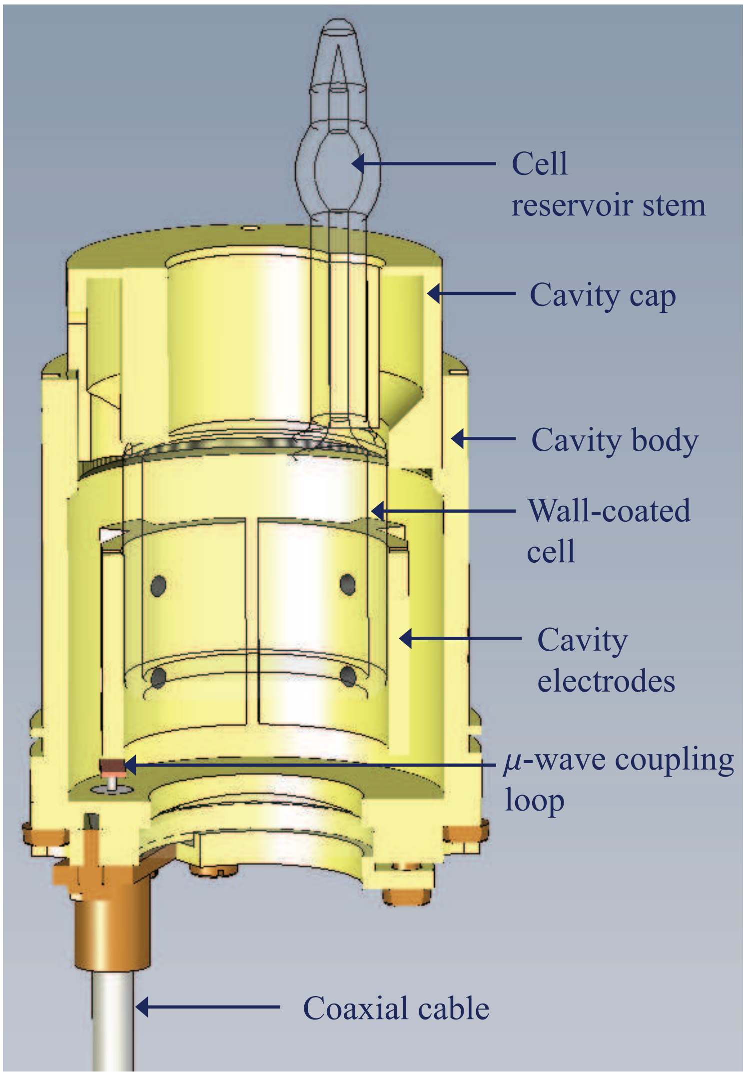

Figure 6.21: *CAD diagram of the compact magnetron type cavity with four electrodes, capable of holding the 14 mm diameter vapor cell.*

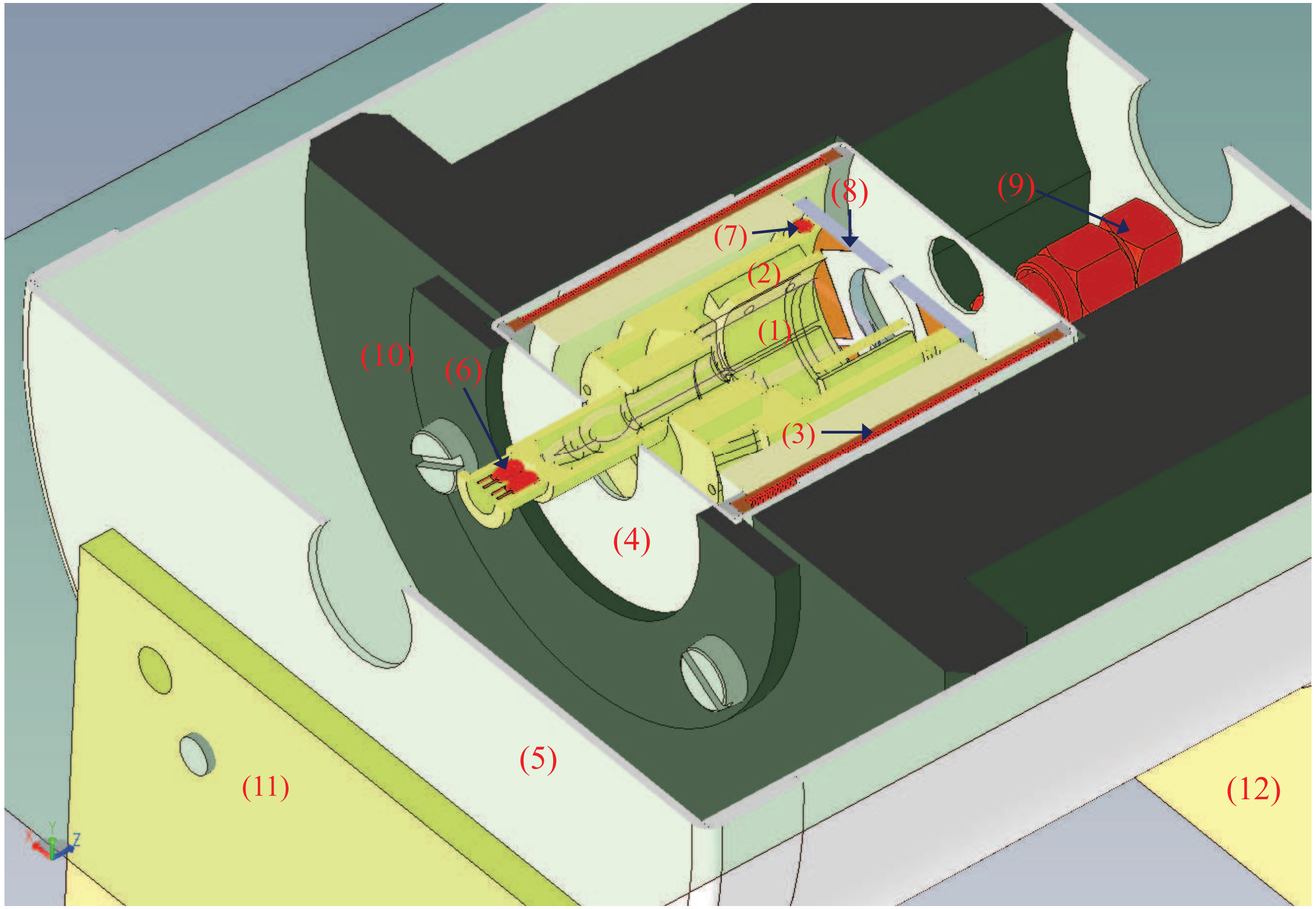

Figure 6.22: *CAD diagram of the completely assembled wall-coated cell physics package (PP), showing: (1) 14 mm diameter wall-coated cell; (2) magnetron cavity with four electrodes; (3) C-field coils; (4) & (5) μ-metal magnetic shields; (6) & (7) temperature control NTCs for stem and cell volume, respectively; (8) Aluminum holder; (9) co-axial cable; (10) delrin holder; (11) & (12) PP holder stands.*

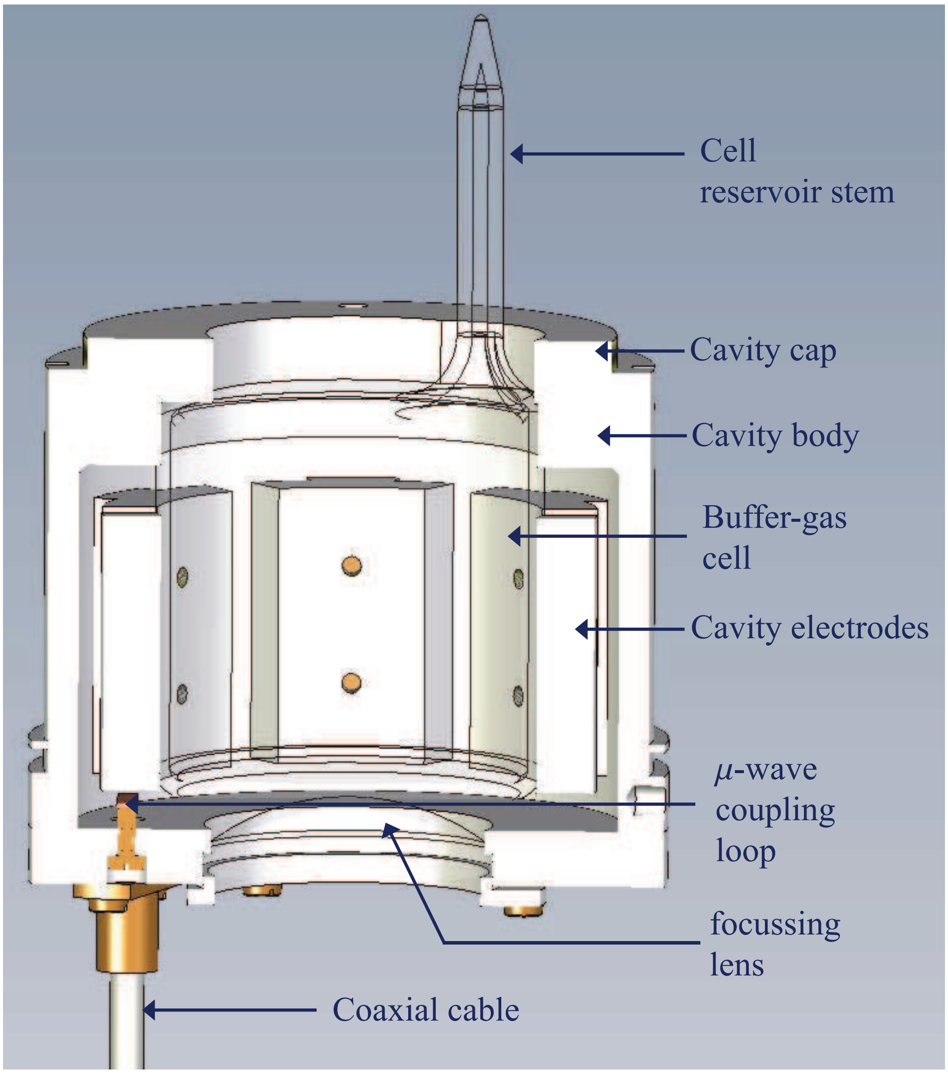

Figure 6.23: *CAD diagram of the newly designed enlarged magnetron type cavity with six electrodes, capable of holding the 25 mm diamter vapor cell.*

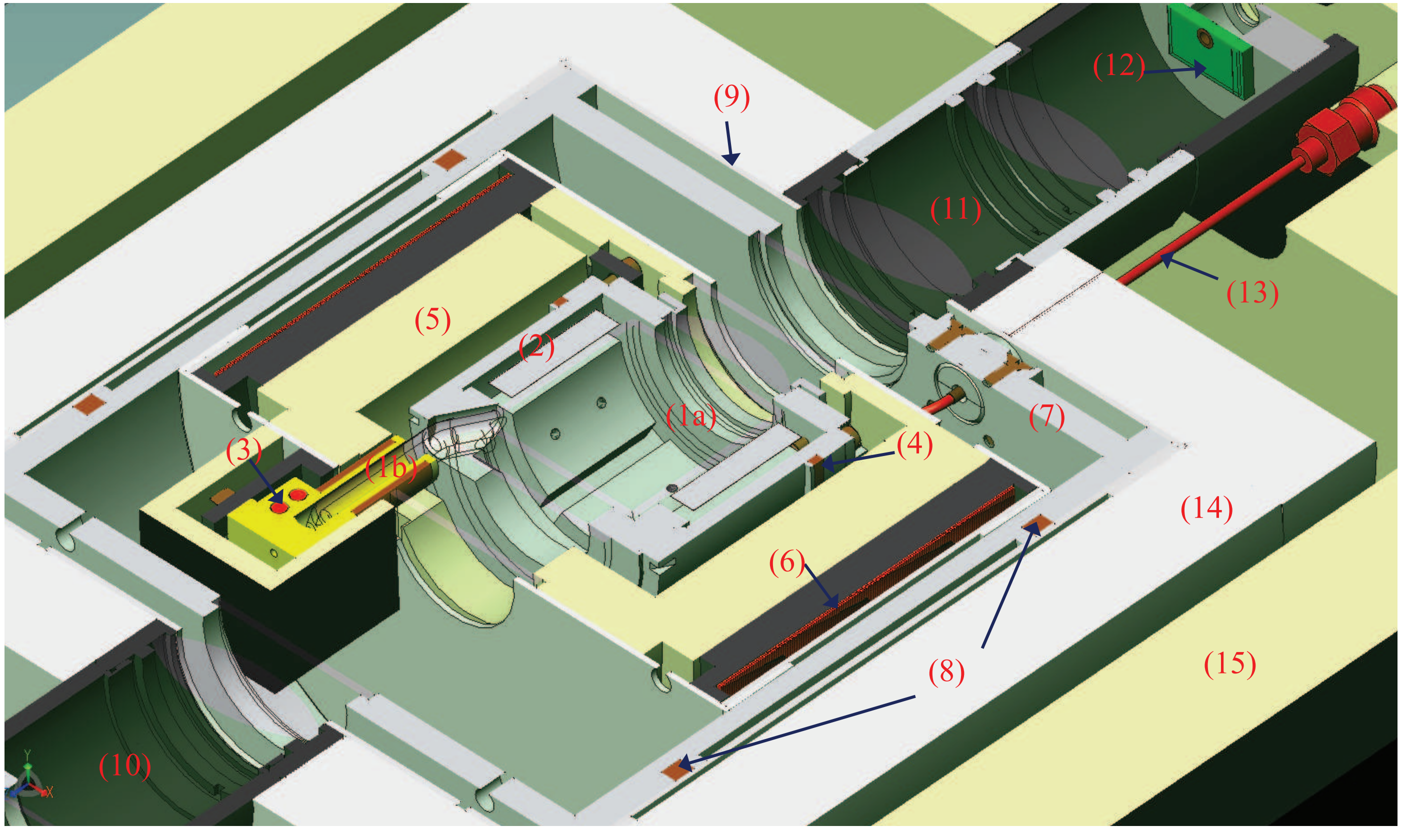

Figure 6.24: *CAD diagram of the completely assembled 25 mm diameter* ^{87}*Rb-buffer-gas cell physics package (PP), showing: (1a) & (1b) 25 mm diameter cell body and stem, respectively; (2) magnetron cavity with six electrodes; (3) heater and temperature control NTCs for stem; (4) heater and temperature control NTCs (not visible here) for the cell body; (5) Polyethylene foam ;(6) C-field coils; (7) Aluminum holder for uniform thermal gradience; (8) external control heaters; (9a) & (9b)* μ*-metal shields; (10) telescope assembly; (11) focussing assembly; (12) photodetector; (13) Co-axial cable; (14) Polysthylene foam ; and (15) Polystyrene insulator (Germatherm®).*